

PROCEEDINGS

***of the International Conference on
“The Technique of Microwave and THz Waves and
its Application in Biomedical and Radar Technologies
and in Remote Sensing”***



**September 23-25, 2010
Ashtarak-Aghveran, Armenia**

Organized by

- ✓ Institute of Radiophysics and Electronics National Academy of Sciences of Armenia
- ✓ International Science and Technology Center (ISTC), Grant SWS-170-10-SB89
- ✓ National Academy of Sciences of Armenia
- ✓ Yerevan State University

Organizing Committee

Chairman: Prof. Radik Martirosyan (Armenia)
Co-chairman: Dr. Arsen Hakhoumian (Armenia)
Co-chairman: Dr. Suren Gigoyan (Armenia)

Dr. Oleg Lapidus (Russia)
Dr. Hrachya Nersisyan (Armenia)
Prof. Karen Kocharyan (USA)
Dr. Emil Asmaryan (Armenia)
Prof. Arsen Hajian (Canada)
Dr. Stepan Yayloyan (Armenia)
Dr. Hapet Barsegyan (USA)
Prof. Vyacheslav Meriakri (Russia)

IRPhE'2010 TOPICS

- ✓ THz waves technologies and applications
- ✓ Microwave systems
- ✓ Microwave antennas and devices

UDC 53:06

ISBN 978-5-8080-0894-6

Preface

The International Conference “*The Technique of Microwave and THz Waves and its Application in Biomedical and Radar Technologies and in Remote Sensing*” (IRPhE’2010) was held in Ashtarak and Aghveran, Armenia, from September 23 to September 25, 2010. The IRPhE’2010 was dedicated to the 50th anniversary of the Institute of Radiophysics and Electronics of Armenian National Academy of Sciences and was directed to the revival of the traditional conferences organized by Institute of Radiophysics and Electronics since 1968. In the framework of the Conference two workshops were organized: “*Terahertz Technology in Biomedical Applications*” and “*Microwave applications in Radar and Remote Sensing*”.

CONTENTS

Section 1: THz Waves and Applications

Terahertz metallic photonic crystals with high metal filling factor <i>G. Torosyan, B. Reinhard, and R. Beigang</i>	3
Simulations of THz Wave Propagation in Gap Plasmon Waveguide Formed by Two Cylindrical Surfaces <i>H. S. Hakobyan, Y. H. Avetisyan, A. A. Barsegyan</i>	6
Terahertz Wave Confinement in Gap Plasmon Waveguide Fabricated by Composite Material <i>V. R. Tadevosyan, H. S. Haroyan, A.H. Makaryan, A. B. Hovsepyan, Yu. H. Avetisyan</i>	10
Integrated Millimeter-wave CPW to Dielectric Image-Guide Transitions in Silicon Technology <i>B. Biglarbegian, M. Basha, S. Gigoyan, S. Safavi-Naeini</i>	15
Whispering Gallery Mode Resonance Beyond 100 GHz <i>M. Neshat, A. Taeb, S. Gigoyan, and S. Safavi-Naeini</i>	18
“Hollow Dielectric Channel” in the Terahertz Range <i>M. Ts. Ayyvazyan, Yu. N. Kazantsev</i>	22
Oxide Nanointerface Engineering for Microwave Electronic Devices <i>K. Y. Constantinian, G. A. Ovsyannikov, A. V. Shadrin, Yu. V. Kislinkii, A. M. Petrzhik, A. V. Zaitsev, J. Mygind and D. Winkler</i>	26
Amplification of Coherent Cherenkov Radiation From One-Dimensional Electron Bunch Moving Inside a Layered Dielectric-Filled Waveguide <i>L. Sh. Grigoryan, H. F. Khachatryan, S. R. Arzumanyan</i>	32
Детектирование терагерцевых волн с помощью вакуумного диода <i>A. С. Ароян, А. А. Ахумян, А. Ю. Вартамян, А. О. Макарян, В. Р. Татевосян</i>	38
THz Pulse Generation in Nonlinear Crystals and Its Application in Medicine <i>A. S. Nikoghosyan</i>	42
Effect of Coherent Low Power Microwave Exposure on Tumor Cells DNA in Vivo <i>V. P. Kalantaryan, R. M. Martirosyan, L. E. Nersisyan, H. M. Stepanyan, J. V. Gharibyan</i>	48
Effect of Non-Thermal Microwave Radiation on Circulatory System <i>V. Kalantaryan, A. Hakhoumyan, T. Adamyan, E. Gevorkyan, H. Hovhanisyan, S. Minasyan</i>	51
Section 2: Microwave Systems	
Survey, Modeling and Simulation of Air to Ground Communication Channel <i>Morteza Faraji, M. A. Masnadi Shirazi, Mehdi Faraji</i>	59
The Russian VLBI Network QUASAR. Real Time and VLBI-Network of New Generation <i>A. Ipatov, A. Finkelstein, S. Smolentsev</i>	66
The Communication Systems for the Small Satellite Flying Laptop <i>U. Beyermann, C. Thibaut, F. Böhringer, H.-P. Röser, J. Baumgärtner, M. Spetzler</i>	72
Introduction to the Near-Field Microwave Microscopy <i>Kiejun Lee, A. Babajanyan, H. Melikyan, B. Friedman</i>	77
Light-Weight Short-Range Ku-Band CW-LFM Radar <i>A. Hakhoumian, R. M. Martirosyan, S. Martirosyan, A. Muzhikyan, V. Nikoghosyan, N. Poghosyan, T. Poghosyan, K. Rustamyan, T. Zakaryan</i>	87
L-Band Doppler Radar for Heartbeat Sensing <i>A. Hakhoumian, H. Hayrapetyan, S. Martirosyan, A. Muzhikyan, N. Poghosyan, T. Zakaryan</i>	91
On the Method of Distant Infrared Monitoring of Forest Spaces	94

<i>R. S. Asatryan, H. S. Karayan, N. R. Khachatryan, L. H. Sukoyan</i>	
Радиофизический комплекс обнаружения и оповещения <i>Р. М. Мартиросян, А. А. Абрамян, А. Г. Гулян, Р. Г. Симонян, Г. А. Пирумян, А. И. Смолин</i>	99
Scientific and Technical Investigations of Industrial Electron Accelerators <i>A. Poursaleh, A. Hakhoumian</i>	105
The New Design of RF System for High-Power Industrial Electron Accelerators <i>A. Poursaleh, A. Hakhoumian, B. Abbasi</i>	109
New Holographic Methods for Creation of 2D and 3D Micro- and Submicro-Scale Gratings in Photorefractive Materials <i>A. Badalyan, R. Hovsepyan, V. Mekhitaryan, P. Mantashyan, R. Drampyan</i>	113
C and Ku-Band, Two-Frequency, Polarimetric, Combined Doppler Scatterometer-Radiometer System for Land and Sea Surface Microwave Remote Sensing <i>A. K. Arakelyan, A. K. Hambaryan, V. V. Karyan, G. G. Hovhannisyanyan, A. A. Arakelyan, M. G. Simonyan, M. L. Grigoryan, T. N. Poghosyan, N. G. Poghosyan</i>	119
Multi-Frequency (at 5.6GHz, 15GHz and 37GHz) and Polarization Measurements of Clouds and Rain Effects on Perturbed Water Surface Microwave Reflection and Emission <i>M. L. Grigoryan, A. K. Arakelyan, A. K. Hambaryan, V. K. Hambaryan, V. V. Karyan, M. R. Manukyan, G. G. Hovhannisyanyan, A. A. Arakelyan</i>	125
Three-Frequency and Multi-Polarization Measurements of Bare and Vegetated Soils Microwave Reflective and Emissive Characteristics Angular Dependences by C, Ku and Ka-Band Combined Scatterometric-Radiometric Systems <i>A. K. Arakelyan, A. K. Hambaryan, V. K. Hambaryan, V. V. Karyan, M. R. Manukyan, M. L. Grigoryan, G. G. Hovhannisyanyan, A. A. Arakelyan</i>	131

Section 3: Microwave Antennas and Devices

Автоматический комплекс для определения параметров антенн диапазона КММВ методом планарного сканирования в их ближнем поле <i>В. Г. Аветисян</i>	139
Coaxial Microwave Radial Power Combiner/Divider <i>A. Hakhoumian, N. Poghosyan, T. Poghosyan, A. Gasparyan</i>	145
Modeling of Double Reflector Spherical Antennas <i>A. Sargsyan, H. Abrahamyan, V. Minasyan</i>	150
Mutual Coupling Reduction in Fractal Patch Antenna Based Phase Array <i>A. Hakhoumian, N. Poghosyan, A. Gasparyan, A. Kuzanyan</i>	155
Radar Cross-Section Near-Field Measurements <i>M. Ivanyan, N. Khachatryan, E. Tagvoryan</i>	159
Temperature Performance of a Two-Stage S-Band 40 Watt LDMOS Power Amplifier <i>A. Barsegyan, V. K. Thangam, J. Titizian</i>	164
High Power RF/Microwave Transistors, Pallets and Amplifiers from Integra Technologies, Inc. <i>A. Barsegyan</i>	169
Development of the Software Architecture for Control and Diagnosis of Devices in Heterogeneous Systems <i>M. V. Markosyan, A. L. Grigoryan, T. A. Papoyan</i>	173
Измеритель мощности миллиметрового и ИК диапазона <i>Р. А. Симонян, А. Г. Гулян, А. А. Саноян, Р. М. Киракосян</i>	176
The Application of the Developed Methods of Materials Joining in Electronic Engineering <i>V. Avagyan, T. Mkrtchyan, R. Mikaelyan</i>	180
Универсальное устройство для определения заряда химических источников тока <i>А. Р. Симонян, А. А. Саноян, А. Г. Гулян, Р. А. Симонян</i>	184
Универсальный термостатный модуль <i>Р. А. Симонян, А. А. Саноян, А. Г. Гулян</i>	187

Section 1:
THz Waves and Applications

Terahertz metallic photonic crystals with high metal filling factor

G. Torosyan¹, B. Reinhard², and R. Beigang^{1,2}

¹ Fraunhofer Institute for Physical Measurement Techniques IPM, 67663 Kaiserslautern, Germany

² Department of Physics, University of Kaiserslautern, 67663 Kaiserslautern, Germany

The excitation of resonant eigenmodes by incident terahertz (THz) pulses in two-dimensional metallic photonic crystals made of metallic cylindrical rods is investigated both experimentally and numerically. Transmission experiments are in excellent agreement with numerical calculations of the crystals' photonic band structures and internal electromagnetic field patterns of the cavities between the rods. The structures show large photonic band gaps in the terahertz spectral range and are highly polarization selective. Despite the high metal filling factor the measured transmittance at the resonant frequencies is extraordinarily high for the "correctly" polarized THz field. Correspondingly, the "wrongly" polarized field is completely reflected back without being coupled into the cavities and exciting no resonances there.

1. Introduction

Photonic crystals [1, 2] can be individually designed to meet specific requirements as to their interaction with electromagnetic radiation. Those may exhibit optical properties which cannot be observed in natural materials, e.g. negative refraction and left-handed transmission [3]. Photonic crystals operating at terahertz frequencies are particularly interesting, since that radiation offers many fields of practical application in science and technology, for which optical components functioning in this spectral range are required. Besides, investigating the transmission mechanisms of photonic crystals in the terahertz range allows easy fabrication of samples, as the wavelengths are comparably large. Although two-dimensional arrays of metallic cylinders have been extensively studied in the past, the regime of photonic crystals with a metal fraction of larger than 50% has remained largely unexplored so far.

2. Experiment

We report here the excitation of resonant modes in two-dimensionally periodic arrays consisting of steel cylinders. The distance between the constituents is kept as small as possible in order to obtain a high metal filling factor.

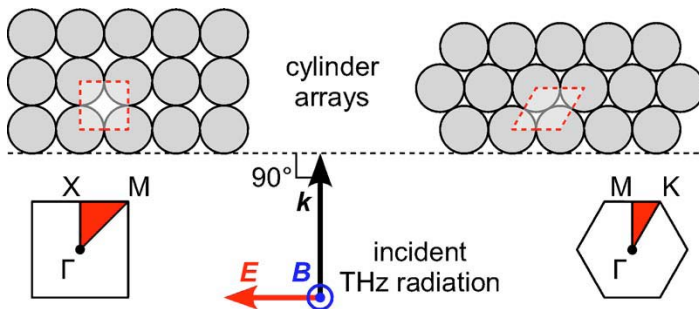


FIG.1. Schematic of the two cylinder patterns under investigation. Also depicted are the structures' Brillouin zones, the direction and polarization of the incident THz radiation.

Two different patterns: square and hexagonal (see Fig.1), of metallic structures with the metal filling factor of 78% and 90%, respectively, are investigated. Highlighted are the structures' unit cells. Note that the unit cell of the hexagonal array contains two separate cavities. The photonic crystals are assembled using 50 mm wide aluminum holders with periodically spaced holes in which 50 mm long steel cylinders are positioned. Transmission measurements are made for three values of the cylinder diameter d (1.0, 1.5, 2.0 mm) and different

sample thicknesses (up to sixteen layers of cylinders). The average distance left between the cylinders is less than $10 \mu\text{m}$ (i.e., less than 1% of the cylinder diameter and less than 5% of the THz wavelength). To investigate the samples' spectral properties a time-domain spectroscopy THz setup is used [4]. With this setup broadband pulses of approximately 1ps duration are created. The bandwidth of the pulses is 3.5 THz and is centred at 1 THz. The samples are placed in the collimated part of the THz beam which is approximately 40 mm in diameter. Progression of the pulses is measured in time domain, and then transformed into frequency domain with a fast Fourier transform. By dividing the spectrum of the transmitted pulse by that of a reference pulse measured without any sample in the beam, the photonic crystals' amplitude

transmittance as a function of frequency is obtained. The pulses are measured over a time period of 200 ps. That corresponds to a spectral resolution of 5 GHz.

3. Results and discussion

According to theory, an incident electromagnetic wave can excite an eigenmode of a photonic crystal if it matches that mode's frequency and the component of the wave vector parallel to the crystal surface. The electromagnetic eigenmodes are obtained from the equation

$$\vec{\nabla} \times \left[\frac{1}{\varepsilon(\vec{r})} \vec{\nabla} \times \vec{H}(\vec{r}) \right] = \left(\frac{\omega}{c} \right)^2 \vec{H}(\vec{r}) \quad (1)$$

which is directly derived from Maxwell's equations [5]. In addition to the experimental investigations,

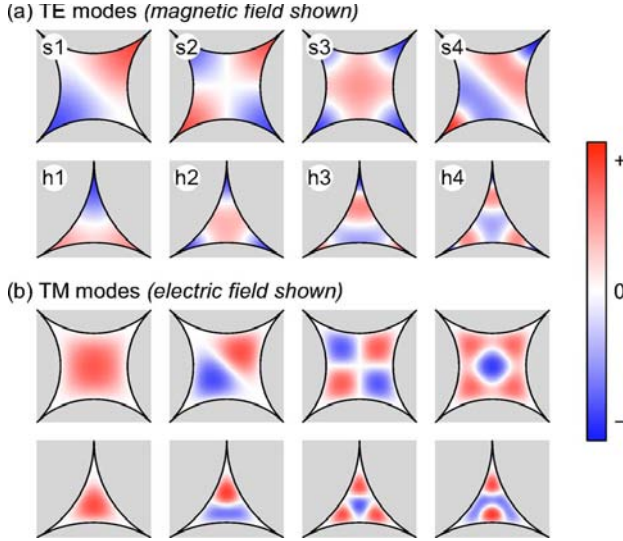


FIG. 2. Numerical calculations of the first **TE** and **TM** Eigenmodes in the cavities of square and hexagonal cylinder arrays.

numerical calculations are performed with the commercial software CST Microwave Studio®. In the calculations the photonic crystals are modelled as arrays of infinitely long, perfectly conducting cylinders in vacuum. The eigenvectors $\vec{H}(\vec{r})$ of this eigenvalue problem are the magnetic field patterns of the modes, the eigenvalues $(\omega/c)^2$ relate to their frequencies ω . The discrete translational symmetry of the problem leads to a discrete set of eigenmodes. Besides, in the case of two-dimensional photonic crystals, the eigenmodes separate into two independent sets according to the polarization angle of the fields with respect to the plane of periodicity. The two polarizations are transverse electric (TE: electric field perpendicular to the cylinder axes) and transverse magnetic (TM: magnetic field perpendicular to the axes). In our samples, the electromagnetic field is concentrated in the cavities between the metallic

cylinders. Depending on the cylinders' arrangement, the eigenmodes of the photonic crystals are similar to those of a waveguide with square or triangular cross

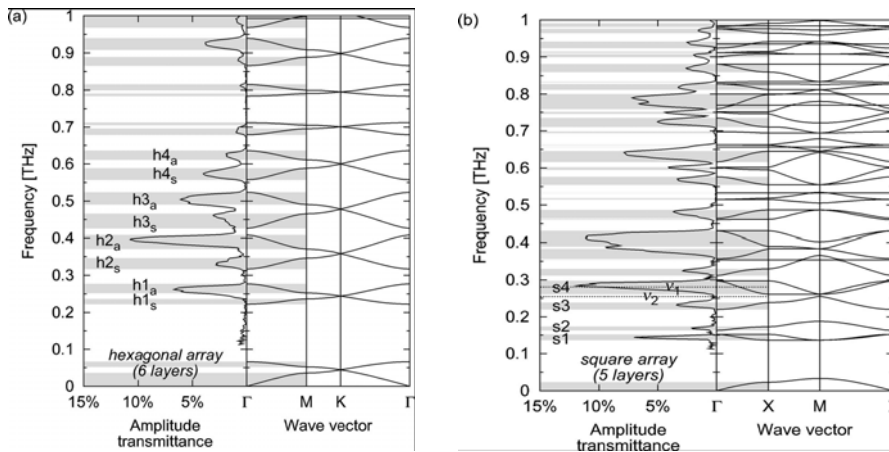


FIG.3. Transmission measurements and numerically calculated band structures of (a) the six-layer hexagonal array and (b) the five-layer square array of cylinders with $d=2.0$ mm.

section. Figure 2 shows some of the modes which our cylinder arrays can support. Note that the fields of all **TM** modes are zero at the points of contact between the cylinders. This is due to the fact that the electric

field has to be perpendicular to the metallic surfaces, and the gaps between the cylinders are small compared to the wavelength. Therefore, **TM**-polarized modes cannot enter the gaps. Neighboring cavities are entirely independent of each other, and the modes cannot propagate through the crystal. Propagating **TE** modes, however, are possible, as their fields are maximal at the points of contact. This leads to strong coupling between the cavities. In the hexagonal array, there is a splitting of the **TE** eigenmodes because the structure's unit cell contains two triangular cavities (cf. Fig. 1). Figure 3 shows numerical calculations of the band structures of a hexagonal and a square cylinder array

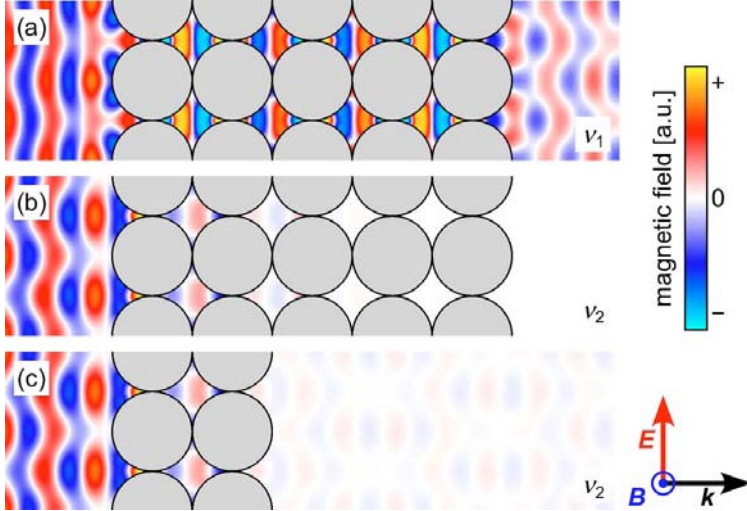


FIG. 4. Numerical simulations of a plane wave hitting a photonic crystal from the left. The magnetic field component perpendicular to the plane of periodicity is shown. (a) Resonant transmission at $\nu_1=0.281$ THz. (b) Evanescent wave at $\nu_2=0.255$ THz (photonic band gap, cf. Fig. 2). (c) Nonresonant transmission through a thin sample at $\nu_2=0.255$ THz.

compared to experimentally determined transmission spectra. Only zeroth-order amplitude transmittance is shown, higher orders of diffraction are not detected. It can be clearly seen that transmission occurs only at the frequencies where there are eigenmodes with wave vectors in the direction of the incident radiation (ΓX and ΓM directions, respectively). In the band gaps, transmission is zero. The results of numerical calculations of the band structures of a hexagonal and a square cylinder array are compared to experimentally determined transmission spectra. Fig. 4 shows the results of simulations for two different cases when the frequency is not in the band gap (resonant case: (a)), and when it is in the band gap (non-resonant case: (b) and (c)).

4. Summary

We have demonstrated that the excitation of resonant eigenmodes in the cavities of two-dimensional photonic crystals consisting of steel cylinders leads to extraordinary transmission of incident terahertz radiation at frequencies in the photonic bands. Each transmission band corresponds to a specific field pattern in the crystals' cavities. The fraction of the incident radiation that is transmitted through the samples is extraordinarily large compared to the very small area fraction of the openings in the structures. Because the gaps between the cylinders are very small compared to the wavelength, only **TE**-polarized radiation is transmitted through the samples. At frequencies in photonic band gaps, the radiation rapidly decays inside the crystals. Therefore, nonresonant transmission is very low and can only be observed with very thin samples.

References

- [1] E. Yablonovitch, Phys. Rev. Lett. **58**, (1987) 2059.
- [2] S. John, Phys. Rev. Lett. **58**, (1987) 2486.
- [3] C. Luo, S. G. Johnson, J. D. Joannopoulos, and J. B. Pendry, Opt. Express **11**, (2003) 746.
- [4] G. Torosyan, C. Rau, B. Pradarutti, and R. Beigang, Appl. Phys. Lett. **85**, (2004) 3372.
- [5] J.D. Joannopoulos, R.D. Meade, and J.N. Winn, Photonic Crystals: Molding the Flow of Light. Princeton University Press, Princeton, NJ, 2008.

Simulations of THz Wave Propagation in Gap Plasmon Waveguide Formed by Two Cylindrical Surfaces

H. S. Hakobyan¹, Y. H. Avetisyan¹, A. A. Barsegyan²

¹*Microwave Eng. Dept., Yerevan State University, Yerevan, 1 Alex Manoogian, 375025, Armenia,*

²*Integra Technologies, Inc., 321 Coral Circle, El Segundo, CA 90245, USA*

The terahertz (THz) wave propagation in gap plasmon waveguide formed by two cylindrical surfaces is simulated by use commercially available finite element method software COMSOL Multiphysics. The *n*-doped Si (with $N = 10^{18} \text{ cm}^{-3}$) is considered as cover material of cylinders. The results of simulation indicate 2-dimensional confined THz-wave propagation with high electric field concentration in a vicinity of the middle of waveguide. The THz beam size is estimated nearly $0.1 \times 1 \text{ mm}^2$ at 0.3 THz. The simulated electric field distribution is compared with results of calculation based on graded-index waveguide model. It is shown that parabolic profile of waveguide's effective refractive index well represent simulation results. THz-wave propagation in waveguide is accompanied by absorption in doped silicon, which is resulted in decay constant $\alpha \approx 0.3 \text{ mm}^{-1}$.

1. Introduction

The terahertz (0.1-10 THz) region of electromagnetic spectrum, located between millimeter wave and infrared frequencies, has found an increasing number of applications in security, biology, environment monitoring, sensing, and so on [1]. Most often, THz waves propagate in the free space, and the beams are usually shaped through quasi-optical technique. Recently, attention has been paid to guiding the THz waves into three dimensional metallic and dielectric waveguides [2]. The advantage of waveguiding techniques over free-space propagation is related to the possibility of guiding the beam along almost any arbitrarily shaped path and of manufacturing compact THz systems. Moreover, the power of the available table top THz sources is still rather low, thus limiting applications in which high intensities are needed.

A major challenge for the concentration of the electromagnetic energy in the THz region is the large radiation wavelength in vacuum ($\lambda = 30 \text{ }\mu\text{m} - 300 \text{ }\mu\text{m}$), where the THz radiation can be only focused to the relatively very large regions of size $\sim \lambda/2$. The developed field of optical energy concentration, which is based on surface plasmon polaritons (SPPs), suggests that one of the ways to solving this problem is to employ the plasmon waveguide. It has been demonstrated that in various type of the plasmonic waveguides the light (in visible and infrared regions) can be guided in a region beyond the so-called diffraction limit [3]. However the idea of SPP is not easily transformable from optics to THz range.

The strong field localization occurs for SPPs with frequencies close to the plasma frequency, which is defined by $\nu_p^2 = Ne^2 / 4\pi^2 m_e \epsilon_0$, where N is the electron density, e electron charge, ϵ_0 is the vacuum permittivity and m_e electron mass. Since the free electron density in metals is typically in order of 10^{22} cm^{-3} , the plasma frequency is limited to the visible and ultraviolet regions. At frequencies significantly below the plasma frequency (like the THz range), large negative permittivity strongly prohibits electromagnetic fields from penetration inside a metal, and plasmon excitation on the metal-dielectric interface becomes challenging. Two major approaches can be employed to increase the confinement of THz SPPs: either electromagnetic waves bound to metal surfaces that mimic surface plasmon polaritons (referred to as spoof SPPs) are obtained by perforating a flat metal surface periodically with holes and grooves [4]; or SPPs are excited in surfaces made of semiconductor instead of metal [5]. As the carrier densities in semiconductors are much lower than those in metals, the plasma frequency is much smaller, being typically at mid- or far-infrared frequencies. Therefore, the permittivity of semiconductors at THz is comparable to that of metals at optical frequencies. A decisive advantage of semiconductors is that their carrier density and mobility, and consequently the SPPs, can be easily controlled by thermal or optical excitation of free carrier.

Recently [6] we have demonstrated undistorted low-loss THz-pulse propagation in the gap waveguide formed by two metal cylindrical surfaces. Here we consider case when doped semiconductor (such as *n*-doped Si) is used as material of cylindrical surfaces with purpose to increase THz field confinement in lateral direction (along *y*-axis in Fig. 1).

The simple graded effective index model ($n_{\text{eff}} = n_{\text{eff}}(y)$ with n_{eff} determined by the ratio of propagation constants in free space and waveguide) is used to calculate THz-field distribution along lateral direction of waveguide. The studied waveguide is considered as plasmonic gap parallel plate waveguide (PPWG) with

adiabatically varying plate's distance $h(y)$. By using approximate formula for effective index in plasmonic PPWG [7], we determine its profile $n_{\text{eff}} = n_{\text{eff}}(y)$ along y -axis and then calculate THz field distribution $E = E(y)$ by technique already developed for dielectric waveguides. To verify the analytically obtained results the field distribution in waveguide is simulated by finite element method software COMSOL Multiphysics. As for THz field distribution along x -axis, it is very similar to that of PPWG.

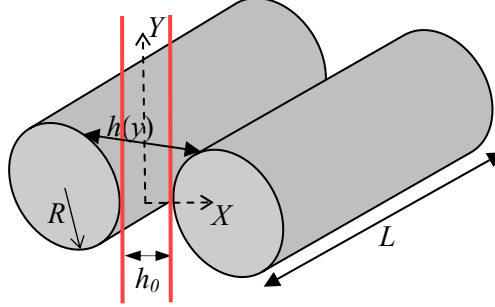


Fig. 1. Schematic view of gap plasmon waveguide.

2. Theory

The effective refractive index in plasmon PPWG is given by [7]

$$n_{\text{eff}} \approx 1 + \frac{A}{h_0}, \quad (1)$$

where $A = 0.23\lambda/\sqrt{|\hat{\epsilon}|}$, λ is the wavelength, $\hat{\epsilon}$ is the complex permittivity, h_0 is the plates separation.

By considering waveguide as plasmonic gap PPWG with adiabatically varying plate's distance $h(y)$, the effective refractive index distribution can be written as

$$n_{\text{eff}}(y) \approx 1 + \frac{A}{h(y)}. \quad (2)$$

As it follows from waveguide geometry, the distance between cylindrical surfaces is given by

$$h(y) = h_0 + 2R - 2\sqrt{R^2 - y^2}, \quad (3)$$

which for distances $|y| \ll R$ can be simplified to form

$$h(y) = h_0 + \frac{y^2}{R}. \quad (4)$$

By substituting it in (2) one can obtain

$$n_{\text{eff}}(y) \approx 1 + \frac{A}{h_0(1 + y^2/h_0R)}. \quad (5)$$

From Eq. (5) follow that effective refractive index in waveguide is highest in middle of gap ($y = 0$) and it is decreased towards to periphery. Therefore, the mechanism of field confinement in plasmon waveguide is related to negative gradient of the effective refractive index, similar to common dielectric waveguide. The theory of dielectric waveguide with cosh- and parabolic-profiles of the refractive index is well developed [8]. For distances satisfying inequality $y^2 \ll Rh_0$, the Eq. (5) can be represented in form of the cosh-profile

$$n_{\text{eff}}(y) \approx 1 + \frac{A}{h_0 \cosh^2(y/\sqrt{h_0R})} \quad (6)$$

or parabolic-profile

$$n_{\text{eff}}(y) \approx 1 + \frac{A}{h_0}(1 - y^2/h_0R). \quad (7)$$

Then fundamental mode field distribution in waveguide is calculated by using methods similar to those that are for dielectric waveguides [8]. In THz range the metal has extremely large permittivity (e.g. $\epsilon_{Au} = -1.12 \cdot 10^5 + i7.22 \cdot 10^5$ for gold at 0.3 THz), which results in small A factor and consequently in

small gradient of effective refractive index. For this reason THz beam confinement in metal waveguide is poor. The use of n -doped Si having relatively small permittivity $\epsilon_{Si} = -6.7 + i251.1$ (for 0.3 THz and $N = 10^{18} \text{ cm}^{-3}$) is favorable for strong THz beam confinement in proposed waveguide.

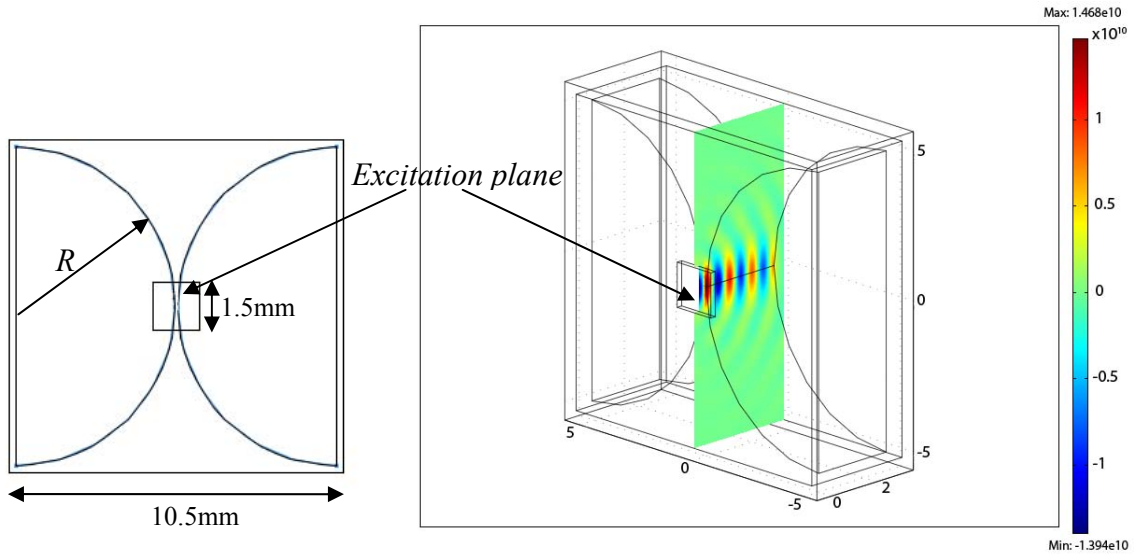


Fig. 2. View of gap plasmon waveguide in COMSOL Multiphysics.

3. Simulation

To investigate the electrical field distribution in waveguide made of n -doped Si (with $N = 10^{18} \text{ cm}^{-3}$) we employ finite element method software COMSOL Multiphysics. We have used a PC with 64-bit quad processors and 12GB RAM, which get at a solution in approximately 1 day for a model with 114010 mesh elements. The simulation of the propagation of 0.3THz waves along waveguide is illustrated in Fig. 2.

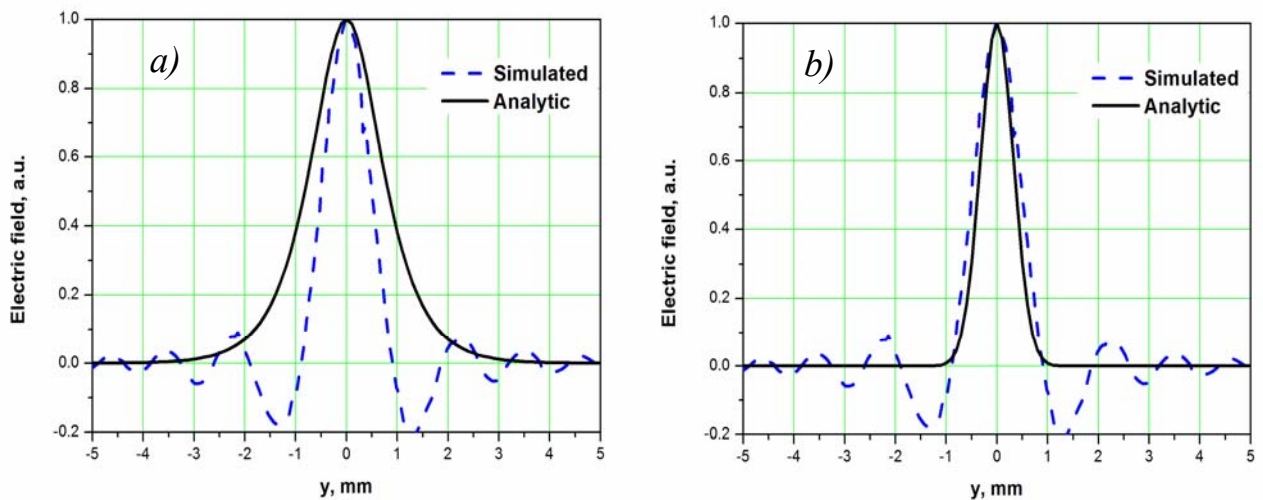


Fig. 3. Simulated and calculated (with hyperbolic cosine (a) and parabolic (b) profiles) electrical field distributions.

Each of the cylinders having the radius $R = 5 \text{ mm}$ are separated by distance of $h_0 = 0.1 \text{ mm}$, and length of the waveguide is $L = 3 \text{ mm}$. The distance between excitation plane ($1.5 \times 1.5 \text{ mm}$) and input face of the waveguide is chosen 0.3 mm . To excite effectively the plasmonic TM_0 -mode in waveguide, the polarization of input electromagnetic wave is oriented along to direction connecting the centers of cylinders (x -axis in Fig.1) The simulation is bounded by enclosing the waveguide geometry in a rectangular box of air ($10.5\text{mm} \times 10.5\text{mm} \times 4\text{mm}$), the walls of which are assigned a low-reflecting boundary condition to minimize the effects of back reflections.

The results of simulation indicate guided mode propagating along the two cylinders, with the largest electrical field (E_x -component) concentration in the $y = 0$ plane. The calculated (for hyperbolic cosine and parabolic profiles of the effective index) and simulated electrical field distributions are presented in Fig. 3.

It is seen that the parabolic profile is better coincide with simulation results. The presence of addition lobes in simulated field distribution is related to THz beam diffraction in input of the waveguide. The electrical field distribution along propagation direction (z -axis) is presented in Fig. 4. As it was expected from theoretical model, there is the decay of THz field with attenuation constant of $\alpha \approx 0.3 \text{ mm}^{-1}$.

The results of simulation for Si cylinders having larger level of the doping ($N = 5 \cdot 10^{18} \text{ cm}^{-3}$) show that

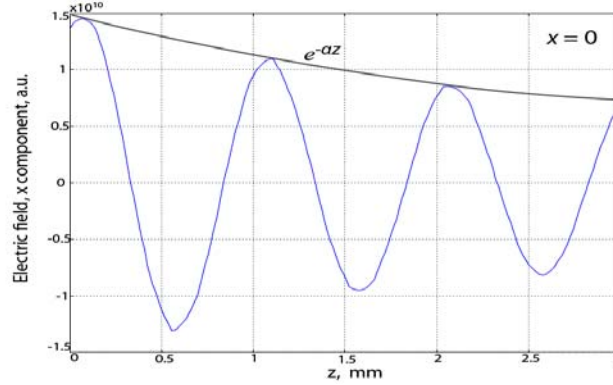


Fig. 4. Electrical field distribution along propagation direction.

attenuation constant α can be decreased, but it is accompanied by increase of mode size in waveguide. Hence, a trade-off has to be found in dopant concentration N according to respective application waveguide.

In conclusion, we have successfully simulated the propagation of THz wave along gap plasmon waveguide by COMSOL Multiphysics. The comparison of the results of simulation with calculated (based on parabolic profile of the graded refractive index) indicates on good agreement.

4. References

- [1] M. Tonouchi, Nature Photon. **1** (2007) 97.
- [2] R. Mendis, D. Mittleman, Opt. Express **17** (2009) 14839.
- [3] S. Bozhevolnyi, Plasmonic Nanoguides and Circuits (Pan Stanford, Singapore, 2008).
- [4] J. B. Pendry, L. M. Moreno, F. Garcia-Vidal, Science **305** (2004) 847.
- [5] J. G. Rivas, M. Kuttge, H. Kurz, P. H. Bolivar, J. A. Sanchez-Gil, Appl. Phys. Lett. **88** (2006) 082106.
- [6] Y. H. Avetisyan, A. H. Makaryan, H.S. Hakobyan, K. L. Vodopyanov, Tech. Dig. CLEO/QELS-2010, paper CTuQ2.
- [7] B. G. Ghamsari, A. H. Majedi, J. Appl. Phys. **104** (2008) 083108.
- [8] H. Kogelnik, Guided-Wave Optoelectronics (Springer-Verlag, Berlin, 1990).

Terahertz Wave Confinement in Gap Plasmon Waveguide Fabricated by Composite Material

V.R. Tadevosyan, H.S. Haroyan, A.H. Makaryan, A.B. Hovsepyan, Yu.H. Avetisyan

Department of Radiophysics, Yerevan State University, Yerevan, 1 Alek Manoogian, Armenia

The undistorted 2D confined THz pulse propagation in gap Waveguide formed by two closely spaced Cylinders made of Composite Material (WGCCM) is demonstrated. Cylindrical surfaces were made of composite material that is a mixture of the paraffin paste and metallic (Cobalt) powder with Co filling factor slightly higher than 0.5. In comparison with pure metal the plasma frequency is significantly reduced that is favourable for plasmonic mode excitation in waveguide. Due to features of this mode, THz-wave propagates in WGCCM without dispersion as it has been verified experimentally. Besides, THz beam is acquired a confinement in the lateral direction of WGCCM as effective refractive index is highest in middle of waveguide and it is decreased towards to periphery. The measured THz beam size in lateral direction of WGCCM is 3.8 mm (at 3 dB level), which is significantly smaller than that of free-propagating THz-wave.

The terahertz (THz) waves that exist between infrared and microwave have many unique properties and are being applied in various scientific research fields and application, such as medical imaging, astronomy, spectroscopy, and chemical detection [1]. Nowadays the terahertz (THz) technology moves toward the component integration and it has become essential to develop THz waveguides with low transmission loss, high confinement, and small group velocity dispersion. Recently we have demonstrated that narrow gap plasmon waveguide formed by two metal cylinders (Fig. 1) is good candidate for THz waveguiding with low propagation losses and negligible group velocity dispersion [2]. However, the strong field localization in waveguide may be originated via surface plasmon-polariton (SSP) excitation only for frequencies close to the plasma frequency ω_p of the cylinders material. Since ω_p for metals is limited to the visible and ultraviolet regions, the large negative permittivity strongly prohibits THz field penetration inside a metal, and plasmon excitation on the metal-dielectric interface becomes challenging. Thus, the materials with lower plasma frequencies are required to effective excite THz SPP-mode in waveguide.

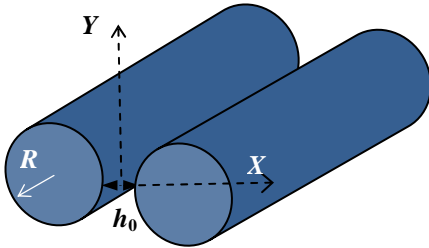


Fig.1 Schematic view of the gap waveguide.

for pure Au ($\epsilon_{Au} = -115 + i \cdot 11$). The similar way can be applied in THz waveband as well. There are many THz transparent dielectric pastes (paraffin, polyethylene, foam plastic) and various metallic (Co, Al, and Cu) powders with small sizes of particles are also available.

In this report, we are focus on composite material, which is mixture of Co powder and paraffin wax. This choice is attributed by easiness of fabrication due to low melting temperature of paraffin. Besides, Co is distinguished by and has relatively small dielectric constant ($\epsilon_{Co} = -8 \cdot 10^3 + i \cdot 10^4$ at 1 THz) in THz waveband [5]. In theoretical part of the paper, the dependence of mixture dielectric constant on filling factor of the metal powder is calculated by effective medium approximation (EMA) model [6, 7]. It is used to design the composite material with THz negative dielectric constant nearly the same that of metals at optical waveband. Then opportunity of THz beam confinement in gap Waveguide formed by two closely spaced Cylinders made of Composite Material (WGCCM) is analyzed.

In experimental part, the THz-pulse propagation through waveguide (made of composite material) is studied by THz time-domain spectroscopy technique in wide frequency region from 0.2 THz to 2.5 THz. The temporal forms of THz pulses after passage through free space and waveguide are compared to demonstrate dispersionless propagation in WGCCM. The knife edge method is used to measure THz beam intensity distribution close to output of the waveguide.

1. Theory

In describing the permittivity of a homogenized composite random media, Burgmann's EMA model is widely utilized [7]. According to EMA, the complex dielectric constant ϵ_c of two-component mixture is given by

$$\epsilon_c = 0.5 \left(a - \sqrt{a^2 + 4\epsilon_m \epsilon_d} \right), \quad (1)$$

with

$$a = \epsilon_d - \epsilon_m + 2f(\epsilon_m - \epsilon_d), \quad (2)$$

where ϵ_m and ϵ_d are the complex dielectric constants of the metal and dielectric components, f is the filling factor of the metal.

The results of calculation for paraffin wax and Co ($\epsilon_d = 2.25$ and $\epsilon_m = -8 \cdot 10^3 + i \cdot 10^4$ at 1 THz) mixture show that real part of ϵ_c become negative since filling factor $f \approx 0.5$. The further increase of the factor f results in growth of the negative permittivity up to value corresponding to ϵ_m . Therefore to realize dielectric constants close to that of metal in optics, the portion of Co powder has to be slightly larger than 0.5. For example, in case of $f = 0.51$ the real part of THz dielectric constant $\text{Re}(\epsilon_c) = -107$ that is close to value for Au in optical waveband.

It is important that relatively small dielectric constant of the cylinders material makes possible to obtain 2D confined TM_0 -mode propagation in. The confinement along x -axis of the waveguide is related to the plasmon nature of TM_0 -mode [8]. The restriction of the mode size along lateral direction of the waveguide (y -axis) is attributed to graded effective index $n_{eff} = n_{eff}(y)$ distribution (where n_{eff} is the ratio of propagation constants in free space and waveguide), which can be presented in form [9]

$$n_{eff}(y) \approx 1 + \frac{0.23 \lambda_{THz}}{h_0 \sqrt{|\epsilon_c|} (1 + y^2 / h_0 R)}, \quad (3)$$

where λ_{THz} is the wavelength and $|y| \ll (h_0 R)^{1/2}$.

From above follows that effective index is highest in center ($y=0$) and it is monotonically decrease towards to periphery, similar to common graded refractive index waveguides. The smaller $|\epsilon_c|$ leads to larger gradient for effective index distribution and therefore it is resulted in stronger THz beam confinement. It is illustrated in Fig.2, where THz beam intensity distributions (at 1 THz) for waveguides made of metal and composite material (with $f = 0.51$) are presented. In the both cases the radiuses of cylinders are $R = 5$ mm and minimal distance between them is $h_0 = 0.1$ mm.

To estimate THz-wave absorption coefficient in WGCCM, it was considered as parallel plate waveguide with adiabatically expanding plate's distance. Taking in account finite conductivity σ of wire's material (where σ is determined by imaginary part of ϵ_c), the absorption coefficient α is estimated as $\alpha = 0.346 \text{ mm}^{-1}$. Such large THz wave attenuation (in comparison with metals) is related with increased penetration of the THz field in absorbing composite material. The existing trade-off between electromagnetic wave decay and confinement is typical feature for plasmon waveguides [10].

2. Experiment

The studied waveguide was fabricated by use two cylinders with radius $R = 5$ mm and length $L = 30$ mm. The material of cylinders was mixture of Co-powder and paraffin with filling factor f slightly higher than 0.5. The cylinders were mounted on differential screws to adjust minimal distance between them $h_0 \approx 0.1$ mm. Waveguide was placed in a TDS setup in such a way that its input face was as close as possible to an InAs surface THz emitter and output face was in focus of a collecting off-axis parabolic mirror. To increase

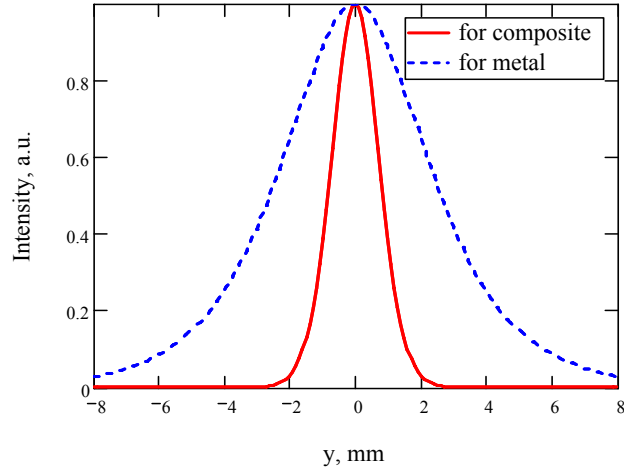


Fig.2. The fundamental mode intensities distributions for PWCS fabricated by metallic (---) and composite (—) materials.

coupling efficiency with incident THz beam the tapered section is formed in input of waveguide. In this section the separation between waveguide's walls is gradually decreased from 3 mm to value of 0.1mm, which corresponds to gap size itself PWCS. In all measurements, the THz beam was polarized parallel to the x -axis (along line connecting the centres of cylinders) to excite fundamental TM_0 mode in WGCCM.

The experimental setup is schematically illustrated in Fig.3. A pulse train derived from a mode-locked Ti:Sapphire femtosecond laser (Spectra-Physics, average power 1.85 W, pulse duration ≈ 80 fs, repetition

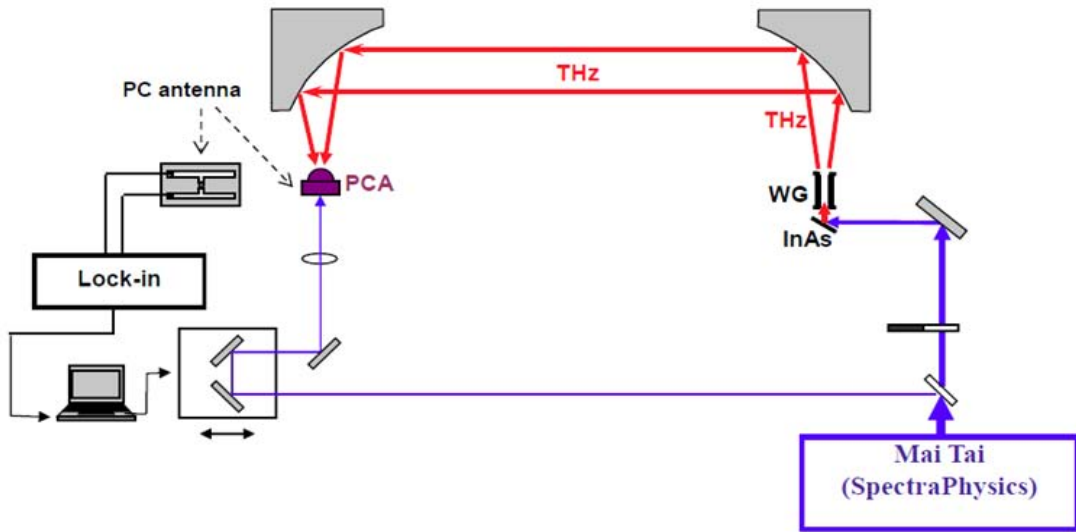


Fig.3. Schematic view of experimental setup

rate 80 MHz) is split into excitation (pump) and detection (probe) pulses. The excitation pulses impinge on an InAs surface field emitter which leads to the emission of THz pulse. THz radiation after propagation through the waveguide (with tapered section in input) is collected with off-axis parabolic mirror. Another mirror is used to focus THz radiation onto a detection photoconductive antenna. This antenna is based on an Auston switch, which is a piece of low-temperature grown GaAs, placed between two metal contacts. The photoconductive switch is gated by probe Ti:Sapphire beam. This enables the time domain detection of the THz field by scanning the time delay between pump and probe pulses with a motorized translation stage. The Fourier transform of measured temporal time forms of THz fields with and without waveguide allows to determine transmission of the waveguide in wide frequency range 0.2 – 2.5 THz.

The temporal forms of THz pulses after passage waveguide and the same distance in free space (ambient air) are presented in Fig. 4a. The oscillations after main pulse are related to THz absorption in water vapor, which is contained in ambient air. The vertical and horizontal offsets are applied for clarity of the picture.

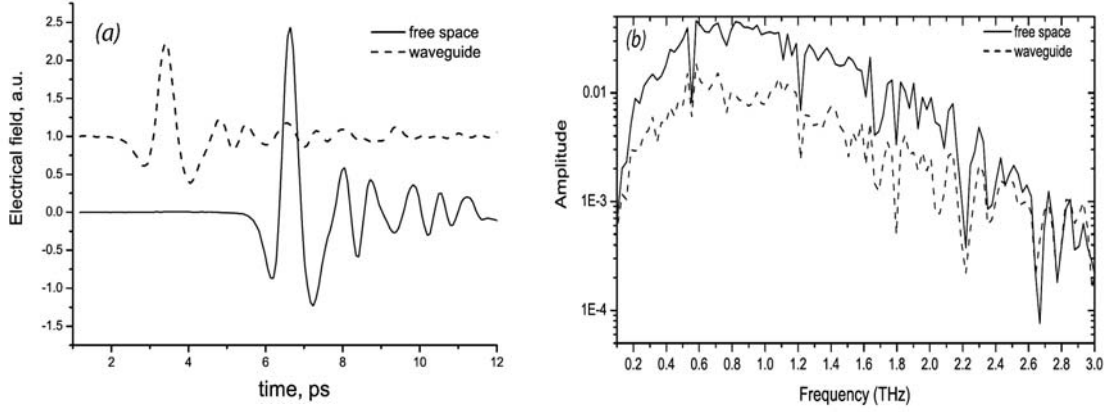


Fig. 4. THz pulses waveforms (a) and corresponding spectra (b) for free space and waveguide propagation.

The comparison of the waveforms indicates the nearly undistorted pulse propagation in the composite waveguide. It is confirmed by the corresponding Fourier amplitude spectrum Fig.4.(b), which gives no indication of a low-frequency cutoff.

To roughly estimate THz beam size (along y -axis) in waveguide, we measure beam intensity distribution in region close to waveguide's output by knife edge method [11]. The dependence of the measured signal on position of the movable metal plate (which partially blocks THz beam) is built. Then, the intensity distribution of THz beam is obtained by differentiation of this dependence (Fig.5). The results of

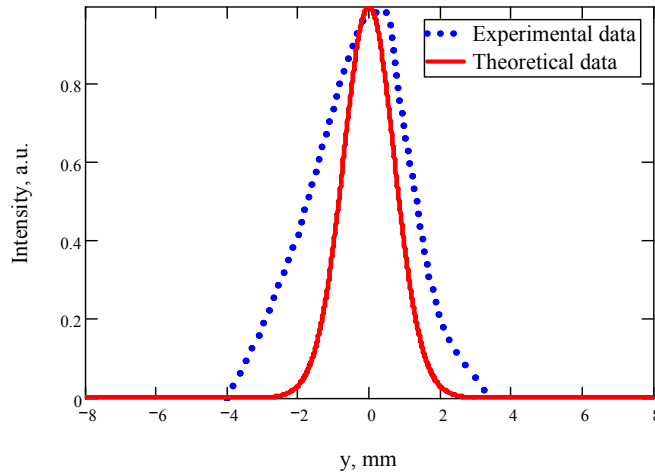


Fig.5. The fundamental mode intensities distribution dataset by experimental ($\bullet\bullet\bullet$) and theoretical (---) investigations.

measurements show that studied waveguide provides THz field confinement in the lateral direction (y -axis) of waveguide, but THz beam size is more than it follows from theory (see Fig.2). The reason of this discrepancy is probably related to inaccuracy of the measurement due to THz wave diffraction caused by both the output of waveguide and movable metal plate used in knife edge method [12].

Conclusion

Undistorted 2D confinement THz pulse propagation in gap waveguide formed by two closely spaced cylinders made of composite material is demonstrated. The comparison of characteristics of waveguides made of composite and metal materials are presented. It was shown what confinement of composite waveguide is significantly stronger than that of metal waveguide. According to experimental measurements, THz beam size in lateral direction of composite waveguide is 3.8 mm, whereas for same metallic waveguide it is 11mm. The increased skin deep in composite material result in increase of attenuation constant

$\alpha = 0.346 \text{ mm}^{-1}$, which is still suitable for short distance application. Experimental results and theoretical calculations have shown satisfactory agreement. The results of investigation show that WGCCM has good potential for THz wave 2D confined undistorted propagation at relatively short distance.

Acknowledgments

This work was supported by NFSAT Grant ECSP-09-42_SASP and State Committee of Science of Armenia.

References

- [1]. M. Tonouchi, *Nature Photon.* **1** (2007) 97.
- [2]. Y. H. Avetisyan, A. H. Makaryan, H. S. Hakobyan, K. L. Vodopyanov, *Tech. Dig. CLEO/QELS-2010*, paper CTuQ2.
- [3]. J. G. Rivas, M. Kuttge, H. Kurz, P. H. Bolivar, J. A. Sanchez-Gil, *Appl. Phys. Lett.* **88** (2006) 082106.
- [4]. Z. Shi, G. Piredda, A. C. Liapis, M. A. Nelson, L. Novotny, R. W. Boyd, *Opt. Lett.* **34** (2009) 3535.
- [5]. M. A. Ordal, Robert J. Bell, R. W. Alexander, Jr, L. L. Long, M. R. Querry, *Appl. Opt.* **24**, (1985) 4493.
- [6]. D. A. Bruggeman, *Ann. Phys.* **24** (1935) 636.
- [7]. T. C. Choy, *Effective medium theory: principles and applications* (Oxford University Press, New York, 1999).
- [8]. S. I. Bozhevolnyi, Kh. V. Nerkararyan, *Opt. Express* **17**, (2009) 10327.
- [9]. H. S. Hakobyan, Y. H. Avetisyan, A. A. Barsegyan, *IRPhE'2010* (in press).
- [10]. S. Bozhevolnyi, *Plasmonic Nanoguides and Circuits* (Pan Stanford, Singapore, 2008).
- [11]. T. Hattori, K. Tukamoto, R. Rungsawang, and H. Nakatsuka, *Tech. Dig. 8th Int. Workshop on Femtosecond Technology*, 1 (2001). (June 28-29, 2001) Tsukuba.
- [12]. H. Lin, Ch. Fumeaux, B. M. Fischer, D. Abbott, *Opt. Express* **18**, (2010) 17672.

Integrated Millimeter-wave CPW to Dielectric Image-Guide Transitions in Silicon Technology

B. Biglarbegian¹, M. Basha¹, S. Gigoyan², S. Safavi-Naeini¹

¹ *Intelligent Integrated Radio and Photonics Group, University of Waterloo, Waterloo, Ontario, Canada*

² *Institute of Radiophysics & Electronics, Ashtarak, Armenia*

Introduction

In the nonstop quest for the higher bandwidth for wireless communications, researchers are becoming increasingly interested in millimeter wave (mm-wave) and sub millimeter wave spectrum. Today, with the rapid scaling of the gate length, CMOS (Complementary Metal-Oxide Semiconductor) technology is pushing further into the mm-wave region. Moreover, CMOS is the most promising technology for system-on-chip design, because it enables integration of the required analog RF circuits as well as the digital signal processing and baseband circuits in the lowest possible chip area. This leads to a lower cost and more compact solution [1]. One of the main challenges in the design of the systems to operate in the mm-wave and sub-mm-wave is the packaging and the interconnection of the active frontend chip and the antenna for various applications. Due to intrinsic metal losses in higher frequencies and the loss of the conventional metal based transmission lines, a high performance interconnection between the CMOS chip and the antenna is essential. Dielectric waveguides (DW) and image-guides (DIG) are of the best solutions to transfer the electromagnetic energy in the Optical and THz spectrum due to absence of the metal and the metal losses in these ranges of frequencies [2]. Utilizing the benefits of the dielectric waveguides in mm-wave and sub mm-wave band, one can design and implement high performance devices and components [3-5]. In this paper, using a novel method of fabrication of dielectric waveguides on SOI (Silicon on Insulator), a DIG at 60 GHz has been designed and implemented. Then, the DIG to CPW transition has been designed to couple the fundamental mode from the DIG to CPW line. This configuration is appropriate the flip-chip bonding in order to package the monolithic chips along with the dielectric waveguide and the antennas.

Image Guide To CPW Transition Design

The image-guide structure and the CPW transition is shown in Figure1. The cross section of the image wave guide consists of: top layer which is the CPW and is patterned using AL thin layer of thickness 2 microns, Second layer made of the device layer of the SOI wafer and form the dielectric wave-guide, and the third and fourth layers which are silicon oxide and high resistivity SI (handle layer of the SOI) having 1 microns and 130 microns respectively. The cross section of the waveguide is 500x800 microns.

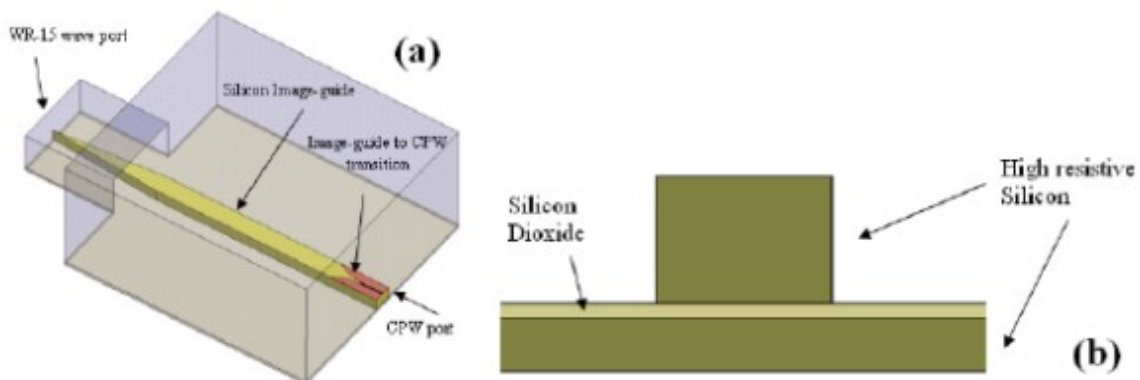


Figure 1: (a) The image-guide structure and the transition to CPW line; (b) Cross section of the dielectric layers (the dimensions are not scaled).

The structure consists of a Silicon image-guide with $500\mu\text{m}$ height and $800\mu\text{m}$ width, on top of a silicon dioxide layer with $130\mu\text{m}$ height. The fundamental mode E_y^{11} can be excited in this waveguide. The DIG is tapered at one end in order to have the transition from DIG to WR-15 rectangular metallic waveguide. At the other end of the DIG, the DIG to CPW transition is patterned over the DIG with a $2\mu\text{m}$ Aluminium. The transition is a CPW line with $W=50\mu\text{m}$ and $\text{gap}=50\mu\text{m}$. The two ground of the CPW line are extended gradually to the sides of DIG. The transition has been designed to couple the fundamental mode of the DIG to the CPW line. The two extended ground planes, forces the electric field to align horizontally along the CPW plane. The direction and intensity of the electric fields at the CPW port at 60GHz is depicted in Figure 2. As it is shown in Figure 2, most of the electric fields has been coupled to the CPW port where a small portion of the energy is still traveling through the dielectric image-guide.

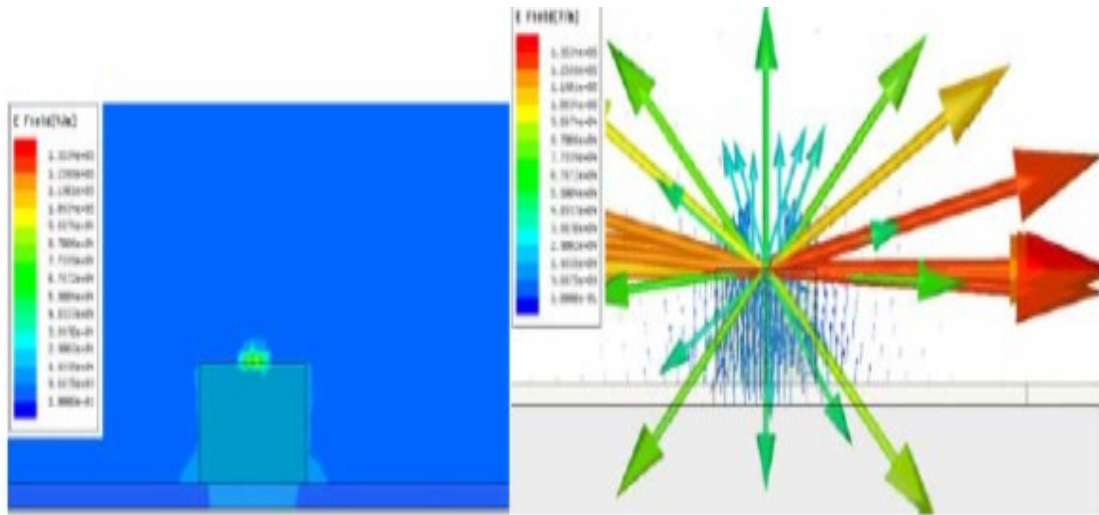


Figure 2: The intensity and direction of the electric fields at the CPW port.

Measurement Results

The aforementioned transition has been fabricated on High resistivity silicon. The metallic test fixture has been designed with WR-15 waveguide port. Figure1 shows the implemented image-guide and the transition on the test fixture. The overall structure has been measured with Agilent N5245A PNA-X series along with the OML modules at the range of $50 - 75\text{GHz}$. The measured results are shown in Figure 3. As it is shown, the insertion loss at 60GHz (including the rectangular waveguide to DIG) is 2.4 dB for the back to back transition which depicts the insertion loss of the single transition is about 1.2 dB . The overall matching is better than 13 dB at the range $62\text{-}67\text{GHz}$. In order to examine the coupling into the CPW line, a tiny absorber is placed over the CPW line. It can be observed that by adding the absorber, the S_{21} would drop by 12 dB where if the same experiment is done over the DIG without CPW transition the added insertion loss is not more than 6 dB .

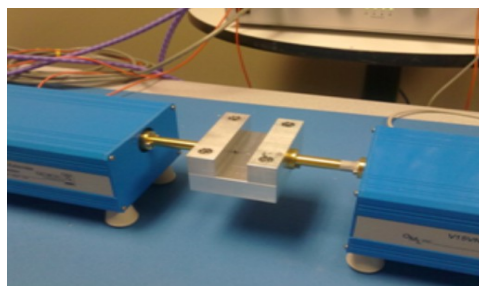


Figure 3: The image-guide to CPW transition in the fixture is measured with OML modules at the frequency range $50\text{-}75\text{ GHz}$.

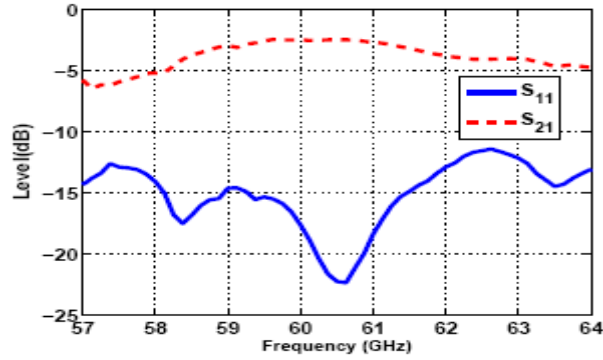


Figure 4: Measurement results of the back to back Image guide to CPW transition.

Conclusion

The design of the image-guide to CPW was explained in this paper. The transition was designed to have maximum coupling from the image guide dominant mode to the CPW line on top of the image-guide. The measurement results show that the total insertion loss of the transition is 1.2 dB at 60 GHz. The suggested design is promising for interconnection of active mm-wave chips to dielectric and image guide waveguides using flip-chip bonding.

References

1. M. Fakharzadeh, M. Nezhad-Ahmadi, B. Biglarbegian, J. Ahmadi-Shokouh, and S. Safavi-Naeini, "CMOS phased array transceiver technology for 60GHz wireless applications", *Accepted for publication in IEEE Trans. on Antennas and Propagation*, 2010.
2. D. Lioubtchenko, S. Tretyakov, and S. Dudorov, *Millimeter-wave waveguides*. Springer, 2003.
3. S. Kobayashi, R. Lampe, R. Mittra, and S. Ray, "Dielectric rod leakywave antennas for millimeter-wave applications", *IEEE Transactions on Antennas and Propagation*, vol. 29, no. 5, p. 822824, 1981.
4. S. G. D. S. S.-N. H. Chen, M. Neshat, "A frequency agile beam steerable tapered dielectric image-line antenna array with novel feeding structure", in *Radio and Wireless Symposium, 2009. RWS'09. IEEE*, 18-22 2009.
5. H. Kogelnik, "An introduction to integrated optics", *IEEE Transactions on Microwave Theory and Techniques*, vol. 23, no. 1, p. 216, 1975.

Whispering Gallery Mode Resonance Beyond 100 GHz

M. Neshat¹, A. Taeb¹, S. Gigoyan, and S. Safavi-Naeini²

¹ *Electrical and Computer Engineering Department, University of Waterloo, 200 University Ave. West, Waterloo, Ontario, N2L 3G1, Canada*

² *Institute of Radiophysics and Electronics, Alikhanian Brothers str. 1, 378410 Ashtarak, Armenia*

In this paper, the design of a whispering gallery resonator excited by a dielectric image guide is presented for sensing applications. A brief overview of the resonance perturbation method on whispering gallery mode is given. Simulation results are demonstrated, and compared against measurements for frequencies above 100 GHz.

Introduction

Whispering-gallery mode (WGM) is among the most sensitive and accurate techniques proposed to date for sensing and dielectric characterization [1]. Whispering-gallery resonance modes can be excited in an axially symmetric dielectric resonator (DR) such as a sphere, disk or ring. WGMs can be described as propagating modes around the center of such a DR with repeated total reflection from the rim of the resonator and phase shift of integer multiples of 2π in each rotation.

WGMs are attractive for sensing applications [2-3] due to their high sensitivity and selectivity resulting from the fact that they exhibit high unloaded Q-factor which is mainly limited by the loss tangent of the resonator material for highly confined modes. Moreover, the open structure of a whispering gallery resonator, unlike the metallic cavity, makes it very convenient to place and remove the sample at predetermined locations close to the resonator. In addition, at millimeter and sub-millimeter frequencies, whispering-gallery resonators have relatively large dimensions and therefore, they are less sensitive to fabrication tolerances especially beyond 100 GHz. In contrast, the size of the resonators at more common lower order TE, TM or hybrid mode regimes becomes impractically small at millimeter waves. Finally, the radiation loss is negligible especially for higher mode numbers.

The resonance perturbation method can be applied to a whispering-gallery mode by placing a sample under test in the evanescent field of the resonator. The sample perturbs the resonance mode, and causes a change in the resonance frequency and Q-factor. Variation in the resonance characteristics can be calibrated to represent the sensing parameter of interest.

Design and simulation

Figure 1 shows the cross section of the proposed WGM exciting structure. It consist of a dielectric disk resonator with diameter of D and thickness of t . The whispering gallery modes are excited in the disk resonator through coupling to a dielectric image guide (DIW). DIW is made of alumina with the width of W and thickness of h . Distance between DR and DIW is G , and both are placed on a metallic support made of bronze.

In the design stage of such structure, first the dimensions of the DIW is determined such a way to ensure single mode operation of the waveguide for the given frequency range. Since the DIW is excited by using standard metallic waveguides, in the next step, a low loss transition from the metallic waveguide to the DIW is implemented by linear tapering of the DIW at both ends. Length of the tapering section is optimized for the minimum transition loss. A low loss material such as alumina or high resistivity silicon is chosen for the disk resonator.

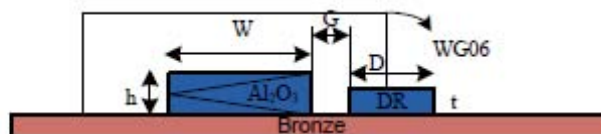


Figure 1 Cross section of a DR coupled to a dielectric image guide.

Once the material is known, the dimensions of the disk resonator are designed to give the desired resonance frequency for a given WGM mode number. A detailed calculation of the resonance frequency and Q-factor for given dimensions of a disk resonator acting on whispering gallery mode has been discussed elsewhere [2]. The distance between DR and DIW (parameter G in Figure 1) determines the coupling strength where at a certain value provides critical coupling. At critical coupling condition the transmission response is extremely sensitive to any external perturbation imposed on the resonator. This condition provides maximum sensitivity when the structure is used for sensing applications.

In an example design, the structure was optimized for 120-150 GHz frequency range. Figure 2 illustrates a 3D view of the structure simulated in full-wave using HFSS, a commercial EM simulator based on finite element method (FEM).

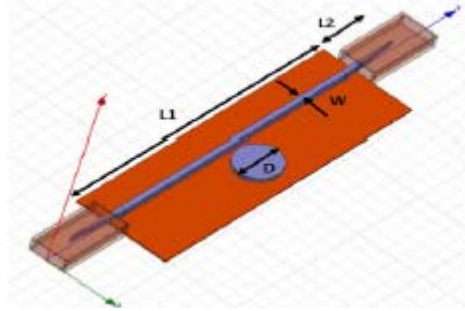


Figure 2 View of the structure in 3D.

Table 1 Parameter values of the designed structure.

Parameter	Value	Parameter	Value
W	470 μm	L_1	26 mm
D	2.8 mm	L_2	3 mm
G	450 μm	ϵ_r	9.8
h	0.65 mm	$\tan \delta$	0.0001
t	0.49 mm	$\lambda_w @ 110\text{GHz}$	0.9 mm

Figure 3 shows the simulation results obtained from HFSS for the parameter values given in Table 1. As seen in Fig. 3, a resonance frequency around 124.8 GHz exists for WGH700 mode. Shown in Figure 4 is the simulated transmission coefficient with respect to frequency and the gap distance as a parameter. As seen in Figure 4, $G=130\mu\text{m}$ provides near critical coupling condition.

Measurement

A prototype of the structure shown in Figure 2 was fabricated. The structure was characterized using Agilent 4252A PNA-X network analyzer along with the frequency extender modules covering 110-170 GHz. Figure 5 shows the measurement result for transmission and reflection coefficients.

Comparing the measurement results with that of simulation shows a very good agreement. The slight difference between simulation and measurement results can be attributed to the numerical error and uncertainty on the values of the physical parameters used in the simulation.

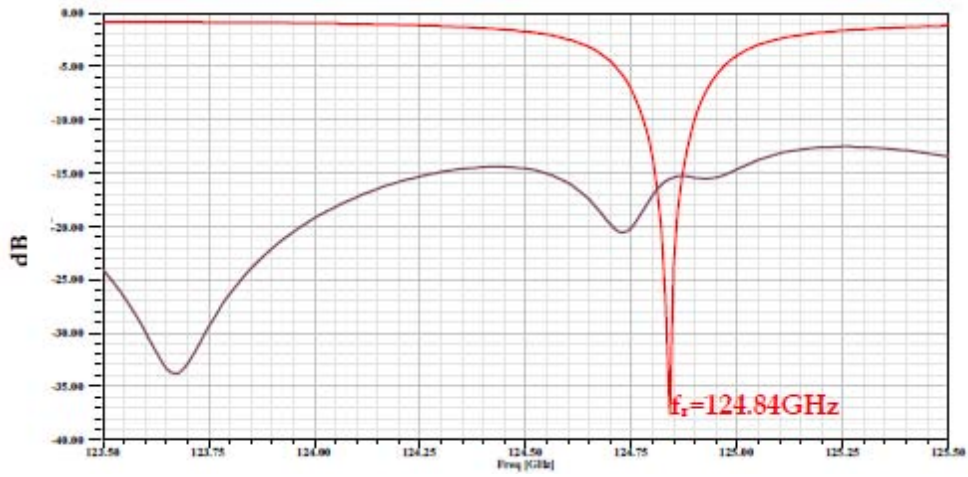


Figure 3 Simulation result for transmission (red) and reflection (blue) coefficients.

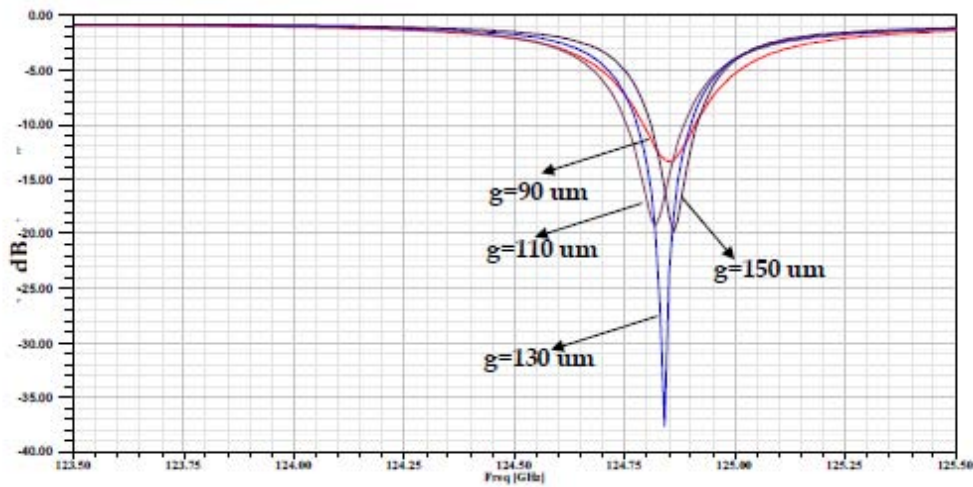


Figure 4 Effect of the gap distance on transmission coefficient (S21).

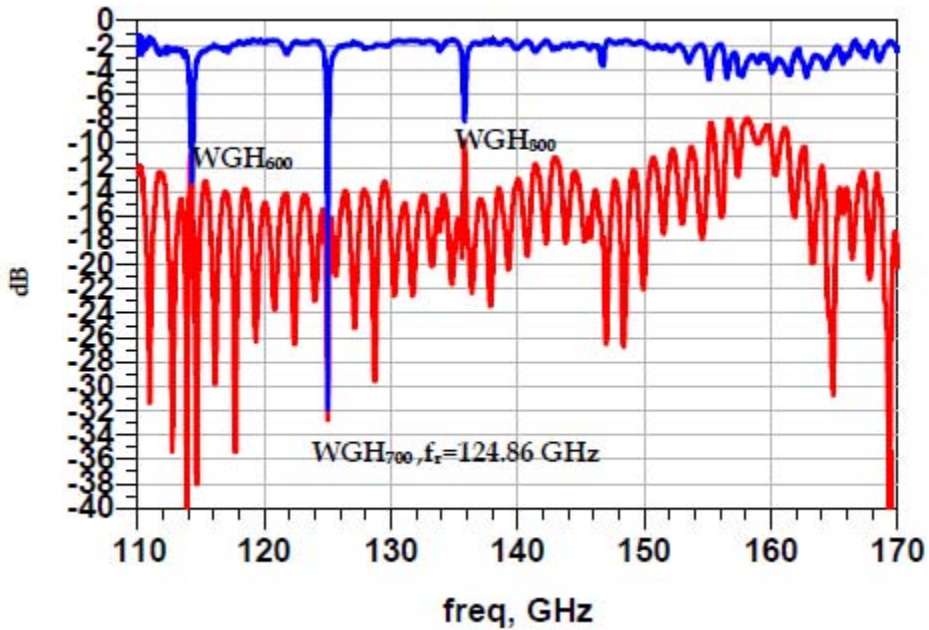


Figure 5 Measurement result for transmission (blue) and reflection (red) coefficients.

References

1. F. Vollmer and S. Arnold, *Nature Methods*, **5** (2008) 591-596.
2. M. Neshat, H. Chen, S. Gigoyan, D. Saeedkia, and S. Safavi-Naeini, *Meas. Sci. Technol.*, **21** (2009) 015202.
3. M. Neshat, S. Gigoyan, D. Saeedkia, and S. Safavi-Naeini, *Electronics Letters*, **44** (2008) 1020-1022.

“Hollow Dielectric Channel” in the Terahertz Range

M.Ts.Ayvazyan¹, Yu.N.Kazantsev²

¹State Engineering University of Armenia (Polytechnic), Teryan st.105, 0009, Yerevan, Armenia.

²Institute of Radioengineering and Electronics of RAS, Mokhovaya 11-7, Moscow, 125009, Russia.

Available in terahertz wavelength range, as a guide system to use the square channel in an infinite dielectric. This refers to the waveguide of class "hollow dielectric channel". On the basis of this class of waveguides in 2mm wavelength range, was created almost a full set of functional elements for the creation of microwave circuits for various purposes. A distinctive feature of this class of waveguides is their oversize, i.e. transverse dimensions of the waveguide are much larger than propagating in them waves. Shown, that the waveguide has a small loss in running and visible itself filtering higher types of waves in terahertz frequency range.

In terahertz wavelengths is a very topical issue of choice of the waveguide system on which you can create the functional elements for different purposes. Due to a number of features (open line, size, weight) the application of quasi-lines is limited, typically measuring system. In [1] are the main technical characteristics of virtually complete set of waveguide functional elements of the range of 120-180 GHz, made on the basis of waveguides class "hollow dielectric channel".

In this paper, we calculated the linear losses in an oversize channel in a solid dielectric (transverse dimensions of the channel $2a$ and $2b$ is much greater than the length of the wave propagating in it λ). The real model for such a waveguide can serve as a thick-walled dielectric tube. In [2] such a waveguide is used as the mode filter. Eigen modes of a rectangular channel in an infinite dielectric (Fig. 1) are presented in the form of so-called longitudinal electric LE_{mn} , or longitudinal magnetic LM_{mn} waves, if the ratio of the transverse dimensions of the waveguide to the wavelength is much greater ratio of the tangential field components at the interface air-dielectric. Metal-dielectric wave guide. Arrows show the distribution of the electromagnetic wave.

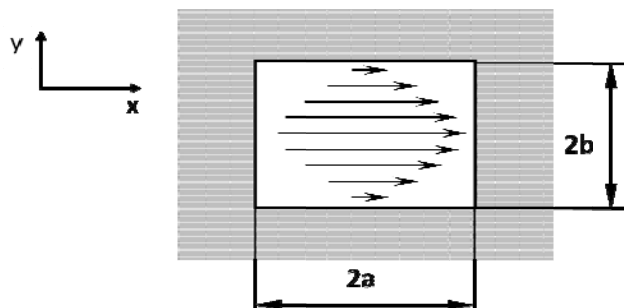


Fig.1. Channel in a solid dielectric

The components of the field longitudinal electric wave (LE) can be written as:

$$\begin{aligned}
 E_x &= 0, \\
 E_y &= -A \frac{h}{k} \cos(\alpha_x x) \cos(\alpha_y y) e^{-jhz}, \\
 E_z &= -jA \frac{\alpha_y}{k} \cos(\alpha_x x) \sin(\alpha_y y) e^{-jhz}, \\
 H_x &= A \left(1 - \frac{\alpha_x^2}{k^2}\right) \cos(\alpha_x x) \cos(\alpha_y y) e^{-jhz}, \\
 H_y &= A \frac{\alpha_x \alpha_y}{k^2} \sin(\alpha_x x) \sin(\alpha_y y) e^{-jhz}, \\
 H_z &= jA \frac{\alpha_x h}{k^2} \sin(\alpha_x x) \cos(\alpha_y y) e^{-jhz},
 \end{aligned} \tag{1}$$

The components of the field longitudinal electric wave (LM) can be written as:

$$\begin{aligned}
H_x &= 0, \\
H_y &= B \frac{h}{k} \cos(\alpha_x x) \cos(\alpha_y y) e^{-jhz}, \\
H_z &= -jB \frac{\alpha_y}{k} \cos(\alpha_x x) \sin(\alpha_y y) e^{-jhz}, \\
E_x &= B \left(1 - \frac{\alpha_x^2}{k^2}\right) \cos(\alpha_x x) \cos(\alpha_y y) e^{-jhz}, \\
E_y &= B \frac{\alpha_x \alpha_y}{k^2} \sin(\alpha_x x) \sin(\alpha_y y) e^{-jhz}, \\
E_z &= -jB \frac{\alpha_x h}{k^2} \sin(\alpha_x x) \cos(\alpha_y y) e^{-jhz},
\end{aligned} \tag{2}$$

where A and B - the amplitude coefficients; h, α_x and α_y - longitudinal and transverse wave numbers, respectively:

$$h^2 = k^2 - \alpha_x^2 - \alpha_y^2, \quad k = \frac{2\pi}{\lambda}, \tag{3}$$

$$\alpha_x = \alpha_x^0 + \Delta\alpha_x; \quad \alpha_y = \alpha_y^0 + \Delta\alpha_y. \tag{4}$$

For LE-mode transverse wave numbers are determined from the relations:

$$\alpha_x^0 = \frac{\pi m}{2a}, \quad \alpha_y^0 = \frac{\pi n}{2b}, \tag{5}$$

where m and n-integers ($m \neq 0$), 2a and 2b - transverse dimensions of the waveguide (Fig. 1)

$$\Delta\alpha_x = j \frac{\alpha_x^0}{ka} \frac{1}{\sqrt{\varepsilon-1}}, \quad \Delta\alpha_y = j \frac{\alpha_y^0}{ka} \frac{\varepsilon}{\sqrt{\varepsilon-1}}, \tag{6}$$

where ε - permittivity of the material of the waveguide.

For LM-modes, α_x^0 and α_y^0 can be written as (5), with ($n \neq 0$), and amendments to the transverse wave numbers are written as:

$$\Delta\alpha_x = j \frac{\alpha_x^0}{ka} \frac{\varepsilon}{\sqrt{\varepsilon-1}}, \quad \Delta\alpha_y = j \frac{\alpha_y^0}{ka} \frac{1}{\sqrt{\varepsilon-1}}, \tag{7}$$

Components H_y (LE-modes) and E_z (LM-modes) are very small (about $1/(ka)^2$) and they practically can be considered equal to zero. Therefore, LE-and LM-modes are both longitudinal electric and magnetic longitudinal, so that these terms are defined, in fact, only the direction of the main (transverse) components of the field (for LE-mode principal components E_y and H_x , for LM-modes E_x and H_y). The indices m and n determine the number of field variations of these komponent in the inner channel along the axes of x and y, respectively, and allow to classify all the waves (eg, $LMmn$ and $LEmn$). Knowing the transverse wave numbers, it is easy to calculate the attenuation as the imaginary part of propagation constant:

for longitudinal magnetic waves

$$h'' = - \left[\left(\frac{\alpha_x^0 a}{ka} \right)^2 \frac{1}{a} \operatorname{Re} \frac{\varepsilon}{\sqrt{\varepsilon-1}} + \left(\frac{\alpha_y^0 b}{kb} \right)^2 \frac{1}{b} \operatorname{Re} \frac{1}{\sqrt{\varepsilon-1}} \right], \tag{8}$$

for the longitudinal electric waves

$$h'' = - \left[\left(\frac{\alpha_x^0 a}{ka} \right)^2 \frac{1}{a} \operatorname{Re} \frac{1}{\sqrt{\varepsilon-1}} + \left(\frac{\alpha_y^0 b}{kb} \right)^2 \frac{1}{b} \operatorname{Re} \frac{\varepsilon}{\sqrt{\varepsilon-1}} \right], \tag{9}$$

From (8) and (9) that: a) attenuation in the channel in a solid dielectric decreases with shorter wavelength as λ^2 , considered waveguides has a high level of losses for higher types modes of (self- filtering), it can be used as the mode filter. The dependence of attenuation on the wavelength of some of the LE-and LM-modes in a waveguide of square cross section is shown in Figure 2.

The solid line corresponds to the attenuation in the channel in an infinite dielectric (getinaks) with the dimensions of cross section of 14x14 mm, dashed line calculated for a waveguide with dimensions 10x10 mm. A narrow channel is recommended for wavelengths less than 0.5 mm, and a wide channel is recommended to use long-wavelength part 0.12÷0,6 of terahertz range.

Selecting different dimensions of the waveguide, depending on the wavelength is due to the following reasons. Prerequisite for effective operation of oversized waveguides is

$$ka \gg 1, \tag{10}$$

However, excessive increase in cross-section of the waveguide is impractical due to the increase in size of the waveguide elements. The criterion for choosing the optimal size of the oversize waveguide can be the value of the total losses in quasi optical corner and in the waveguide cross, determined from the formula given in [3]:

$$h'' = \frac{4}{3} (\pi/2k\xi)^{3/2}, \tag{11}$$

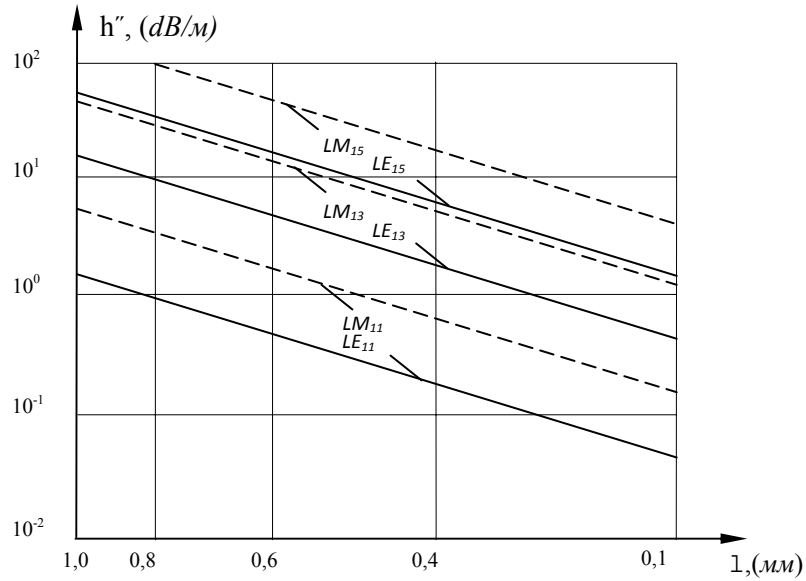


Fig.2. The dependence of attenuation on the wavelength of some of the LE-and LM-modes in a waveguide of square cross section.

where the break in the E-plane $\xi = a$, and for the break in the H-plane $\xi = b$. This recommendation stems from the fact that in microwave circuits, these functional elements are the most used. Dependence of the losses of electromagnetic waves from a cross section of the waveguide is shown in Figure 2. Thus, the quasi-optical angle, which is a break in the waveguide 90° with a flat metallic mirror, with dimensions of 14x14 mm cross section at wavelength $l = 1$ mm is the estimated loss of 0.03 dB. These and smaller losses are provided in the corners of the quasi-waveguide channel with dimensions 10x10 mm, at wavelengths shorter than 0.5 millimeters.

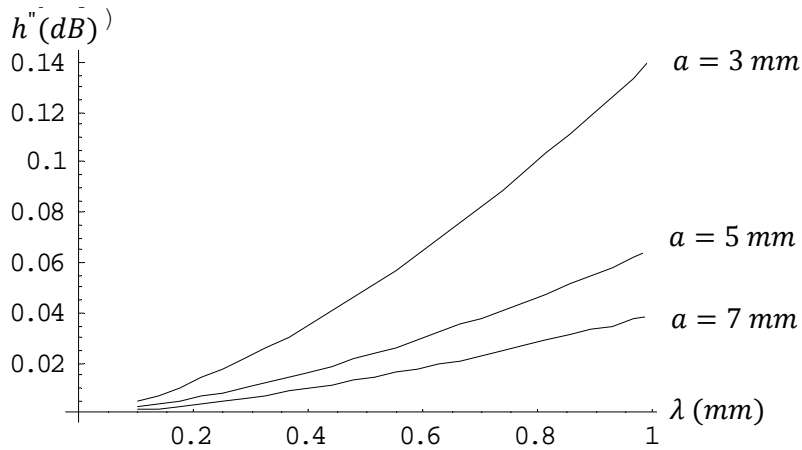


Fig.3. Dependence of the losses of electromagnetic waves from a cross section from the waveguide.

Thus, due to small losses, self-filtering of higher order modes are linearly polarized working mode, waveguides class "hollow dielectric channel" can be used in the terahertz waveband.

References

- [1] Yu.N.Kazantsev, Rectangular waveguides by class "hollow dielectric channel "- Radiotechniques and Electronics, 1978, v.23, N 10
- [2] R.S.Avagian, K.R.Agababian, M.Ts.Ayvazyan, Yu.N.Kazantsev, R.M.Martirosian. Complete set of waveguide elements for 120-180 GHz band.16-th International Conference on Infrared and Millimeter Waves. Lausanne, 1991.
- [3] Мериакри В.В., Матвеев Р.Ф., Ваганов Р.Б. Многоволновые волноводы со случайными нерегулярностями. М. Сов.Радио. 1972, 162с.

Oxide Nanointerface Engineering for Microwave Electronic Devices

K.Y. Constantinian¹, G.A. Ovsyannikov¹, A.V. Shadrin¹, Yu.V. Kislinkii¹,
A.M. Petrzhik¹, A.V. Zaitsev¹, J. Mygind² and D. Winkler³

¹ Kotel'nikov Institute of Radio Engineering and Electronics RAS, Moscow, Russia

² Department of Physics, Technical University of Denmark, Lyngby, Denmark

³ Chalmers University of Technology, Gothenburg, Sweden

We report on experimental studies of electron transport, microwave properties and noise in the multilayer hybrid superconducting heterostructures with magneto-active interlayer. The base electrode was copper oxide superconductor used for forming the interface with magnetic material made from either cuprate antiferromagnetic CaSrCuO, or underdoped LaMnO, or Ca doped manganite. The upper electrode was Au/Nb bilayer. In the case of antiferromagnetic CaSrCuO interlayer (with thickness $12 \div 50$ nm) the I - V curves demonstrated good fit to RSJ-model showing critical frequency f_c of order 100 GHz at $T=4.2$ K. At the same time, non-integer Shapiro steps were observed along with the sub-harmonic detector response. The second harmonic of the current-phase relation of order $10 \div 20\%$ of the first one was evaluated via measurements of integer and half-integer Shapiro steps.

1. Introduction

Coexistence of superconducting and magnetic ordering in solids is of great interest for fundamental physics and electronic applications. The exchange mechanism of ferromagnetic ordering tends to align spins of superconducting pairs in the same direction preventing singlet pairing [1-2]. At the interfaces between superconducting (S) and magnetic matter (M), however, the superconducting and magnetic correlations may interact due to the proximity effect (penetration of superconducting correlations into magnetic matter) resulting in interplay between superconducting and magnetic ordering, and novel physical phenomena may appear. However, up to now most of the activity was devoted to investigations of heterostructures where M-interlayer is a ferromagnetic (F). However, much less attention was paid to superconducting structures with M-interlayer having AF- ordering. Recently L. Gor'kov and V. Kresin [3] assumed a model (G-K model) of the S/AF/S structure where an AF interlayer consists of F-layers with antiparallel magnetizations and aligned perpendicular to the surface of the S-electrodes. The G-K model predicts existence of critical current like in S/N/S structures with spacing between S electrodes larger than the coherence length ξ_N in normal metal N. The G-K model also predicts that a minor change in canting of magnetic moments in the F-layers caused, say, by external magnetic field H will reduce sharply the critical current I_c . Theoretical investigation of a S/M/S structure with M-interlayer composed of N F-layers each one with a thickness exceeding the atomic-scale was carried out also in [4] by A.V. Zaitsev. The orientation of the F-layer magnetizations in the latter model was parallel to the S/M interface and it was shown that for AF- ordering the long-range proximity effect takes place. Experimental observation of the Josephson effect in S/AF/S structures Nb/Cu/FeMn/Nb has been demonstrated in [5], where AF- interlayer was γ -Fe₅₀Mn₅₀ alloy. If instead of using a polycrystalline metallic AF-material one would substitute it by an array of F-layers with alternating directions of magnetization, according to the G-K model the dependence $I_c(H)$ should then exhibit rapid oscillations. Recently experimental observations of such oscillations and the critical current dependence on M-interlayer thickness have been shown [6-8].

In order to observe long-range proximity effect in superconducting structure with M-interlayer, a transparent S/M interface is needed. This is also why in-depth investigations of such interfaces composed of the superconducting and antiferromagnetic cuprate materials are highly relevant. At the same time mutual influence of antiferromagnetism and the d-wave superconductivity at S/M interfaces in Josephson junctions also is necessary to unveil. In this paper we report on the experimental studies of dc and microwave current transport through S/M interfaces realized in hybrid Nb/Au/M/YBa₂Cu₃O_{7- δ} mesa heterostructures (MHS) with the in-plane size L varied from 10 to 50 μ m. Here Nb is a conventional s-wave superconductor (S'), YBa₂Cu₃O_{7- δ} (YBCO) is a cuprate superconductor with the dominating d-wave order parameter (S_d), and Au is a normal metal (N). The M-interlayer is either the Ca_{1- x} Sr _{x} CuO₂ (CSCO) ($x=0.15$ or 0.5) which is a quasi-two-dimensional Heisenberg antiferromagnetic cuprate, or underdoped manganite LaMnO₃, or doped ferromagnetic half-metal La_{1- y} Ca _{y} MnO₃ manganite.

2. Experimental technique

The double-layer epitaxial thin film structures M/YBCO were grown *in-situ* by pulsed laser ablation on (110) NdGaO₃ (NGO) substrates. The c-axis of the M/ S_d heterostructures is perpendicular to the substrate surface. Typically, the $d=5\div 100$ nm thick M-films were deposited on the top of 150 nm thick YBCO films. The Ca_{1-x}Sr_xCuO films ($x=0.15$ and $x=0.5$) were used as M-interlayers, and La_{1-y}Ca_yMnO₃ ($y=0$ and $y=0.3$) as possible candidates for magnetic interlayer as recommended in [3]. The M/YBCO heterostructures were covered *in-situ* by a $10\div 20$ nm thick Au film and afterwards, a 200 nm thick Nb film was deposited *ex-situ* by dc-magnetron sputtering in an Ar atmosphere. In order to fabricate Nb/Au/M/YBCO mesas we utilize optical photolithography, reactive plasma etching, and Ar ion-milling techniques. A SiO₂ protective layer was deposited by RF-magnetron sputtering. An additional 200 nm thick Nb/Au bilayer film was deposited on the top of the MHS and patterned in order to form the superconducting wiring. The square S'/N/M/S_d MHS with areas $S=L^2$ from $10\times 10\ \mu\text{m}^2$ up to $50\times 50\ \mu\text{m}^2$ were fabricated (see Fig. 1).

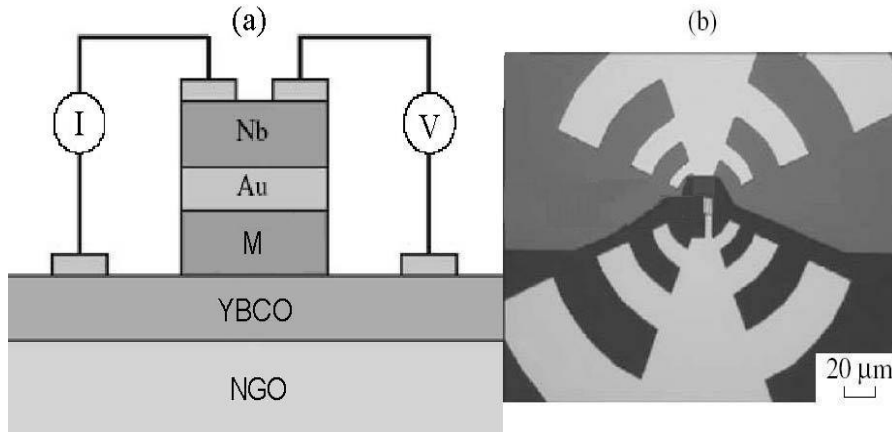


Fig. 1. (a) - The cross section of the MHS. The layers thicknesses are: YBCO –150 nm, M-interlayer $5\div 100$ nm, Au - $10\div 20$ nm, Nb – 200 nm. (b) - Top view of MHS incorporated with log periodic antenna.

For comparison, a similar fabrication procedure was used for structuring of the MHS without M-interlayer [9]. Direct Nb deposition on top of the YBCO film results in formation of Nb/YBCO interface with very high resistance ($\sim 1\ \Omega\cdot\text{cm}^2$) due to the Nb film oxidation. Thus, if the Au layer is locally damaged because of the finite surface roughness of the M/S_d interface then niobium oxide prevents pinholes formation.

3. Results and discussion

The resistance of MHS is $R=R_{YBCO}+R_{M/Y}+R'_M+R_b+R_{Nb/Au}+R_{Nb}+R_{Au}$, where R_{YBCO} comes from YBCO electrode, $R_{M/Y}$ is the M/YBCO interface resistance, R'_M is the resistance of the M-interlayer, R_b is the Au/M interface barrier resistance, and the resistances R_{Nb} and R_{Au} for Nb electrode and Au film, respectively. The contribution of thin Au film can be neglected [9]. Fig.2. shows temperature dependences of MHS resistance and the CSCO layer. Independently measured characteristic resistivity of the Nb/Au interface ($\sim 10^{-11}\ \Omega\cdot\text{cm}^2$) [9] results in $R_{Nb/Au} \sim 1\ \mu\Omega$ - a negligibly small contribution to total resistance of MHS. Taking into account the epitaxial growth of the CSCO/YBCO structure and similar parameters of the crystal structure of contacting materials, one can assume that interface resistance $R_{M/Y}$ is small compared to the resistance R_b of the Au/CSCO interface, for which the difference between Fermi velocities of Au and the CSCO is significant [9]. The thickness dependencies of specific resistance $R_N S$ of MHS is given in Fig.3. Although the structures with manganite M-interlayer had no critical current, the most of samples with AF CSCO interlayer demonstrated Josephson effect and symmetric RSJ-type [10] I - V curve without excess current had $I_C R_N \sim 200\ \mu\text{V}$ at $T=4.2$ K. All junctions had dimensions $L < \lambda_J$, where λ_J is Josephson penetration depth, and McCumber parameter $\beta_C=1\div 3$. Thickness dependence of critical current density $j_C(d)$ for S/AF/S junction with $x=0.5$ in CSCO interlayer is shown in Fig. 4.

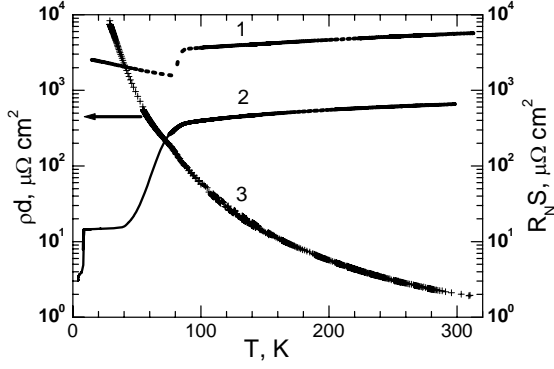


Fig.2. Temperature dependences of junction resistance: (1) $d=20$ nm, $S=10 \times 10 \mu\text{m}^2$, (2) $d=40$ nm, $S=50 \times 50 \mu\text{m}^2$ and (3) resistance $\rho d/S$ of a bare CSCO film with $x=0.5$, $d=40$ nm, $S=50 \times 50 \mu\text{m}^2$ deposited on NGO substrate.

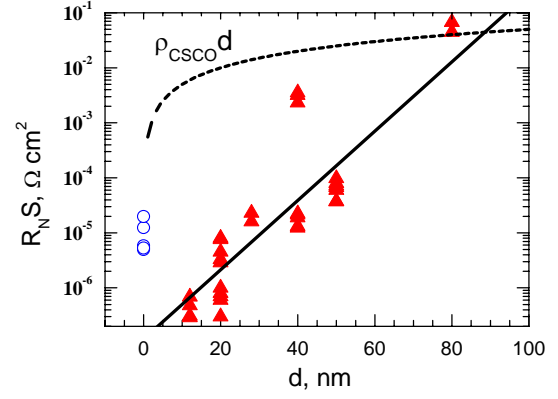


Fig.3. Thickness dependencies of specific resistance $R_N S$ for CSCO with $x=0.5$. Bold line corresponds to $\xi_{AF}=7 \pm 1$ nm. Open circles - for junctions without AF interlayer. Dash line is calculated resistance for bare CSCO AF layer.

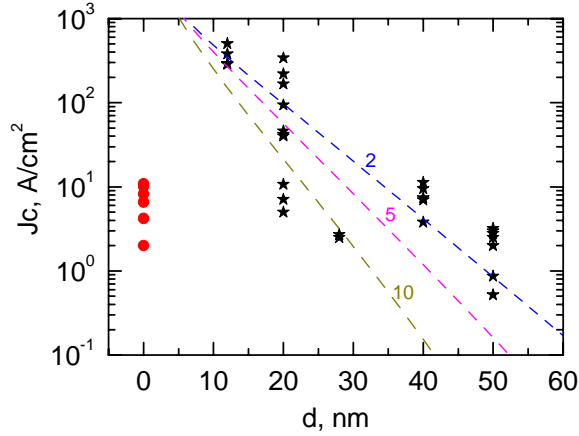


Fig. 4. Thickness dependencies of critical current density for junctions with (and without $d=0$) AF interlayer. Dashes are theoretical dependences for S/AF/S junctions with different intensity of exchange field h (numbers) in F.

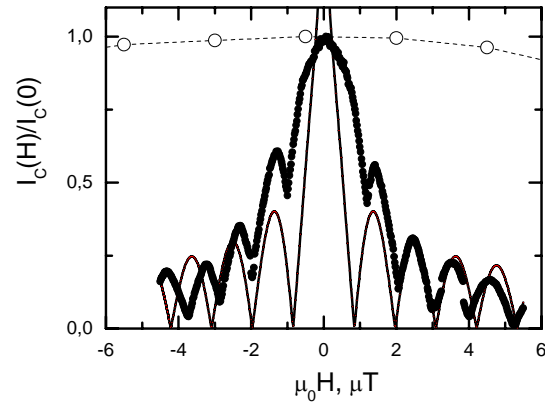


Fig.5. Magnetic-field dependence $I_c(H)$ for structures with $L = 50 \mu\text{m}$. With AF interlayer - black points, thin line is theory [3]. A central part of $I_c(H)$ for a structure without AF layer - open circles.

Theoretical dependences $j_c(d)$ are also plotted for a model of S/AF/S junction with a magnetic interlayer consisting from $N=20$ ferromagnetic layers with opposite magnetization. The best fit gives the theoretical dependence for the exchange field $h=H_{ex}/\pi kT=5$ plotted for the case when coherence depth in AF $\xi_{AF}=10$ nm. Fig.5 demonstrate magnetic-field dependence $I_c(H)$ for junctions with the same dimensions, $L = 50$ nm, one with, and other without AF interlayer. The calculation of $I_c(H)$ by [3] for S/AF/S junctions shows huge increase in sensitivity to applied H -field in comparison with structures without AF interlayer.

The dominant d-wave symmetry of the S_d electrode results in a non-sinusoidal CPR for MHS with c-axis oriented YBCO: $I_s(\varphi)=I_{c1}\sin\varphi+I_{c2}\sin2\varphi+\dots$. The values of the second harmonics of the CPR were defined from measurements of Shapiro steps at $f_e=36\div120$ GHz. All MHS demonstrated Shapiro steps with strong modulation as a function of the microwave power (inset to Fig. 6). The modulation of the amplitudes of the Shapiro steps vs. applied microwave power (Fig. 6) confirms the Josephson effect origin of the superconducting current. Less than 20% difference has been observed between the critical frequency $f_c=2eV_c/h=71$ GHz calculated from $V_c=I_c R_N=147\mu\text{V}$ (static estimation of f_c) and the $f_c=56$ GHz determined from the maximum value of the first Shapiro step using the RSJ model approach (dynamic f_c) [10].

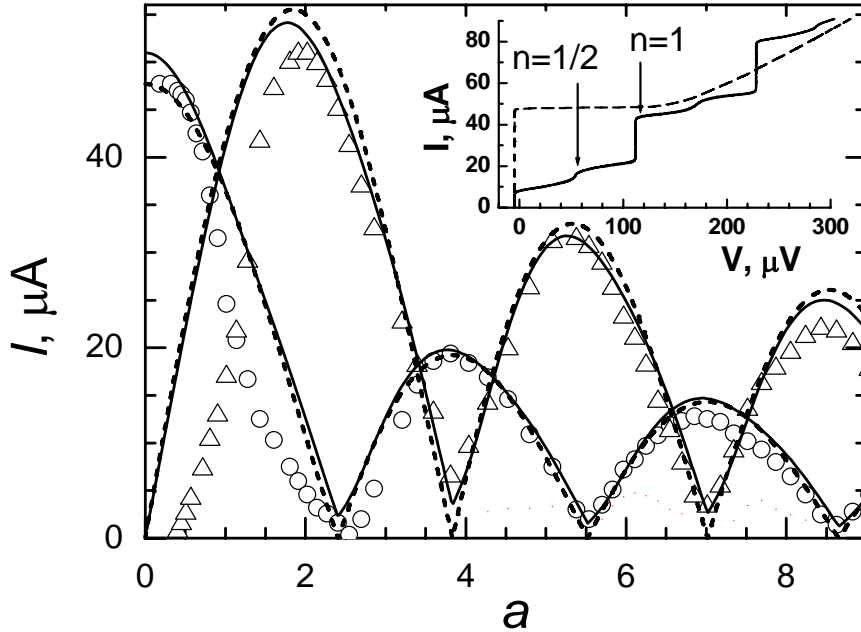


Fig. 6. The critical current I_c (circles) and first Shapiro step I_1 (triangles) vs normalized $a=I_e/I_c$ microwave current I_e at $T=4.2$ K, microwave frequency $f_e=56$ GHz. The solid lines correspond to the $I_c(a)$ and $I_1(a)$ curves numerically calculated from the modified RSJ model taking into account the second harmonic in CPR for $q=0.2$, dashes - for $q=0$. The $I-V$ curves with (solid line) and without (dashes) external microwaves are shown in the inset. Positions of integer $V_1=n\hbar f_e/2e$ ($n=1$) and half-integer $n=1/2$ Shapiro steps are indicated by arrows.

The deviation of experiment from model calculations becomes smaller if we take into account a presence of the second harmonic component in the CPR, which is manifested by fractional Shapiro steps (inset Fig. 6) observed at all experimental frequencies up to 120 GHz. At the same time it is known, that fractional Shapiro steps may originate also from the finite capacitance C of the Josephson junction (McCumber $\beta_c=(2e/\hbar)I_c R_N^2 C > 1$) [9]. We estimated $\beta_c=2\div 6$ from the hysteretic $I-V$ curves. In order to investigate the influence of the second harmonic in the CPR and the capacitance C on dynamics of MHS we have studied dependences of the critical current $I_c(a)$ and the first Shapiro step $I_1(a)$ vs. normalized amplitude $a=I_e/I_c$ of external microwave current I_e . Amplitudes a were determined [9, 10] from the attenuation levels of applied microwave power. The performed calculations of the Shapiro step amplitudes based on the modified RSJ model (taking into account the β_c parameter) show that at frequencies $f_e > f_c$ the impact of capacitance C on Shapiro steps amplitudes is small, and the $I_c(a)$ and $I_1(a)$ dependences are determined mainly by the first and the second harmonics of the CPR. The experimental data presented in Fig. 6 are fitted well to the theoretical dependencies calculated taking into account the amplitude I_{c2} of the second harmonic in the CPR $q=I_{c2}/I_c=0.2$. Note the sign of q can be determined by analyzing the experimental dependence of half integer Shapiro step $I_{1/2}(a)$ in comparison with the theoretical calculated one [9]. This procedure gives us negative $q < 0$. The presence of the second harmonic in the CPR of the MHS indicates an existence of a portion of d-wave component in M-interlayer.

For a junction with c -oriented YBCO film a “devil” staircase structure on $I-V$ curve was observed under microwave irradiation at 45 GHz. Fig. 7 shows such $I-V$ curves evolution when applied power was changed. Distortion of the 2nd Shapiro step is seen at large power levels (Fig. 7b) observed within narrow attenuation range $\alpha=3$ dB. Fig.7a demonstrates unusually large half-integer $n=1/2$ Shapiro steps: up to 0.4 of critical current I_c . That could be caused by superposition of two processes, first one is due to existence of the second harmonic in current-phase relation, and the second one could be related to the period doubling under the large microwave signal when frequency of applied signal f_e is not far from plasma frequency of Josephson junction $f_p=(2eI_c/\hbar C)^{1/2}$, where e is electron charge, \hbar is Planck’s constant. Fig. 7c shows $I-V$ curves with

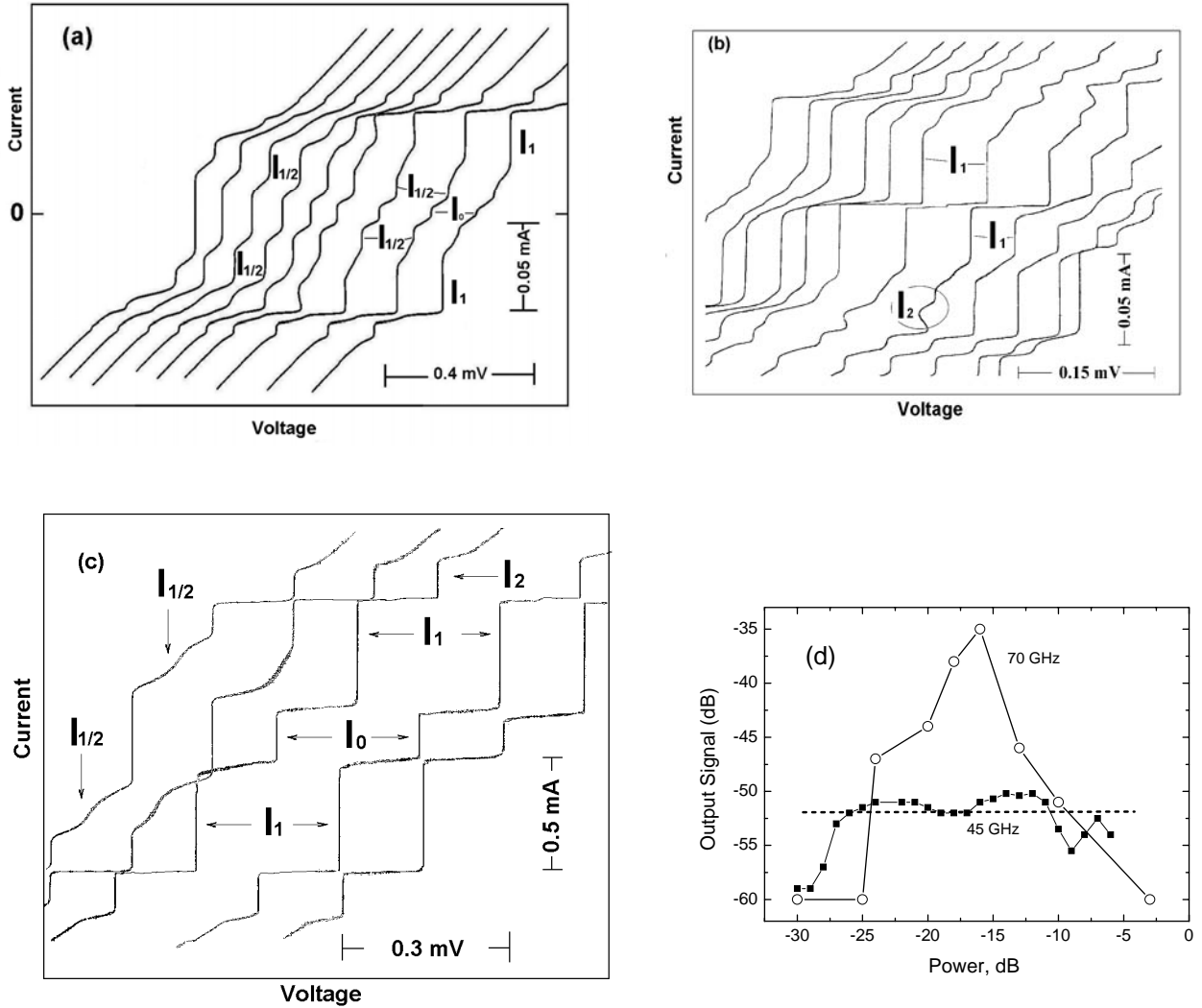


Figure 7. Families of I - V curves under different power levels of microwave irradiation $f=45$ GHz (a, b) and $f=70$ GHz (c). Critical current I_C , integer I_1 , I_2 and half-integer $I_{1/2}$ Shapiro steps are indicated. (b): $n=2$ Shapiro step distortion is pointed by circle. (c): Chaotic noise rise corresponds to the jerks on $I_{1/2}$ steps. All curves are shifted by voltage to the right with increase of applied power. AF interlayer was $\text{Ca}_{0.5}\text{Sr}_{0.5}\text{CuO}_2$, dimensions $20 \times 20 \mu\text{m}$, $d=20$ nm, $I_C=55 \mu\text{A}$, $R_N=5.5 \Omega$, and $\beta_C=2$. (d): Output signal measured in 1-2 GHz frequency band under microwave power P at 45 GHz (black symbols) and 70 GHz (open symbols). Dash line shows saturation level for frequency mixing.

the jerks at biasing voltages between integer Shapiro steps when 70 GHz signal was applied and a giant noise rise was registered by cooled amplifier within 1-2 GHz band. Note, power of applied signal was large enough and a frequency mixing effect also takes place due to existence of self-Josephson radiation. In order to compare intensities of the frequency mixing products with the chaotic oscillations we estimated the output signal saturation in frequency mixing regime. Fig. 7d shows the dependences of output signal levels vs. applied power of microwave signals at $f_e=45$ GHz and 70 GHz when current bias was fixed, keeping the voltage near the half-integer Shapiro step $V_{1/2}=(2e/h)/f_e$, where chaotic behaviour was observed. The output signal saturation level in frequency mixing process is also shown. Experimental conditions for chaotic oscillations in Josephson junctions were analysed [11] and were experimentally observed [12] in the case of superconducting tunnel junctions with $\beta_C > 25$. However, our junctions had relatively small β_C parameters. Recently chaotic dynamics was predicted [13] for S/F/S Josephson structures with magnetic interlayer consisted of 3 separated F-layers with rotated magnetization. Although we did not obtain experimental evidence for the triplet Josephson effect in our structures, the latter finding points on very complicated high frequency dynamics in Josephson junctions with magnetic interlayer. These results show that along with the

search for promising materials of magnetic interlayer aiming at applications at microwaves the dynamics of such junctions with magnetic interlayer should be studied in details in order to avoid chaotic behaviour and unstable operation.

4. Conclusions

Hybrid superconducting Josephson junctions with an antiferromagnetic $d=10 - 50$ nm thick interlayer were fabricated on NdGaO₃ substrates. Exponential decrease of critical current density with AF layer thickness was observed. Superposition of magnetic and microwave fields did not lead to distortion in symmetry of $I-V$ curves: equal Shapiro step amplitudes were registered at positive and negative voltage biasing. The sensitivity to applied magnetic field for these junctions was found much higher than for conventional Josephson junctions. Then, half integer Shapiro steps observed along with the sub-harmonic frequency selective detector response. That points on deviation of current-phase relation from sinusoidal one. At the same time at the certain experimental conditions a “devil” staircase appears on $I-V$ curves and the giant noise-like signal was registered for the junction fabricated using c -oriented YBCO electrode.

Acknowledgment

This work was supported by Russian Academy of Sciences, Scientific School Grant 5423.2010.2, Russian Ministry of Education and Science - contract 02.740.11.0795, RFBR proj. 08-02-00487, ISTC proj. 3743.

References

- [1]. A.I. Buzdin. Rev. Mod. Phys. **77** (2005) 935.
- [2] F.S. Bergeret, A.F. Volkov, K.B. Efetov. Rev. Mod. Phys. **77** (2005) 1321.
- [3] L. Gor'kov, V. Kresin. Appl. Phys. Lett. **78**, 3657 (2001), Physics Reports **400** (2004) 149.
- [4]. A.V. Zaitsev. JETP Lett. **90** (2009) 521.
- [5].C. Bell, E.J. Tarte, G. Burnell, C.W. Leung, D.-J. Kang, and M.G. Blamire. Phys. Rev. **B68**, (2003) 144517.
- [6]. P.V. Komissinskiy, G.A. Ovsyannikov, I.V. Borisenko, Yu.V. Kislinskii, K.Y. Constantinian, A.V. Zaitsev, D. Winkler. Phys. Rev. Lett. **99** (2007) 017004.
- [7]. Y.V. Kislinskii, K.Y. Constantinian, G.A. Ovsyannikov, P.V. Komissinskiy, I.V. Borisenko, A.V. Shadrin. JETP **106** (2008) 800.
- [8]. A.V. Zaitsev, G.A. Ovsyannikov, K.Y. Constantinian, Y.V. Kislinskii, A.V. Shadrin, I.V. Borisenko, P.V. Komissinskiy. JETP **110** (2010) 336.
- [9].P. V. Komissinskiy, G. A. Ovsyannikov, K.Y. Constantinian, Y.V. Kislinski, I.V. Borisenko, I.I. Soloviev, V.K. Kornev, E. Goldobin, and D. Winkler. Phys. Rev. **B78** (2008) 024501.
- [10].A. Barone, G. Paterno (N.-Y. Awaley-Interscience Publication John Wiley and Sons, 1982).
- [11].R. Kautz, R. Monaco. J. Appl. Phys. **57** (1985) 875.
- [12]. Gubankov V.N., Constantinian K.Y, Koshelets V.P., Ovsyannikov G.A., Vystavkin A.N. IEEE Tr. on MAG-**19** (1983) 968.
- [13] V. Braude and Ya.M. Blanter. Phys. Rev. Lett **100** (2008) 207001.

Amplification of Coherent Cherenkov Radiation From One-Dimensional Electron Bunch Moving Inside a Layered Dielectric-Filled Waveguide

L.Sh. Grigoryan, H.F. Khachatryan, S.R. Arzumanyan

Institute of Applied Problems in Physics, Hr. Nersessian str. 25, 0014 Yerevan Armenia

The coherent Cherenkov radiation (CCR) from a one-dimensional bunch of relativistic particles uniformly moving along the axis of cylindrical waveguide filled with semi-infinite stack of dielectric plates alternated with vacuum gaps is investigated. The values of the parameters of problem under which the self-amplification of CCR at a separate waveguide mode have been determined. This radiation may prove to be many times as strong as CCR in the waveguide filled with semi-infinite solid dielectric without vacuum gaps. The visual explanation of this effect of self-amplification of radiation is given. It is proposed to use this effect for amplification of the power of coherent CR from pico- and subpicosecond electron bunches observed by J.B. Rosenzweig with co-authors in 2009 [1, 2].

1. Introduction and background

Modern electron accelerators show great promise as tools for creating radiation in the terahertz spectral region that is of considerable interest for applications in physics, chemistry and biology [3]. A typical scenario involves the passage of an electron beam through a perturbing element such as an undulator, stack of plates, or other structure that causes it to radiate. The structure under our study is a cylindrical waveguide filled with a semi-infinite layered dielectric.

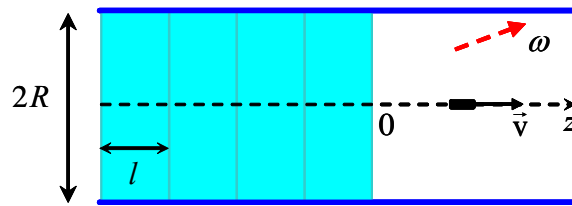


Fig.1. The radiation from a bunch of relativistic particles uniformly moving along the axis of cylindrical waveguide filled with a semi-infinite layered material.

Let us consider the case of one-dimensional bunch of $N \gg 1$ particles that uniformly travels along OZ axis of a cylindrical waveguide of R radius, that is filled with semi-infinite layered material (see Fig.1). In the present work the energy of radiation

$$W = \sum_{n=1}^{\infty} \int_{\omega_n}^{\infty} I_n^{(N)}(\omega) d\omega = \sum_{n=1}^{\infty} W_n, \quad (1)$$

passing through the waveguide cross section far from the medium-vacuum interface throughout the time of bunch motion is investigated. In (1) ω_n is the lower boundary of the n -th mode of waveguide, and

$$I_n^{(N)}(\omega) = I_n^{(1)}(\omega)[N + N(N-1)f(\omega)] \quad (2)$$

is the spectral distribution of radiation energy on this mode. The first multiplier $I_n^{(1)}(\omega)$ in (2) is the spectrum of radiation from a single particle, and the second one is a structural factor describing the nature of interference of radiations from bunch particles. Here the coherence factor is determined by equality [4,5]

$$f(\omega) = \left| \int \rho(z) \exp(-i\omega z/v) dz \right|^2, \quad (3)$$

where $\rho(z)$ is an one-particle distribution function of the bunch along the waveguide axis.

The problem was that the waves propagating in the layered medium were the Bloch electromagnetic waves (travelling waves modulated with periodicity of medium), not the plane ones. However, the waves propagating inside the hollow part of the waveguide are plain and, therefore, the radiation spectrum of a single particle is determined by wave amplitudes according to the well known formula. We managed to

calculate this amplitude with no limitations on the amplitude and variation profile of the layered medium permittivity ε .

The aim of the present work is to reveal and visually demonstrate the cases when the waveguide and periodical structure of the layered medium jointly influence the Cherenkov radiation (CR) of the particle bunch.

In Section 2 the case of a single particle and in Section 3 the case of finite length particle bunch are treated.

2. Radiation from a single particle

2.1. Results of numerical calculations

In Fig.2 three curves of the spectral distribution $I_n^{(1)}(\omega)$ of the energy of CR from a single electron on the 3-rd mode of waveguide are shown.

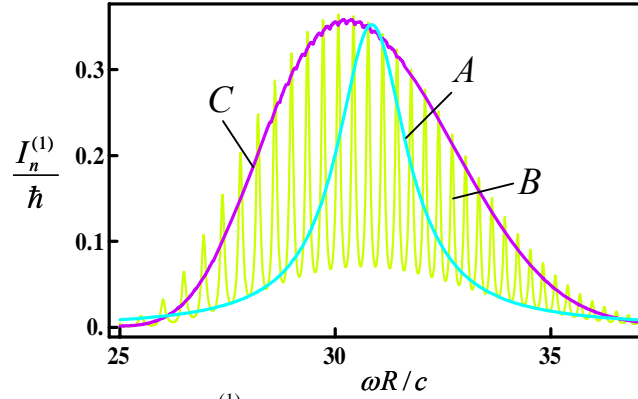


Fig.2. The density of spectral distribution $I_n^{(1)}(\omega)$ of energy of CR from a single electron on the 3-rd mode of waveguide, half-filled either with a continuous dielectric (curve *A*), or a stack of plates of the same dielectric (curves *B* and *C*).

The energy of electron is $E_e = 1.2 MeV$,

$$\varepsilon = \varepsilon_b + 0.005i \quad \text{with} \quad \varepsilon_b = 1.3 \quad (4)$$

is the dielectric permittivity of material filling the waveguide (the allowance for the dispersion of electromagnetic waves is not made).

In case of curve *A* the waveguide is filled with semi-infinite continuous dielectric. The position of maximum in the spectrum of CR is determined from a well known equality

$$\omega_n^{Ch} = \frac{\alpha_n v}{R \sqrt{\varepsilon_b v^2 / c^2 - 1}} \quad (5)$$

for $n = 3$. α_n are the zeroes of Bessel function: $J_0(\alpha_n) = 0$, $n = 1; 2; 3 \dots$ is the number of waveguide mode. Equality (5) determines the frequencies of CR from the electron traveling at superrelativistic velocity along the axis of waveguide completely filled with dielectric. The finite height and finite width of the peak are stipulated for the fact of the allowance of radiation absorption in the matter (refer to (4)).

The case *B* differs from case *A* in that some part of dielectric is removed from the waveguide to leave there a semi-infinite stack of plates with vacuum gaps (see Table 1 and Fig.4). At its travel along the waveguide axis the particle generates CR in each plate and the pulses formed in different plates superimpose and interfere. The oscillations in curve *B* reflect this fact. The case *C* differs from case *B* by the thickness of vacuum gap (see Table 1). The integral (total) energy of radiation is practically the same for curves *A* and *B*, whereas for curve *C* it is twice as large:

$$W_3^A \approx W_3^B \approx 0.95c\hbar / R, \quad W_3^C \approx 1.94c\hbar / R. \quad (6)$$

How can one explain that?

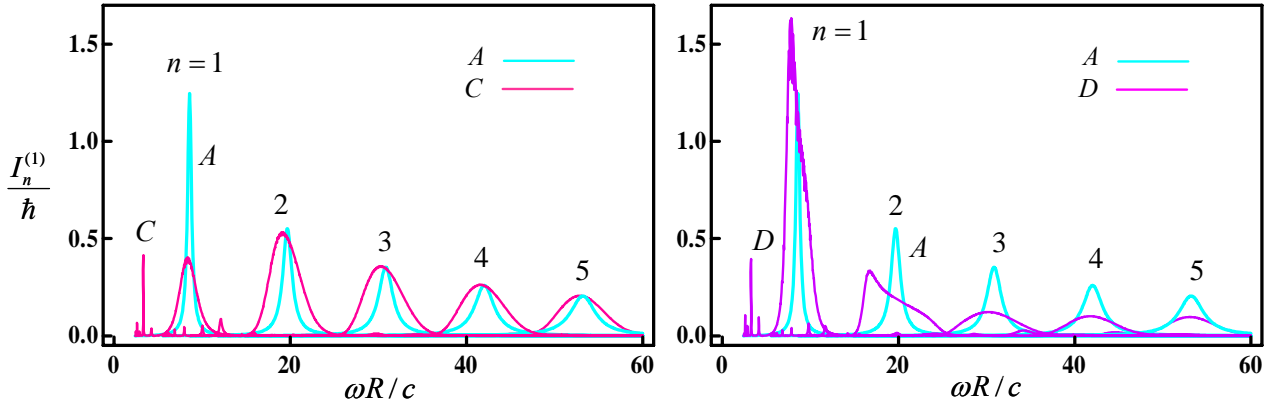


Fig.3. CR spectra from a single electron at the first five modes of waveguide either half-filled with continuous dielectric (curve A on the left and right), or with stack of plates (curve C on the left and curve D on the right).

In Fig.3. the radiation spectra on the first five modes of the waveguide are shown. The numbers of modes are seen beside the curves. The curves on the left and right (C and D) correspond to slightly differing thicknesses of vacuum gap between the plates (about several percents, see Table 1). Curve A is shown here for comparison (the waveguide filled with continuous semi-infinite dielectric). From Fig.3 it follows that (a) at the transition $A \rightarrow C$ the total energy of radiation increases on the 2,3,4 and 5-th modes and does not increase on the 1-st mode of waveguide and (b) at the transition $A \rightarrow D$ the total energy of radiation increases in 3.6 times on the 1-st mode and does not increase on successive modes of waveguide (2,3,4,5). A slight (several per cent) variation in thickness of vacuum gaps in the stack of plates changes the waveguide modes at which the energy of CR increases. What is the matter? How can we explain this amplification?

2.2. Visual explanation

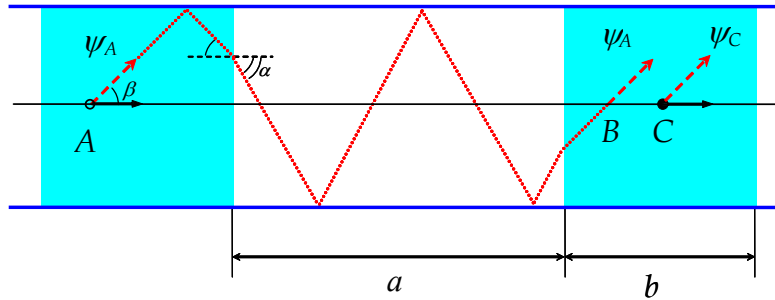


Fig.4. Two neighboring plates inside the waveguide filled with semi-infinite stack of dielectric plates. In case of $C \equiv B$ the pulse Ψ_C of CR generated by the particle in the vicinity of point C is «superimposed» on the pulse Ψ_A of CR generated by the particle in the vicinity of point A prior to that.

In Fig.4 two neighboring plates inside the waveguide are seen. Now consider the instant when the charged particle was in the left plate. Now observe the pulse Ψ_A of CR, generated by a superrelativistic particle in a small vicinity of point A , that is emitted under a specific angle β (angle of CR) with respect to the waveguide axis (dashed line). At the propagation this pulse is found in the right plate and at some instant of time traverses the trajectory of particle (the waveguide axis) in a certain point B under the same angle β . By this time the relativistic particle emits the pulse Ψ_C of CR in a small vicinity of some (generally) other point C (see Fig.4). However, one may ascertain that if the following equalities are satisfied

$$\frac{a+b}{v} = \frac{a}{c \cos \alpha} + \frac{b \sqrt{\epsilon_b}}{\cos \beta}, \quad \frac{a \tan \alpha + b \tan \beta}{2R} = 4s, \quad s = 1, 2, 3, \dots \quad (7)$$

(α is an angle giving the direction of CR with respect to the waveguide axis in vacuum between the plates), then $C \equiv B$ and for this reason the particle will traverse the vicinity of point B concurrently with pulse Ψ_A .

As a result, the pulse Ψ_C emitted at the same angle β in the vicinity of point C will «superimpose» on the pulse Ψ_A emitted earlier in the 1-st plate. The result of superimposition (interference) may be accompanied either by the suppression or amplification of pulses depending on the particular value of phase difference. The factor 4 in the right side of the second equation of (7) provides the observation of the condition of pulse superposition synchronism. Thus, if conditions (7) are met, the Cherenkov waves are generated inside the plate and at once physically interfere with those emitted by particle in preceding plates.

For curve C in Figs.2 and 3 the values of a/R and b/R (see Table 1) have been determined from (7) in case of $s = 1$. The increase of total energy of CR on the 2,3,4 and 5-th modes of waveguide at the transition from curve A (waveguide filled with a semi-infinite continuous dielectric) to curve C (waveguide filled with a semi-infinite stack of plates) is explained by the above fact.

Equalities (7) are valid in the framework of ray optics when the wavelength of the emitted wave is much less than R , a and b . Equations (7) require more accurate definition on the first mode of waveguide. It is not surprising hence that in Fig.3 the increase in the energy of CR on the 1-st mode of waveguide at the transition from curve A to curve D occurs for a/R somewhat different from its value determined from (7) (compare the values of a/R in rows C and D in Table 1).

Thus, the increase in the total energy of CR at the replacement of continuous dielectric in the waveguide by a stack of plates is due to the fact that in each plate of the stack in the zone of CR formation there simultaneously occur two processes of generation and a physical interference of Cherenkov waves emitted by the particle in the preceding plates.

The synchronous superposition of waves is followed by an increase in the resultant field in the zone of radiation formation and, hence, also by an increase of the force retarding the particle motion along the waveguide axis. In this situation additional work of the external forces that sustain the uniform motion of the particle shall be spent on the generation of more intense CR.

3. Coherent radiation from the bunch of particles

For evaluation of the degree of coherence of CR we shall avail of a simple model when the distribution of particles on the waveguide axis is Gaussian:

$$\rho(z) = \frac{1}{\sqrt{2\pi}\sigma} \exp\left(-\frac{z^2}{2\sigma^2}\right) \quad (8)$$

with the root-mean-square deviation σ . The factor of coherence of such a bunch is

$$f(\sigma; \omega) = \exp(-\sigma^2 \omega^2 / v^2). \quad (9)$$

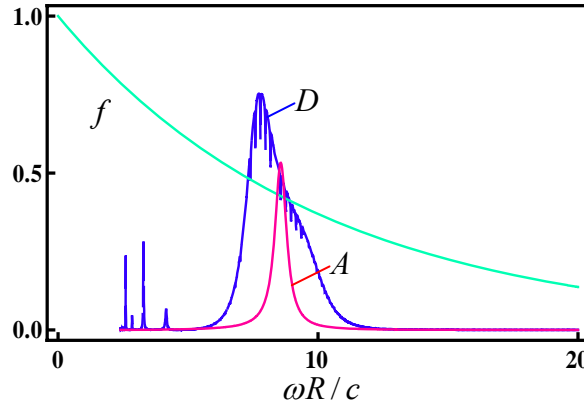


Fig.5. Spectra of CR of the bunch consisting of $N = 10^3$ electrons on the 1st mode of waveguide half-filled with continuous dielectric (curve A) or the stack of plates (curve D). $I_n^{(N)}$ is in units of $N^2 \hbar$ (curves A , D). Curve f is the factor of coherence of CR.

Curve D of the spectral distribution $I_n^{(N)}(\omega)$ of CR of the bunch of $N = 10^3$ electrons with $\sigma = 0.09R$ on the 1-st mode of waveguide filled with the semi-infinite stack of plates is shown in Fig.5. The parameters of stack are given in Table1, the energy of electrons and ε being the same as those in Fig.2.

Table 1

	a/R	b/R
A	0	--
B	308.6	13.74
C	15.43	13.74
D	15.05	13.74

For comparison in Fig.5 also curve A of the spectral distribution of CR of the same bunch is given in the case when the vacuum gaps between the plates are absent (the waveguide is filled with the semi-infinite continuous dielectric). Also the curve of coherence factor of radiation $f(\omega)$ is given. From comparison of curves A and D a conclusion may be made that the total energy of CR of bunch increases more than three times at the transition from the continuous dielectrical filling of the waveguide to the stack of plates (the self-amplification effect). Moreover, the behavior of curves D and f testifies that the average value of the coherence factor $\bar{f} \approx 0.5$, and therefore (see (2)) the energy of CR on the particle bunch exceeds the energy of a single particle multiplied by $N(N-1)/2 \cong 5 \cdot 10^5$. The value of $\bar{f} \approx 0.5$ is not casual.

CR is generated close to the frequency determined by equality (5). Substituting this expression in (9) we arrive at a conclusion that on the n -th mode of waveguide the coherence factor satisfies the inequality $0.5 \leq f(\omega) \leq 1$, if the roof-mean-square deviation of particles inside the bunch

$$\sigma \leq \sigma_n \quad (10)$$

with limiting value

$$\sigma_n \approx \frac{R}{\alpha_n} \sqrt{(\varepsilon_b v^2 / c^2 - 1) \ln 2}. \quad (11)$$

As for the 1-st mode of waveguide $\sigma_1 = 0.088R$, it is very close to the value of $\sigma = 0.09R$ in Fig.5, we have therefore $\bar{f} \approx 0.5$ (see Fig.5).

To sum up we conclude that the coherent CR of the bunch of electrons traveling inside the waveguide filled with a stack of plates is self-amplified at the selection of the thickness of plates and of vacuum gaps between the plates according to equalities (7).

4. Discussion

In 2009 J.B. Rosenzweig with co-authors [2] reported the first direct observation of narrow-band terahertz coherent CR (CCR) driven by a subpicosecond electron bunch traveling along the axis of a hollow cylindrical dielectric-lined waveguide. The measurements of the radiated energy indicate a peak power of $\approx 150kW$. Now the authors of [2] "consider structure variations that would give improved results". We propose to modernize the part of experimental set up of [2], in which CCR from a picosecond electronic bunch is generated. It is a hollow cylindrical dielectric tube coated on the outer surface with metal to form a dielectric-lined waveguide.

The modernization is reduced to the following. The hollow cylindrical dielectric tube inside the waveguide (the length of tube is L) shall be cut in k identical parts (each of the length $b = L/N \gg \lambda$, where λ is the wavelength of CCR) and then a periodic structure consisting of these parts alternated with *vacuum gaps* shall be combined. *If the length a of each vacuum gap in the stack of shorter tubes inside the waveguide is selected correctly, then nearly a k -fold increase in the peak power of CCR from subpicosecond electron bunch as compared with the case of $a = 0$ is expected.*

5. Conclusions

In this paper the coherent Cherenkov radiation from a one-dimensional bunch of relativistic particles uniformly moving along the axis of cylindrical waveguide filled with semi-infinite layered dielectric that weakly absorbs the radiation is investigated.

- Expressions for calculation of the spectral distribution of total energy of radiation passing through the transverse section of waveguide in vacuum (at large distances from the boundary of laminated medium) are derived with no limitations on the amplitude and variation profile of the laminated medium permittivity.
- The results of numerical calculations for emission of coherent Cherenkov radiation (CCR) in the layered material consisting of dielectric plates alternated with vacuum gaps are given. The values of the parameters of problem under which the self-amplification of CCR at a separate waveguide mode have been determined. This radiation may prove to be many times as strong as CCR in the waveguide filled with semi-infinite solid dielectric without vacuum gaps. The visual explanation of this effect of self-amplification of radiation is given.
- It is proposed to use this effect for amplification of the power of coherent CR from pico- and subpicosecond electron bunches observed by J.B. Rosenzweig with co-authors in 2009 [1,2].

References

- [1] E. Hemsing, J.B. Rosenzweig, *J. Appl. Phys.*, **105** (2009) 093101.
- [2] A.M. Cook, R. Tikhoplav, S.Y. Tochitsky, G. Travish, O.B. Williams, J.B. Rosenzweig, *Phys. Rev. Lett.* **103** (2009) 095003.
- [3] G.P. Williams, *Reports on Progress in Physics*, **69** (2006) 301.
- [4] G.M. Garibian and C. Yang, *X-Ray Transition Radiation* (AN Arm. SSR Press, Yerevan, 1983) (in Russian).
- [5] M.M. Nikitin and V.Ya. Epp, *Undulator Radiation* (Energoatomizdat, Moscow, 1988) (in Russian).

Детектирование терагерцовых волн с помощью вакуумного диода

А.С. Ароян, А.А. Ахумян, А.Ю. Вартамян, А.О. Макарян, В.Р. Татевосян

*Ереванский Государственный Университет, Кафедра СВЧ радиофизики и телекоммуникации,
ул. Алека Манукяна 1, Ереван, 0025, Армения*

The detection of subterahertz (up to 0.14 THz) electromagnetic radiation in the propagation of electromagnetic radiation in the waveguide formed by the parallel plate electrodes of a vacuum diode is experimentally demonstrated. The dependence of the detected signal from the incident radiation power, direction of wave polarization, current characteristics and frequency of modulating signal has been investigated.

A simple theoretical model, according to which the detection is due to nonlinearity associated with the uneven distribution of electrons along the direction of the electric field, has been proposed to explain the mechanism of detection. The measured detection characteristics are reasonable agree with theoretical based on low-level signal approximation and presenting diode's current-voltage characteristic by law of the $3/2$.

Терагерцовый (ТГц) диапазон электромагнитных волн (0.1 – 10 ТГц) чрезвычайно перспективен для спектроскопии, диагностики различных объектов, мониторинга окружающей среды, обнаружения взрывчатых и ядовитых веществ [1-3] и т.д, поскольку частоты вращательных переходов молекул газов и жидкостей, частоты колебаний сложных биологических молекул, а также оптических фононов твердых тел расположены именно в этом диапазоне. Неионизирующий характер и слабое рассеяние ТГц излучения в мелкодисперсных средах делает его весьма привлекательным также для использования в биологии и медицине.

Ключевыми узлами всех ТГц систем являются источник и приемник (детектор) излучения. В настоящее время одна из основных проблем при освоении терагерцового диапазона - это отсутствие быстродействующих, высокочувствительных и доступных детекторов данной области [2-4], наличие которых особо важно при работе с микромощными источниками ТГц излучения.

Несмотря на то, что ТГц волны занимают диапазон между инфракрасной и СВЧ диапазонами, однако по ряду причин как оптические, так и СВЧ методы приема электромагнитного излучения малоэффективны для регистрации ТГц сигналов.

Быстродействующие и чувствительные приемники оптического диапазона, работающие на основе внешнего или внутреннего фотоэффектов непригодны для регистрации ТГц излучения из-за малой энергии терагерцового фотона. Что касается широко распространенным в СВЧ диапазоне диодам Шоттки, то их чувствительность резко падает в ТГц области в виду сравнительно больших длительностей времен релаксации в полупроводниках и сложности согласовки падающего излучения с точечным контактом диода [5]. В ТГц области достаточно чувствительны тепловые приемники (болометры, пироэлектрические приемники и др.), однако они обладают большой инерционностью, и поэтому не могут быть применены для регистрации быстрых процессов. Кроме того, болومترические приемники ТГц излучения требуют охлаждения до температуры жидкого гелия.

Следовательно, для успешного освоения терагерцового диапазона частот чрезвычайно актуальна разработка быстродействующих, высокочувствительных и доступных детекторов, работающих при комнатной температуре [5-9].

В настоящей работе исследовано детектирование субтерагерцовых электромагнитных волн с помощью вакуумных электронных ламп, которые все еще не нашли применение для регистрации электромагнитного излучения ТГц области, несмотря на многочисленные работы по нелинейному взаимодействию электромагнитного излучения с электронным потоком в вакууме [7,9].

Основная проблема при использовании электронных ламп в качестве детектора - это трудности подвода электромагнитного излучения к электродам лампы.

Однако, эта проблема автоматически снимается если электромагнитная волна распространяется в межэлектродной области лампы, т.е. в самой нелинейной среде. В данном случае нелинейная среда представляет собой неоднородно распределенный пространственный заряд между электродами, чем обусловлена нелинейность вольт-амперной характеристики вакуумного диода, описываемая по закону $3/2$. Таким образом, при обеспечении проникновения электромагнитного излучения в межэлектродное пространство вакуумной лампы возможно нелинейное взаимодействие с потоком электронов, а в результате чего можно получить генерацию гармоник, преобразование частот, детектирование и т.д.

Нами исследовалось детектирование амплитудно-модулированного электромагнитного излучения низкочастотной области терагерцового диапазона (до 0.14 ТГц), где имеются удобные и достаточно мощные источники излучения.

Блок-схема экспериментальной установки представлена на рис. 1.

В качестве источника электромагнитного излучения был использован стандартный генератор Г4-161 с волноводным выходом. Максимальная выходная мощность составляла ~ 10 мВт а диапазон перестройки частоты 129-142 ГГц. Модуляция излучения осуществлялась с помощью генератора стандартных сигналов, частота которого изменилась от 1 КГц до 100 КГц. Исследовались вакуумные приборы с параллельными электродами (триоды с заземленной сеткой и диоды), обладающие наиболее удобной конструкцией.

На лампу от регулируемого источника постоянного напряжения 4 через балластный резистор R подавалось напряжение смещения U_0 . Детектированный сигнал снимался с анода лампы и регистрировался с помощью осциллографа 5 (Tektronix 453).

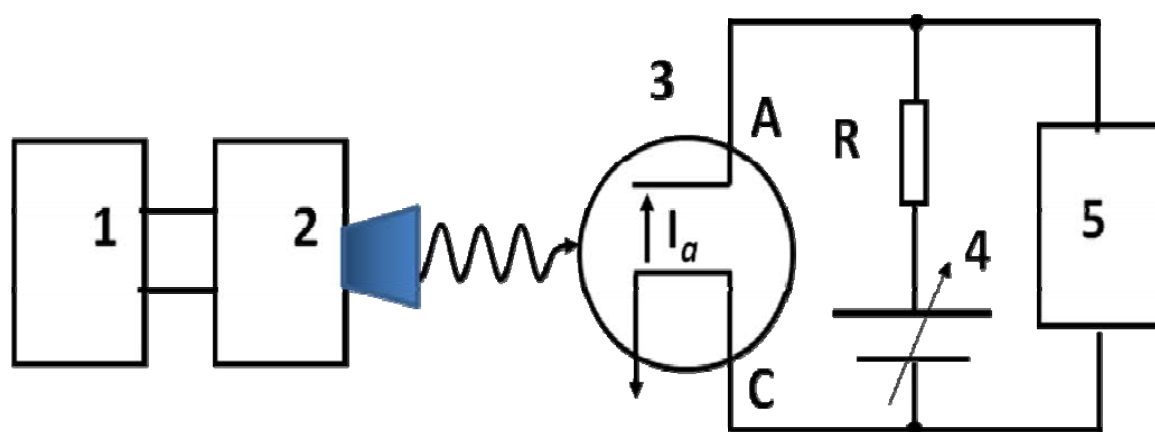


Рис. 1. Блок-схема экспериментальной установки:

1 - генератор модулирующих сигналов ($F=1\div 100$ КГц), 2 - генератор субтерагерцового излучения Г4-161 ($f=129\div 142$ ГГц), 3 - электронная лампа, 4 - регулируемый источник питания, 5 - осциллограф Tektronix 453, R - балластное сопротивление

Для обеспечения проникновения электромагнитной волны в межэлектродное пространство, вакуумная лампа располагалась непосредственно на пути распространения электромагнитной волны с вектором поляризации параллельным направлению электронного потока в лампе, как показана на рис. 2а.

Минимальная мощность, при которой было получено уверенное детектирование при размерах электродов лампы $l = 15$ мм, $d = 2$ мм, $h = 0.5$ мм составляла ~ 10 мкВт.

Исследовалась зависимость детектированного сигнала от мощности падающего излучения (см. рис. 3.). Исследовалась также зависимость детектированного сигнала от угла θ между направлениями электрического поля волны E и электростатического поля E_0 в лампе (см. рис. 2б.). Эта зависимость приведена на рис. 4.

Как и следовало ожидать, детектированный сигнал сильно зависит от поворота плоскости поляризации. При перпендикулярном расположении электродов относительно плоскости поляризации сигнал максимален, а при параллельном расположении-минимален. Следует отметить, что для всех ламп, использованных в качестве детектора во всем исследуемом диапазоне при изменении частоты модуляции в пределах $1\div 100$ КГц детектированный сигнал всегда оставался в противофазе относительно модулирующего сигнала и практически без искажения повторял его форму. Это свидетельствует об увеличении анодного тока лампы при увеличении мощности модулированного сигнала.

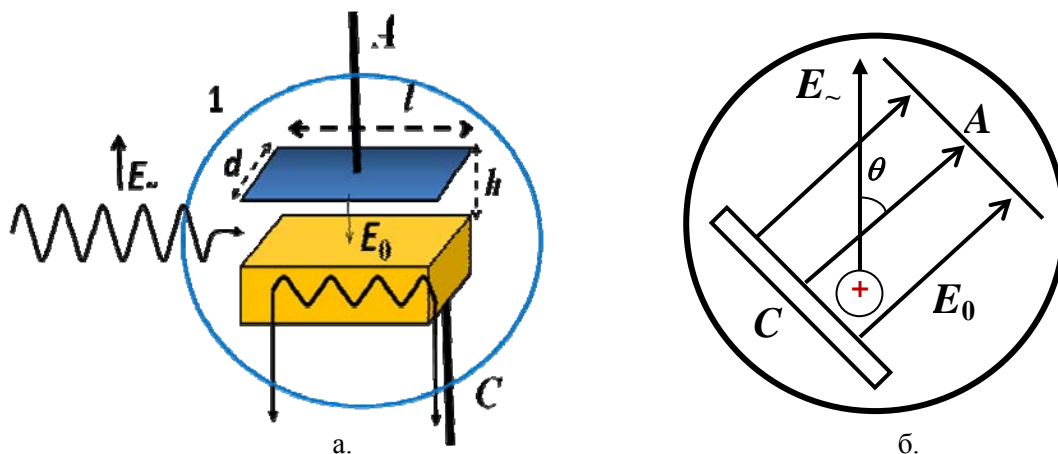


Рис.2.- расположение лампы на пути распространения электромагнитной волны:
 1-вакуумный диод (А-анод, С-катод, F-накал), l и d - размеры электродов, h - расстояние между электродами, E_{\sim} - электрическое поля волны, E_0 - электростатическое поле, θ - угол между направлениями электрических полей E_{\sim} и E_0 , + - направление распространения волны.

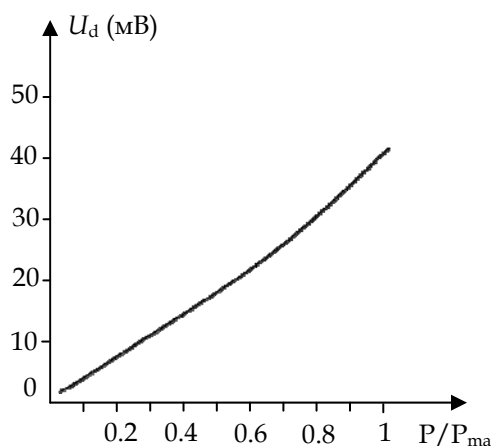


Рис. 3. Зависимость детектированного сигнала от мощности излучения.

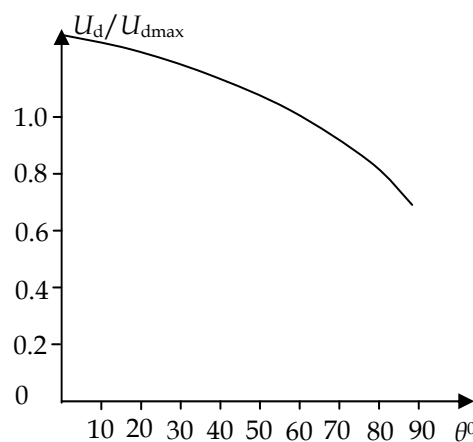


Рис. 4. Зависимость детектированного сигнала от угла θ между направлениями электрического поля волны E_{\sim} и электростатического поля.

Для объяснения механизма детектирования была предложена простая теоретическая модель, согласно которой детектирование в вакуумном диоде обусловлено нелинейностью, связанной с неравномерным распределением заряда (электронов) вдоль направления электростатического поля, чем и обусловлена нелинейность вольт-амперной характеристики (ВАХ) диода. Считая, что вольт-амперная характеристика диода подчиняется закону $3/2$ и не зависит от частоты приложенного поля, оценивалась величина детектированного сигнала, когда плоскость поляризации волны перпендикулярна электродам диода. Если электрическое поле волны в межэлектродном пространстве считать однородным, то для разности потенциалов между электродами созданной волной можно написать:

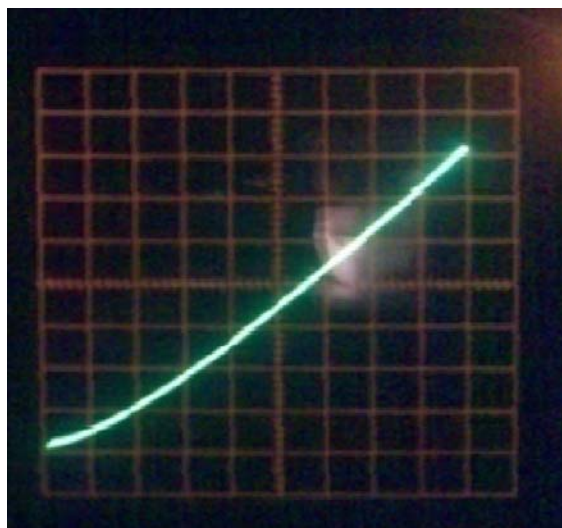
$$U_{\sim} = E_{\sim} d = E_{0\sim} d \cos \omega t = U_{0\sim} \cos \omega t, \quad (1)$$

где E_{\sim} электрическое поле волны, $E_{0\sim}$ его амплитуда, $U_{0\sim}$ амплитуда созданного напряжения, d межэлектродное расстояние, ω частота волны. Если на анод лампы приложено также постоянное напряжение U_0 , то в ненасыщенном режиме лампы для анодного тока имеем

$$I_a = a U_a^{3/2} = a (U_0 + U_{\sim})^{3/2}. \quad (2)$$

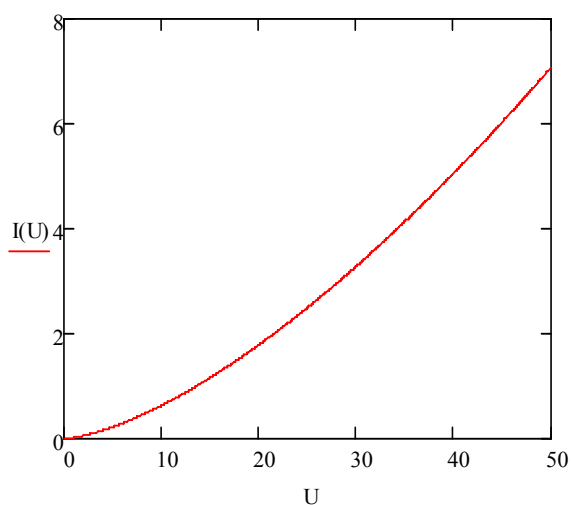
График этой зависимости при значении коэффициента $a = 0.02 \text{ mA/V}^{3/2}$ приведена на рис.5б., которая полностью соответствует типичной ВАХ использованных вакуумных ламп (см. рис.5а.).

2 мА/дел



5 В/дел

1 мА/дел



1 В/дел

Рис. 5. а. - типичная ВАХ исследуемых электронных ламп, б. - расчетная ВАХ по формуле (2) ($a = 0.02 \text{ mA/V}^{3/2}$).

Оценки по формуле (2) показывают, что при интенсивности электромагнитной волны $\sim 10 \text{ мВт/см}^2$ и $U_0 = 2 \text{ В}$ максимальное значение детектированного тока будет $I \approx 0.03 \text{ мА}$. Ток, регистрируемый во время эксперимента составлял $I \approx 0.01 \text{ мА}$. Такое отличие вполне объяснимо, т. к. во время эксперимента не было обеспечено согласование, и поэтому в межэлектродное пространство проникал лишь малая часть мощности излучения.

Отметим, что исследуемые лампы были опробованы также на детектирование оптического излучения (3.39 мкм, 1.15 мкм и 0,63 мкм). Поскольку ТГц волны занимают промежуточную область спектра между оптическим и миллиметровым диапазонами, то полученные результаты могут быть использованы, в дальнейшем, для разработки ТГц детектора на основе вакуумного диода.

Несмотря на то, что чувствительность в оптическом диапазоне сильно уменьшается (~ 100 раз), однако, оценки указывают на то, что при решении вопросов согласования и при увеличении области взаимодействия излучения с межэлектродным пространственным зарядом вакуумные лампы могут быть успешно применены как для детектирования, так и для преобразования частот терагерцового диапазона.

Работа выполнена при поддержке гранта МНТЦ А-1544.

Литература

- [1]. "Sensing with terahertz radiation," ed. by D. Mittleman, Springer, Berlin, 2002.
- [2]. P.H. Siegel, IEEE Microwave Theory and Tech. **50** (2002) 910.
- [3]. M. Tonouchi, Nature Photon., **1** (2007) 97.
- [4]. K. Sakai, Terahertz optoelectronic. Springer, Berlin, 2005.
- [5]. Г.Д. Лобов, Устройства первичной обработки микроволновых сигналов, Москва, МЭИ, 1990.
- [6]. А. Ахумян, А.О. Макарян, К. Мовсисян, К. Хачатрян, Сб. трудов конф. Лазерная Физика -2007, (2008) 174.
- [7]. А.О. Макарян, В.Р. Татевосян, Ю.О. Аветисян, Сб. трудов конф. Лазерная Физика -2007, (2008) 182.
- [8]. N.S. Koreika and N.H. Farhat, IEEE Trans Electron Devices, **ED-22** (1975) 534.
- [9]. Д.И. Трубецков, А.Е. Храмов, Лекции по СВЧ электронике для физиков, т.1,2. Москва 2004.

THz Pulse Generation in Nonlinear Crystals and Its Application in Medicine

A.S. Nikoghosyan

*Department of Microwave and Telecommunication, Yerevan State University,
1 Alex Manoogian, Yerevan, 0025 Armenia
nika@ysu.am*

The results of the effective generation pulse of terahertz radiation in band 0.1-3.5 THz via optical rectification of femtosecond laser pulses in nonlinear LiNbO₃, ZnTe, crystals are presented. It is shown that placing the crystal in the free space or in the waveguide both the phase-matching and time and spectral features of the emitted THz field are changed. The spectrum of the generated THz beam can be modified also by the change of transverse position of crystal in the waveguide. It is shown that THz-rays can image tooth cavities, starting dotted caries in human teeth. The research has been conducted on teeth tissue in-vitro aiming to establish the characteristic THz properties of teeth tissue, enamel and dentine as well as to trace early detection of teeth erosion abnormalities.

1. Introduction

Broadband terahertz (THz) radiators are of great importance as coherent effective sources for spectral THz imaging systems, in medicine, space science, high-speed communications and high resolution of THz waveguide spectroscopy. However, the value of the generated THz power limits the major specifications of the THz coherent techniques application in imaging and tomography.

There are numerous ways of generating THz radiation, but most of useful sources and detectors can be divided into two groups - those based on electronics and those based on nonlinear-optical techniques. The electronic sources, which include Gunn diodes, backward wave oscillators (BWO) and super-lattice electronic devices can only operate at the microwave end of the THz region. The upper frequency limit for electronic sources is approximately 300 GHz (up to 1.5 THz for a BWO) and they usually provide limited power at THz frequencies. Their use is not currently widespread in medical applications. By comparison, photonic sources – lasers (CO₂ and GCL lasers), photoconductive dipole antennas (PDA), and devices relying on optical mixing to generate THz radiation (DFR, OR) - are ubiquitous in medical applications. They are used to provide both narrowband continuous wave (CW) radiation and broadband THz pulses across a wide range of frequencies. Perhaps the most commonly used generation method in medical applications employs *optical rectification*, whereby the high frequency oscillations of a femtosecond laser pulse are rectified by an optical crystal, leaving only the envelope of the laser signal, that is a THz pulse.

To effectively generate radiation sum or difference frequency with high power, it is necessary to provide the phase-matching condition for all spectral components of the optical pulse participating in a nonlinear process. The phase matching condition is fulfilled by different methods: by birefringence, dispersion in the pump frequency range, wave front tilting, artificial periodic structure (APS) made of nonlinear media. i.e. quasi-phase matching, in this case the group velocity of the pump wave is equal to phase velocity of THz wave. Another approach is to incorporate the nonlinear material in a waveguide to use the dispersion of the waveguide for adjusting the phase velocity of the THz wave with the group velocity of an optical pulse. The possibility of increasing light conversion efficiency into GHz-THz range by nonlinear crystal partially filling the metallic rectangular waveguide was suggested, theoretically grounded and experimentally realized in [1, 2]. This approach broadens the choice of material for THz generation. Another advantage of this method is that by choosing the crystal thickness and its disposition regarding the narrow wall of the waveguide it is possible not only to control mode type, but also to make the absorption loss of the waveguide with crystal much less than the intrinsic loss of the crystal.

The results of the effective generation pulse of terahertz radiation in band 0.1-3.5 THz via optical rectification of femtosecond laser pulses in nonlinear LiNbO₃, ZnTe, crystals and their application in medicine are presented.

2. THz pulse generation in nonlinear crystals LiNbO₃ and ZnTe

Nonlinear optical technique of THz radiation generation are based on interaction of short powerful laser pulses and matter resulting in polarization pulse formation, their relaxation during 10^{-13} - 10^{-12} s forms a wave of electromagnetic radiation. Requirements to nonlinear optical medium are low absorption on laser

and THz frequencies (low values α_{opt} and α_{THz}), high nonlinearity, conditions of phase-matching ($n_{\text{opt}} = n_{\text{THz}}$), high radiation resistance. In the propagation of femtosecond optical pulse in the medium with the second order of nonlinear susceptibility a conversion of energy in radiation sum and difference frequency owing to coherent mixing spectral components of optical pulse occurs. Using the second-order optical nonlinearity the conversion of femtosecond laser pulse in broadband difference frequency radiation (DFR) of far-to mid-IR range is also referred to as optical rectification of light pulse in nonlinear medium [3].

The coherent nature of nonlinear interaction allows to generate and detect the THz radiation with a great ratio signal/noise of the order of 10^4 , without using low-temperature cooling of the detector which is inaccessible for other methods of THz radiation. The coherent THz detector has superlow sensing threshold $\sim 10^{-16}$ W/Hz. Moreover, by measuring phase and polarization relationship between interacting waves the intensity of nonlinear process can be controlled.

Optical excitation of THz radiation in crystal was performed by 50 fs pulses of a Ti:sapphire laser ($\lambda=800\text{nm}$), with repetition frequency of 82 MHz [2]. The average power on the crystal was between 1.2 W or 750 mW. By placing the same nonlinear crystal in the free space and then inside a hollow metal waveguide the phase-matching and consequently efficiency, time and spectral features of the emitted THz field are changed. Using the dispersion of the waveguide the phase matching was provided both by changing the degree of partial filling the waveguide by the crystal and position of the crystal regarding narrow wall of the waveguide. The nonlinear crystal acts as a nonlinear frequency converter, and waveguide-crystal structure fulfils a function of a setup increasing the THz phase velocity up to group velocity of laser pulse. This method provides phase-matching on certain frequencies simultaneously for difference frequency radiation in THz range. Figures 2 and 3 represent time dependence of THz field (a) and its spectrum (b) after fast Fourier transform when the crystals ZnTe and LiNbO₃ is placed in the free space, respectively. Two pulses in the waveform of Fig.3a result in appearing oscillations in the spectrum (3b). Two single-cyclic pulses irradiated from the front and end faces of LiNbO₃ crystal having thickness 1.08 mm.

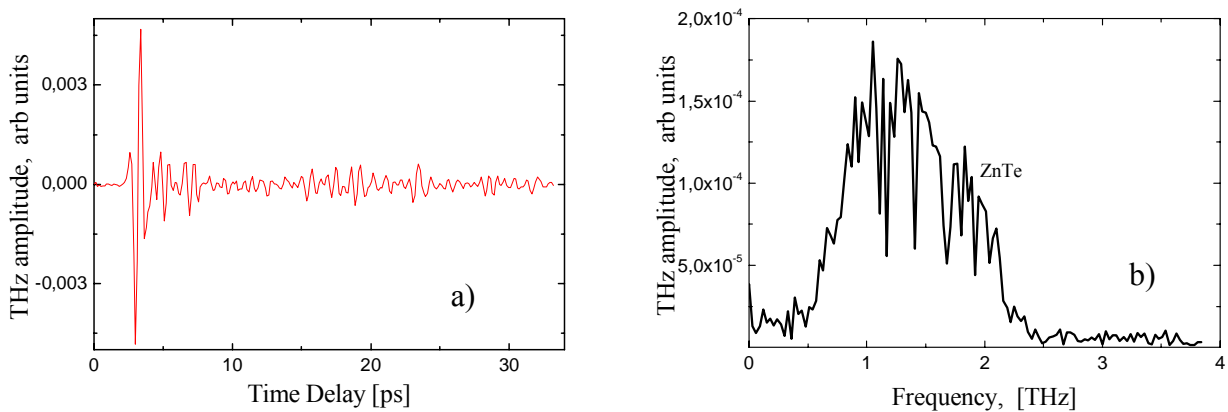


Fig. 2. Time dependence of THz field (a) and its spectrum (b) after fast Fourier transform when the crystal ZnTe is placed in the free space.

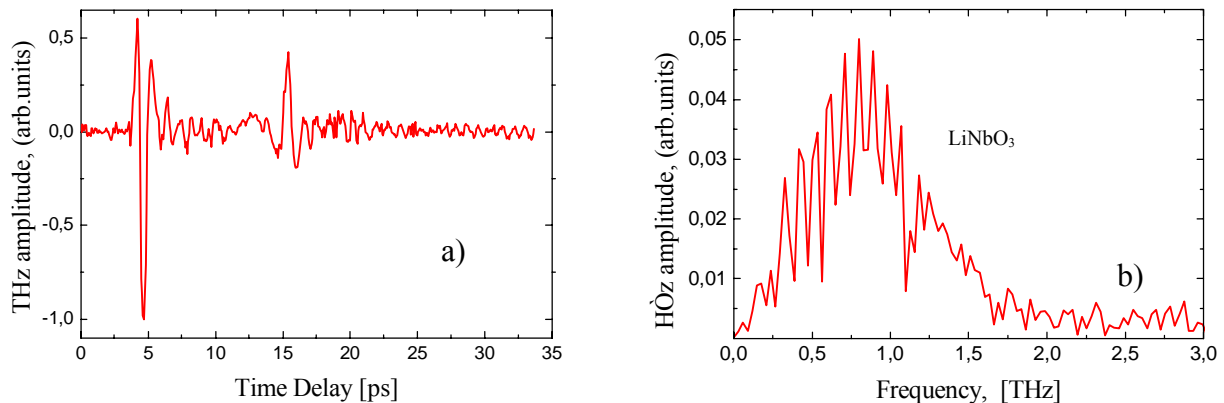


Fig. 3. Time dependence of THz field (a) and its spectrum (b) after fast Fourier transform when the crystal LiNbO₃ is placed in the free space.

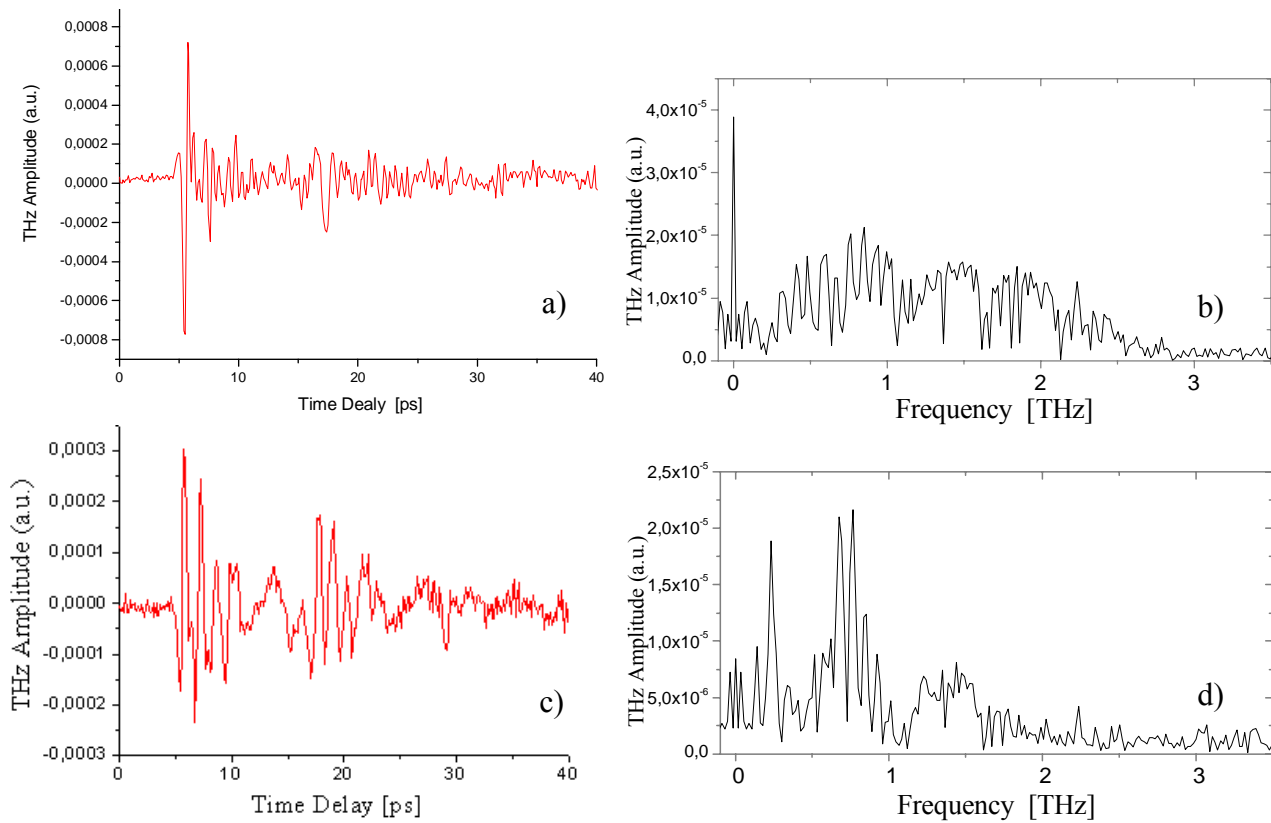


Fig. 4 Time dependence (a) and the THz spectrum (b) of radiation of crystal LiNbO₃ in the waveguide with cross-section 5.2x2.6 mm², when the crystal is located centrally–symmetrically in the waveguide, then it is shifted to the narrow wall (c, d) of the waveguide.

Figure 4 represents time dependence (a, c) and the THz spectrum (b, d) of radiation from crystal LiNbO₃ in the waveguide with cross-section 5.2x2.6 mm², when the crystal is located centrally–symmetrically (a, b) in the waveguide, then it is shifted to the narrow wall (c, d). Changing the position of the crystal in the waveguide the temporal waveform and spectrum of THz radiation can be controlled, thus THz pulse waveform shaping is realized. The results of THz field generation in waveguides with cross-sections 2.4x1.2 mm² and 1.8x0.9 mm² are given in [2, 4].

3. Applications of terahertz spectral imaging diagnostics in medicine

An imaging modality built upon interactions of coherent THz waves with matter has shown its applicability to various kinds of tasks in security and medicine [5-8]. Due to its non-invasion (THz quanta are far less energetic than those of X-rays and pose no ionization hazard for biological tissue) the THz waves unlike the X-ray allow to make without any harm for the human diagnostics including osteoporosis, tumour, skin cancer, tooth cavities, starting dotted caries in human teeth, bone diseases, depth and degrees of skin burns. The main advantage of THz diagnostics is that it features spectral imaging within a broad band of frequencies, from the gigahertz band up to tens of THz. This allows selecting and imaging a spectral property, e.g. the chemical composition of the sample, and providing information on surface composition and molecular structure. Vibration and rotation frequencies of many biological molecules are at THz range [9] which may provide characteristic fingerprints to differentiate biological tissues in a region of the spectrum not previously explored for medical use. While this is also true of microwaves, the shorter the wavelengths of the THz band, the greater spatial resolution. The comparatively long THz wavelengths can penetrate in biological tissue, much further than visible light or the near infrared - the longer THz wavelengths being less susceptible to effects such as Rayleigh scattering [10]. The unique properties of THz radiation allow to “see” it farther and in more detail than imaging methods such as X-rays, ultrasound and radar.

Terahertz pulse imaging is based on the ‘pump – probe’ technique (Figure 5). The laser pulse is split into two beams - a pump beam for generating THz pulses, and a probe beam for detecting coherently the

amplitude and phase of the THz electric field. The typical THz pulse, generated by optical rectification, is shown in Figs. 1, 2. The average power of the THz radiation was \sim mW. THz imaging is based on measuring the image scan of a propagating THz wave through a medium of thickness d . The research has been conducted on teeth tissue in-vitro aiming to establish the characteristic of THz and optical properties of teeth tissue, enamel and dentine as well as to trace early detection of teeth erosion abnormalities. The THz beam is collimated and focused on the tooth into the spot \sim 0.5 mm in diameter with the set of parabolic off-axis mirrors. The collected THz radiation is used in the probe arm of the imaging system configured as a free space electro-optic sampler. Using interferometric control over the optical delay between the pump (50 fs) and probe pulses, the time domain dependence of THz electric field is recorded at a number of discrete points [8, 9]. A spatial image is mapped pixel by pixel using X–Y translation of the sample or beam in the focal plane. Two image parameters were investigated: the minimum of the terahertz impulse function (E_{\min}) and the ratio of E_{\min} to the maximum of the terahertz impulse function (E_{\min}/E_{\max}). Normal tissue has an impulse function with a large positive amplitude, defined as E_{\max} , while a tumor has an impulse function with a large negative amplitude, defined as E_{\min} . There are substantial differences in the optical properties (refractive index and absorption coefficient) between normal and diseased tissues. Experimentally the 3D stack of data is obtained as a time or frequency-resolved image by means of X-Y mapping of the time dependence of transmission images. Two spectra, THz field and phase, are processed via the fast Fourier transform from originally obtained time-domain dependence. The data obtained in the experiment were normalized to those obtained from an unoccupied space of the sample holder. This removes a great deal of residual noise to improve the quality of both amplitude and phase measurements. Spectral images were collected within the range of the spectrum between a few GHz and 3.5 THz with spectral resolution approximately within 20–50 GHz. The spectral range of THz frequencies depends on the choice of the THz source and can span several tens of terahertz (\sim 100 THz if the duration of laser pulse is \sim 8 fs). The probe beam gates the detector and thereby determines the amplitude of the THz electric field at a fixed time point. The detection is based on an electrooptic effect, where the presence of a THz frequency electric field induces a birefringence in optically transparent nonlinear crystal. The magnitude of this effect, and thus the state of the THz field, can be ascertained by analyzing the change of the polarization states of fast optical pulses transmitted through the material. It is important to emphasize that THz pulsed imaging offers an advantage over many existing imaging techniques because it offers spatial localization, combined with spectroscopic capabilities, in the unprecedentedly wide band of frequencies, from DC up to several THz.

Figure 6 shows the results on THz imaging of abnormalities due to caries erosion of tooth tissue in vitro for several frequencies. The image contrast for different types of tooth tissue becomes significant above approximately 1 THz. One can notice from the series of frames 1, 2 of Fig.6 how the degree of spatial resolution is increased with THz frequency. Spectral THz images clearly resolve enamel and dentine areas, the crown and the surface cement layer. The last one, however, is enveloped with diffraction along the edges. The second advantage of spectral imaging is in classification of conformities found between the tooth abnormalities and relevant spectroscopic features. This will be used for mapping the locations of abnormalities in a sample. The mechanisms giving rise to contrast are mostly associated with the change of complex refractive index (the absorption coefficient and refractive index) with frequency. The region of abnormality is seen as the dark area in the diagram 2, Fig.6. A striking result is observed within a certain band of frequencies. A strong spatially resolved absorption band is found in the area affected by caries (compare THz images 1 and 2 with the digital photo 3 in Fig.6. The caries spot in THz imaging becomes detectable only within this band of frequencies. It is interesting that X-ray high resolution image hardly shows traceable abnormality in this area (image 4, Fig.6). The area of increased contrast surrounding the dark central spot, attributed to caries erosion on THz image 2, Fig.6, resembles a ring form. Note that these structures in the THz image are only seen in the frequency resolved (spectral) image. The following systematics can be deduced from the experimental data: the band at low frequencies (up to 0.5 THz) appears as a common signature of the tooth tissue over the whole sample, where no effect of any abnormality is found. Note that in the same tooth sample the X-ray shows no detectable sign of tooth decay.

These results give a clear proof of a high diagnostic value of THz spectral imaging technique. THz radiation has been shown to be capable of the early detection of dental carries. It is shown that THz-rays can image tooth cavities, starting dotted caries in human teeth abnormalities. Preclinical stage of caries hard teeth tissue lesion development is not visualized on the X-ray diagram. THz image clearly shows starting dotted caries. Spectral imaging delivers selective information on the abnormalities rather than integrated data obtained with time domain imaging.

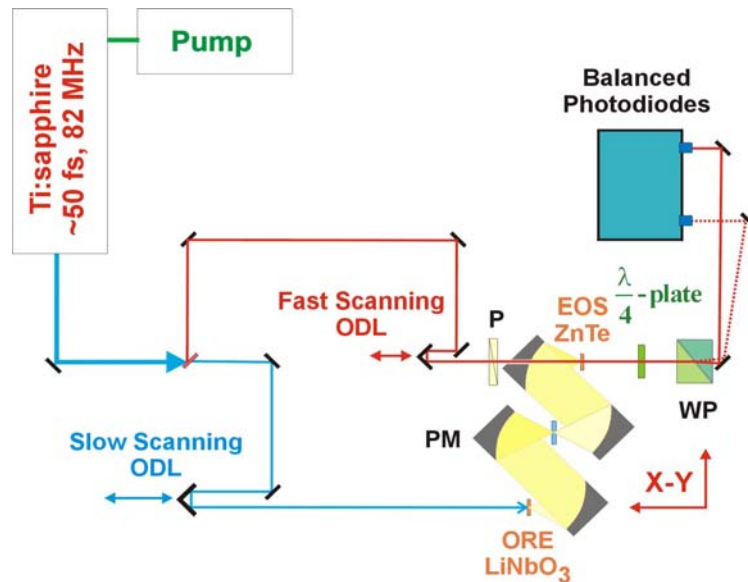


Figure 5. Schematic diagram demonstrates the principle of THz imaging.

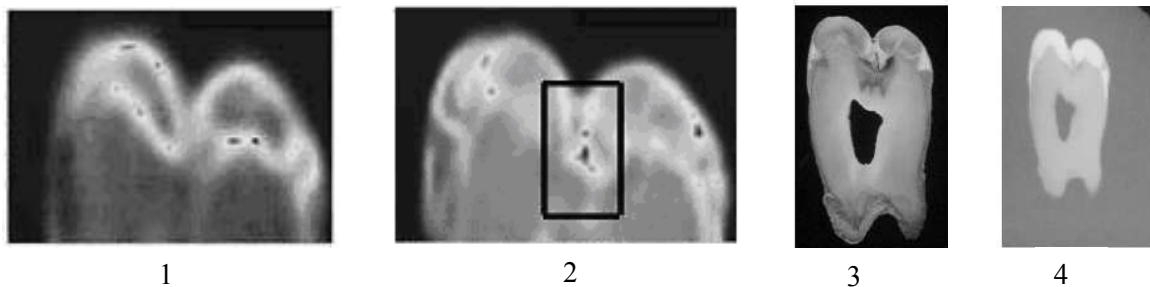


Figure 6. THz images of a tooth with detected abnormality: the diagrams 1 and 2 show THz images at two frequencies, 0.64 THz and 1.065 THz respectively: here the image size is 80×115 , the pixel size is $100 \mu\text{m}$; 3 is the photograph of the section and 4 is the high resolution X-ray diagram. The rectangular frame in the diagram 2 surrounds the spot of abnormality - caries.

4. Conclusions

THz generation via the mechanism of DFG has shown a marked gain of efficiency in a partially loaded waveguide. The rise of conversion efficiency in the order of magnitude has been obtained in waveguide structures partially filled with LiNbO_3 crystal. Such a strong effect on generated THz power will improve the performance of coherent THz spectral imaging and tomography systems in terms of penetration depth, signal-to-noise ratio and dynamic range. By placing the same nonlinear crystal in the free space and then inside the waveguide the phase-matching and consequently time and spectral features of the emitted THz field are changed. The spectrum of the generated THz beam can also be modified by the change of transverse position of non-linear crystal in the waveguide.

THz radiation has been shown to have good tissue differentiating abilities. It has chemical specificity. It is shown that THz-rays can image tooth cavities, starting dotted caries in human teeth, by helping visualization of demineralized areas.

References

- [1] A.S. Nikoghosyan, *Kvant. Electron. (Moscow)*, [*Sov. J. Quantum Electron*], **15**, (1988), pp. 569-571.
- [2] A.S. Nikoghosyan, R.M. Martirosyan, A.A. Hakhoumian, J.M. Chamberlian, R.A. Dadley, N.N. Zinovev. *Generation of THz Radiation in Waveguides Partially Loaded with Nonlinear Crystal. Electromagnetic Waves and Electronic Systems*, **11**, (2006), pp. 47-55.
- [3] M.Bass, P.A. Franken, J.F. Ward, G.Weinreich. *Optical Rectification. Phys.Rev.Lett*, (1962), 446.
- [4] A.S. Nikoghosyan. *Laser Driven Terahertz Dielectric Wedge Antenna Placed in Free Space or in*

Hollow Metallic Waveguide. 35th Inter. Conf. on Infrared, Millimeter and Terahertz Waves, September 5-10, 2010, Rome, Italy, (2010), Tu.54.

- [5] M.C. Nuss. Chemistry is right for T-ray imaging. *IEEE Circuits and Devices Magazine* **12**, (1996), pp.25–30.
- [6] D.M. Mittleman, R.H. Jacobson, and M.C. Nuss. T-Ray imaging. *IEEE Journal on Selected Topics in Quantum Electronics*, **2**, (1996), pp. 679-692.
- [7] S. Micken, D. Abbott, J. Munch, X.C. Zhang, T.van Doorn. Analysis of system trade-offs for terahertz imaging, *Microelectronics Journal*, **31**, (2000), pp. 503-514.
- [8] A.J. Fitzgerald, E.Berry, N.N. Zinovev, G.C. Walker, M.A Smith, J.M. Chamberlain. An introduction to medical imaging with coherent terahertz frequency radiation. *Phys. Med. Biol.***47**, (2002), R67–R84.
- [9] S.W. Smye, J.M. Chamberlain, A.J. Fitzgerald, E. Berry. The interaction between terahertz radiation and biological tissue *Phys. Med. Biol.*, **46**, (2001), R101–R112.
- [10] P.Y. Han, G.C. Cho, X-C. Zhang. Time-domain transillumination of biological tissues with terahertz pulses. *Opt. Lett.*, **25**, (2000), 242–4,

Effect of Coherent Low Power Microwave Exposure on Tumor Cells DNA in Vivo

V.P.Kalantaryan¹, R.M.Martirosyan¹, L.E.Nersisyan², H.M.Stepanyan², J.V.Gharibyan²

¹ Yerevan State University, Department of Microwave Radiophysics and Telecommunication, A.Manoozian str.1, 0025, Yerevan, Armenia

² Fine Organic Chemistry Institute Armenian National Academy of Sciences, Azatutyan av.26, 0023, Yerevan, Armenia

The influence of low-intensity millimeter range electromagnetic radiation on tumors triggered great interest among researchers mostly due to the absence of harmful side-effects opposed to the widely used X-ray therapy. Unlike ionizing X-rays, the method proposed here is non-ionizing and hence is completely of any harmful side effects. In [1-3] the influence of millimeter electromagnetic waves (MMWs) on various tumors has been investigated. The present study was undertaken to investigate whether low-intensity (non-thermal) MMWs at 42.2GHz can act on tumor of mice in vivo without cytostatic agents.

1. Introduction

In case of malignant transformation the cells undergo changes, which lead to uncontrolled cellular proliferation and abnormal differentiation. The investigation of the possible structural changes in DNA of tumor cells under the influence of millimeter-radio waves in the absence of cytostatics is actual since the MM-therapy used in complex antineoplastic treatment promotes relaxation of the toxic antitumor effect of chemo- and radiotherapy and enhances the antitumor effect.

In the above mentioned literature data the tumor inhibition by means of MM-therapy, in the absence of cytostatic agents, it was shown mostly in experiments *in vitro* [4,5].

The process of DNA-methylation is closely related with the appearance of tumors. Imbalance of DNA-methylation is observed in all, without exception, studied neoplasias. The violation of methylation process manifests itself at the early stages of malignant transformation of cells, and content of 5-methylcytosine (5MC), which is the only methyl bases in DNA of animals and humans, could serve as a diagnostic test for tumor genesis, and this opens the possibility for early diagnostics and treatment of disease [6, 7].

Hypermethylation of tumor-DNA, the mechanism of which in many tumors is not clear, destabilizes the secondary structure of DNA as well, what may cause the selective sensitivity of malignant cells toward the influence of millimeter-waves in the absence of chemo- and radiotherapy and to allow receiving of expressed antitumor effect.

2. Materials and methods

To clarify the characteristics of the influence of MM-therapy with different modes of irradiation onto DNA of tumor-bearing animals in the absence of cytostatic drugs, a study of effects of millimeter-waves on 40 outbreed stock white mice, weighing 20-22 g, which is transplanted sarcoma-37 by a known method. Previously, before the transplantation, animals were divided into 4 groups of 10 mice in each group. The course of influence of millimeter-waves started 3 days before transplantation. In the first group (control) the tumor has no impact. In the second group an exposure of influence during one seance was 15 min. In the third group it was 30 min. The course of exposure was 15 days. On the fourth day animals was woven by sarcoma-37 and daily exposure was continued according to the above mentioned scheme. As a source of millimeter-wave-radiation there was used the generator of coherent EHF-oscillations G4-141, operating in range of frequencies of 38,5÷53,5 GHz. Irradiation of animals was carried out in the far field of a cone-shaped antenna at a distance of 40 cm from the radiating plane in the mode of continuous generation with incident power density at the location of the object about $10 \mu\text{W}/\text{cm}^2$. The output power of the generator was measured with the help of a M5-49 thermistor head and a M3-10A wattmeter (Istok, Fryazino, Russia). The frequency of output signal was controlled by a CH2-25 wavemeter (Istok, Fryazino, Russia). To calculate the SAR, we used dielectric parameters of the skin $\epsilon' = 14$, $\epsilon'' = 18$ and skin density $\rho = 1.15 \text{ g}/\text{cm}^3$ [8].

The specific absorption rate on the surface of skin of the animals back was calculated by the formula [9]

$$SAR = \frac{\sigma \xi (1 - R) P_0}{n \rho},$$

where $\sigma = \varepsilon_0 \varepsilon'' \omega = 50.4$ S/m is the electric conductivity of skin at the frequency of 50,3GHz, $\varepsilon_0 = 8.85 \cdot 10^{-12}$ F/m is the vacuum dielectric constant, ω is the circular frequency, $\xi = 377 \Omega$ is the vacuum wave impedance, P_0 is the incident power density, $R=0.5$ is the reflection coefficient, $n = 4.2$ is the refractive index of the skin. The calculated value for the rate of the specific absorption is approximately equal to 2 W/kg. Animals of the fourth group were sham-exposed by placing into the exposure zone when the generator was turned on but the output power was attenuated to zero. Duration of the exposure and sham-exposure was 30 minutes.

3. Results and discussion

As can be seen from the table, the pronounced effect of MM-therapy appears in the group with a half-hour continuous irradiation, there is observed a sharp suppression of the level of DNA-methylation of sarcoma-37, what can be explained as follows: MM-waves of low intensity, acting on the growth and proliferation of cells, the enzyme activity, the genetic apparatus of cells, not accelerating tumor growth, exert an inhibitory influence on the development of the transplanted sarcoma and increase the lifetime of experimental animals [10].

A similar effect was revealed in our experiments. It is established that the duration of the procedure the 30 min-MM exposure caused inhibition of tumor growth by 33,5%, and 15-minute-exposure did not exert an inhibitory effect on the tumor. Correlation of tumor growth delay with the level of DNA-methylation is obvious. After 15 seances of MM-therapy without cytostatic drugs, in animals of the third group (exposure 30 min) was observed an inhibition of by 33,5% compared with a first one and a sharp suppression of DNA-methylation level 2.5 times as much. DNA-demethylation in the tumor tissue under the influence of a half-hour exposure of MM-waves can be explained by enzymatic demethylation of remains of 5-MC, i.e. the mechanism of action of the studied waves basically involves demethylation of tumor DNA, which in its turn could sensitize the damage of chromatin, inhibit an efficient repair of DNA, providing genomic instability, which can lead to apoptosis of tumor cells, leading to inhibition of tumor growth [11,12].

In case of MM-therapy with 15 min-duration of action there was not observed an inhibition of DNA-methylation level of the tumor and was not marked delay in tumor growth. Thus, these studies revealed a correlation between antitumor activity of MM-therapy with inhibition of methylation of tumor DNA *in vivo*, because the therapeutic effect of coherent MM-waves was estimated by inhibition of tumor growth and changes in the level of methylation. General toxic influence of MM-waves on the experimental animals with sarcoma-37 without cytostatics was insignificant and has an inhibitory effect on the development of the transplanted sarcoma. Consequently, the obtained in this experiment results, on our opinion, can be seen from the point of view of possibilities MM-therapy in relation to the mechanisms of anticancer drug resistance and may be an important criterion for assessing the molecular influence. The antitumor effect of MM-waves, obtained without cytostatics, shows promising development of MM-therapy for clinical oncology in the treatment of malignant neoplasms.

Table 1. The nucleotide composition of tumor DNA in the control and under the influence of MM-wave

Experimental conditions Source of DNA	Content of bases in DNA, mol. %					
	G	C	5-MC±ξ	A	T	G+C+5-MC
Animals with tumors Tumor (C-37) without treatment	21,9	17,8	4,7±0,0 1	28,0	28,0	44,4
C-37+MM-impact exposure for 15 min	21,8	17,4	5,7±0,0 1	28,0	28,0	44,9
C-45+MM-impact exposure for 30 min	21,9	18,1	2,2±0,0 1	28,9	28,9	42,2

Note: In each group – 10 animals. Number of definitions – 9. These changes were reliable ($p < 0.05$) compared with control (untreated tumor).

References

1. M.Logani,I.Szabo,V.Makar,A.Bhanushali,S.Alekseev,M.Ziskin *Bioelectromagnetics* **27** (2006) 258.
2. V.Kalantaryan,Yu.Babayan,J.Garibyan. Abstracts book, PUB-306, World Cancer Congress (2008) Geneva,Switzerland.
3. V.Kalantaryan,Yu.Babayan, A.Tadevosyan. Abstracts book, POS-A288,World Cancer Congress (2008) Geneva,Switzerland.
4. Chidishimo G., Beneduci A., Nicoleta M. et al., *Anticancer Research* **22** (2002) 1681.
5. Кузьменко А.П., Соловьев И.Е., Бундюк Л.С. и др., *Эксперимент. Онкология* **14** (1992) 72.
6. Burnham C.M. *Drug Discover Today* **2, N8** (2003) 54.
7. Partha M.Das, Rakesh Singal. *J.Clinical Oncology* **22** (2004) 4632.
8. Gapeyev, A.B., Sokolov, P.A.,Chemeris, N.K. *Biophysics* **47** (2002) 759.
9. Gapeyev, A.B., Mikhailik, E.N., Chemeris, N.K. *Bioelectromagnetics* **29** (2008) 197.
10. Теппоне М.В., Авакян Р.С. Миллиметровые волны в биологии и медицине **1(29)** (2003) 3.
11. Jean-Mare Barret, Bernard Salles, Cristian Provot. *Carcinogenesis* **18, N12** (1997) 2441.
12. Bhattacharya S.K., Ramchandani S. Cervoni N.et al. *Nature* **397** (1999) 579.

Effect of Non-Thermal Microwave Radiation on Circulatory System

V. Kalantaryan¹, A.Hakhoumyan¹, T. Adamyan², E. Gevorkyan², H.Hovhanisyan², S.Minasyan²

¹*Yerevan State University, Department of Microwave Radiophysics and Telecommunication, A.Manoogian str.1, 0025, Yerevan, Armenia*

²*Yerevan State University, Department of Human and Animal Physiology, A.Manoogian str.1, 0025, Yerevan, Armenia*

The present studies were undertaken to investigate 1) regeneration processes in the circulatory system under condition of bone-marrow deficiency and 2) blood catalase activity change of rabbits under a long-term exposure effect of low-power extremely high frequency electromagnetic radiation (EHF EMR). The data obtained demonstrate that living organisms react to a low-intensity monochromatic radiation mobilizing their internal resources.

In the 2) case the obtained data demonstrate that the increase of catalase activity in peripheral blood was observed, maximum of which was registered in 20-fold and on the 10-th day after 25-fold influences. The observed in experiments activation of the peroxisomatic catalase enzyme, probably, promotes the enhancement of the power antioxidant system of the organism.

1. Introduction

Revealing the effects which electromagnetic radiation at millimeter wavelengths have on the organism and its biological significance serve as a basis for using microwave exposure as a physiotherapeutic procedure for treating various diseases. Their list includes cancer of different organs, cardiovascular diseases, diabetic angioneuropathies, peptic ulcers, leucopenia, pain relief, skin disorders, infantile cerebral palsy, bronchial asthma, wound healing, etc [1-5]. According to literature facts, the millimeter-wave therapy increases the level of immune resistance, influences different stages of pathogenesis, changes enzymatic reaction activity and growth rate, destroys microorganisms [6-9]. It has shown that millimeter waves have strong effect on the process and bioelectric activity of neurochemical functions of the brain, increase the cortical tension [10-11]. Penetrating into the organism (the penetration depth of Millimeter Waves in tissues is about 0,3-0,5mm due to high absorption by water molecules), this radiation is transformed into information-carrying signals performing guidance and adaptation control or rehabilitation processes in the organism. Different physical factors, affect the organism, in the same way as electromagnetic waves, provoking changes in the functioning of different organs/systems. Erythron plays an essential role in development of such processes, as it actively contributes to the maintenance of functional state of the organism.

2. Materials and Methods

The experiments were carried out on rabbits of the same weight, age and sex. Marrow was taken out from femur, shin and ischium (6 ml/weight) with the help of Kasyrsky's needle. The animals underwent 30-day exposure with G4-141 coherent electromagnetic waves generator (Russian made) with frequency of 50.3 GHz, in correspondence with resonance frequency of vibrations of hexagonal structures of water. The frequency stability of the generator in continuous wave mode was 20MHz. A whole-body exposure of rabbits to Extremely High Frequency Electromagnetic Radiation (EHF EMR) was conducted in the far-field zone of conical antenna at a distance of 500 mm from the radiating end of the antenna. Incident power density (IPD) value in the plane of exposed object was of 0,05 mw/sm². In the studying of a blood catalase activity the head of the animals was irradiated. The irradiation was realized in continuous mode generation, with non-thermal powers from 150 mm distance. The IPD value was same as in the previous case. The output power of the generator was measured with the help of a M5-49 thermistor head and a M3-10A wattmeter (Istok, Fryazino, Russia). The frequency of output signal was controlled by a CH2-25 wavemeter (Istok, Fryazino, Russia). To calculate the SAR, we used dielectric parameters of the skin $\epsilon' = 14$, $\epsilon'' = 18$ and skin density $\rho = 1.15 \text{ g/cm}^3$ [4]. Specific absorption rate on the surface of skin of animals back was calculated by the formula [11]

$$SAR = \frac{\sigma \xi (1 - R) P_0}{n \rho},$$

where $\sigma = \varepsilon_0 \varepsilon'' \omega = 50.4 \text{ S/m}$ is the electric conductivity of skin at the frequency of 50,3GHz, $\varepsilon_0 = 8.85 \cdot 10^{-12} \text{ F/m}$ is the vacuum dielectric constant, ω is the circular frequency, $\xi = 377 \Omega$ is the vacuum wave impedance, P_0 is the incident power density, $R=0.5$ is the reflection coefficient, $n = 4.2$ is the refractive index of the skin. Calculated value for the SAR is received about 2 W/kg. Animals of the control group were sham-exposed by placing the rabbits into the exposure zone when the generator was turned on but the output power was attenuated to zero. Duration of the exposure and sham-exposure was 60 minutes.

Normally, 24 hours after the bone marrow extraction and on the 5th, 10th, 15th, 20th, 25th, 30th days and 2 weeks after the exposure the following features of erythropoiesis were analyzed: the quantity and colorimetric characteristics of erythrocytes, reticulocytes, hemoglobin, maturation rate of reticulocytes, the cellular content of the bone marrow. In order to assess the functional alternations of erythroid branch, the bone marrow index of erythronormoblasts protoplasm maturation has been revealed.

The catalase activity was determined by manganese metric method, based on decomposition of hydrogen peroxide. Were calculated the Catalase Number: Cn, represented as quantity (in millimeter) of decomposition hydrogen peroxide - H₂O₂ in 30 minutes, the absolute number of erythrocytes in blood periphery, Catalase Index: Ci – the ratio of Cn to the numbers of erythrocytes in 1 mm³ of blood (in millions). The animals were exposed under a single, 5-, 10-, 20-, and 30-fold radiation. In case of a single radiation the studies were carried out before the radiation effect and on the 5-th, 30-th, 90-th minutes after it. In multiple radiation the studies of the mentioned characteristic values were carried out before the radiation effect and after it on the 5-th minute. The obtained experimental data were statistically processed; the reliability of the changes was determined according to Students t-method. The results were statistically processed by Student's method.

3. Results and Discussion

Hypochrome changes of erythrocyte and hemoglobin amounts were observed without irradiation during 24 hours after the bone marrow withdrawal. As compared to the starting point, the amount of erythrocytes had fallen by 13.5%, hemoglobin by 21.33% (Fig.1). Thus the color index changed to value 0.68. The latter was accompanied by increase in relative and absolute quantities of reticulocytes, as well as their maturation rate, respectively becoming 117.03% ($p < 0,001$), 135.29% ($p < 0,02$), and 133.33% (Fig.2). On the 5th day of bone marrow extraction and irradiation, normochrome decrease of erythrocytes and hemoglobin content, respectively to values 84.83% ($p < 0,01$) and 82.85% ($p < 0,01$) was observed. Reticulocytosis and high level of their maturation rate were the same in the mentioned period. In the phase of marrow extraction, the amount of myelocaryocytes and erythroid branch cells was low. The myelocaryocytes level is 95300 ± 3115 and erythroid branch cells 38.0 ± 1.2 in normally. On the 5th day of irradiation they were respectively 68000 ± 2045 ($p < 0,001$) and $27,0 \pm 0,678$ ($p < 0,001$). However, the marrow index of erythronormoblasts protoplasm maturation remained unchanged (0.6).

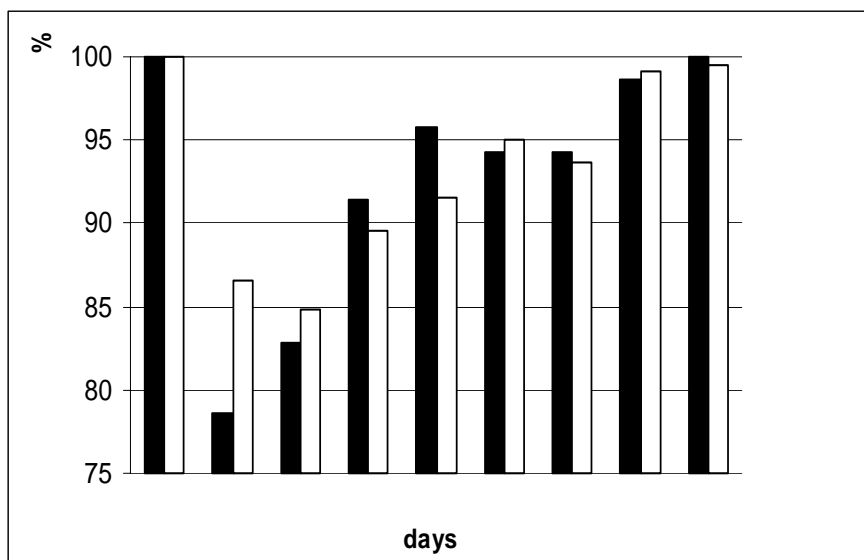


Fig. 1. The change by percent amount of erythrocytes in 1 ml blood (black) and amount of hemoglobin (gram/%) (white) under influence of electromagnetic radiation (EMR).

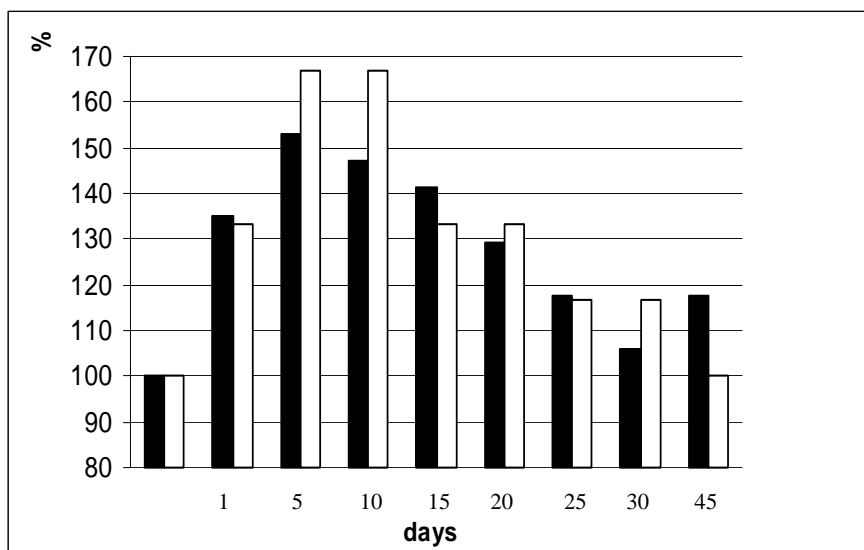


Fig. 2. The change by percent relative amount of reticulocytes ($\frac{0}{00}$) (black) and the rapidity of reticulocytes ripening in an hour (white) under influence of electromagnetic radiation (EMR).

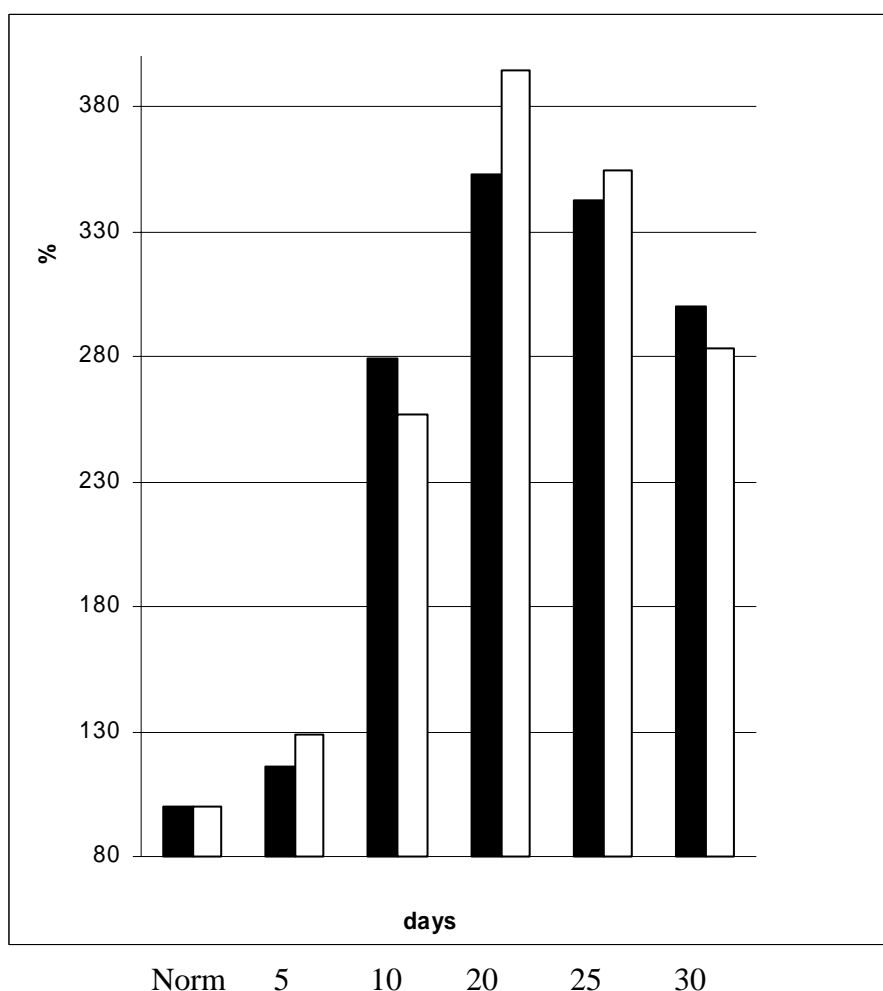


Fig. 3. The change by percent catalase number Cn (black) and catalase index Ci (white) in the blood under influence of electromagnetic radiation (EMR).

On the 10th day of the experiment, moderate increase of erythrocytes and hemoglobin amount has been observed (5% and 9% correspondingly). On mentioned time the increase of cells, not containing hemoglobin proerythroblasts and erythroblasts was seen in marrow, which confirms the acceleration of proliferative processes. On the 15th day of marrow extraction and irradiation, the growth of erythrocyte and hemoglobin

quantities continued, reaching 91.57 % ($p < 0.05$) and 95.71%. The quantity of reticulocytes and their maturation rate were high. On the 20th day of studies the erythrocyte and hemoglobin quantities were within the limits of physiological vibration 94.48%, 94.28%. As compared to the 15th day, the absolute and relative amounts of reticulocytes had decreased, but still were on the high level compared to the starting point. (141.17%, $p < 0,001$; 129.28%, $p < 0.001$ respectively).

The observed variations in the peripheral red-blood indices are likely to be related with intensification of marrow proliferative and maturatoin processes. This fact is confirmed by high activity of erythroid cells in the extracted marrow domain and the growth of hemoglobin-containing normoblasts quantity.

During 25 to 30 days after exposure the quantities of erythrocytes and hemoglobin have not undergone any essential changes compared to the 20th day . The absolute and relative amounts of reticulocytes on the 30th day varied within the limits of starting point. In 2 weeks after stopping the irradiation, all parameters of erythropoiesis have returned to the initial values. It should be noted that the marrow index of cytoplasm maturation of erythronormoblasts have not changed during the whole investigation period.

The carried out investigations for blood catalase activity have shown that on the 5-th minute after low intensity EMR influence Cn and Ci have an increase up to 16.93% and 31.42% correspondingly compared with the norm. The absolute number of erythrocytes in peripheral blood increased up to 11.46%. A gradual increase of the Cn level up to the norm was registered deduring the following 30, 60, and 90 minutes. Analogical changes were registered for the Ci characteristic values, but for the all mentioned periods of time it was on the relatively higher level: on the 30-th minute by 17.14%, on the 60-th minute by 17.14%, and on the 90-th minute by 14.28% higher.

In our experiments in case of a single radiation effect the catalase activity and the absolute number of erythrocytes were not changed synchronously. Thus, along with catalase activity increase (to 16.93%) on the 5-th minute of radiation effect, the decrease of the erythrocyte number was observed (by 11.46%). During the following minutes against the background of gradual fall of Cn and Ci a reliable decrease of erythrocyte number was observed, which made 10.5% on the 30-th minute, 13.3% and 13.5% on the 60-th and on the 90-th minutes correspondingly, comparing with the norm.

Table1. The change of catalase activity and the total number of erythrocytes in the blood of rabbits under the influence of multiple, non- thermal EMR of millimeter range.

The Studied Values	The Norm	The Days of Irradiation			10-th Day After 25-fold Irradiation	10-th Day After 30-fold Irradiation
		5th	10th	20th		
Erythrocytes number (in millions)	5.05±0.104	4.95±0.019	5.83±0.194*	4.88±0.245	5.28±0.019	5.75±0.021***
Cn	1.89±0.006	2.20±0.106*	5.29±0.161***	6.67±0.2***	6.54±0.049***	5.69±0.049***
Ci	0.35±0.004	0.45±0.015*	0.90±0.025***	1.38±0.106***	1.24±0.012***	0.99±0.009***

Note: * - $p < 0.05-0.02$; ** - $p < 0.01$; *** - $p < 0.001$

After 5- fold radiation effect the character and value of the changes of Cn, Ci and the total erythrocyte number were analogical to the changes compared to a single radiation effect (Table 1). After 10- and 20- fold radiation effect an increase of the catalyze activity was observed. Thus, in 10-fold radiation effect Cn level exceeded the norm by 2.79 ($p < 0.001$) and Ci – 2.57 ($p < 0.001$) times. In 20-fold radiation effect data of Cn exceeded the norm by 3.59 ($p < 0.001$) and Ci – 3.94 ($p < 0.001$) times. On the 10-th day after 25-fold radiation effect the activity of Cn and Ci exceeded the norm by 3.46 ($p < 0.001$) and 3.54 ($p < 0.001$) times and after 30 times radiation by 3.01 ($p < 0.001$) and 2.82 ($p < 0.001$) times correspondingly. The total number of erythrocytes on the 10-th day after 25-fold, 30-fold radiation effect increased in 4.55 and 8.08% correspondingly compared to the norm.

According to the data, in the interaction between centimeter radio waves the changes in a number of its enzymes, e.g. that of catalase and glucose -6-phosphodehydrogenase take place. Catalase enzyme is widely

spread in the organism of people and animals, and the most quantity of the ferment was found out in erythrocytes.

After 5-fold radiation effect, together with the decrease in the number of erythrocytes the increase of catalase activity was observed as well. Analogical character of changes was also observed in 20-fold radiation effect. But in this case and on the 10-th day after 25- and 30-fold radiation effect synchronous increase of the total number of erythrocytes in peripheral blood and catalase activity was also observed (Table 1).

4. Conclusion

Thus the results obtained show that, after removal of the marrow, repeated application of millimeter electromagnetic waves activates the erythropoiesis, enhances the long-lasting reticulocyte maturation process, increases the erythrocytes and hemoglobin content. Stability of erythrocytes and hemoglobin quantities during 20 to 30 days after extraction and irradiation of marrow, strong intensification of reticulocyte maturation process, as well as the acceleration of proliferative branch erythroids and maturation processes allow us to conclude that multiple exposure of living organism to coherent electromagnetic radiation in millimeter wavelength range mobilizes its preservation power. The latter tends to enhance the regenerative processes and broaden the capacities of compensational mechanisms, as a result of which the removal of marrow does not seriously affect erythropoiesis. Our obtained results agree on the literature [28], according to which in case of combined action of electromagnetic waves in millimeter range and anti-tumor preparations the impairment of hemopoietic system decreases significantly and stimulates the proliferative activity of stem cells of marrow, as compared with isolated effect of the mentioned drugs.

The data obtained prove that in single, 5-, 10-, 20-fold and on the 10-th day after 25-, 30-fold radiation effect of 60- minute-duration of EMI radiation on the rabbits' head the increase of catalase activity in peripheral blood was observed, maximum of which was registered in 20-fold and on the 10-th day after 25-fold influence. The character of changes of the catalase activity do not depend on the changes of total number of erythrocytes. The observed in our experiments activation of the peroxisomatic catalase enzyme, probably, promotes the enhancement of the power antioxidant system of the organism.

References

1. Betsky O.V., and N.N. Lebedeva. Millimeter Waves in Biology and Medicine **3** (2001) 5.
2. Pakhomov A.G. and M.R. Murphy. IEEE Trans Plasma Sci **28** (2000) 34.
3. Pletnev S.D. Critical Review of Biomedical Engineering **28** (2000) 573.
4. Gapeyev A.B., P.A., Sokolov, N.K. Chemeris. Biophysics **47** (2002) 759.
5. Lebedeva N.N., and T.I. Kotrovskaya. Millimeter Waves in Biology and Medicine **1** (2003) 20.
6. Zhukova G.V., L.H. Garkavi, L.P. Barsukova, L.Ya. Maryanovskaya, N.K. Pchenichnaya. Biomed Technologii i Radioelectron **6** (2005) 3.
7. Gapeyev A.B. and N.K. Chemeris. Biophysics **45** (2000) 299.
8. Tadevosyan A.H., V.P. Kalantaryan, A.H. Trchounyan. Cell Biochemistry and Biophysics **51** (2008) 97.
9. Tadevosyan A.H., V.P. Kalantaryan, A.H. Trchounyan. Biophysica **52** (2007) 893.
10. Minasyan S.M., G.Yu. Grigoryan, S.G. Saakyan, A.A. Akhymyan, V.P. Kalantaryan. Neuroscience and Behavioral Physiology (USA), **37 N2** (2007) 175.
11. Gapeyev A.B., E.N. Mikhailik, N.K. Chemeris. Bioelectromagnetics **29** (2008) 197.

Section 2: Microwave Systems

Survey, Modelling and Simulation of Air to Ground Communication Channel

Morteza Faraji¹, M.A Masnadi Shirazi², Mehdi Faraji³

¹ Shiraz Electronics Industries, P.O. BOX: 71365-1589, Shiraz, IRAN

² Shiraz University, IRAN

³ Islamic Azad University, DARAB Branch, IRAN

In this paper surveying, modelling and simulation of air to ground channel will be presented and statistical model will be studied. It will be tried to determine parameters such as average path loss, variation on average path loss, fading depth, small scale fading for scatters, maximum channel delay spread, channel delay profiles, maximum Doppler frequency and other effective parameters in multipath communication channel modelling. Although it has not been presented an overall model for air to ground communication link up to now and there is no complete prediction for its parameters, but it is necessary for designing new generation of airborne communication systems. In this regards, this paper after determining methods of airborne communication channel modelling, will present simulation results by taking account of these methods.

1. Introduction

Multipath is the main characteristic of each radio channel which causes fast variation on envelope of received signal by defused waves and slow changes in mean power of received signal by specular wave and shadowing (figure1). The reason for multipath is the transmitted signal is presented from paths with different length, time delay, attenuation and phase shift in receiver input. The signals with same phase are added to each others and out of phase signals attenuated each others. Fading is result of this combination. Multipath makes problems like attenuation in amplitude of transmitted signal, fast variation in phase of received signal and ISI (Inter symbol interference). Fading are categorized as small scale and large (or medium) scale fading. Small scale fading model is used for studding changes in shape, spectrum and frequency of signal and channel transferring capacity. In addition to small scale fading because of large obstacles, signal could be confronted with large scale fading or shadowing phenomenon. Large scale fading model is used to predict average power of received signal. Chart in figure (2) categorizes different types of fading and figure (3) shows a general model for received signal power.

In term of small scale fading, parameters like channel delay spread and Doppler spread are used for measuring of channel fading. Maximum deference in delay of paths is known as delay spread. Delay spread defines a limitation for maximum channel transferring capacity. Corresponding to delay spread there is channel coherence bandwidth which is used to determine maximum bandwidth of signal for transmitting in channel without ISI. Corresponding to Doppler spread there is coherence time, which is corresponding with inverse of Doppler spread. Coherence time is used to determine time domain which minimum value of fading is occurred.

In general, there are two main contributions to fading in air to ground communication links: due to ground multipath or due to reflection from ground objects like mountains or hills and due to atmospheric impairments (reflection, refraction, ducting etc). For frequency bellow 10 Giga hertz and elevation angles above few degrees, atmospheric contribution is negligible in compare with ground multipath [1]. So for prediction of large scale fading, we just consider ground multipath.

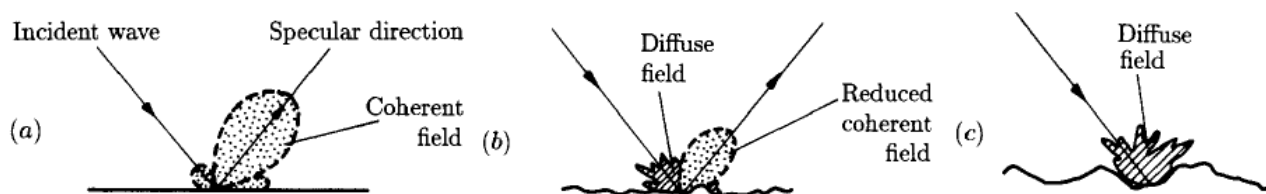


Fig1. Coherent and defuse field due to surface reflection

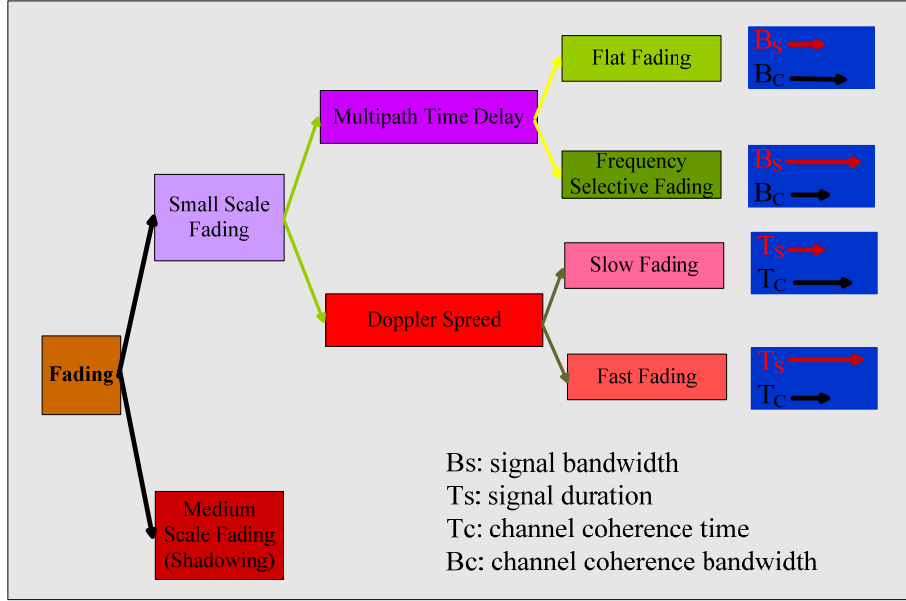


Fig2. Fading types

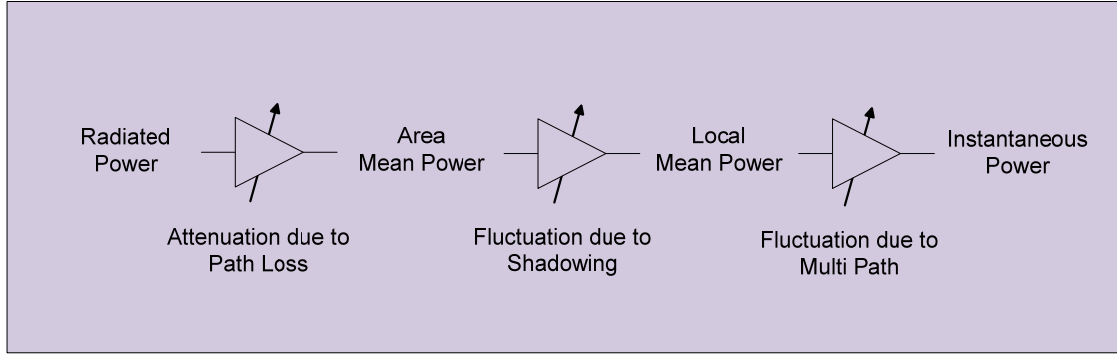


Fig3. General model for received signal power

2. General model for multipath in air to ground link

Before going further into details of the description of air to ground multipath propagation channel, we need to introduce a set of fundamental functions representing large and small scale fading, which will be used to describe mathematically these concepts.

Multipath propagation channel may be described with a time varying sum of attenuated a_k and delayed τ_k replicas of the transmitting signal, $h(\tau, t)$ may be written as [2]:

$$h(\tau, t) = \sum_{k=1}^{N(t)} a_k(t) \delta(\tau - \tau_k(t)) \quad (1)$$

where $\delta(\cdot)$ is the Dirac distribution. The multipath propagation channel could be divided between large scale and small scale fading terms. So it is interesting to make this distinction clear and rewrite Equation (1) [2]:

$$h(\tau, t) = \underbrace{\sum_{k=1}^{N_{LS}(t)} a_k^{LS}(t) \delta(\tau - \tau_k^{LS}(t))}_{h_{\text{Large Scale}}(\tau, t)} + \underbrace{\sum_{k=1}^{N_{SS}(t)} a_k^{SS}(t) \delta(\tau - \tau_k^{SS}(t))}_{h_{\text{Small Scale}}(\tau, t)} \quad (2)$$

In Equation (2), the time varying impulse responses governing large scale (LS) and small scale (SS) fading are introduced. For this distinction to have a physical meaning, the number of paths in the large scale part must be low (usually 1 or 2), while the number of paths in the small scale part must be high. The parameters of these impulse responses are usually determined using deterministic or stochastic methods.

The propagation channel characteristics may equivalently be defined in the frequency domain. The time varying transfer function of the channel $H(f,t)$ is simply the Fourier Transform in τ of $h(\tau,t)$, that is [2]:

$$H(f,t) = \underbrace{\sum_{k=1}^{N_{LS}(t)} a^{LS}_k(t) e^{-j2\pi\tau^{LS}_k(t)f}}_{h_{\text{Large Scale}}(f,t)} + \underbrace{\sum_{k=1}^{N_{SS}(t)} a^{SS}_k(t) e^{-j2\pi\tau^{SS}_k(t)f}}_{h_{\text{Small Scale}}(f,t)} \quad (3)$$

Equations (2) and (3) show that the multipath propagation channel acts as a linear time varying filter on the signal.

Small scale fading involves variation of the signal on very short distances (typically half of a wavelength). The reason for small scale fading is a large number of scattering waves with random phase, amplitude and delay are received, so according to central limit theorem the received signal can be considered as stochastic signal (Gaussian distribution). The equations (4) and (5) show the time varying impulse response of small scale fading [2], [3], [4]:

$$\tilde{h}_{SS}(\tau,t) = \sum_{k=1}^{N_{SS}(t)} \alpha^{SS}_k(t) e^{-j2\pi f_0 \tau^{SS}_k(t)} \delta(\tau - \tau^{SS}_k(t)) \quad (4)$$

$$\tilde{h}_{SS}(\tau,t) = \frac{C}{\sqrt{N}} \sum_{k=1}^N e^{j(\theta_k + 2\pi f_{Dk}t)} \delta(\tau - \tau_k) \quad (5)$$

where f_0 is the center frequency of transmitted signal and each path has an individual random null-phase θ_k , a delay τ_k , a Doppler frequency f_{Dk} and a constant amplitude $C/N^{1/2}$. The $C/N^{1/2}$ normalization term ensures that the average energy of the small scale fading process is C^2 . The random numbers f_{Dk} ($-f_{Dmax} < f_{Dk} < f_{Dmax}$) and τ_k ($0 < \tau_k < \tau_{max}$) have to be generated in accordance with the probability density functions describing the time variance and the delay spread of the channel which will be studied and modeled in this paper while θ_k ($0 < \theta_k < 2\pi$) only needs to be uniformly distributed.

The combination of large scale fading (equ. 3) and small scale fading (equ. 5) results time varying channel impulse response as:

$$\tilde{h}(\tau,t) = \underbrace{\alpha_D(t) e^{-j2\pi f_0 \tau_D(t)} \delta(\tau - \tau_D(t)) + \alpha_R(t) e^{-j2\pi f_0 \tau_R(t)} \delta(\tau - \tau_R(t))}_{\text{Deterministic Large Scale Fading}} + \underbrace{\frac{C}{\sqrt{N}} \sum_{k=1}^N e^{j(\theta_k + 2\pi f_{Dk}t)} \delta(\tau - \tau_k)}_{\text{Stochastic Small Scale Fading}} \quad (6)$$

According to equation (6), if a dominant signal component is present (LOS or strong Reflected wave), then a Rician distribution is observed for the fading envelope. The dominant component is defined to have a power larger than the diffuse components by a factor of K Rician distribution. But if $K=0$ (non LOS) Rayleigh distribution is observed for the fading envelope. Also in real situation impulse function is replaced by T duration pulse.

The following sections present prediction of large scale fading and modelling of small scale fading probability density functions for air to ground communication link.

3. Prediction of large scale fading

Let define fade depth (F) as sum of all extra propagation losses due to multipath and shadowing in compare with ideal free space propagation. An accurate estimation of fade depth is of great importance for the design of a highly reliable communication link. This estimation is necessary for link budget design analysis and simulation of outage probabilities of communication systems. The transmitter power or the transmit or receive antenna gains must be increased by F to sustain the reliable link operation as compared to the case of unfaded propagation channel.

Two ray multipath channel as shown in figure (4) is used for the LOS air to ground link scenario. In this scenario, the airborne transceiver communicates with the ground station through a multipath channel. The

two-ray ground multipath model adapted to more or less realistic scenarios of hilly or mountainous terrain for fade depth prediction when the main contribution is due to the ground reflection and the atmospheric contribution may be neglected, which is the case for frequencies lower than 10 GHz and for elevation angles above few degrees [1].

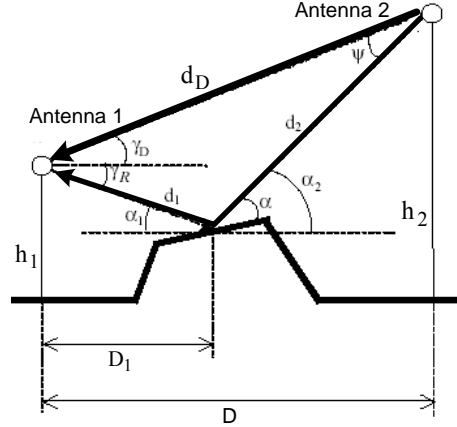


Fig4. Two ray air to ground communication link scenario

In this scenario according to [1] the fading depth is being derived as following equation. For deriving equation (12) there are some assumptions which can be found in [1].

The total received energy in receiver is equal to (7):

$$E_{\text{total}} = |E_D + E_R e^{j\Delta\phi}| \quad (7)$$

The minimum received signal level is:

$$E_{\text{min}} = E_D - E_R \quad (8)$$

The worst case fade depth is as (9):

$$F = \left(\frac{E_D}{E_{\text{min}}} \right)^2 = \left(1 - \frac{E_R}{E_D} \right)^{-2}$$

After using the geometric optics approximation:

$$F = \left(1 - \Gamma \frac{d_D}{d_1 + d_2} G_1(\gamma) G_2(\Psi) \right)^{-2} \quad (10)$$

$$\Gamma_V = \frac{-\epsilon_r \sin(\alpha) + \sqrt{\epsilon_r - \cos^2(\alpha)}}{\epsilon_r \sin(\alpha) + \sqrt{\epsilon_r - \cos^2(\alpha)}}, \quad \Gamma_H = \frac{-\sin(\alpha) + \sqrt{\epsilon_r - \cos^2(\alpha)}}{\sin(\alpha) + \sqrt{\epsilon_r - \cos^2(\alpha)}} \quad (11)$$

Where V and H stands for vertical and horizontal polarization correspondingly, ϵ_r is the relative ground permittivity, and α is the local incidence/reflection angle at the reflection point. After some assumption and acceptable approximation fading depth in vertical and horizontal polarization is:

$$F_V \approx \frac{1}{\gamma^2 \epsilon_r}, \quad F_H \approx \frac{\epsilon_r}{\gamma^2} \quad (12)$$

Where $\gamma = \gamma_D + \gamma_R$ is the path clearance angle. Figure (5) shows fading depth for vertical and horizontal transmission polarization in a L band (1 Giga hertz) communication link.

3.1. Prediction of variation in average received power or shadowing

Shadowing is the slow variation observed around the mean path loss. It has been found from analysis that the shadowing (in dB) follows a zero-mean Normal distribution about the mean path loss (in dB), with a distance-dependent standard deviation σ_s [5]. This variation could be estimated as (13):

$$\sigma_x [\text{dB}] = \rho(90 - \theta)^\gamma \quad (13)$$

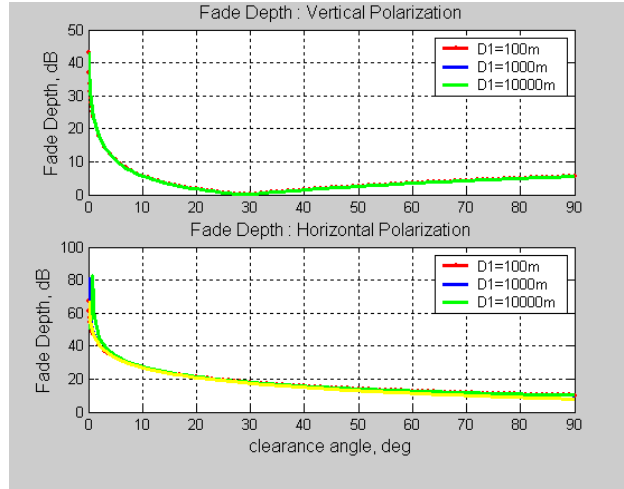


Fig5. Simulation result of fading depth for vertical and horizontal polarization transmission in a L band (1 Giga hertz) communication link

For LOS channels, σ_s is modelled for different frequencies and antenna heights. θ is elevation angle of path. ρ and γ are constant value depended on frequency and height of airborne equipment in LOS link [5]. So fading depth including variation in average power could be estimated by equations (14) and (15).

$$F \approx (1 - \Gamma)^{-2} + \sigma^2_v \quad (14)$$

$$F_V \approx \frac{1}{4\sin^2(\alpha) \cdot \epsilon_r} + \sigma^2_x \approx \frac{1}{\gamma^2 \epsilon_r} + \sigma^2_x, \quad F_H \approx \frac{\epsilon_r}{4\sin^2(\alpha)} + \sigma^2_x \approx \frac{\epsilon_r}{\gamma^2} + \sigma^2_x \quad (15)$$

If we add attenuation due to atmosphere, so the total loss for link budget design requirements is calculated as (16). Table (1) shows attenuation due to atmosphere for 1 GHz frequency.

$$\text{Total Loss} = \text{Free Space} + F (\text{Fading depth}) + \text{Atm. Loss} \quad (16)$$

Table1. Attenuation due to atmosphere for 1 GHz frequency [6]

	Distance of airborne equipment from ground station			
	0.5 N.M	100 N.M	200 N.M	250 N.M
Attenuation due to atmosphere	0.0 dB	0.9 dB	1.4 dB	1.6 dB

4. Small scale fading

As mentioned, statistical models is used for describing the small scale fading in air to ground channel between the transmitter and the receiver that represent a general view of the received signal. Such models are suitable for simulating the performance of communication link. The wide-band stochastic multipath propagation channel models are characterized by the Doppler power spectrum and the delay power spectrum, i.e., the scattering function $P_s(\tau, f_D)$ [3]. According to [3] the Doppler power spectrum is assumed to be independent from the delay power spectrum. So two-dimensional function $P_s(\tau, f_D)$ can be presented by 1-D function delay power spectrum $P_s(\tau)$ and 1-D function Doppler power spectrum $P_s(f_D)$.

Because of different conditions during the flight of an aircraft, there are different channel scenarios for air to ground channel. These scenarios are characterized by the different types of fading, the Doppler, and the delays in the system, where the Doppler and the delay power spectra represent the diffuse scattered multipath components. Reference [3] describes these functions and parameters for en-route, arrival and takeoff, taxi

and parking phases of flight. As an example for en-route scenario channel modelling parameters are as below:

- Rice factor (K): 2 to 18dB (average=15dB)
- Multipath arriving angel width: $\beta = \phi_{aH} - \phi_{aL} = 3.5$ deg (equation 17)
- Maximum Doppler frequency: 6600 Hz
- Maximum Multipath delay: 200 usec

Equation (17) shows pdf of Doppler power spectrum $P_s(f_D)$ for en-route scenario.

$$P_{f_D}(f_D) = \begin{cases} \frac{1}{(\phi_{aH} - \phi_{aL}) f_{D_{max}} \sqrt{1 - (f_D / f_{D_{max}})^2}}, & \text{if } f_{D_{max}} \cos \phi_{aH} < f_D < f_{D_{max}} \cos \phi_{aL} \\ 0, & \text{else.} \end{cases}$$

$$P_{f_D}(f_D) = \begin{cases} \frac{1}{(\phi_{aH} - \phi_{aL}) f_{D_{max}} \sqrt{1 - (f_D / f_{D_{max}})^2}}, & \text{if } f_{D_{max}} \cos \phi_{aL} < f_D < f_{D_{max}} \cos \phi_{aH} \\ 0, & \text{else.} \end{cases} \quad (17)$$

Figures (6) and (7) show simulating result of received signal for different site of a L band communication system. Combination of large scale fading, small scale fading and air traffic condition are taken into account for this simulation. For each condition, simulation is compared with measurement which is performed by [7].

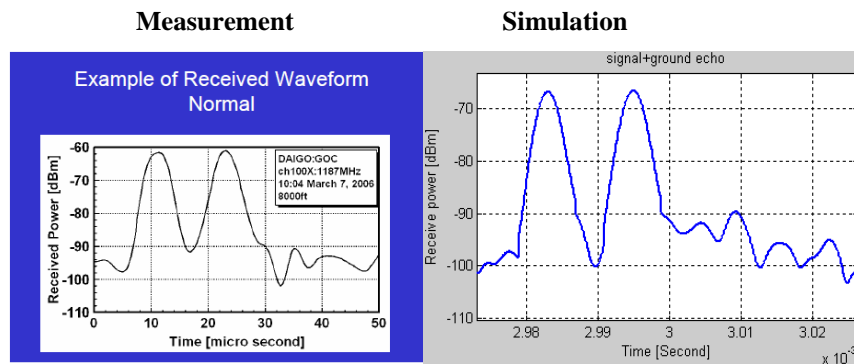


Fig6.a. Air to ground channel simulation and measurement results for a normal site

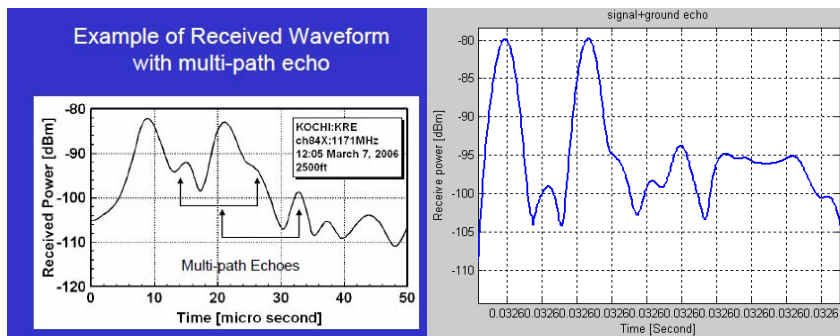


Fig6.b. Air to ground channel simulation and measurement results for a multipath condition

References

- [1] S. Loyka, A. Kouki, F. Gagnon, Fading Prediction on Microwave Links for Airborne Communications, Department of Electrical Engineering, Canada.
- [2] Working Group D, Honolulu, Hawaii, a general model for VHF aeronautical multipath propagation channel, 19-28 January 1999.
- [3] Erik Haas, Aeronautical channel modeling, IEEE Transactions on vehicular technology, VOL. 51, NO. 2, MARCH 2002.
- [4] William G. Newhall, Radio Channel Measurements and Modeling for Smart Antenna Array Systems Using a Software Radio Receiver, April 2003.

- [5] Qixing Feng, Joe McGeehan, Eustace K. Tameh, and Andrew R. Nix, Path Loss Models for Air-to-Ground Radio Channels in Urban Environments, 2006 IEEE.
- [6] Michael C. Stevens, Secondary Surveillance Radar, Artech House, 1988.
- [7] Shigeru Ozeki, Takuya Otsuyama, Electronic Navigation Research Institute, Onboard measurement for multipath Echo, DME/TACAN Beacon Signal Environment Evaluation in Japan, 2006.

The Russian VLBI Network QUASAR. Real Time and VLBI-Network of New Generation

Alexander Ipatov, Andrey Finkelstein, Sergey Smolentsev

Institute of Applied Astronomy, Russian Academy of Sciences

The paper deals with a real time situation with VLBI network QUASAR and a new project of Russian VLBI network dedicated for Universal time determinations in quasi on-line mode. The basic principles of network design and location of antennas are explained. Variants of constructing receiving devices, digital data acquisition system and phase calibration system are specially considered. The frequency ranges and expected values of noise temperature are given.

Introduction

The QUASAR project, which is carried out under the guidance of the Russian Academy of Sciences, involves creation of the full time operating VLBI network, consisting of the 3 radio astronomical observatories. These observatories are located on the Svetloye site, the Leningrad region; the Zelenchukskaya site, the Republic of Karachaevo-Cherkessia, and the Badary site, the Republic of Buryatia and linked by connecting channels with the processing center, located in the IAA, St-Petersburg (Fig. 1).



Observatory Svetloe
 $\varphi = 60^{\circ}32'$, $\lambda = 29^{\circ}47'$



Observatory Zelenchukskaya
 $\varphi = 43^{\circ}47'$, $\lambda = 41^{\circ}34'$



Observatory Badary
 $\varphi = 51^{\circ}46'$, $\lambda = 102^{\circ}14'$

Fig. 1.

The telescopes are provided with radiometers with HEMT-transistors for bandwidth 1.35, 2.45, 3.5, 6.0, 13 and 18/21 cm (Fig. 2), which allows to produce simultaneous receiving session of two orthogonal polarization. To maintain simultaneous receiving at 3.5 and 13 cm bandwidth in both orthogonal polarization (to eliminate ionosphere influence), that are the basic for fundamental astrometry and geodesy research, a combined horn has been constructed. To switch wavelengths and to be able to provide multi-bandwidth observations quasi simultaneously, the Cassegrainian antenna with an asymmetrical secondary mirror and additional focuses located not on the axis of the main mirror, but at some circle with center located at this axis is constructed. Input horns of different wavelength are located above this circle, and switching of the wavelength is achieved by turning of the secondary mirror at certain angle.

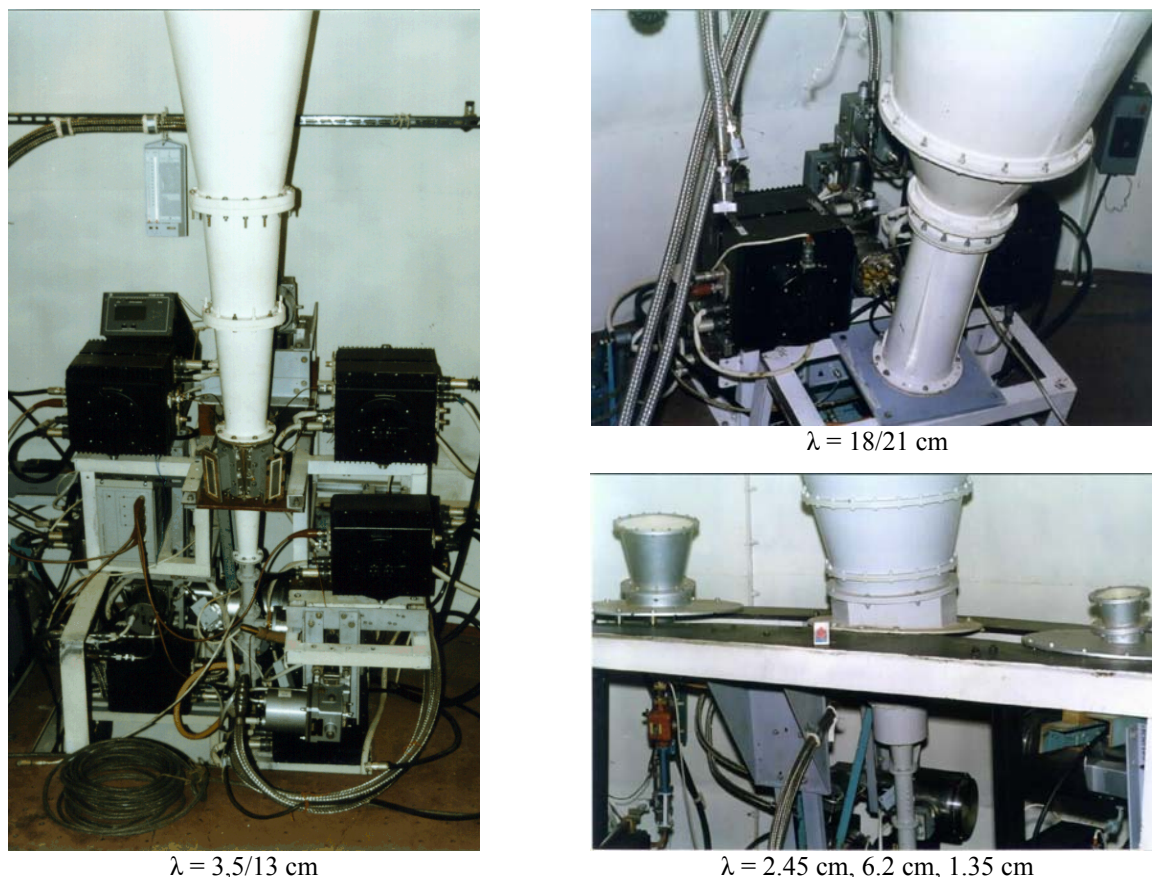


Fig. 2. QUASAR — network radiometers.

Since 2006 radio astronomical observatories of the VLBI Network “Quasar” have actively participated in both international and national programs of observations. In 2008–2009 essential upgrade and development of the “Quasar” Network was performed including replacement of gear and pointing system electronics, modernization of frequency and time keeping system, replacement of data acquisition and data recording systems [1]. All observatories were linked by optical fiber lines, providing operational determinations of the Universal time from 1-hour sessions in e-VLBI mode. In 2010–2011 the further modernization of the Network “Quasar” will include co-location of radio telescopes with “Sazhen-TM” SLR system and combined GPS/GLONASS/Galileo receivers at the observatories.

Further development of GLONASS navigation system puts forward higher requirements to its fundamental segment particularly in maintenance of celestial and Earth fixed coordinate systems and in monitoring the Earth orientation parameters in real time mode. Moreover, Russian VLBI Network gives the unique possibility for quasi on-line Universal time determinations for supporting GLONASS. According to these requirements the designing of the new generation Russian VLBI network has been initiated.

Design principles

The following principles are assumed as a basis of the new generation Russian VLBI network:

- The network should have maximum longitudinal separation of sites for precise determination of the Universal time;
- Equipment of observatories should be compatible with VLBI-2010 system and that of the “Quasar” network;
- Infrastructure of new observatories should be similar to ones of the “Quasar” Network.

The supposed geometry of the new VLBI Network presented on Fig. 3. The largest baseline of new VLBI Network is more than 1.5 times larger than that of the “Quasar” Network. All the sites have good infrastructure, optical fiber communication lines and comparatively good radio climate with low level of radio interferences. The specific features of the main parts of the radio telescope will be described below.



Fig. 3. Proposed location of sites of the new generation Russian VLBI Network.

Front-end

Typical configuration of a VLBI site includes an antenna equipped with receives for 2–14 GHz frequencies. The receiving of radio signals should be fulfilled not in the whole range 2–14 GHz but in several sub-bands (Fig. 4). Such a solution arises from the requirement to have two circular polarizations in S/X bands and to avoid different radio frequency interference. Block diagram of the new receiver is shown on Fig. 5.

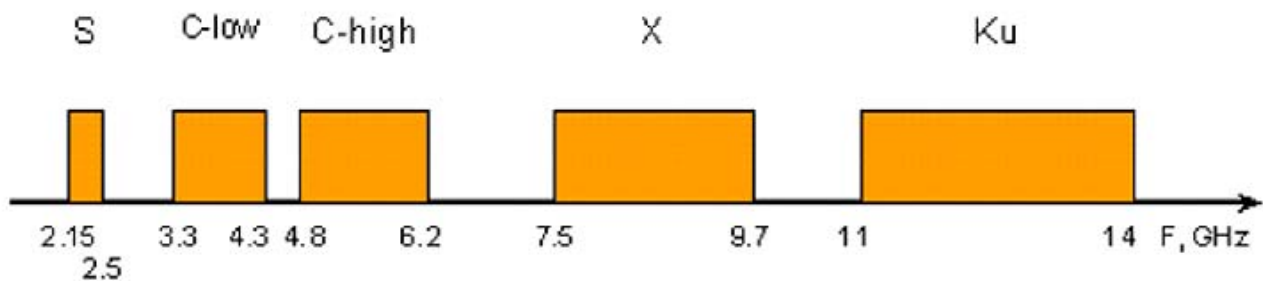


Fig. 4. Working frequency bands for the new generation Russian VLBI Network.

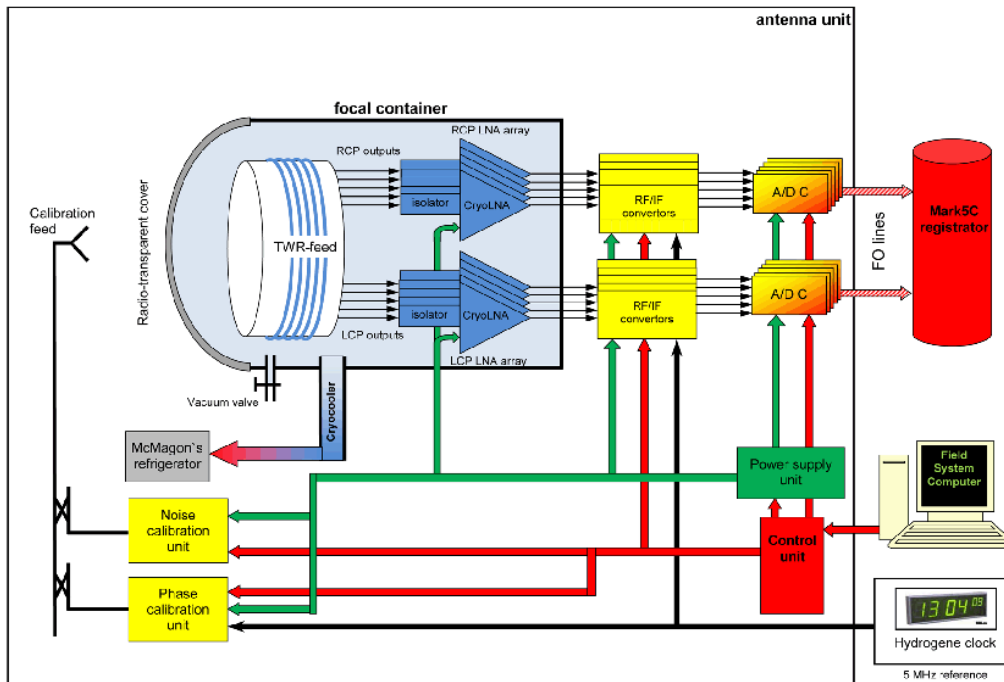


Fig. 5. Block-diagram of radio telescope for the new generation Russian VLBI Network.

The output signals from the receivers should be processed by digital signal processing (DSP) units, recorded to disk modules and transmitted through optical fiber lines.

It is suggested to use relatively lightweight 12-meter antenna with high slew rates. We are considering an option of either constructing such an antenna in Russia or purchasing an existing communication antenna.

An assembly of receiver and feed will be placed in primary focus. It is considered to use a circular travelling-wave-resonator (TWR) antenna as the feed. The TWR antenna should be cooled by a cryogenic system to 20 K level, and the heat shield — to 80 K level. The low noise amplifiers should be cooled down to 20 K and their gain is about 30 dB. The total system noise temperature is expected to be 16–20 K.

Digital DAS

The new generation digital data acquisition system (DAS) consists of a 10-channel RF/IF down converter and four identical DSP units (Fig. 6). The RF/IF down converter transfers input signals spectrum from a multi-band radio irradiator of the radio telescope (*C*, *X*, *S* and *Ku* bands) to IF range of 1–2 GHz. Eight out of ten channels of RF/IF down converter can be tuned in the wide frequency range of 3–14 GHz. There is no down conversion in the rest two channels intended for *S*-band because it can be directly digitized by ADC but the signal is amplified and filtered. Each DSP unit can be connected to the outputs of RF/IF down converter through IF switch. Each channel of the DAS requires one Mark 5C. As the DAS is located on the antenna, the signal is transmitted to the control room by an optical-fiber line in a digital form.

The DSP unit is the basis of the DAS and contains the following devices:

- analog digital converter (ADC),
- field programmed gate array (FPGA),
- clock oscillator,
- demultiplexer of the ADC output signal,
- flash RAM to store FPGA firmware,
- microcontroller,
- optical transmitters.

It will be implemented as a single multilayer printed circuit board (PCB).

The FPGA is the basis of the DSP unit. It performs the following operations:

- measurement of an rms level of the input signal,
- dividing of the full band input signal into narrowband channels and converting it to the baseband (if necessary),

- calculation of a rms level of the narrowband channels,
- 2-bit quantization of output signals,
- generation of a test vector to check a transmission line and data recording system,
- formatting the output data in accordance with a data recording system interface and sending them to the optical transmitters.

The prototype of the DSP unit was made to check the basic principles. The prototype consists of evaluation boards of the following devices:

- 10-bits ADC (AT84AS008-EB),
- high-frequency demultiplexer 1:4 (AT84CS001-EB),
- FPGA XC5VFX70T (ML507),
- optical transceiver AFCT-5710LZ.

The following tests have been made by using the prototype:

- transmitting of an internally generated test signal from ADC through demultiplexer to FPGA,
- transfer of the test signal from one FPGA to another by fiber-optical line,
- digitization of a signal from external signal generator,
- measuring of the input signal power.

The tests of the prototype prove an opportunity to implement the digital DAS with modern electronic components.

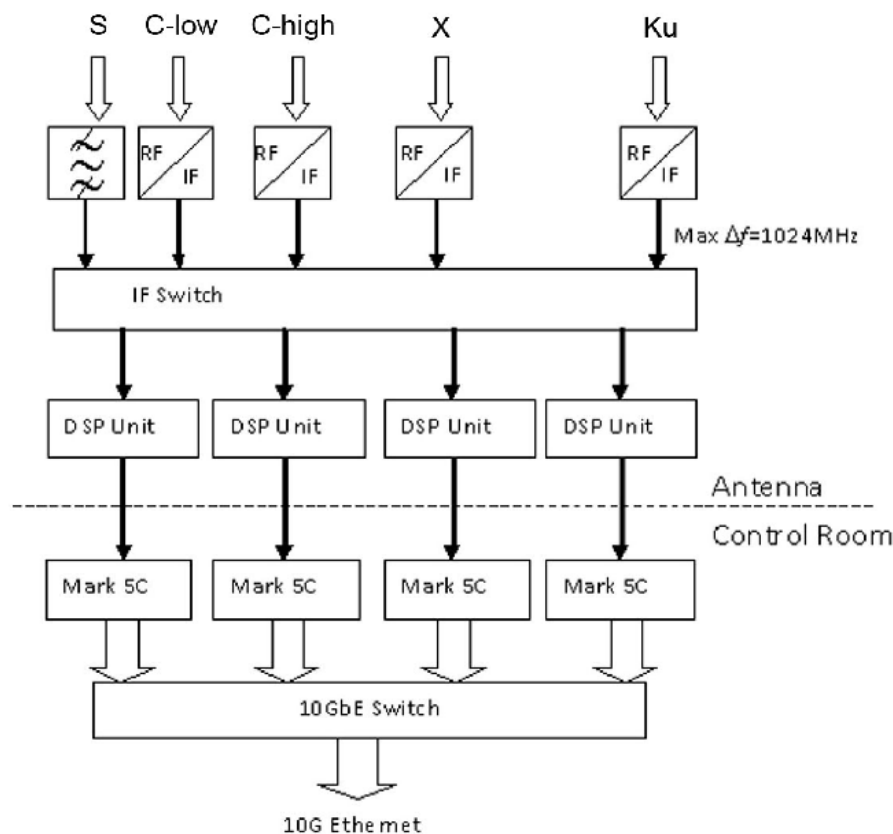


Fig. 6. The Digital Data Acquisition System for the new generation Russian VLBI Network.

Phase calibration

A phase calibration system for the new generation Russian VLBI Network of is now under development. The main purpose of the phase calibration system is to monitor the instrumental delay of receiver and data acquisition equipments. For monitoring instrumental delays a pulse generator is suggested to use. A spectrally pure 5 MHz signal is transmitted by cable to the location of the receiver, where it is converted to 1 MHz signal which makes a charge storage diode to generate pulses of very short (≈ 30 ps) duration (Fig. 7).

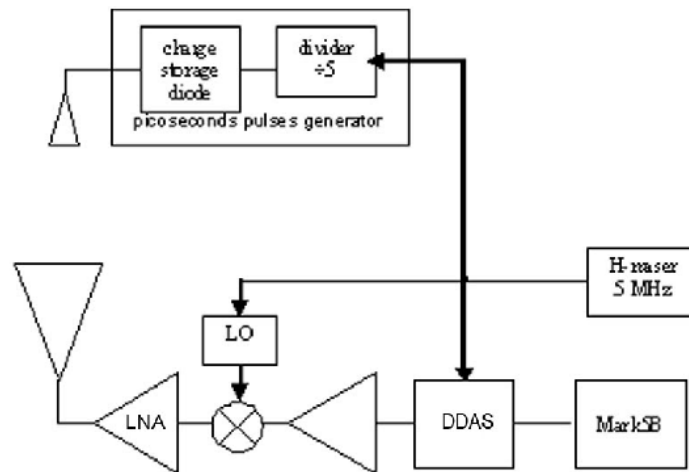


Fig. 7. The phase calibration system for the new VLBI Network.

The possibility of locating the phase calibration injection point ahead of the horn is studied. Phase calibration impulses are radiated from a special broadband feed fixed on one of legs supporting the focal box. To meet the requirement of a distant radiation zone the feed is to be placed to a point faraway from a mirror. The key advantage of such a system is that the horn and all the following devices are included into the phase calibration loop.

The prototype of transverse electromagnetic (TEM) horn with TEM double-ridged transition for 2–14 GHz frequency has been already made in IAA RAS and it is tested now. The prototype parameters measured prove the possibility of using this feed for phase calibration purpose.

Coaxial cables connecting the H-maser and the pulse generator are selected taking into account the low temperature coefficient and mechanical stress sensitivities. For the LMR type cable the temperature coefficient is about 10 ppm/K. If 10 meters of this cable are exposed to significant temperature fluctuations its stability should be under 0.3 ps/K. Typical cable length change with a 360° wrap of 4 inch radius is under 1 ps. So, in this case cable measurement system is not need.

References

[1] Finkelstein A., Ipatov A., Smolentsev S., The Network “Quasar”: 2008–2011, Proc. 5th IVS General Meeting, 39–46, 2008.

The Communication Systems for the Small Satellite Flying Laptop

U. Beyermann¹, C. Thibaut¹, F. Böhringer¹, Prof. Dr. H.-P. Röser¹,
J. Baumgärtner¹, M. Spetzler¹

¹ *Institute of Space Systems, Pfaffenwaldring 31, 70569 Stuttgart, Germany*

This paper deals with the communication systems for the small satellite Flying Laptop. It is a project from the Institute of Space Systems at the University of Stuttgart. The satellite will test different new types of communication systems. The telecommand, tracking and control system is developed as software defined radio with Flash FPGAs as computing element. Three types of high speed communication systems will be flown. The first uses S-band with data rates up to 1 Mbps, the second uses X-band with data rates up to several 100 Mbps and the last one is an optical downlink for data rates up to 1 Gbps. Also a system for rain rate determination measuring the difference in attenuation between Ku- and Ka-band will be tested.

1. Overview

While analyzing the space market a new trend is getting obvious: future satellites will be smaller. More and more missions are so called small satellites with a mass below 500 kg - examples are GRACE, SWARM, or Proba-V. The advantages over big satellites are in general the shorter development time, the lower risk and lower costs. Hence it is very unlikely that a huge mission like Envisat is build again.

The Institute of Space Systems (IRS) at the University of Stuttgart will contribute to this development with its own space craft: the small satellite Flying Laptop (FLP). The main mission goals are Earth observation, science experiments and technology demonstration. The dimensions of the satellite are 600 x 700 x 800 mm³ and it has a mass of 120 kg. Figure 1 gives an overview of the satellite. In this shown CAD model some major experiments are colored. Green is the Multispectral Imaging Camera System (MICS) for Earth observation and orange the panoramic camera PAMCAM, also for Earth observation. The science experiments are in blue the Star Trackers used for the search of Near Earth Objects and yellow the antenna system for high speed communication and rain rate determination. Examples for technology demonstration are the non explosive panel release mechanism and COTS NiMH battery cells. For further information about the Flying Laptop mission visit www.kleinsatelliten.de.

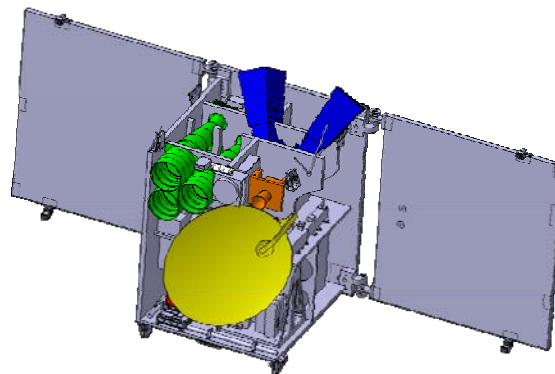


Figure 1: CAD model of the Flying Laptop, experiments are colored

The communication systems play a big role for this mission. To get the scientific and image data from the satellite to the earth is still the bottleneck also for other missions. The Flying Laptop will test three different systems for data downlink to show that even on small satellites high data rates are possible. The frequency bands used are S-band, X-band and one system uses an optical downlink. Also a new concept for the Telemetry, Tracking and Control System is tested. The last system that deals with communications is the rain rate determination experiment which uses common communication frequencies to measure the rain rate.

2. Telemetry, Tracking and Control System

Analyzing the future trends for new communication systems for space applications, Software Defined Radios (SDR) are getting more and more important [1]. But in terrestrial applications like mobile communication SDRs are already the state-of-the-art [2]. Following this trend the Telemetry, Tracking and Control System

for the Flying Laptop will also be a SDR. The reasons are the higher flexibility, the faster development time and lower costs. Further boundary conditions which have to be considered are the need of omnidirectional receiving and transmitting, data rates up to 100 kbps and the usage of ham radio frequencies which is typically for university projects.

As computing element for the FLP system Flash FPGAs from Actel were chosen. Since 2010 Actel offers a new type of FPGA for space applications, the RT version of the ProASIC3 Flash FPGA. The advantages are the good radiation tolerance, reprogrammability and low power consumption at lower costs compared to antifuse FPGAs which are predominantly used in actual high reliability systems [3].

2.1. Hardware Design

The implementation of the system as SDR means moving carrier modulation and demodulation to the digital domain. This allows for the implementation of different modulation schemes in software without applying any changes to the hardware. All digital signal processing will be done on Flash-FPGAs, which will run at relatively low frequencies to decrease the system's sensitivity to radiation.

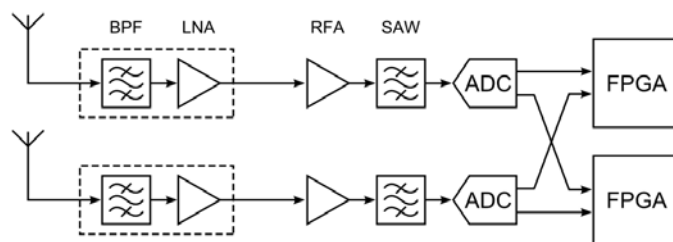


Figure 2: Simplified block diagram of the TT&C receiver

In order to obtain maximum re-configurability, the conversion between analog and digital signals needs to be done as close to the antennas as possible. The use of UHF frequencies for telemetry uplink permits the application of band-pass undersampling in the receiver, abolishing the need for a downconverting mixer. This simplification of the system is bought with strict requirements concerning the analog-digital-converters (ADC), which need to be high-speed and high bandwidth types, and the clock signal, which must have extremely low phase noise and low jitter performance. This principle is shown in Figure 2. Two analogue receiving paths for increased reliability are planned. Each path consists of band pass filters, two amplifying stages and an ADC. At the end the two paths are cross coupled to Flash FPGAs. This design is one failure tolerant both in the analogue and in the digital part.

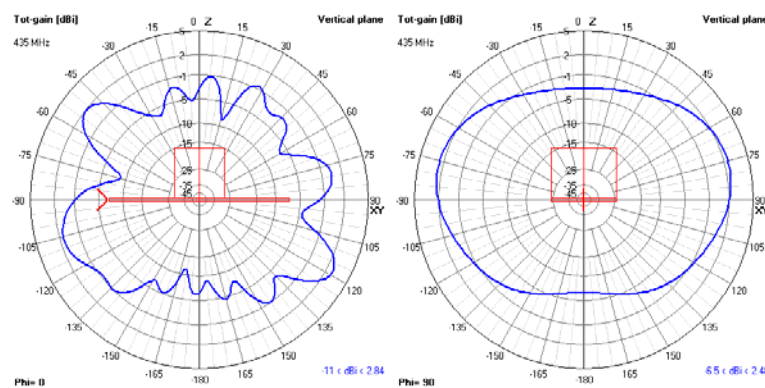


Figure 3: Computed antenna gain of one of the receiving antennas in two different planes

The telemetry transmitter will apply undersampling to output a high intermediate frequency which can be upconverted to S-band in just one step, therefore limiting the amount of analog components in the design. Direct undersampling to radio frequency is not possible due to the limitations of currently available high-speed digital-analog-converters. Also the FPGAs have a clocking limitation in radiation exposure because the higher the radiation the more failures occur.

Both the receiver and the transmitter will be equipped with v-dipole antennas to obtain omnidirectional characteristics, since the availability of the telecommand and telemetry link in all possible attitudes is a

mission requirement. Figure 3 shows a computation of the antenna gain of a receiving antenna in two different planes. The computation was performed with the freeware 4NEC2. Although the antenna gain is not uniformly distributed there is no zero point in the antenna pattern.

2.2. Algorithms Development

Typical algorithm development for FPGAs is done in VHDL or Verilog. Both programming languages are very near to hardware and logic inside the target FPGA. For a good design you need either an experienced software engineer or lots of time with a large number of different designs to learn how to build the algorithms right. For the FLP project both possibilities are not feasible. An experienced software engineer is too expensive and the strict timeline does not allow the trial-and-error method.

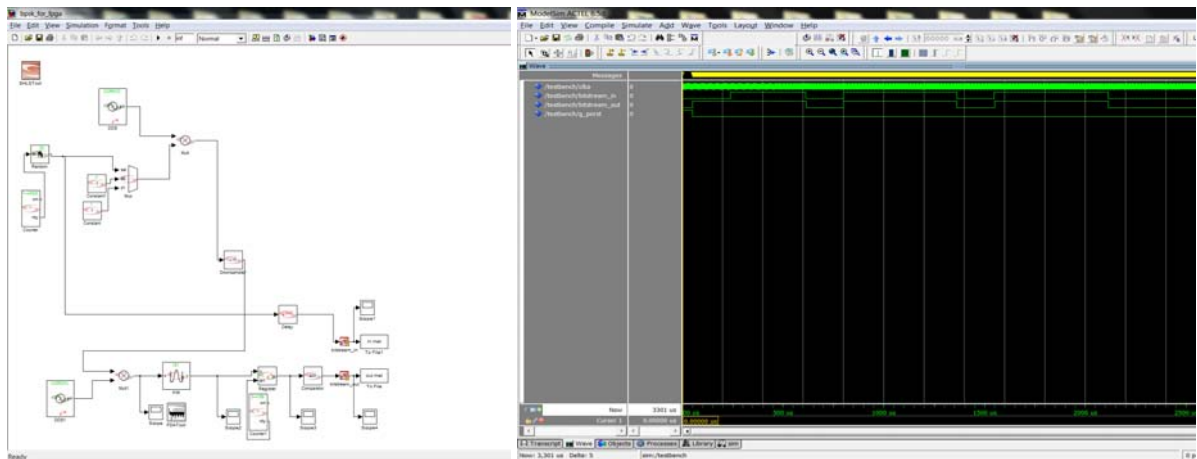


Figure 4: Algorithm development in Matlab/Simulink and algorithm simulation in ModelSim [4]

But the increasing computing power of actual FPGAs is the solution. Nowadays it is possible to develop algorithms in Matlab/Simulink including fixed point calculations and simulation so as to apply automated code generation to VHDL. The left side of Figure 4 shows a simple BPSK demodulator developed in Simulink. The right side of Figure 4 shows the simulation of the automatic generated code in time domain with ModelSim. As last step the algorithms are tested on an equivalent FPGA on a development board. The complete design flow is controlled by the Libero IDE Software Package [5]. Figure 5 gives an overview over the Libero project manager and the used FPGA development board from Actel.

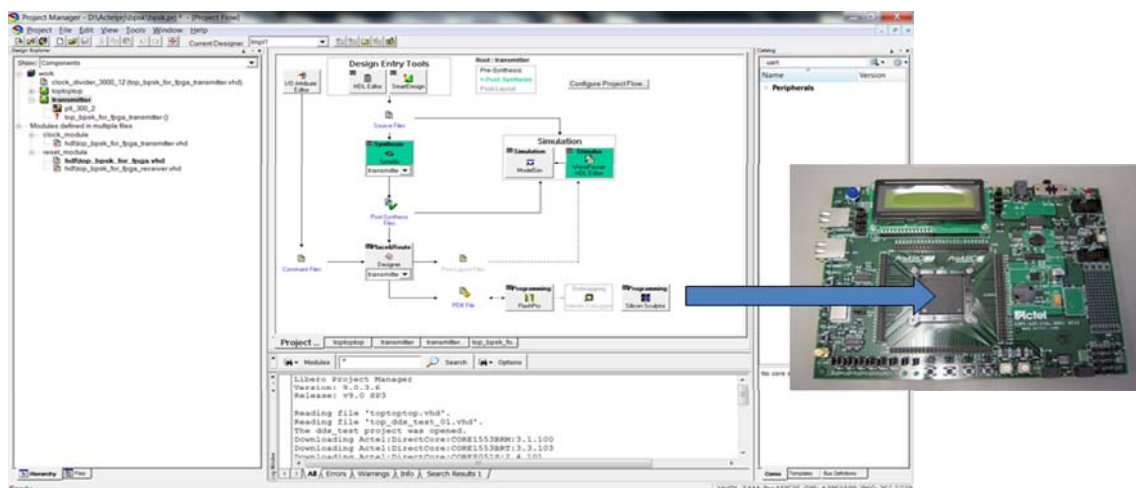


Figure 5: Libero IDE project manager and FPGA development board [5]

3. Data Downlink System for S-band

The data downlink system for S-band is a further development of the TT&C transmitter. It uses nearly the same hardware; only minor changes are made like different filters, an additional power amplifier, a high gain

antenna and different clock frequencies. Data rates up to 1 Mbps are possible, lower data rates will be selectable. It is also planned to implement different modulation schemes for testing which is the best scheme at given data rate and environment conditions. To get the most possible flexibility the FPGA can be reprogrammed in space. So software updates are even after launch possible. For increasing the reliability of the data transmission simple forward error correction codes are also implemented.

4. Optical High Speed Downlink System

The Optical High Speed Downlink System on Flying Laptop is a technology demonstrator designed and developed by the Institute of Communications and Navigation of DLR at Oberpfaffenhofen. Its goal is the demonstration of a cost-efficient optical downlink terminal with low technical complexity which can be used on future micro-satellite missions.

As RF-downlink systems reach more and more their limits with downlink rates from low earth orbit of a view hundreds megabits per second, free space optical (FSO) communication allows data rates of several gigabits per second. Beside this major advantage FSO-systems require less space, less mass and most importantly less power than their counterparts in the RF-spectrum.

Nevertheless, the blockage of the optical signal by clouds is a big issue when short delays between the data acquisition and the data downlink are needed. This problem can be reduced by placing ground station at locations with statistical less cloud coverage, by using ground station networks or by storing the data on-board until the next unhindered ground station access [6].

Due to the small beam divergence angle FSO-systems have strong requirements on the pointing accuracy of the optical transmitter towards the receiver.

Flying Laptop was designed to perform target pointing maneuvers aiming at a fixed point on the earth surface during a flyover for multiangular multispectral Earth observation. This capability is also used for the FSO-communication so that no steerable optical antenna is needed for the FSO-system. This reduces cost, complexity and risk. Although the total pointing error during the pointing maneuver of 150 arcsec (2sigma) is fairly low the beam divergence angle of the FSO-system has to be wider than typically anticipated to ensure a continuous signal reception on ground. The Optical Ground Station in Oberpfaffenhofen as shown in Figure 6 will be used as the receiving station for the experiment.



Figure 6: The optical ground station in Oberpfaffenhofen

The FSO-terminal itself has a mass of less than 1kg, a maximum power consumption of 35 W and was designed to transmit up to 1.2 Gbps. Although, the data rate will have to be lowered due to the abstinence of a high-accurate steerable antenna, the demonstration and in-orbit verification of the system for future missions will be performed.

5. Rain Rate Determination System

One of the main missions of the Flying Laptop is the rain determination experiment. In fact during its propagation through the atmosphere, a signal emitted from a satellite is attenuated because of weather conditions such as rain. This attenuation especially depends on the satellite's elevation and the signal's frequency.

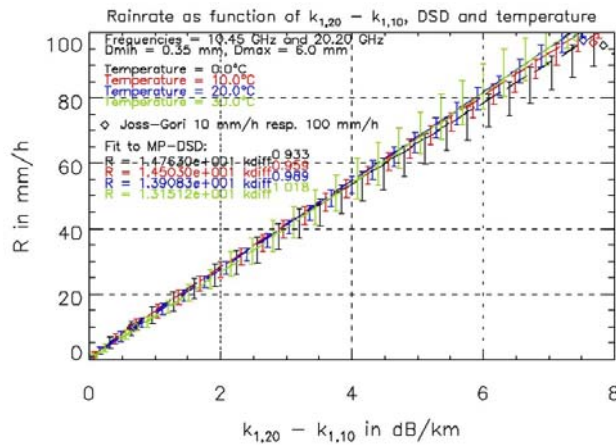


Figure 7: The relation between Ku- and Ka-Band and the rain rate obtained by computations

Computations have shown that there is a linear relation between the difference of attenuation between Ku- and Ka-Band signals and the amount of water in the atmosphere. One calculation is shown in Figure 7. This allows us to determine the rain rate at a specific location, and in the case of a mobile receiving platform, it is possible to determine the rain rate in different locations. For this experiment we don't need to modulate the signal the same way as if it was used for telecommunications. We only need to modulate the signal a simple way so we can measure the attenuation between the Ku- and the Ka-Band.

The calibration is done while pointing to the ground station as shown in Figure 8. The further information needed for the experiment about the cloud layer and atmospheric conditions are obtained e.g. with a polarimetric radar. Then measurements can be done and rain rate can be evaluated in different locations thanks to mobile measuring platforms.

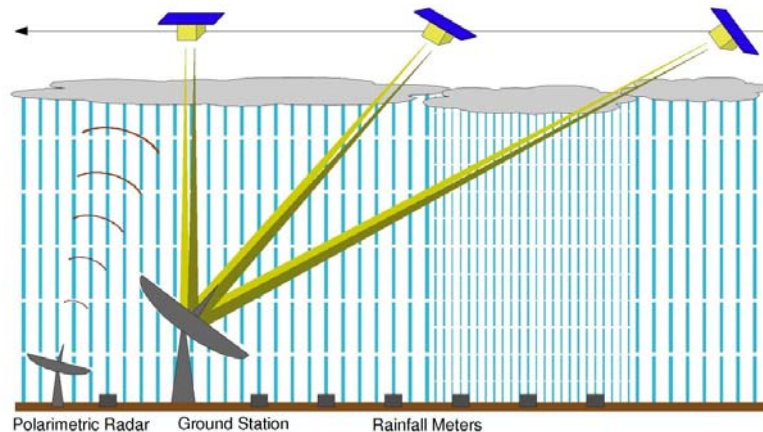


Figure 8: Rain Rate Determination System principle

References

- [1] M. C. Scardelletti et al., Software Defined Radio Architecture for NASA's Space Communications, July 2007 High Frequency Electronics
- [2] P. Burns, Software Defined Radios for 3G, Artech House, Inc., Norwood, USA
- [3] System Critical FPGAs Product Catalog, July 2010, Actel Corporation, Mountain View, CA, USA
- [4] Matlab/Simulink is a trademark of the The Mathworks, Inc., Natick, MA, USA
ModelSim is a trademark of Mentor Graphics Corp., Wilsonville, OR, USA
- [5] Libero IDE is a trademark of Actel Corp., Mountain View, CA, USA
- [6] D. Giggenbach et al., Optical Satellite Downlinks to Optical Ground Stations and High-Altitude Platforms, Advances in Mobile and Wireless Communications, 2008, Springer Berlin Heidelberg

Introduction to the Near-Field Microwave Microscopy

Kiejun Lee¹, Arsen Babajanyan¹, Harutyun Melikyan¹, Barry Friedman²

¹ *Department of Physics and Interdisciplinary Program of Integrated Biotechnology,
Sogang University, Seoul 121-742, Korea*

² *Department of Physics, Sam Houston State University, Huntsville, Texas 77341, USA*

The near-field microwave microscope (NFMM) is a powerful method to characterise the physical structures, such as thin films, bulk material, fluids, etc. The NFMM is a noncontact, nondestructive and label-free evaluation tool to obtain material properties such as electrical conductivity, dielectric permittivity, magnetic permeability to distinguish the spatial changes of these parameters in materials under various preparation and measurement conditions with high contrast and with high spatial resolution. The results clearly show the sensitivity and the usefulness of NFMM for many device applications at microwave frequency such as 3D surface mapping and topography, material characteristics (permittivity, permeability, conductivity, carriers density, etc.) point-by-point distribution, and label-free biosensing (DNA, SAM, etc.).

1. Introduction

Near-field microwave microscopy (NFMM) is the quantitative way to measure the electrodynamic properties of materials at microwave frequencies [1-4]. This is a direct observation method that allows visualizing electromagnetic properties of thin films and bulk samples. The near-field microwave reflection coefficient (S parameter) image from the sample directly visualizes the dielectric, electric and magnetic characteristics and their changes. This NFMM approach is based on nondestructive probing of a local electromagnetic near-field interaction between the probe-tip and the materials, and can be used in exploring material behaviors [5-8].

There are a number of ways to access the near-field component of electromagnetic fields to gain sub wavelength resolution. A technique that uses microwaves, NFMM has a number of interesting features [9-11]. Firstly, there is not much structure in the electromagnetic properties in this frequency range, so one is in fact measuring the low frequency properties, which are of considerable practical importance. In addition, “subsurface” information is obtained because microwaves penetrate well into materials, i.e. in good conductors where the skin depth is still of the order of a micron. Finally, in comparison to other frequency regimes, it should be straightforward to obtain quantitative information, again because the electromagnetic properties are relatively simple [12]. Indeed, by consideration of frequency shifts, quantitative measurement of the local dielectric constant and electrical conductivity has been done using numerical modelling based on cavity perturbation theory [13,14]. Another, perhaps more natural observable in NFMM experiments, is the microwave reflection coefficient S_{11} as a function of frequency (from which, of course, the frequency shift can be obtained) or S_{11} as a function of some sample property for a fixed frequency [15,16].

In this paper we review the general concept of near-field interactions between a probe-tip and sample and discuss a quantitative interpretation of near-field microwave images in view of material characteristics such as complex dielectric permittivity (ϵ), complex magnetic permeability (μ) and electrical conductivity (σ). Recently, several NFMM techniques have been developed for the microwave and millimeter-wave ranges [5-8]. An important ability of the NFMM is noncontact characterization of multilayer structures and single crystals, and thin films. The main advantages of NFMM compared to the usual electrical measurement is that NFMM can directly image the electric properties at interfaces and surfaces with high sensitivity and simplicity, because the NFMM directly evaluates and images the dielectric, conducting and magnetic characteristics and these parameter changes under varying of the external influences.

2. Theory

2.1. Near-field microwave interaction

The microwave frequencies are defined as electromagnetic waves between 300 MHz and 300 GHz [17]. Electromagnetic waves below 300 MHz are called very high frequency (VHF) or radio frequency (RF); above 300 GHz sub-millimeter wave spectrum begins as shown in Fig. 1 (a). The following distinction between millimeter-waves and microwaves is almost universally accepted: frequencies with free-space wavelengths less than one centimeter but greater than one millimeter are referred to as millimeter-waves.

Thus, the millimeter-wave spectrum starts at 30 GHz, and runs to 300 GHz, where the wavelength in free-space is less than one millimeter. The sub-millimeter-wave band corresponds to infrared radiation and terahertz frequencies.

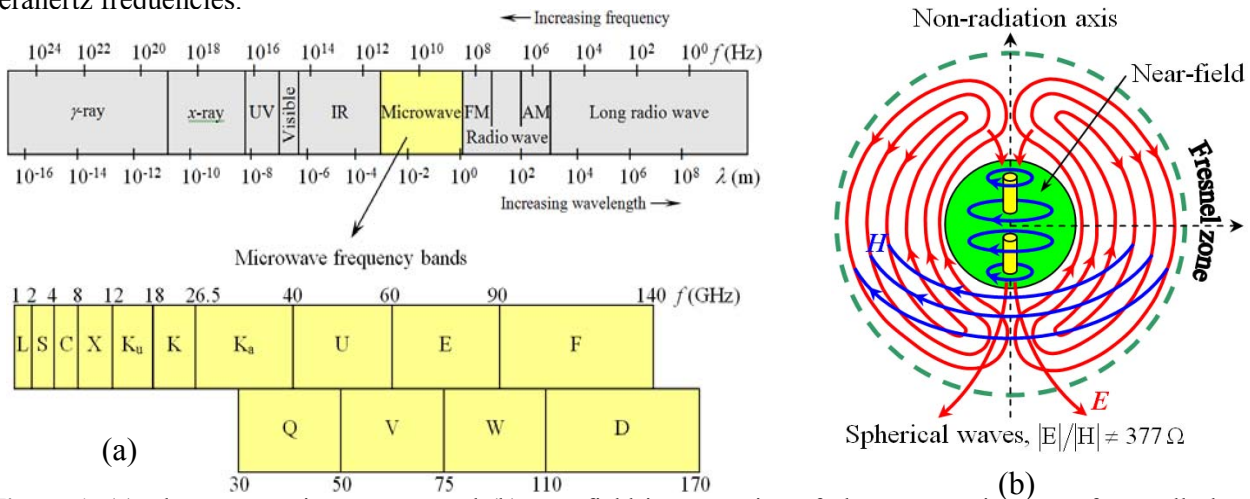


Figure 1. (a) Electromagnetic spectrum and (b) near-field interpretation of electromagnetic waves for small electric dipoles.

An important strategy for understanding natural and artificial materials is to study the interaction of the material with electromagnetic fields. The properties of metals, semiconductors, and dielectrics at low frequency have been a fruitful area of investigation. The first experiments were transmission experiments done in the far-field region from source, and typically required that the sample size be of the scale of the wavelength [18]. In the second generation some experiments were carried out in resonant cavities, which are on the order of the wavelength in at least one dimension [19]. As a result the electrodynamic properties of the sample are still averaged over macroscopic length scales. However, properties of the material can vary on much shorter length scales, even into the nanometer range. Currently, the materials of most interest are complex multi-component compounds or nanoscale composites and can rarely be made homogeneous on the millimeter or micro length scales required for electrodynamic measurements [20-22]. Finally, the typical dimensions of devices into which some of these functional materials are integrated are orders of magnitude smaller than the wavelength at the operation frequency of the device. Electrodynamic measurements where the wavelength is longer than the sample characteristic size has emerged in recent years in condensed matter physics [23,24] and is associated with the concept of near-field interactions between a source and a sample in which evanescent waves are created and interact with the sample. The NFMM is one aspect of near-field interaction.

Electromagnetic waves are created by time-varying currents and charges. Their interactions with materials obey Maxwell's equations supplemented with boundary conditions [25]. Electromagnetic waves can be guided by structures (transmission lines) or propagate in free space. Near-field behavior is most clearly seen surrounding small electric dipoles as shown in Fig. 1 (b). The near-field consists of the reactive near-field, also known as the quasi-static near-field, and the radiating near-field also known as the Fresnel zone. In the quasi-static near-field the fields strongly resemble the electrostatic fields of a charge dipole for a dipole antenna and the fields of a magnetic dipole for a loop antenna. In large antennas the quasi-static field can be seen near edges. In the Fresnel zone the waves are clearly not plane waves and may have phase shifts that do not vary linearly with distance from a fictitious phase center. A common feature of all electrically small (less than a wavelength) antennas is that the near-field excites the environment in which the antenna resides. In the far field, the power density ($E \times H$) drops as R^{-2} , while in the near-field region it drops as R^{-3} .

2.2. Transmission line theory and perturbation theory

Transmission line theory can be approached from the extension of circuit theory or from Maxwell's equations [25]. A transmission line is a distributed parameter network, where voltages and currents can vary in magnitude and phase over its length. A transmission line is often schematically represented as a two wire line and is a conducting structure that guides an electromagnetic wave. Most transmission lines use two conductors, where one is considered ground. This includes coax (the outer conductor is ground), microstrip, and strip-line. The transmission lines have two important properties that depend on their geometry: their

inductance per unit length, L' and their capacitance per unit length, C' . The characteristic impedance of a system is calculated as the square root of the ratio of these two:

$$Z_c = \sqrt{\frac{L'}{C'}}.$$

(1)

The exact characteristic impedance of free-space is $Z_0 = 377$ ohms. Impedance matching of source and load is important to get maximum effective connection and minimum return losses.

In order to match the impedance of the probe-tip-sample system for near-field imaging, we study the reflection of microwaves (scattered from the probe as a source) from the sample surface and the mismatching condition due to the external influence of the structure of the sample. Here we present the transmission line theory model for the probe-tip-sample system. For simplicity we consider the two-layer sample: a thin film on the bulk substrate as shown in Fig. 2 (a).

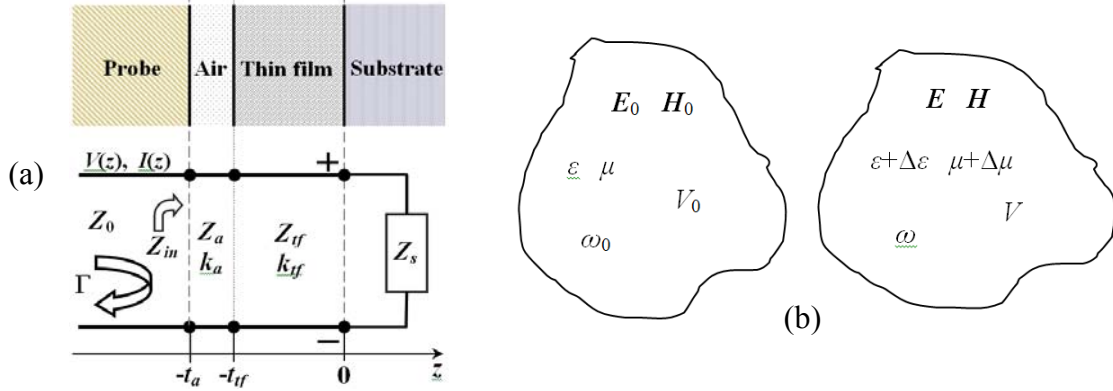


Figure 2. (a) Schematic and equivalent transmission line circuit of the probe-tip and the two layer sample system. (b) (a) Original and (b) perturbed resonant cavity perturbed by a change in the permittivity or permeability of the cavity material or by a change of the cavity volume.

An expression of the dependence of reflection coefficient S_{11} depends on material parameters of the sample can be derived by using standard transmission line theory, assuming impedance matching between the probe and the microwave source

$$S_{11} = 20 \log \frac{Z_{in} - Z_0}{Z_{in} + Z_0},$$

(2)

where Z_0 is the impedance of probe-tip (50Ω) and Z_{in} is the complex input impedance of the sample. The calculation of the input impedance is performed through the transmission line analogy and the impedance transformation [17] for every layer with layer parameters; thickness, wave number, and surface impedance:

$$Z_{in} = Z_{tf} \frac{Z_s + jZ_{tf} \tan(k_{tf} t_{tf})}{Z_{tf} + jZ_s \tan(k_{tf} t_{tf})},$$

where Z_s is the impedance of the substrate, and Z_{tf} , k_{tf} , t_{tf} are the impedance, wave number, and thickness of the thin film, respectively. Applying Eq. (3) to the dielectric/metal interface we obtain the effective surface impedance [26]:

$$Z_{in} \approx jZ_{tf} \tan(k_{tf} t_{tf}),$$

which does not easily reduce to Z_{tf} , it is immediately apparent that resonance can appear.

In practice cavity resonators are often tuned by making small changes in their shape or by the introduction of small pieces of dielectric or metallic material. For example, the resonant frequency of a cavity can be easily tuned by changing the cavity volume or adding dielectric material or by a metallic screw. This approach allows the determination of material characteristics (permittivity, conductivity, permeability, etc.) by measuring the shift in resonant frequency [27,28]. One useful technique to do this is the perturbation method, which assumes that the actual fields of the cavity with a small material perturbation are not greatly different from those of the unperturbed cavity.

Figure 2 (b) shows a cavity perturbed by a change in the permittivity ($\Delta\epsilon$) and permeability ($\Delta\mu$) of the material of the cavity in the volume (ΔV) of the cavity. If \vec{E}_0, \vec{H}_0 , are the fields of the original cavity, and

\vec{E} , \vec{H} are the fields of the perturbed cavity and $\Delta\epsilon$ and $\Delta\mu$ are small changes, the perturbed fields can be approximated by the original fields, to give the fractional change in the resonant frequency as [17]

$$\frac{\Delta f}{f_0} = \frac{f - f_0}{f_0} = -\frac{\int_{v_0} (\Delta\epsilon |E_0|^2 + \Delta\mu |H_0|^2) dv}{\int_{v_0} (\epsilon |E_0|^2 + \mu |H_0|^2) dv}$$

(5)

This result shows that any increase in permittivity or permeability at any point in the cavity will decrease the resonant frequency. Thus this decrease in resonant frequency can be related to the increase in stored energy of the perturbed cavity according to Eq. (5).

By consideration of frequency shifts obtained by NFMM, quantitative measurement of the local electromagnetic characteristics has been done using numerical modelling based on cavity perturbation theory [13,14].

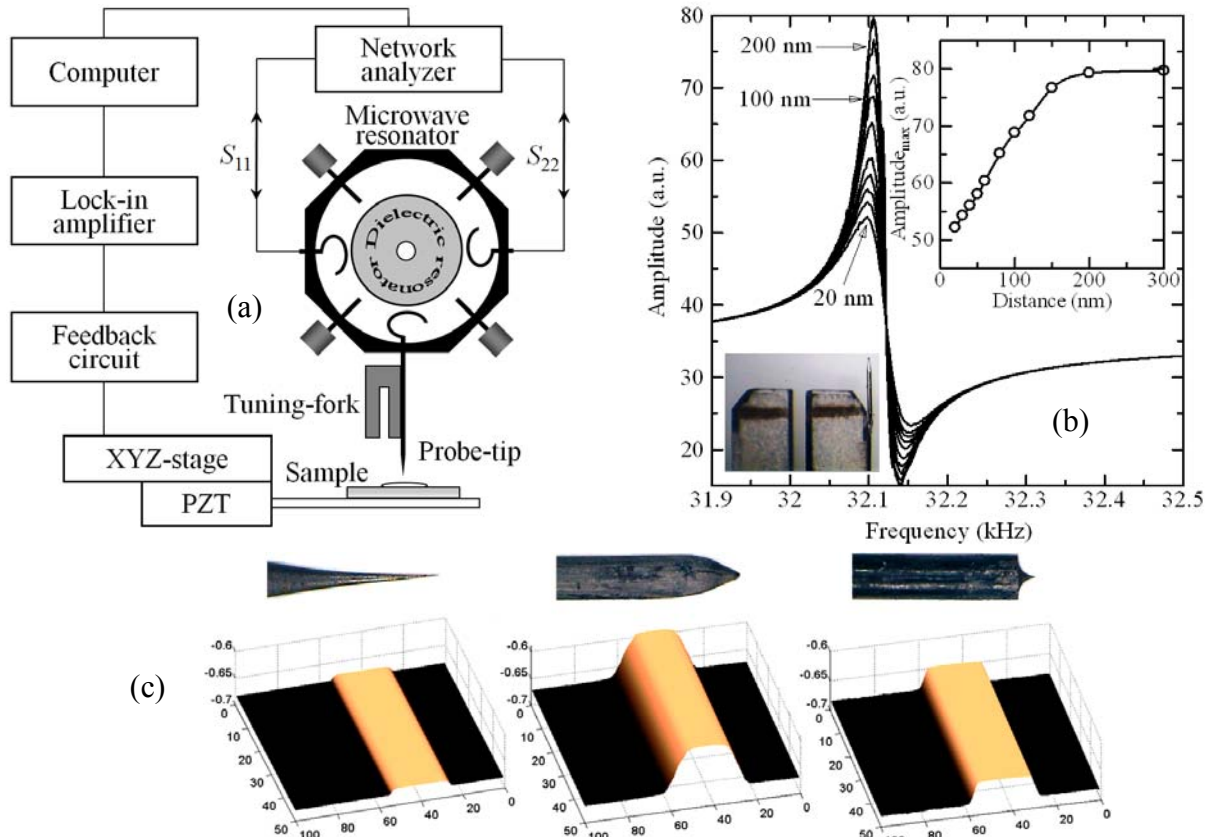


Figure 3. (a) A schematic of NFMM experimental setup. (b) Image of a 32 KHz resonant frequency quartz tuning-fork with an attached sharpened tungsten tip. (b) The amplitude-frequency characteristic of the quartz tuning-fork resonant system at various tip-sample distances. The upper inset shows the amplitude maximum vs. tip-sample distance and the lower inset is the image of a 32 KHz resonant frequency quartz tuning-fork with an attached sharpened tungsten tip. (c) Tip shape and corresponding obtained NFMM images for thin tip, thick tip, and hybrid tip.

3. Experiment

3.1. The basic experimental setup of NFMM

To illustrate the basic operation of NFMM we have presented a detailed description. In our design of NFMM experiments, the probe-tip is simply a sharpened metal wire or metal coated commercial triangular AFM probe-tip in which voltage oscillations are present at microwave frequencies [29-31].

Figure 3 (a) shows the experimental setup of the NFMM. The probe-tip is brought to a distance of 10 nm from the sample surface. Because tip-sample interactions take place over a distance of nanometers, much less than the microwave wavelength (~ 1 cm), these interactions occur in the near-field region. If the sample is translated under the tip, changes in tip-sample coupling can be used to obtain images of the sample with

submicron resolution. The resolution is governed by tip geometry rather than the diffraction limit. At its other end, the probe is inserted into a microwave resonance cavity, or "resonator", populated by standing microwaves. The resonator microwave fields drive the electronic oscillations in the probe and the microwaves are continually excited through an input wire line connected to an external source. We designed a NFMM with a tuning fork distance control system to keep a constant distance between the sample and the probe-tip [30].

The typical conical shape probe-tip is made of tungsten or stainless-steel wire with a diameter of 50 μm with tapered end-size of about 1 μm prepared by a chemical etching method (apex angle is 30°). The probe-tip was oriented perpendicular to the sample surface and the other end of the tip was directly connected to a coupling loop in the dielectric resonator. The resonance frequency of a given TE_{011} mode (4-4.5 GHz) was measured with a network analyzer (Agilent 8753ES). To drive the tuning fork, an AC voltage was applied to one contact on the tuning fork at its resonant frequency using the oscillator of a lock-in amplifier (Signal Recovery 7265). The output from the lock-in amplifier was fed into the feedback system to control the tip-sample distance (10 nm) using a piezo electric tube (PZT) that supports the sample stage. All NFMM measurements were done at the same sample-tip distance (constant-distance mode). The sample was mounted onto an x-y-z-translation stage for coarse adjustment which was driven by a computer-controlled microstepping motor with a resolution of 100 nm, whereas fine movement of the sample was controlled by a PZT tube with 10 nm resolution.

3.2 Tip-sample distance control in NFMM

One of the strengths of near-field microscopy is that measurements can be made without any physical contact between the probe-tip and the sample or the device being measured. However, the measurement requires that the separation between the probe-tip and the surface of the sample be small compared to the characteristic tip size and it has to be kept constant. The precision of any near-field measurement is directly related to the precision with which the tip-sample distance can be maintained. Although the absolute value of the mean height is not critical, the variance must be less than 1% of the tip size in order to obtain high precision measurements. For example, for a tip with a characteristic end-size of 0.1 μm , the tip-sample separation will have to be maintained at approximately 10 nm, with a precision of 1 nm. This precision can be obtained using a shear-force distance control systems [32-34].

The basic idea is that a probe-tip is flexible and can therefore be mounted onto a quartz tuning-fork oscillator with amplitude of a few nanometers. Figure 3 (b) shows an image of a 32 KHz resonant frequency quartz tuning-fork and the amplitude-frequency characteristic at various tip-sample distances. As the tip the metal wire is brought into close proximity of the sample surface, the amplitude and frequency of the tip oscillations are changed by interactions between the tip and the sample surface. The motion of the probe-tip is detected electrically and a feedback loop allows for precise distance control down to 10 nm. In addition, the height at which this control can be performed is a function of the amplitude of the oscillation. For smaller amplitude, a smaller control distance can be maintained as shown in the inset of Fig. 3 (b). It has been demonstrated that this type of force feedback can be effectively applied to probe structures making it applicable for use in NFMM. The general principle is that the tip-sample separation is modulated with fixed amplitude and frequency, and the modulated signal is used to control the separation.

3.3 Probe-tip for NFMM

Microwaves incident on the sample drive an effective field both inside and outside the sample. To obtain of this effective field, the probe-tip must have dimensions as small as the sample and must be located near the sample, where the effective field is strongly influenced by the sample [35]. In this case the probe-tip and sample form an interacting subsystem. As a result, the effective field of the sample produces microwaves scattered from the probe-tip which reach the network analyzer (NA). To extract the microwave near-field interaction during the reflection process, one needs to use a probe-tip (made from special material and with special geometrical shape) that is sensitive only to high-spatial frequency components relevant to the local effective field around the specimen. This is why the technique of fabricating fine probes is of primary importance. Figure 3 (c) shows three typical probe-tips and the corresponding 3D near-field images. The thin tip with apex angle 5° provides high spatial resolution but low sensitivity for differentiating the signal, while the thick tip with apex angle 30° provides low spatial resolution but high signal sensitivity. In the case of the hybrid tip with multi-angle apex the obtained images have both high spatial resolution and signal sensitivity. The tapered part of thin and thick tips has a simple conical shape and the cone angle θ is clearly defined. The

hybrid tip has a multiple tapered shape with three continuously increasing apex angles (5° , 10° , and 30°) which can be controlled by varying the etching condition. The end-size of the tip makes an important contribution for the determination of the spatial resolution and sensitivity of the microscope.

4. Experimental results and discussion

4.1 NFMM characterization of DNA array and SAMs

In bioassay applications, for DNA detection is often accomplished in an array format. For investigating this type of sample a prototype array is prepared consisting of an immobilized sequence of DNA, P2 (CGT TGT AAA ACG ACG GCC AG) [36]. Figure 4 shows NFMM images of the (a) as-prepared single-DNA array and (b) after dehybridization to sequences complementary to P2 (5' CGT TGT AAA ACG ACG GCC AG-(CH₂)₃-SH 3') spots (the image of the hybridized DNA not shown here). Sequence-specific hybridization is the dominant change identified. From the data, deactivation of a fraction of capture strands would be expected to decrease the change in S_{11} realizable in response to hybridization of immobilized sequence P2. Moreover, target molecules can absorb through sequence-nonspecific physical interactions, in this instance increasing the measured change.

These various contributions to S_{11} , representing important but difficult-to-track aspects of surface modification with DNA molecules and hybridization protocols, merit a more detailed study separate from the current focus on the near-field microwave imaging technique. Hybridization between target (free) and capture (immobilized) sequences leads to changes in the microwave reflection coefficient (S_{11}) which are measured by the NFMM. These changes are caused by hybridization-induced modification of the dielectric constant profile of the DNA film. Our NFMM system was reported capable of detecting coverages down to 1×10^9 fluorophores/cm² or about 300 zeptomoles (10^{-21}) in a 150 micrometer diameter microarray spot.

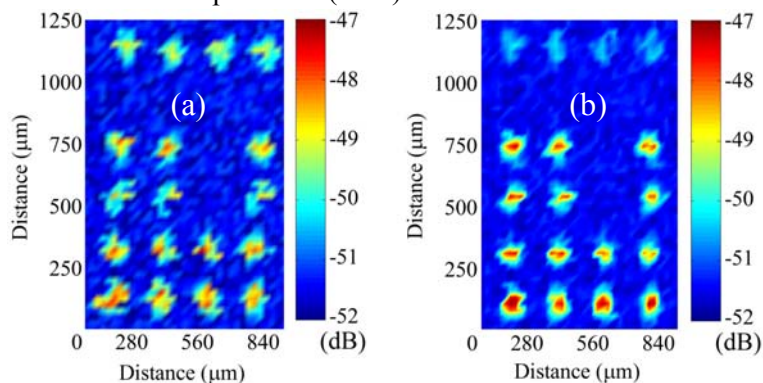


Figure 4. The NFMM images confirm layout of the immobilized P2 sequences: (a) the as-prepared single DNA array, (b) dehybridization to sequences complementary to P2.

The near-field microwave probing technique can achieve the noncontact detection of the thickness of self-assembled monolayers (SAMs) by measuring the microwave reflection coefficient S_{11} at an operating frequency near 5.3 GHz. The formation and structure of SAMs based on metal bonding have been well-characterized as a model system for understanding organic monolayer interfaces [37,38]. SAMs on a gold (Au) interface are of significant interest and have been widely investigated since the adsorption of di-*n*-alkyl disulfides on gold has been reported [39]. SAMs of *n*-alkanethiol have been investigated and characterized by various methods, which have revealed a densely packed, highly ordered and oriented monolayer structure on gold.

Figure 5 shows 2D microwave reflection coefficient S_{11} image of hexanethiol (C6) SAMs with the thickness of 0.72 nm. The microwave images showed clear contrast between the SAMs (upper level) and the Au substrate (lower level). The right inset of Fig. 5 shows a C6 SAMs microwave reflection coefficient S_{11} line scan and the topography of the SAMs sample pattern. The possibility of determining different thiol terminations is determined by physical properties differences in the microwave range.

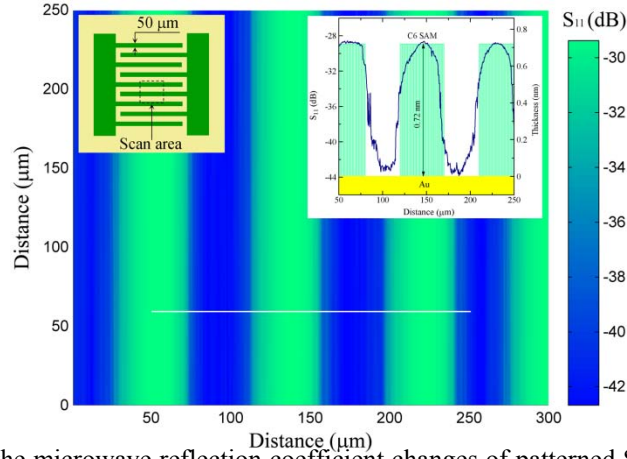


Figure 5. 2D NFMM image of the microwave reflection coefficient changes of patterned SAMs on Au substrates. The left inset shows SAMs pattern as a periodic structure with 50 μm stripe width. The right inset shows the cross sectional profile indicated by white line (left axis) and schematic topography (right axis) of C6 SAMs sample pattern with 0.72 nm thickness.

4.2 NFMM characterization of photosensitive heterojunction

Solar cells work using a semiconductor that has been doped to produce two different regions, an n -doped region and a p -doped region. Across this heterojunction, the two types of charge carrier, electrons and holes, are able to cross. In doing so, they deplete the region from which they came and transfer their charges to the new region. These migrations of charges result in a potential gradient or electrical slope, which charge carrier tend to slide down as they approach the junction. In particular, our solar cells consisted of five layers: the metallic back contact, the p -type semiconductor, the n -type semiconductor, the antireflection coating, and the transparent adhesive. How the reflection coefficient S_{11} depends on the photovoltaic conducting properties of solar cells can be derived by using standard transmission line theory [17].

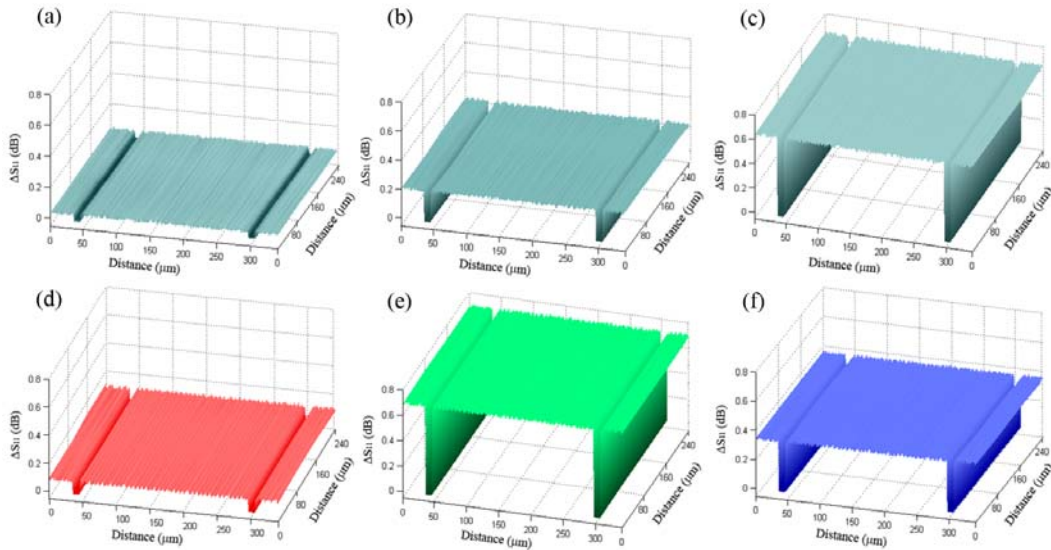


Figure 6. 3D NFMM images of microwave reflection coefficient changes of solar cells dependence on the incident light intensity and wavelength with the scan area of $340 \times 240 \mu\text{m}^2$ at 4.1 GHz. Here $\Delta S_{11} = S_{11}^i - S_{11}^0$, where S_{11}^0 is the reflection coefficient for dark condition and $i = 1,2,3$ indicates the incident white light intensities of (a) 122 mW/cm^2 , (b) 146 mW/cm^2 , and (c) 166 mW/cm^2 and the incident light wavelengths of (d) 625 nm (Red), (e) 526 nm (Green), and (f) 460 nm (Blue) with fixed intensity of 166 mW/cm^2 .

To visualize the photoconductivity of solar cells under external light sources, we directly imaged the reflection coefficient changes ΔS_{11} of solar cells at 4.1 GHz. Figure 6 shows the three-dimensional (3D) NFMM images of the microwave reflection coefficient changes $\Delta S_{11} = S_{11}^i - S_{11}^0$ of solar cells dependence on the incident light intensities and on the incident light wavelengths, where S_{11}^0 is the reflection coefficient for dark condition and $i = 1,2,3$ indicates the incident white light intensities of (a) 122 mW/cm^2 , (b) 146 mW/cm^2 , (c) 166 mW/cm^2 for intensity variation and (d) 625 nm (Red), (e) 526 nm (Green), (f) 460 nm

(Blue) with the light intensity of 166 mW/cm^2 for wavelength variation, respectively. The lower baseline of the 3D images is the minimum level of the Ag electrode. Note that the reflection coefficient changes originate from the changes of the photoconductivity of solar cells. The changes of reflection coefficient ΔS_{11} is significantly increased when the incident light intensity is bigger than 122 mW/cm^2 , which is the threshold electron injection. In addition, the changes of reflection coefficient ΔS_{11} shows the maximum at 526 nm incident light wavelength. The above NFMM image directly visualizes how the reflection coefficient changes ΔS_{11} of solar cells depend on the external light intensity and wavelength of the solar cells. So, the NFMM could directly image the photoconductivity changes inside the solar cells by measuring the change of reflection coefficient S_{11} from the cell.

4.2 NFMM characterization of magnetic domains

Here, we also report a NFMM system incorporating an AFM cantilever probe-tip at an operating frequency of $f = 4.4 \text{ GHz}$ [40]. We demonstrate improved sensitivity and spatial resolution better than 50 nm for the magnetic domain images of a 1.2 Gb magnetic HD platter under an external magnetic field. To demonstrate local microwave characterization of magnetic domains by NFMM we imaged domains and directly compared with images received by MFM. The dependence of the magnetic domains on the external magnetic field could be imaged by measuring the microwave reflection coefficient S_{11} and interpreted by transmission line theory [17]. When an external magnetic field is applied, the domains align such that all the domains reorient themselves in the direction of the external field. To visualize the magnetic domains of a hard disk under the external magnetic field, we directly imaged the microwave reflection coefficient S_{11} of the HD at 4.4 GHz.

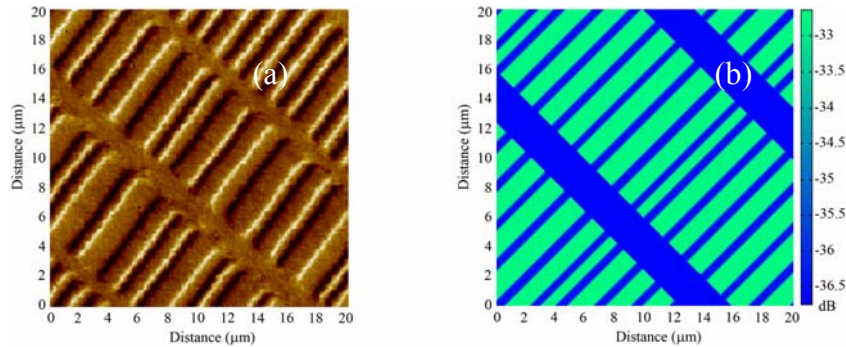


Figure 5.10. 2D (a) MFM and (b) NFMM images of the hard disk surface. Scanned surface area was $20 \mu\text{m} \times 20 \mu\text{m}$.

Figure 7 shows the two-dimensional (a) MFM, and (b) NFMM images of a hard disk surface with surface area of $20 \mu\text{m} \times 20 \mu\text{m}$ under 100 Oe external magnetic field applied parallel to the surface. Note that the reflection coefficient changes originate from the changes of the magnetic permeability of the CoCrPtTa magnetic layer due to its change under external magnetic field. The changes of reflection coefficient S_{11} is significantly increased until the external magnetic field intensity reach 50 Oe with further increase of magnetization up to 100 Oe. This nano-scale measurement of the magnetic domains has a great potential for investigating the magnetic profile with high sensitivity.

5. Conclusion

We have demonstrated the possibility of near-field microwave imaging of physical structures, such as thin films, bulk material, fluids, etc. by using a NFMM. We have developed theoretical models for the microwave reflection coefficient S_{11} and resonant frequency shift $\Delta f/f_0$ dependence on electromagnetic characteristics, in particular, electrical conductivity, dielectric permittivity, magnetic permeability to distinguish the spatial changes of these parameters in materials under various preparation and measurement conditions. The smallest detectable change in permittivity (dielectrics) is about 0.2 at $SNR = 30 \text{ dB}$, the smallest detectable change in conductivity (semiconductors and perfect metals) is about 0.01 S/m at $SNR = 60 \text{ dB}$, the smallest detectable change in permeability (Permalloy) is about 10 at $SNR = 40 \text{ dB}$, and the smallest detectable change in thickness (SAMs) is 2 nm at $SNR = 50 \text{ dB}$. These results clearly show the sensitivity and usefulness of NFMM for these material and device applications.

Acknowledgements

This work was supported by Sogang University Special Research Grant (2009), Seoul Research and Business Development Program (10816), Korea Research Foundation Grant (KRF-2008-615-C00001), and National Research Foundation of Korea Grant (2009-0073557, 2009-0093822, and 2010-0012037).

References

- [1] B. Michel, W. Mizutani, R. Schierle, A. Jarosch, W. Knop, H. Benedickter, W. Bachtold, H. Rohrer, *Rev. Sci. Instrum.* **63** (1992) 4080.
- [2] D. W. van der Weide, *Appl. Phys. Lett.* **70** (1997) 677.
- [3] B. Knoll, F. Keilmann, A. Kramer, R. Guckenberger, *Appl. Phys. Lett.* **70** (1997) 2667.
- [4] C. Gao, X.-D. Xiang, *Rev. Sci. Instrum.* **69** (1998) 3846.
- [5] D. E. Steinhauer, C. P. Vlahacos, S. K. Dutta, F. C. Wellstood, Steven M. Anlage, *Appl. Phys. Lett.* **71** (1998) 1736.
- [6] M. Tabib-Azar, P. S. Pathak, G. Ponchak, S. LeClair, *Rev. Sci. Instrum.* **70** (1999) 2783.
- [7] M. E. Rodriguez, A. Mandelis, G. Pan, J. A. Garcia, *J. Appl. Phys.* **87** (2000) 8113.
- [8] M. Kunst, F. Wunsch, D. Jokisch, *Mat. Sci. Engin.* **B102** (2003) 173.
- [9] M. Tabib-Azar, N. S. Shoemaker, S. Harris, *Meas. Sci. Technol.* **4** (1993) 583.
- [10] M. S. Kim, S. Kim, J. Kim, K. Lee, B. Friedman, J. Kim, J. Lee, *Rev. Sci. Instrum.* **74**, 3675 (2003).
- [11] M. Golosovsky, D. Davidov, *Appl. Phys. Lett.* **68** (1996) 1579.
- [12] S. V. Kalinin, A. Gruverman (Eds) *Scanning Probe Microscopy: Electrical and Electromechanical Phenomena at the Nanoscale* (Springer-Verlag, New York, 2006).
- [13] D. E. Steinhauer, C. P. Vlahacos, F. C. Wellstood, Steven M. Anlage, C. Canedy, R. Ramesh, A. Stanishevsky, J. Melngailis, *Rev. Sci. Instrum.* **72** (2001) 2073.
- [14] C. Gao, B. Hu, I. Takeuchi, K. S. Chang, X.-D. Xiang, G. Wang, *Meas. Sci. Technol.* **16** (2005) 248.
- [15] M. Abu-Teir, M. Golosovsky, D. Davidov, A. Frenkel, H. Goldberger, *Rev. Sci. Instrum.* **72** (2001) 2073.
- [16] B. Friedman, M. A. Gaspar, S. Kalachikov, K. Lee, R. Levicky, G. Shen, H. Yoo, *J. Am. Chem. Soc.* **127** (2005) 9666.
- [17] D. Pozar, *Microwave Engineering* (Addison-Wesley, New York, 1990).
- [18] E. H. Synge, *Phil. Mag.* **13** (1932) 297.
- [19] F. Buchy, B. Lemaire, *Phys. Lett.* **A26** (1968) 170.
- [20] M. Tabib-Azar, S. Neil, Shoemaker, S. Harris, *Meas. Sci. Technol.* **4** (1993) 583.
- [21] M. Golosovsky, D. Davidov, *Appl. Phys. Lett.* **68** (1996) 1579.
- [22] X. -D. Xiang, C. Gao, *Mat. Character.* **48** (2002) 117.
- [23] Atif Imtiaz, Steven M. Anlage, John D. Barry, John Melngailis, *App. Phys. Lett.* **90** (2007) 143106.
- [24] V. V. Talanov, Andre Scherz, Robert L. Moreland, Andrew R. Schwartz, *Appl. Phys. Lett.* **88** (2006) 134106.
- [25] David J. Griffiths, *Introduction to Electrodynamics*, 3th ed. (Prentice, New York, 1999).
- [26] E. Silva, M. Lanucara, R. Marcon, *Supercond, Sci. Technol.* **9** (1996) 934.
- [27] Jongchul Kim, Arsen Babajanyan, Artur Hovsepyan, Kiejin Lee, Barry Friedman, *Rev. Sci. Instrum.* **79** (2008) 089107.
- [28] Tigran Sargsyan, Artur Hovsepyan, Harutyun Melikyan, Youngwoon Yoon, Huneung Lee, Arsen Babajanyan, Mijung Kim, Deokjoon Cha, Kiejin Lee, *Ultramicroscopy* **108** (2008) 1062.
- [29] S. Kim, H. You, K. Lee, B. Friedman, M. Gaspar, R. Levicky, *Appl. Phys. Lett.* **86** (2005) 153506.
- [30] A. Babajanyan, J. Kim, S. Kim, K. Lee, B. Friedman, *Appl. Phys. Lett.* **89** (2006) 183504.
- [31] A. Babajanyan, K. Lee, E. Lim, T. Manaka, M. Iwamoto, B. Friedman, *Appl. Phys. Lett.* **90** (2007) 182104.
- [32] D. A. Lapshin, E. E. Kobylkin, V. S. Letokhov, *Ultramicroscopy* **83** (2000) 17.
- [33] Daniel Haefliger, Marc Muenchinger, Georg Schitter, Andreas Stemmer, *Sens. Actuators* **A103** (2003) 353.
- [34] G. Y. Shang, W. H. Qiao, F. H. Leia, J. -F. Angiboust, M. Troyon, M. Manfait, *Ultramicroscopy* **105** (2005) 324.
- [35] M. Ohtsu (Ed.), *Near-Field Nano/Ato Optics and Technology* (Springer-Verlag, Tokyo, 1998).
- [36] Barry Friedman, Mariafrancis A. Gaspar, Sergey Kalachikov, Kiejin Lee, Rastislav Levicky, Gang Shen, Hyunjun Yoo, *J. Am. Chem. Soc.* **127** (2005) 9666.

- [37] M. Tominaga, Sh. Maetsu, A. Kubo, I. Taniguchi, *J. Electroanal. Chem.* **603** (2007) 203.
- [38] A. Widge, M. Jeffries-El, X. Cui, C. Lagenaur, Y. Matsuoka, *Biosens. Bioelectron.* **22** (2007) 1723.
- [39] P. Laibinis, C. Bain, R. Nuzzoand, G. Whitesides, *J. Phys. Chem.* **99** (1995) 7663.
- [40] H. Melikyan, T. Sargsyan, A. Babajanyan, S. Kim, J. Kim, K. Lee, B. Friedman, *J. Magn. Magn. Mater.* **321** (2009) 2483.

Light-Weight Short-Range Ku-Band CW-LFM Radar

A.Hakhoumian, R.M.Martirosyan, S.Martirosyan, A.Muzhikyan, V.Nikoghosyan,
N.Poghosyan, T.Poghosyan, K.Rustamyan, and T.Zakaryan

*Institute of Radiophysics and Electronics, Armenian National Ac.Sci.
Alikhanian 1, Ashtarak, 0203, Armenia*

Short-range CW-LFM radar design is discussed. Hybrid mode operation consisting of pure CW and CW-LFM periods is implemented. Such algorithm allows sufficiently simplify the processing and reduce the false alarm probability.

Introduction

Portable short-range detection devices arouse a growing interest for many civil and military applications such as collision avoidance systems (ACAR) or target detection in shielding systems [1]. Recently this field of application is exclusively devoted to FMCW radars, which allow detection and direct measurement of range and radial velocity very like to pulsed radars, but are less expensive, more portable [2]. Moreover, they have less power consumption and have no blind-zone. Complexity of small-sized radars consists in coexistence of inconsistent requirements. For example, application of combined receiver/transmitter antenna on the one hand leads to desirable reduction of overall system sizes, but on the other hand excludes the possibility of use of relatively high transmitter power to increase the target detection range due to unacceptably rising power leakage. Such inconsistent requirements dictate the necessity of subsystems' careful design to optimally combine their advantages.

Overall design

The simplified block diagram (excluding filters) of the developed radar is shown on Fig.1 and represents the receiver-transmitter with two-step frequency conversion. Such design owes to a number of reasons. First, in radar, intended for measurement of small Doppler frequencies, it is necessary to reduce phase noise of the transmitter as much as possible. Application of direct modulation on carrier frequency or repeated frequency multiplication from lower frequencies, leads to inadmissible level of phase noise. On the other hand, it is known that at frequency upconversion, phase noise is defined by the greatest phase noise. We use Lucix LO-149-XB 15GHz phase locked DRO with internal reference with -96dBc/Hz phase noise level @ 1kHz, and Minicircuits ZX95-1000C VCO with -96dBc/Hz phase noise level @ 1kHz. Second, such design facilitates also simultaneous achievement of high gain and linearity, as the necessary gain is distributed between amplifiers at different frequencies. Total gain of all receiver RF amplifiers (12dB) and the antenna (27dB) partially compensates propagation losses and provides required target detection range. Video amplifier should achieve the missing part. Due to the limited isolation of circulator and non-ideal matched antenna, there is a large parasitic leakage on mixer's input, and further conversion feeds it to filters passband (this represents the main limiting factor of all single-antenna systems). To improve transmitter-receiver isolation, some kind of reflected power canceller should be used. We use one operating at baseband (video) frequencies. Canceller signal is formed from the triangle-modulating signal and is applied to differential input of video amplifier. As a result the leakage originated video component is effectively suppressed in the output signal. However, canceller signal waveform may vary due to variation of reflected signal phase. Thus the use of adaptive canceller with feedback loop will allow to reduce the dependence of reflected signal's phase variations.

Slotted Waveguide Antenna Array

Principal requirements of short-range and low-power radar antenna are high performance in gain, efficiency, flat profile and fixed beam. These criteria limit our choice to flat profile antennas only. The most commonly used ones with good gain property are microstrip patch and slotted waveguide array systems. The advantages of microstrip patch antennas are light weight, low profile, high gain, but low antenna efficiency due to dielectric losses, make them unacceptable for low-power radar system. Meanwhile slotted waveguide arrays

find wide application in radar systems due to their high performance, gain, efficiency, and flat profile. These properties make it good candidates for short-range radar application.

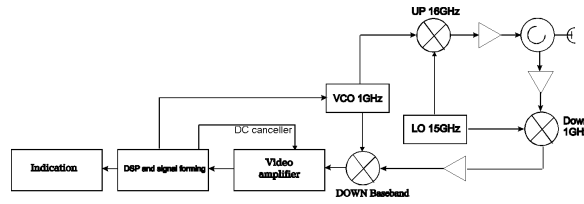


Fig.1 Hybrid-Mode CW-LFM Radar simplified block-diagram

The design of slotted waveguide array begins with determining the aperture distribution, and hence the slot excitation, required to achieve the beam width, gain, and sidelobe level needed at the central frequency. Antenna consists of set of linear radiating arrays. In this design longitudinal slots are arranged in the broad wall of the waveguides. The choice of waveguide has two criteria. First, we need to keep inter-element spacing less than a free-space wavelength to prevent the appearance of grating lobes. Second are mechanical restrictions. The array pattern is controlled by number of elements and their excitation amplitudes. Each element pattern is considered as dipole pattern by Booker postulate [4]. To permit fixed beam criteria the central feeding of radiating waveguides and resonant slotted waveguide was used. The slots excitation amplitudes are controlled only by offsetting the elements from the centerline of the waveguide without rotation of slots.

Slotted waveguide array antenna have been developed by using FEM simulation techniques, but to save memory and CPU time over the full wave simulation in large arrays, aperture distribution are calculated by using existing well known formulas for slot amplitudes (admittance) [5] to obtain the first order design which does not include the mutual coupling effects at all. To achieve the beam width, gain, and side lobe level requirements, the antenna should have 8 radiating waveguides with 24 linear slots on each waveguide. Designed feeding network for radiating waveguides represents the waveguide 1x8 power divider, which consists of H-plane 3dB waveguide in-phase dividers. Radiation patterns of the antenna in H- and E-planes are presented on Figs.2 and 3. Here firm lines represent simulation results, while the dashed lines correspond to measured ones.

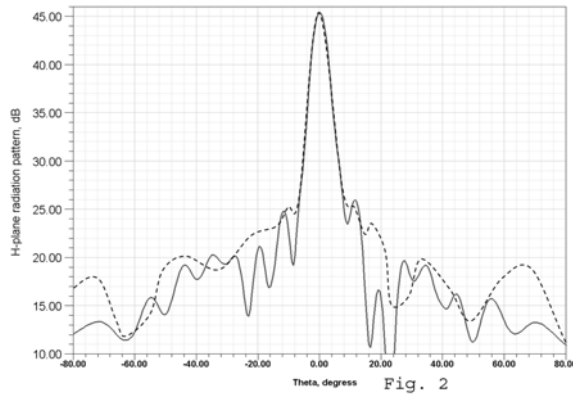


Fig. 2

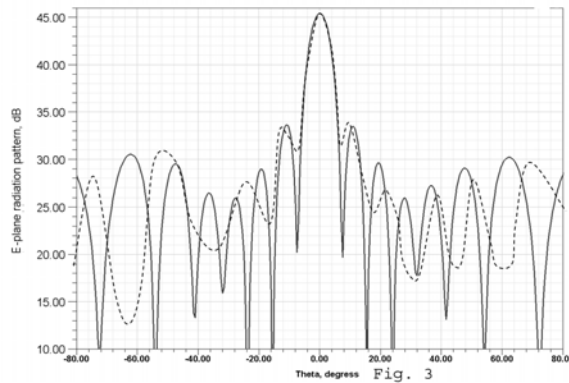


Fig. 3

Spatial Azimuthal Scanning

The most suitable surveillance scanning is realized using step motor. Special microcontroller (MC) controls the motion. All low-level operations are implemented in step motor firmware, and only high-level commands are sent to MC from central processor to set the scanning sector central direction and span. Angular feedback is sent back to MC. Moreover, radar signal measurements are made during periodic resting conditions of motor and then the motor induced noise is significantly reduced.

Signal Processing, Target Detection and Localization

Digital signal processing unit represents the main unit, which allows to achieve the whole potential of radar system. TMS320C2000 based DSP unit simultaneously forms the transmitter modulating waveform of transmitted signal and measures the received signal. As it is well known, the pure CW radar provides only moving targets detection and can say nothing concerning the target localization. Using CW-LFM radar provides somewhat “coloring” of transmitted signal and allows directly measure the target’s range. Presence of multiple targets makes the problem more complex.

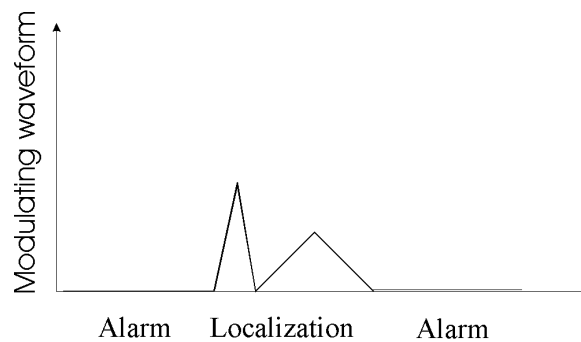


Fig. 4 Hybrid Modulating waveform

Likely, the method of transformable periods LFM (TPS-LFM) [6,7] solves this problem and is able to identify as many targets as needed. Main purpose of short-distance radars is to alarm about presence of moving targets and then localize them if needed. The most time the system operates in a spatial scanning mode as Doppler monochromatic radar. In this mode modulating voltage of the shaper does not change. When moving targets are detected, very simple and elegant algorithm is triggered to identify and localize multiple moving targets [6]. Such combination of pure CW and CW-LFM algorithms allows reduction of false alarm probability. Fig.4 shows basic stages of hybrid alarm/localization algorithm. Transformable periods of LFM are used against false detection of unnecessary targets. Information on presence and velocities of moving targets in alarming mode is considered as primary one, and then is used for acceleration of algorithm to exclude false unnecessary targets, which consumes a lot of CPU time rising as square of number of targets. Using the best available 1024-point FFT allows to obtain frequency resolution of 60 Hz.

Dynamic Range Consideration

Inconsistent requirements to the radar first of all dictate necessity of maintenance of a sufficient dynamic range (100dB), which is a big problem first of all because of rather weak isolation between the transmitter and the receiver. One way to overcome this problem is to use several amplifiers with various gain and pass-bands, which correspond to various kinds of targets’ ranges and velocities. We use the bank of electronically switching video amplifiers with discrete gain from 60 to 80 dB, which provides optimal overall processing gain for given environment under observation.

As final remark and conclusion, the parameters of presented radar are as follows

- Detection range – up to 5 km
- Velocity range – 3 to 90 km/h
- Azimuthal resolution – 4 deg.
- Simultaneously tracking targets – up to 7

References

1. F.Bekkadal - Novel Radar Technology and Applications. 17th International Conference on Applied Electromagnetics and Communications (ICECom-2003), 1-3 October, 2003. Dubrovnik. Croatia, pp.6-12
2. A.G.Stove - Linear FMCW Radar Techniques. IEE Proceedings-F, vol.139, no.5, October 1992, pp.343-350
3. T.Wu, X.H.Tang, and F. Xiao - Research on the Coherent Phase Noise of Millimeter-Wave Doppler Radar. Progress in Electromagnetics Research Letters, vol. 5, pp.23-34, 2008
4. H.G.Booker - Slot Aerials and their Relation to Complementary Wire Aerials, J. IEE, 1946, pp.620-626
5. A.A.Oliner - The Impedance Properties of Narrow Radiating Slots in the Broad Face of Rectangular Waveguide, Parts I and II, IRE Trans. Antennas Propagat., vol.AP-5 (1957). pp.4-20
6. W.Wang, J.Cai, Y.Yang - A Novel Method to Identify Multi-target by Transformable Periods LFM Waveform - Proceedings of International Conference on Communications, Circuits and Systems, 2005. vol. 2, 27-30 May, 2005, pp.744-747
7. W.Wang - An Approach for Multiple Moving Targets Detection and Velocity Estimation, Proc. of IEEE Conf. on Radar, 24-27 April, 2006, pp.749-753
8. A. Muzhikyan, A. Hakhoumian, S. Martirosyan, V. Nikoghosyan, N. Poghosyan, T. Poghosyan, K.Rustamyan, T. Zakaryan, "Short-range Ku-band hybrid-mode CW-LFM radar," Radar Symposium (IRS), 2010 11th International, Lithuania, 16-18 June 2010, pp. 1-3.

L-Band Doppler Radar for Heartbeat Sensing

A.Hakhoumian, H.Hayrapetyan, S.Martirosyan, A.Muzhikyan, N.Poghosyan, and T.Zakaryan

*Institute of Radiophysics and Electronics, Armenian National Ac .Sci.
Alikhanian 1, Ashtarak, 0203, Armenia*

Doppler radar with simple design is presented which allows to detect human heart beating and respiration. Block diagram and preliminary examples are presented.

Introduction

Microwave Doppler radar has been used for wireless sensing applications for many years. Beginning from 1970s, microwave Doppler radar found new applications in human healthcare monitoring and detection. It offers new opportunities, such as physiological movement and volume change sensing [1], human vital signal detection for finding trapped people under earthquake rubble [2]. First works were done with heavy and bulky waveguides, but recent advances in microwave and radar technologies made it possible to integrate such a system on a single chip [3,4], which is compact, light-weight and low-cost. With inexpensive and compact design, microwave Doppler radar could be used in home healthcare monitoring, particularly for detecting sleep apnea [5,6].

Microwave Doppler radar was first used for sensing of respiration rate and the detection of apnea in 1975 [1]. Since 1980s, similar systems were developed for finding victims trapped in earthquake rubble and an avalanche [7] and sensing human presence behind a wall or other barriers [8]. All these systems were designed using bulky and heavy microwave components and large antennas, which are acceptable for using in diagnostic institutions, but are impractical for home healthcare monitoring. Alternatives to this for heart and respiration home monitoring are polar straps [9], chest expansion measuring straps [10] for respiration monitoring, acoustic monitors, nasal and oral sensors. All these methods require contact with body and careful placement. Compact Doppler radar may provide portable and more flexible noncontact alternative.

Doppler-type motion-sensing radar systems typically transmit continuous-wave (CW) signal (sometimes frequency-modulated), which is reflected off the target and received by the receiver. According to Doppler theory, a moving target will cause frequency shift in transmitted signal, which can be detected by detector. A stationary person has chest movement, and, therefore, Doppler radar with chest as target will receive transmitted signal with Doppler shift caused by movement of the chest, which contains information about heartbeat and respiration. By using existing wireless and radar technologies, it would be possible to design inexpensive and portable device performing such monitoring.

In this paper we propose single antenna microwave Doppler radar with simple design to investigate human heartbeat and respiration.

Overall Design

The block-diagram is presented in Fig.1. The system operates on 1GHz signal generated by Mini-Circuits ZX95-1000C LO. The signal is amplified and feed to antenna through circulator. We use applicator-type antenna filled in with dielectric liquid with permeability equal to water to maintain the matching with propagation area (human body). Received signal has Doppler shift caused by the heartbeat. Received signal is down-converted to baseband and amplified by video amplifier to satisfy the ADC dynamic range requirements. As a digitizer we use NI USB6009 connected to PC.

Due to single antenna system we have to deal with transmitted signal leakage in circulator (decoupling around -20dB), which leads to DC component at the input of video amplifier (gain 40dB) causing its saturation. To overcome this problem we use NI USB6009 DAC channel to suppress DC component manually.

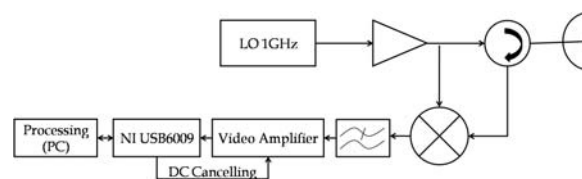


Fig. 1. The block-diagram of medical radar

Using this design we obtain profiles of human heart beating in time and frequency domains, which can be processed. An example is presented in Fig. 2.

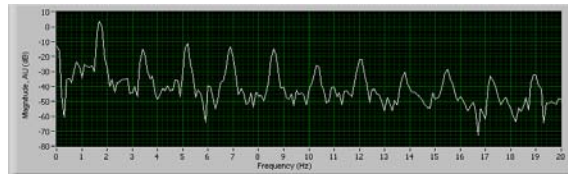


Fig. 2. Example of obtained measurement of heart beating

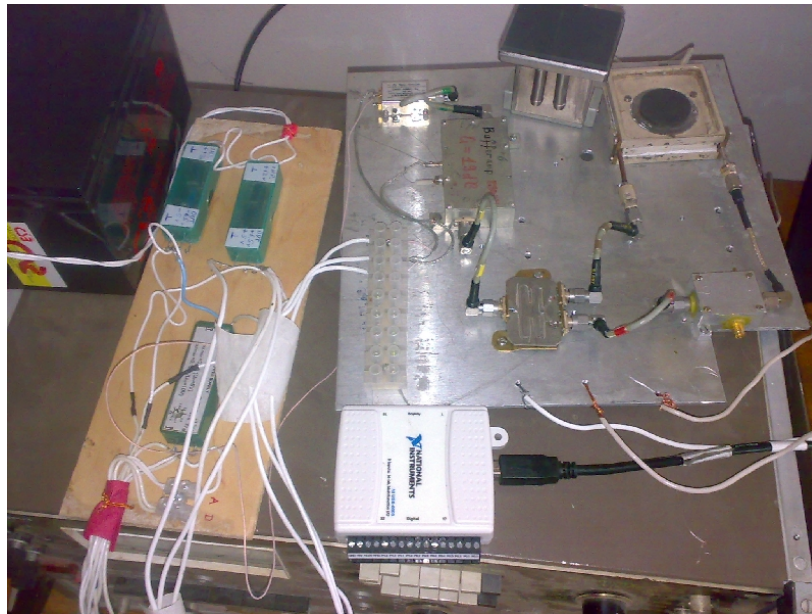


Fig. 3 Experimental Setup

Noise consideration

The sensitivity of a microwave direct conversion Doppler radar for vital sign detection depends significantly not only on the strength the respiration and cardiac signals but also the effect of noise at both RF and baseband frequencies. Since received signals are small, they are very sensitive to the noise. Therefore, it is important to understand the sources of noise in the system. There are three main sources of noise in radar system affecting detection of physiological signals: thermal noise, phase noise, and Flicker noise. These three noise sources are taken into account separately at RF frequency and then combined at baseband after a mixer.

DC component adaptive cancellation

Application of combined receiver/transmitter antenna on the one hand leads to desirable reduction of overall system sizes, but on the other hand excludes the possibility of use of relatively high transmitter power to increase the target detection range due to unacceptably rising power leakage in circulator, which leads to DC component at the input of video amplifier causing its saturation. To improve transmitter-receiver isolation, some kind of reflected power canceller should be used. We will use one operating at baseband (video) frequencies. For LFM operating mode canceller signal is formed from the triangle-modulating signal and is applied to differential input of video amplifier. As a result the leakage originated video component is effectively suppressed in the output signal. However, canceller signal waveform may vary due to variation of reflected signal phase. Thus the use of adaptive canceller with feedback loop will allow to reduce the dependence of reflected signal's phase variations.

Conclusion and Further Development

Such simple design can be used to detect and analyze human vital signals. As a first step it implies further improvements. Further development will focus on some main aspects such as obtained measurements analysis, identification and interpretation, and noise level consideration [5]. For the next generation we plan to switch to quadrature design, which will allow to struggle against possible fading.

References

- [1] J. C. Lin, "Microwave sensing of physiological movement and volume change: A review," *Bioelectromagnetics*, vol. 13, pp. 557-565, 1992.
- [2] K. M. Chen, Y. Huang, J. Zhang, and A. Norman, "Microwave life-detection systems for searching human subjects under earthquake rubble and behind barrier," *IEEE Trans. Biomedical Engineering*, vol. 27, pp. 105-114, Jan. 2000.
- [3] A. D. Droitcour, O. Boric-Lubecke, V. Lubecke, J. Lin, and G. T. A. Kovacs, "0.25 μ m CMOS and BiCMOS single-chip direct-conversion Doppler radars for remote sensing of vital signs," in *Int. Solid-State Circuits Conf. Dig.*, vol. 1, San Francisco, CA, 2002, p. 348.
- [4] A. D. Droitcour, O. Boric-Lubecke, V. Lubecke, J. Lin, and G. T. A. Kovacs, "Range correlation effect on ISM band I=QCMOS radar for noncontact sensing of vital signs," in *IEEE MTT-S Int. Microwave Symp. Dig.*, vol. 3, Philadelphia, PA, 2003, pp. 1945-1948.
- [5] "Infantile apnea and home monitoring," NIH, Bethesda, MD, Consensus Statement, vol. 6, Sept. 1986.
- [6] R. Ferber *et al.*, "Portable recording in the assessment of obstructive sleep apnea," *Sleep*, vol. 17, pp. 378-392, June 1994.
- [7] K. M. Chen, Y. Huang, J. Shang, and A. Norman, "Microwave life-detection systems for searching human subjects under earthquake rubble or behind barrier," *IEEE Trans. Biomed. Eng.*, vol. 27, pp. 105-114, Jan. 2000.
- [8] J. Seals, S. R. Crowgey, and S. M. Sharpe, "Electromagnetic vital signs monitor," Georgia Tech. Res. Inst., Atlanta, GA, Final Rep. Project A-3529-060, 1986.
- [9] R. M. T. Laukkanen and P. K. Virtanen, "Heart rate monitors: State of the art," *J. Sports Sci.*, vol. 16, pp. S3-S7, Summer 1998.
- [10] K. Leino, S. Nunes, P. Valta, and J. Takala, "Validation of a new respiratory inductance pletysmograph," *Acta Anaesthesiologica Scandinavica*, vol. 45, no. 1, pp. 104-111, Jan. 2001.
- [11] A. Muzhikyan, A. Hakhoumian, S. Martirosyan, V. Nikoghosyan, N. Poghosyan, T. Poghosyan, K. Rustamyan, T. Zakaryan, "Short-range Ku-band hybrid-mode CW-LFM radar," Radar Symposium (IRS), 2010 11th International, Lithuania, 16-18 June 2010, pp. 1-3.

On the Method of Distant Infrared Monitoring of Forest Spaces

R.S. Asatryan¹, H.S. Karayan², N.R. Khachatryan¹, L.H. Sukoyan¹

¹Radiophysics Researches Institute, Komitas ave. 49/4, 0051, Yerevan, Armenia

²Yervan State Universit, 1 A. Manoogian str., 0025, Yerevan, Armenia

The development results of a new method of aerial (on a helicopter or airplane) infrared (IR) scanning of extensive forest spaces with the purpose of detecting weak heat sources (fire centers at an early stage of their development) to prevent the occurrence of large-scale fires are presented. In the paper there is presented the description of the IR radiometer as well as the measurement method of point and extended thermal sources wavelength range of 2.5 to 5.5 microns.

1. Introduction

The environment monitoring, investigation and control of ecological conditions attract a great attention of the mankind, especially at the present stage of development of industry, energetics and urban building. Optoelectronic systems and devices designed for application in ecological studies and in arising extremal situations are always in the center of the scientists' and engineers' attention. In particular, research complexes for early detection of fire hearthes arising during natural calamities are irreplaceable.

Therefore, the development and creation of infrared devices and systems of thermal monitoring of environment, in particular, large forest spaces is a rather important problem.

The development of modern distant and effective methods of ecological monitoring of large forest spaces is more than actual. In such a situation the only method is remote monitoring from an aircraft (e.g., from a helicopter) while flying over large forests at the altitude up to 1000 m.

2. Brief Technical Description of a Measuring System

Structurally the measuring complex consists of two basic units: an optico-mechanical unit of the IR radiometer and an electronic control unit joined to a personal computer. It is designed to measure spectral radiance and radiation temperature (or its drops) of point and extended sources of infrared radiation under laboratory and field conditions [1-3]. To automate data acquisition and processing the spectroradiometer is joined to a computer of Pentium type via a series port RS 232. Optical scheme of the optico-mechanical unit (OMU) is shown in Fig.1.

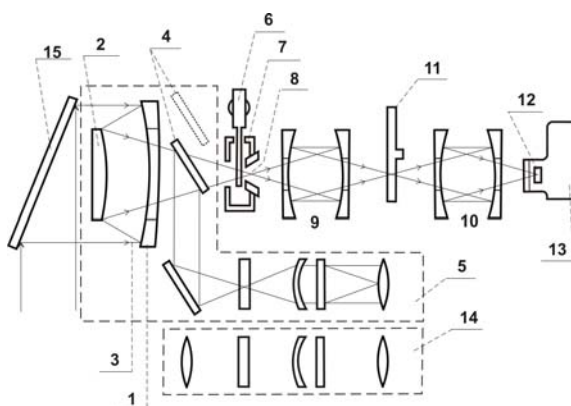


Fig. 1. Optical scheme of OMU

1-Primary mirror of the objective; 2-secondary mirror of the objective; 3-radiation from an object; 4-removable plane mirror; 5-a sight; 6-a modulator; 7-a reference cavity; 8-a field diaphragm; 9,10-projection objective; 11-a disk with interferential light filters; 12-a sensing site of the photodetector; 13-a thermos for liquid nitrogen; 14-a telescope; 15-a deflectin mirror.

- Input mirror objective of Cassegrain type;
- A telescope for operative pointing to an object under test, equipped with a sighting grid visible through an eyepiece on the OMU back panel;
- Parallax free sight for accurate pointing the spectroradiometer to an area to be measured. The sight has a sighting grid with a cross and a circle which defines visual field boundaries of the device;

- Projection objectives which serve for refocusing the radiation from a field diaphragm to the plane with light filters and to a sensing site of the photodetector. They represent pairs of spherical mirrors the application of which enables to avoid achromatic aberrations;
- A block of removable ring wedge variable light filters which provide a total working spectral range of 0.4 to 14 μm;
- A photodetector which structurally represents a removable block with a photodetector placed inside it in accordance with the spectral range, a preamplifier, and an adjusting.

Full working spectral range of the device is covered with the help of three sets of removable light filters and photodetectors in the subbands of 0.4 to 1.1 μm, 2.5 to 5.5 μm, and 8 to 14 μm. Main technical parameters of the device are given in the Table.

№	Parameter Name	Value
1.	Input objective diameter	180 mm
2.	Focal distance mechanism.	200 mm
3.	Distances to be focused	from 5m to ∞
4.	Working spectral range I subband (spectral resolution of 10 %) II subband (spectral resolution of 3 %) III subband (spectral resolution of 8 %)	from 0,4 to 14 μm from 0,4 to 1,1 μm from 2,5 to 5,5 μm from 7,9 to 13,5 μm
5.	Photodetectors: I subband II subband III subband	Si – photodiode InSb – photoresist CdHgTe – photoresist
6.	Field of vision	3 mrad
7.	Noise equivalent difference of the radiation temperatures (at 295° K)	0,05 K
8.	Continuous work time	8 hours
9.	Time of preparation to work	15 min
10.	Dimensional size of spectroradiometer: OMU ECU	415x278x254 mm 500x420x210 mm
11.	Weight: OMU ECU	not more than 12 kg not more than 15 kg
12.	Climatic conditions of operation: Ambient temperature Atmospheric pressure Air relative humidity	from -35° to +45° from 84 to 107 kPa (from 630 to 800 mm Hg) up to 98% at 35°C
13.	Supply voltage Frequency	(220 ± 22) V (50 ± 1) Hz
14.	Power consumed	not more than 200W

During operation the OMU, by means of the wedge guide, is placed on a rotary mechanism which is fastened to the horizontal platform of a specially prepared tripod.

The electronic control unit (ECU) is structurally of on-top variant. All indication and control elements are mounted on the front panel of the ECU.

Under laboratory conditions the ECU is placed on the table, and under field conditions it can be mounted in a helicopter with the help of dampers.

In brief, the operation principle of the spectroradiometer consists in the following: Inside the OMU the radiation flow from the object under test is collected by means of an optical system (see Fig.1) and focused onto a sensing site of the photodetector. Further, a preamplifier amplifies an electric signal and transmits it to the ECU. In the ECU the electronic schemes amplify, demodulate and filter the signal from the photodetector output, and as a result of this there appears a signal at the output the amplitude of which is a measure of the radiation temperature of the object. Knowing the value of the collected radiation power (through the data of preliminarily conducted energetic calibration of the device), spectral filter features of the system and

amplification degree, the output signal can be exactly transformed into an absolute measurement of radiation temperatures of the objects under test.

Let's notice some advantages of the IR radiometer developed by us [4] compared to the existing close analogs. To widen functional capabilities in the sphere of spectral investigations of thermal objects, besides wideband interferential light filters for spectrum parts of 0.4 to 1.1, 2.5 to 5.5, and 8 to 14 μm , the device is also provided with ring readjustable light filters. To eliminate chromatic aberrations the device optical scheme includes two pairs (see Fig.1) of mirror projection objectives in the focuses of which there are placed light filters and the receiving site of photodetectors.

The IR radiometer is mounted in the helicopter and, with the help of a deflecting plane mirror, by its field of vision scans (through the bottom hatch, along the helicopter motion ruoting) terrestriil surface of large forests, see Fig.2.



Fig. 2. Helicopter IR scanning of large forests

In the presence of fire hearthes the radiation temperature in this region (within the wavelength range of 2.5 to 5.5 μm) considerably increases that is registered by the electronic control unit.

At the helicopter flight altitudes of 200, 500 and 700 m the radiometer covers, with its field of vision, surface areas of about 120, 750 and 1500 sq.m, correspondingly. With the helicopter speed of 150-200 km/hr the time of one measurement cycle is 0.1 sec.

3. Measurement Technique of IR Flows From Extended and Point Thermal Sources

Before carrying out quantitative measurements of IR radiation emitted by an unknown source, it is necessary to fulfill energetic calibration of the spectroradiometer, the aim of which is the measurement of the device response to the known standard source (usually a black body with known temperature). By definition, the device calibration means obtaining an electrical signal at the output, which corresponds to a radiation flow unit incident into the radiometer inlet. The calibration is expressed by some function $k(\lambda)$ called spectral calibration characteristic of the device, which includes combi unit, ned effect of optical elements and electronic amplification of the whole system. An output signal of the device is proportional to the difference between the IR radiation flows coming to the photodetector from an external source and from the internal modulated reference black body. In calibrating the radiation from the calibration black body (with known temperature) entirely fills the device field of vision. An output signal $S(\lambda)$ is expressed by the following ratio:

$$S(\lambda) = k(\lambda) \cdot \{r(\lambda, T) \cdot \tau(\lambda, l) - r(\lambda, T_0) + r(\lambda, T_B) [1 - \tau(\lambda, l)]\}, \quad (1)$$

where $r(\lambda, T)$ is Plunk function at the temperature T and the wavelength λ ; T —temperature of the calibration black body; $\tau(\lambda, l)$ —atmospheric transparency over the path l between the calibration source and device; T_0 —temperature of the internal reference black body; T_B —temperature of the air during the experiment.

In the windows of the atmosphere transparency (e.g. for the wavelength range of 2.5 to 5.5 μm), where the transmission is high, $\tau(\lambda, l)$ may be taken as 1, if the calibration is carried out from the distance “ l ” equal to several meters. Therefore in this approximation for $S(\lambda)$ we can write:

$$S(\lambda) = k(\lambda) \cdot [r(\lambda, T) - r(\lambda, T_0)] \quad (2)$$

with the amplification coefficient equal to 1. And in measuring with the amplification coefficient different from 1 the $S(\lambda)$ value decreases by the same factor. The Plunk function value is calculated according to the ratio:

$$r(\lambda, T) = \frac{c_1}{\lambda^5} [\exp(c_2 / \lambda T) - 1]^{-1},$$

where $c_1 = 3,74 \cdot 10^4 \text{ W } \mu\text{m}^4/\text{cm}^2$, $c_2 = 1,438 \cdot 10^4 \text{ } \mu\text{m deg}$.

The objects studied the radiation flow of which completely fills the device field of vision are extent in these measurements. In this case radiance spectral density ($W(\lambda, T) \text{ W/cm}^2 \text{ } \mu\text{m}$) of the object is measured. The ratio (1) may be rewrite as:

$$S(\lambda) = k(\lambda) \{W(\lambda, T) \cdot \tau(\lambda, l) - r(\lambda, T_0) + r(\lambda, T_B) [1 - \tau(\lambda, l)]\} \cdot \beta \quad (3)$$

where $W(\lambda, T)$ is the radiance spectral density of the object studied, β is an amplification coefficient of the whole system, and the rest symbols remain previous. The atmosphere transparency $\tau(\lambda, l)$ is either measured simultaneously, or calculated with the help of data from literature [5,6]. From the ratio (3) we can get for $W(\lambda, T)$:

$$W(\lambda, T) = \frac{S(\lambda) / k(\lambda) \beta + r(\lambda, T_0) - r(\lambda, T_B) \cdot [1 - \tau(\lambda, l)]}{r(\lambda, l)} \quad (4)$$

Usually the radiation of point sources does not fill the visual field of the device. If the area A of a radiating object is known we can measure its spectral radiance according to the above-stated technique, that is

$$W_p(\lambda, T) = W(\lambda, T) \cdot \omega \cdot \frac{l^2}{A} \quad (5)$$

Where ω is a solid angle of the spectroradiometer visual field, $W(\lambda, T)$ is a total spectral radiance measured according to (4); l is the distance from the object under test to the spectroradiometer. While measuring point sources spectral contrast of a radiation source is also of interest, when the background radiance is comparable to the object radiation. In this case it is necessary to separate the background signal $S_\Phi(\lambda)$ from the signal “source+background” $S(\lambda)$. For the spectral radiation contrast of the source we can get the ratio:

$$W(\lambda) = \frac{\Delta S(\lambda) \cdot \omega \cdot l^2}{\beta \cdot k(\lambda) \cdot \tau(\lambda, l) A} \quad (6)$$

Where $\Delta S(\lambda) = S(\lambda) - S_\Phi(\lambda)$. If A is unknown we may define the contrast of the spectral luminous intensity of the source (in $\text{W/strad.}\mu\text{m}$):

$$I(\lambda) = W(\lambda) \cdot A = \frac{\Delta S(\lambda)}{\beta \cdot k(\lambda) \cdot \tau(\lambda, l)} \cdot \omega \cdot l^2 \quad (7)$$

Calculation of the radiation temperatures of the objects under test is carried out in accordance with specially developed algorithms and programs.

4. Conclusion

Application of the given method of remote ecological monitoring of vast forest spaces will undoubtedly bring to the considerable technical-economical effectiveness and will also have a great importance in the problem of preventing the fire occurrences, especially of large-scale ones.

References

- [1] R.S. Asatryan, Optoelectronic Methods and Means of Intesting Physico-Ecological Parameters of Atmosphere and Thermal Objects, News of NAS RA, Techn. Sciences, Vol. LX, No. 2, (2007) 307.
- [2] R.S. Asatryan, S.R. Asatryan, et al., Infrared Scanning Complex for Preventing Large-Scale Fires, Ecological

Systems and Devices, No. 1, (2008) 17.

- [3] R.S. Asatryan et al. Universal Infrared Spectral Radiometer. Intern. Journal of IR and MM Waves, vol. 24, No. 6. (2003), 1035.
- [4] R.S. Asatryan, H. G. Gevorgyan et al. The Spectroradiometer, Patent of RA, No.1678A2, Appl. No. P20050042, (11.04.2005).
- [5] P. Kruz, L. Macgloulin, P. Maccvistan, Bases of Infrared Technique, M. Voenizdat, (1964) 464.
- [6] A.V. Pavlov, Optoelectronic Devices, M. Energia, (1974), 360p.

Радиофизический комплекс обнаружения и оповещения

Мартirosян Р. М., Абрамян А. А., Гулян А. Г., Симонян Р.Г., Пирумян Г. А., Смолин А.И.

Приведено описание автоматизированной охранной системы предназначенной для защиты территориально распределенных объектов. Указаны преимущества и перспективность применения подобных систем для решения специальных задач охраны, где требуются скрытность установки, оперативность изменения контролируемого рубежа и быстроразвертываемость. Оповещение о нарушениях передается на централизованный пункт наблюдения (до 30км), а также на носимый приемник группы оперативного реагирования (до 3км) по одному из 640-а цифровых препрограммированных радиоканалов.

1. Назначение изделия.

Комплекс предназначен для создания автоматизированной системы охраны контролируемых участков местности территориально-распределенных объектов от несанкционированно проникновения людей (групп лиц) так и от автотранспортных средств.

Обнаружение нарушения (вторжений) осуществляется посредством применения средств обнаружения (сенсоров) построенных на различных физических принципах (магнитные, сейсмические, обрывные), которые расположены на путях возможных маршрутов следования нарушителей. Информация о нарушении немедленно передается по каналу УКВ радиосвязи на централизованный пункт наблюдения, а так же на носимый радиоприемник, которым снабжается группа оперативного реагирования.

2. Состав комплекса.

Упрощенная схема комплекса с указанием примерных расстояний по дальности действия элементов системы приведена на рисунке 1.

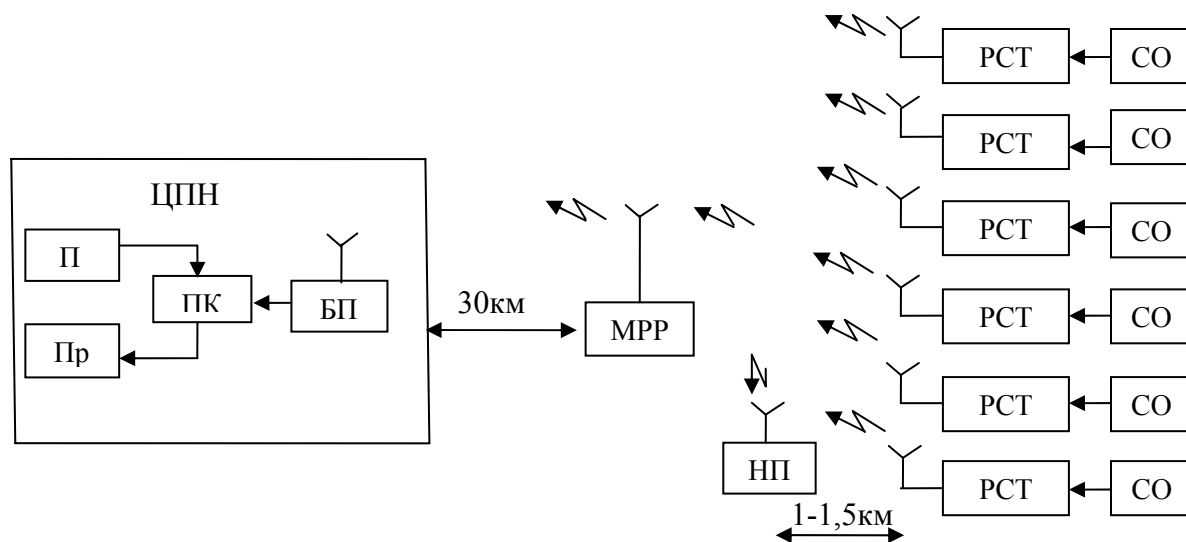


Рис.1 Схема дислокации комплекса

Комплекс состоит из набора нескольких типовых элементов:

- малогабаритный радиопередатчик сигналов тревоги (РСТ) в комбинации с одним из средств обнаружения (СО) сейсмическим, магнитным или обрывным;
- носимый приемник (НП) для приема и отображения сигналов тревоги;
- центральный пункт наблюдения (ЦПН) на основе персонального компьютера со встроенным радиоприемным устройством и специальным программным обеспечением;
- многоканальный радиоретранслятор (МРР) для увеличения дальности связи.

3. Краткое описание элементов и устройств входящих в комплекс.

3.1 Сейсмический датчик (Рис.2).

НАЗНАЧЕНИЕ. Регистрация малых колебаниях грунта и соответствующее извещение.



Рис.2.

ТЕХНИЧЕСКИЕ ДАННЫЕ

Дальность обнаружения:

- пешеход до 30 м
- легкой техники до 100 м
- тяжелой техники до 200 м

Спектр колебаний 0.1 – 10 Гц

Коэффициент усиления до 60 дБ

Ток покоя 50 мкА

Напряжение питания 7.5 – 10 VDC

Вес 230г.

3.2 Магнитометрический датчик (Рис.3).

НАЗНАЧЕНИЕ. Регистрация возмущений магнитного поля Земли, вызванного присутствием металлического предмета.



Рис.3.

ТЕХНИЧЕСКИЕ ДАННЫЕ

Дальность обнаружения: до 50 м

Мощность, потребляемая в ждущем режиме 2 мВт

Амплитуда выходного сигнала 5 VDC

Длительность выходного сигнала 5 сек

Размеры 25x55x85мм³

Вес 120 г

3.3 Датчик обрыва провода (Рис.4).

НАЗНАЧЕНИЕ. Фиксация нарушения границы охраняемого рубежа обрывом микропровода.

ТЕХНИЧЕСКИЕ ДАННЫЕ

Длина обрывного провода до 100м

Диаметр обрывного провода 0,05мм

Ток покоя	20 мкА
Напряжение питания	7.5 – 10 VDC
Габариты	53x53x36 мм ³
Вес	150 г.



Рис.4.

3.4 Радиоизвещатель сигнала тревоги (Рис.5).

РСТ совместно с любым из датчиков СО выполняют задачу обнаружения факта вторжения с передачей сигнала тревоги по радиоканалу на носимый приемник, ЦПН или ретранслятор. При размещении на местности устройство устанавливается скрытно в грунт на глубину до 10см за исключением передающей антенны, представляющей собой четвертьволновый штырь из сталистого провода диаметром 1мм, что обеспечивает практически полную визуальную маскируемость передатчика (Рис.5).

В целях увеличения дальности связи с высокой помехозащищенностью, ипри передаче пакета используется сверточное кодирование (Convolution Coding) с одним из видов Манчестерского кодирования. Для проверки целостности пакета данных использован алгоритм CRC 32. При передаче сигналов тревоги в целях исключения потерь связи в условиях сильных естественных или умышленных радиопомех предусмотрен режим многократной передачи сообщений через программно задаваемый интервал времени и последующей обработке принимаемого сигнала путем мажорирования.

НАЗНАЧЕНИЕ. Обнаружение факта вторжения с передачей сигнала тревоги по радиоканалу



Рис.5.

ТЕХНИЧЕСКИЕ ДАННЫЕ

Длительность передачи сигнала	0,2сек.
Частотный диапазон	138-154МГц
Передаваемая мощность (регулируемая)	до 3-х Вт
Количество радиоканалов	640
Питание	4x700мА/ч
Габариты	114x90x82мм
Вес	500 г

3.5. Носимый приемник (Рис.6).

НАЗНАЧЕНИЕ. Прием, извещение, декодирование, и отображение каждого из 640 радиоканалов, сохранение в архиве последних 10-и извещений.



Рис.6

ТЕХНИЧЕСКИЕ ДАННЫЕ

Диапазон рабочих температур	от -20 ⁰ до + 55 ⁰ С
Питание	сменная батарея 2x700мА/ч
Габариты	150x74 ммx40мм ³
Вес	490г

Носимый приемник (НП) служит для приема и отображения сигналов тревоги от средств обнаружения и предназначен для обеспечения работы в полевых условиях. Он также может быть применен при монтаже и пусконаладке устройств комплекса. В рабочем режиме, НП декодирует и выдает на дисплей извещение от любого СО расположенного на рубеже охраны (в пределах допустимой дальности радиосвязи).

3.6. Многоканальный радиоретранслятор (Рис.7).

НАЗНАЧЕНИЕ. Прием и ретрансляция радиосигналов из зоны расположения РСТ.

ТЕХНИЧЕСКИЕ ДАННЫЕ

Чувствительность канала приема	-120dBm:
Уровень излучение	до 5Вт
Программируемые каналы	640
Частотный диапазон	138–154МГц
Питание	U=12В, 10А/ч
Габариты и вес	320x220x150мм ³ , 16кг
Рабочая температура	-30 +55 ⁰ С



Рис.7

МРР служит для приема и ретрансляции радиосигналов из зоны расположения РСТ до пунктов приема, в качестве которых могут быть ЦПН, другой МРР или НП. МРР относится к классу автономных устройств и может быть длительное время не обслуживаться если есть условия для своевременной автоматической подзарядки встроенной батареи от электросети, солнечной батареи или другого источника питания.

3.7. Центральный пункт наблюдения (ЦПН)

ЦПН является стационарной частью комплекса, и фактически представляет собой автоматизированное рабочее место (АРМ) оператора работающее непрерывно в круглосуточном режиме и обеспечивающее прием и обработку поступивших по радиоканалу извещений о нарушениях, а также контрольных сообщений о состоянии связи. Основу АРМ оператора составляет персональный компьютер (ПК) со встроенным в его процессорный блок радиоприемным

устройством и специальным программным обеспечением (ПО). ПО в реальном масштабе времени производит полное декодирование принятых сообщений, архивацию и отображение на экране монитора ПК, в том числе с использованием электронной карты местности (графическим планом).

На рис.8, рис.9 приведены снимки с экрана монитора с изображениями электронной карты местности, где квадратиками отражены установленные СО привязанные к координатам карты, а также пример страницы архивированной информации. Поступление принятого сообщения о тревоги сопровождается звуком и световым сигналами.

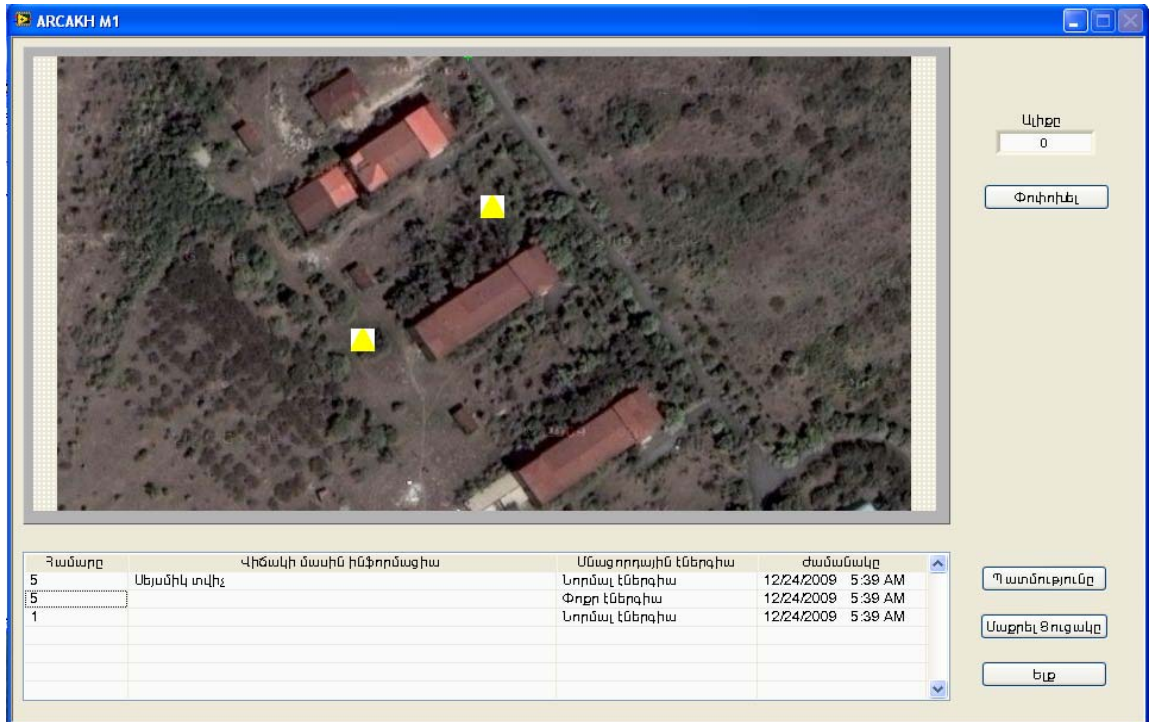


Рис.8



Рис.9

4. Заключение

Комплекс относится к классу сравнительно новых и стремительно развивающихся так называемым быстроразворачиваемых систем имеющих автономное питание и осуществляющим передачу сигнала по радиоканалу.

Особенно перспективно применение таких систем для защиты рубежей в условиях горной местности, где сильная изрезанность рельефа и наличие скальных пород может практически исключать возможность монтажа стационарной системы и прокладки протяженных кабельных линий связи и электропитания.

Отметим основные отличия быстроразвертываемых систем, как класса, от традиционных систем охраны периметров:

- малое время установки элементов системы на местности;
- возможность быстрого изменения конфигурации элементов комплекса в зависимости от изменения обстановки;
- возможность установки на неподготовленных в инженерном отношении местности;
- возможность применения системы как самостоятельно, так и совместно с традиционными стационарными системами охраны.

Scientific and Technical Investigations of Industrial Electron Accelerators

A. Poursaleh, A. Hakhoumian

Institute of Radiophysics and Electronics, Alikhanian Brothers str.1,378410

In this paper Industrial electron accelerators including electrostatic accelerators, RF linear accelerators, and also RF single cavity accelerator systems are introduced. By classification of these industrial accelerators their parameters such as energy and power are determined. Electron accelerators with different commercial names ELV and ILU type accelerators, dynamitron, industrial microwave linac and rhodotron and also different model are investigated. By these descriptions and comparison of these parameters such as energy, power and efficiency, it is easy to select suitable accelerator for specific purpose in industrial application such as food irradiation , sterilization of medical devices and other material, corsslinking of wire and cable, heat shrinkable products, tire component, environment, material treatment, and other industrial application considering total cost.

1. Introduction:

The industrial electron accelerators developed for industrial irradiation propes such as food preservation, medical disposals sterilization , polymer cross-linking (tapes, tubes, cables), industrial material treatment, tire component curing, wast water treatment, etc.. [1] The most important parameter of accelerators are energy and power of accelerator that energy is proportional depth of penetration of electron beam and definition by "eV" and power of accelerator is proportional of speed of irradiation and definition by "KW". according the IAEA prescription the maximum energy of industrial accelerator is 10 MeV. there are two type of industrial accelerator the fist type is electrostatic or DC and the second is time varying or RF accelerator. Dc accelerators such as Van de Graff accelerator - cockcroft walton accelerator-dynamitron use electrostatic field by DC high voltage [2] .the rf accelerator can accelerated electrons from low energy to very high much energy does not like dc accelerator which has the dc voltage break. In a rf accelerator electrons are accelerated by the action of radiofrequency electromagnetic waves the mostly of RF electron accelerators are linear accelerator with multi cavity that called linac and some are single cavity accelerator. rf accelerator can work at a pulsed mode and cw mode [3,4]. There are many different types of accelerators offering a wide range of performance ratings, only few would be suitable for industrial application that in this paper presented.

2. DC accelerator

2.1 ELV type accelerator

In case of DC accelerators machines are based on transformer type modified cockcroft walton to produce high dc voltage and acceleration tube in which electron from a small heated cathode are accelerated. The ELV d.c. accelerators has cascade generator with a parallel inductive coupling as the high voltage source and employ a coreless step transformer with sectionalized secondary coil. General view of the ELV type and ELV8 accelerator is given in Figure 1. Inside the tank filled with the SF6 gas are located: primary winding, high voltage rectifier with a built in accelerating tube. There are several module of ELV accelerators such as ELV4, ELV6, ELV8, ELV12, These ELV accelerators are available in the energy range 0.2 to 2.5 MeV with the beam currents up to 200mA and maximum power of up to 400 KW [5].

2.2 Dynamitron accelerator

The dynamitron use a similar diode column but the alternating potential is applied in parallel to each diode from a cylindrical capacitively coupled electrode such DC accelerators are filled with insulating SF6 gas under pressure and large dimension vessels separate the anode and cathode. figure 2 show the structure of dynamitron accelerator and view of 3 MeV dynamitron accelerator made by IHEP. The basic dc circuit used in the dynamitron insures smooth and reliable operation at high voltage .the rate of energy in dynamitron models available in the 550KeV to 5 MeV. the maxium power up to 250KW . [2],[4]

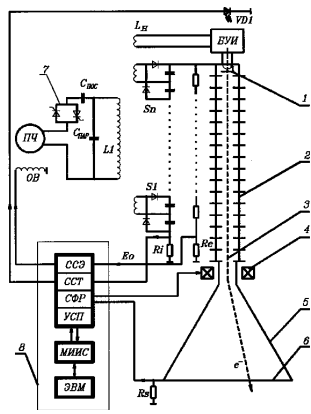


Fig. 1: The ELV accelerator

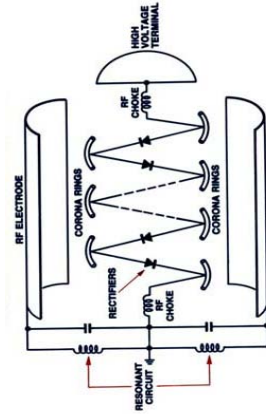
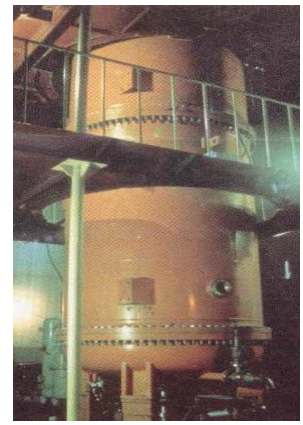


Fig. 2: The dynamitron accelerator



3. RF linear accelerators

In a rf linear accelerator that called linac electrons can be resonantly accelerated along a linear orbit by rf electrical field .the rf accelerating field is either a traveling wave in loaded waveguides or a standing wave in loaded cavities. The frequency of waves In most electron linear accelerators is around 3 GHz. and usually of length of a metre or more with corrugations on its inside. These corrugations, or iris diaphragms, cause the waves to travel at a velocity determined by the iris and waveguide dimensions. so some where called microwave linac. High energy linacs deliver powers up to 50 kW are available. There are two structure for rf linear accelerator such as standing wave and traveling wave but There are many commercial name for rf linac. Figure 3 show the linac use a traveling wave method and disk loaded structure.

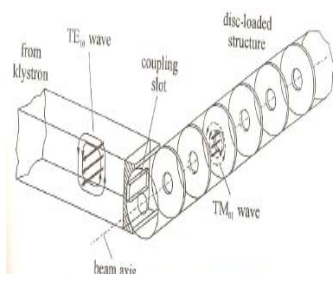


Fig. 3. Industrial rf linear accelerator

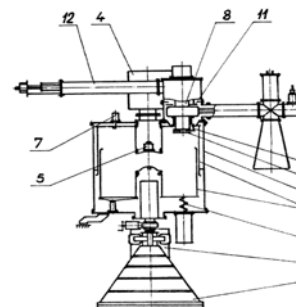


Fig. 4. General view of ILU6 accelerator



The main component of the RF system is the microwave source. There is a variety of microwave tubes for generating and amplifying microwave signals. The two most common used in linacs are magnetrons and klystrons. Rf linear electron accelerator contain some part such as: electron gun, rf system, acceleration tube, vacuum system, cooling system, magnet system , beam line contain scanning magnet and horn .figure 3 show the one kind of rf industrial linac [3,4,6-8].

4-RF single cavity accelerator

4.1 The ILU type accelerator

The ILU accelerator type are based rf pulse accelerator and produced in the Institute electron beam cover the energy range from 0.7 MeV to 4.0 MeV and the maximum beam power is 50 KW .There are several modle of ILU accelerator such as ILU6,ILU8,ILU10. Figure 4 shows the ILU6 modle of this kind of accelerator. The ILU accelerating system consists of copper toroidal resonator. The resonator consists of top and bottom halves on the internal protrusions of which the electrodes forming an accelerating gap are installed. the specific frequency of ILU6 is 115.435MHz and pulse repetition frequency up to 50 HZ with 2.5 MeV and 20KW beam power. The ILU12 of a new design it will be efficient maching having 5 MeV energy and average beam power up to 300 KW [9,10].

4.2 Rhodotron accelerator

The rhodotron is a new kind of high power and high energy rf single cavity electron accelerator based on the principle of recirculating a cw beam through a single coaxial cavity resonating in metric waves. The beam passes several times along different diameters in the middle of cavity. Each time the electron crosses the cavity their energy increases by 1 MeV after each pass, the beam is bent by a magnet and then sent back to the accelerating cavity the trajectories having a rosette shape so ten passes and nine magnets are therefore required to obtain a 10 MeV. Figure 5 shows the rhodotron.

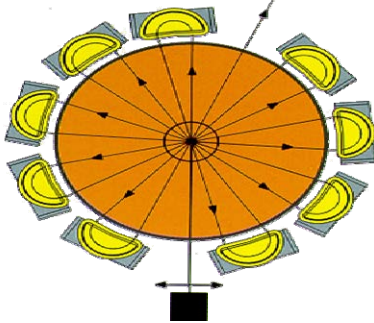


Fig. 5. Rhodotron structure



Fig. 6. TT200 rhodotron accelerator

The rhodotron consists of the following major components: an electron gun, the cavity, the deflection magnets, a RF system, a cooling system, a vacuum system and the beam delivery system. Five industrial rhodotron models such as TT100, TT200, TT300, TT400, TT1000 ranging from 35 kW to 700 kW beam power at 10 MeV are manufactured at IBA company in Belgium. The resonating frequency on cavity is 215 MHz for TT100 and 107.5 MHz for other models. Figure 7 shows the rhodotron TT200. The RF system consists of a voltage controlled oscillator followed by a chain of amplifiers. High power amplification uses tetrode or diacode vacuum tubes [11,12].

5. Comparison of rhodotron with other industrial accelerator

The rhodotron electrical efficiency is more than 36%. The rhodotron operates in a cw mode but linac operation is in pulse mode. The rhodotron uses a tetrode tube instead of a klystron. The tetrode may have a useful life span up to 4 times that of a klystron installed in a similarly rated linac unit. The rhodotron's ability to scan at a higher frequency generates a more uniform distribution of dose over the width of the beam scan. In the rhodotron, the energy spectrum is tight. In many linac designs, there is a tail in the energy spectrum. The rhodotron has a designed energy spread tolerance of less than 100 keV at 10 MeV; the rhodotron does not use the SF₆ gas for insulation or venting, unlike many dc electron accelerators. SF₆ is heavier than air and is hazardous [11,13].

6. Conclusion

The most important requirements to be considered before industrial accelerator selection are: electron energy, average beam power, beam current, electrical efficiency, application, narrow energy spread, self-shielding area and total cost. The main parameters of industrial accelerators are presented in table 1. Electrostatic type were efficient but limited in voltage due to electrical breakdown. DC accelerators give high average beam power whereas the RF accelerators generally operated in the pulsed mode give low average power. On the other hand, RF accelerators have high energy gain per unit length [14]. The electron energy necessity for some industrial applications is presented in table 2. Figure 7 shows the comparison of two important parameters of some suitable industrial electron accelerators. In this curve, the rhodotron is the high energy and highest power industrial accelerator. The investment cost is high for any electron accelerator facility because of the accelerators' price and costs of the building for biological shielding. There is also auxiliary equipment needed like conveyor under beam, cooling and ventilation systems, control and monitoring and safety system.

Table1:parameter of industrial accelerator

parameter	dc	Rf single cavity	Rf linear
electron energy	0.05-5MeV	0.3-10 MeV	2-10MeV
avrage beam current	<1.5A	<100mA	<100mA
average beam power	400KW	700KW	50KW
electrical efficiency	60-80%	20-50%	10-20%
frequency	-	100-200MHz	1.3-9GHz

Table2:electron beam energy market end

Market segment	Typical energy
surface curing	80-300 kev
shrink film	300-800 kev
wire&cable	1.5 MeV
Tube	1.5-2 MeV
Waste water tretmant	300-2.5 MeV
Sterilization	10 MeV

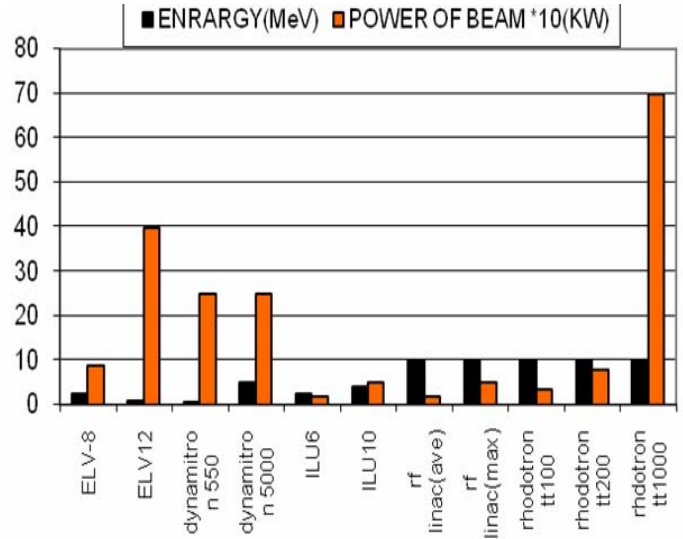


Fig7:comparison of energy and power of industrial accelerators

Usually low energy accelerators maybe offer the lowest cost. but with low electrons energy decrease penetration level and loss of flexibility .However economic evaluation should include accelerator and operating cost of industrial radiation facility.

References

- [1] M.R Cleland. "industrial applications of electron accelerators" Ion beaapplication,edgewood.ny11717,usa
- [2] e.cttereau, "dc accerators" tandetron cnrs/cea,france
- [3]thomas p.wangler , "rf linear accelerator"
- [4] Humphries, "Principles of Charged particle acceleration", wiley & sons, new york
- [5] India-thpma118-2007"electron accelerator of ELV-type and their world wide application",
- [6] M.f vorogush,y.u gavrish,M.I demsky,o.l maslennnikor,v.m.nikolaev,A.M.Fialkovsky, "linear electron accelerator for vadiation processing current status"
- [7]M.F vorgogushin npkluts,"linear accelerator for radiationsterilization".nifea Russia,1997
- [8] shu-hong wang "rf electron linac",IHEP,china
- [9]V.Lauslender,A.bryazgin,V.G.cheskidog,I.v.gomakor,B.L.faktorovich,V.e.nekhaev,"industrial electron accelerators type ILU"proceeding of particle accelerator conference ,konxville.2005
- [10] v.l auslender,v.a gorbunov,v.enekhacv"high frequency powerful electron accelerators type ilu for industrial applications" russian academy of sciences
- [11] Y.jongen "manufacturing of electron accelerators" IBA,Belgium,2001
- [12] J.pottier , "a new type of RF electron accelerator:the rhodotron".phys.res.vol b40,943
- [13] y.jonges,m.abs,t.delvigne, "rhodotron accelerators for industrial electron beam processing" iba
- [14] a.j.berejkaHuntington, "advances inself-shilded accelerators" new York,usa-IAEA- tecdoc-1386

The New Design of RF System for High-Power Industrial Electron Accelerators

A. Poursaleh¹, A. Hakhoumian¹, B. Abbasi²

¹ *Institute of Radiophysics and Electronics, Alikhanian Brothers str.1,378410*

² *University of Tarbiat Modares, Faculty of Electrical Engineering, Tehran, Iran*

The conceptual design a low cost solid state amplifier optimized for rf industrial electron accelerators presented in this paper. We design 200 KW solid state rf amplifier instead of a rf vacuum tube in high power industrial electron accelerator such as rhodotron accelerator. The base of design for rf power amplifier is 107.5 MHz, 1 KW solid state modules .each modules including the MRF6V11KH LDMOS and impedance matching and circulator and also water cooling .the new design of rf system for rf industrial electron accelerator including LLRF and control system and high power rf amplifier consist more than two hundred 1 KW cw modules combined to produce a cw total output power of 200 KW.

1. Introduction

High power rf amplifiers have been built for many years using rf vacuum tube similar tetrode, klystron, ion diode, twt because the solid state technology has been for low power amplifier. the recently mosfet technology allows using the solid state in rf high power [1]One of the application of high power rf system use in the accelerators machine for example the synchrotron accelerator of soleil used the high power solid state amplifier for first time in the research accelerators.[2].industrial electron accelerator use for industrial purposes such as medical sterilization, food preservation, industrial materials treatment, polymerization, etc [3] we design the solid state high power amplifier for high power and high energy industrial electron accelerators instead of vacuum tube considering advantages of solid state amplifier.

2. The RF system by high power vacuum tube

There is several model of RF electron accelerator for industrial application one of them is rhodotron. The rhodotron is a new recirculating high power and high energy industrial electron accelerator. This accelerator have been manufactured by iba company. The TT200 model of this accelerator with the maximum beam power 100 KW at 10 MeV .the cavity based on coaxial line shorted at both ends and resonating in the $\lambda/2$ mode at 107.5 MHz. The electron beam accelerate several times along different diameters of the cavity. Outside the cavity the beam is deflected by magnets. So the deflected magnets send back into the cavity after each crossing in order for them to undergo another acceleration cycle another role of magnets is fine tune the phase between the beam and the accelerating field .figure1 show the rhodotron structure. The rf system of the rhodotron has been designed to deliver about 200KW. around 80 KW are needed to build the electric field into the cavity allowing an energy gain of 1 MeV by each crossing .the remaining 120 KW is available to accelerate the electrons. The RF system comprises an RF Low Level rack containing the oscillator and a 1W low level amplifier, a solid state 100 W predriver amplifier, a tetrode 10 KW driver amplifier, , and a tetrode 200 KW amplifier. The low level RF oscillator is a VCO oscillator. It is continually adjusted to the RF cavity resonance frequency by the phase discriminator that continuously measuring the phase difference between the voltage read by the input pickup in the cathode-grid tube cavity and the voltage read by the output pickup in the screen-anode tube cavity of the final RF amplifier during Rhodotron startup. The final RF power is set to a low safe levels by the modulator, and the voltage regulation board switches the input of the integrator to the constant voltage generator (case shown in Figure 2, part a). The integrator will then supply sweeping voltage to the reference input of the VCO. While the RF rack is in sweeping mode, the voltage regulation board measures the RF voltage inside the RF cavity. If at some time the changing oscillator frequency matches the resonance frequency of the RF cavity, the voltage regulation board will detect an increase of the RF voltage in the RF cavity and will connect the input of the integrator to the output of the phase discriminator via the up/down detector. The RF voltage regulation system adjusts continuously the RF voltage amplitude inside the RF cavity to match a preset value .that is the optimum for the acceleration of the electrons.

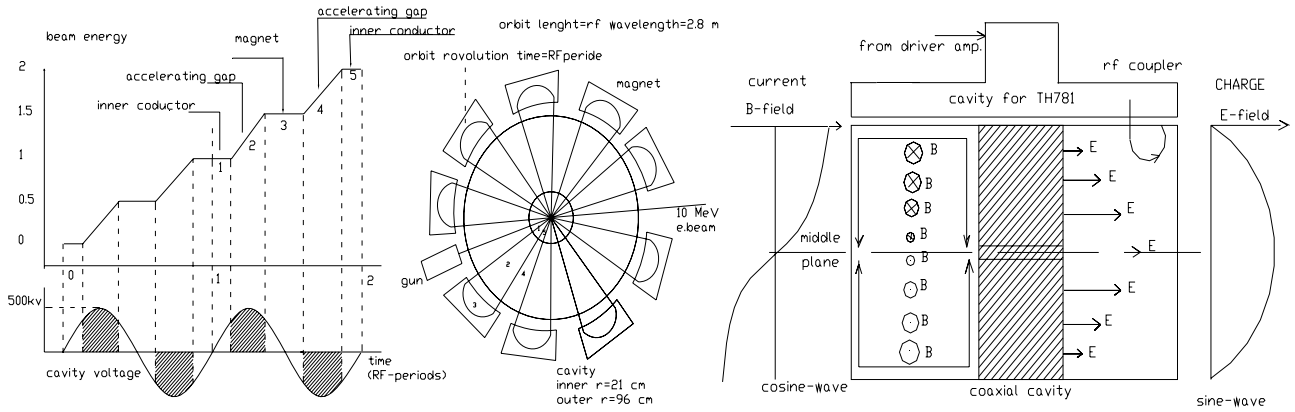


Figure 1: The rhodotron accelerator structure.

The last part of the RF low level rack is a 1 W low level amplifier that receives the RF coming from the modulator, amplifies it and feeds it to the input of the 100 W predriver amplifier. The 100 W predriver amplifier is an air-cooled solid state amplifier shown in part (b) of figure 2. Its input is the output of the RF low level rack, and its output goes to the input of the 10 KW driver amplifier. The 10KW driver amplifier is a standard commercially available air-cooled broadcast amplifier using a grid-driven tetrode TH341 shown in figure 2. The RF final amplifier is designed so that all the RF field it generates is contained within cavities. The final amplification using TH781 tetrode tube is shown in part (c) of figure 2 that is located above the accelerating cavity partially inside the inner conductor. This configuration makes it possible to directly connect the anode cavity and the accelerating cavity with a short $\frac{1}{4}$ resonant inductive loop for production of 200KW cw rf power [4-6].

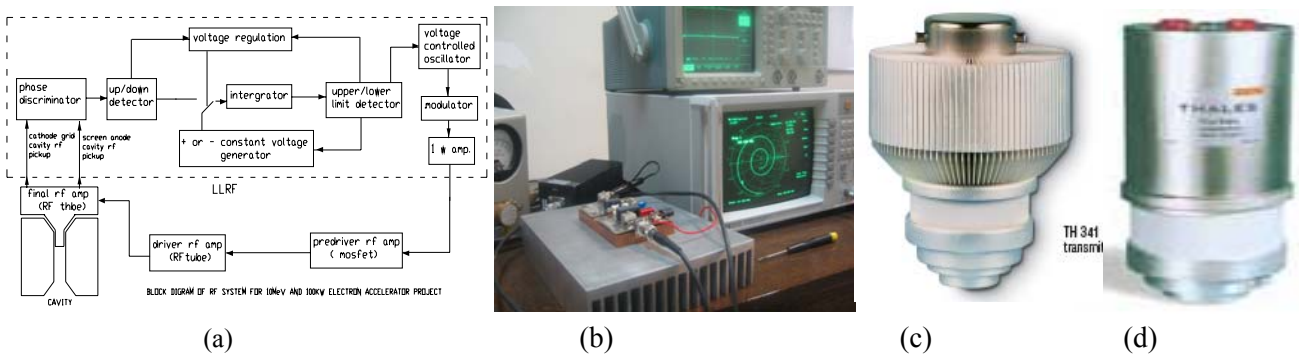


Figure 2: components of rf system of rhodotron accelerator

3. The new RF system by solid state amplifier

An investigation into development of 200 KW cw solid state rf power system design to replace the existing rhodotron rf system that uses novel solid state devices. The conceptual new rf system consists of several 1KW cw modules. These rf power amplifiers are based on parallel assemblies of 1KW modules equipped with MOSFET and impedance matching and circulators. Each module includes the Freescale MRF6VP11KH LDMOS rf power transistor. The data sheets of this device declare a 1 KW at 150 MHz with a power gain of 26 dB and operation junction temperature 225°C [7-9]. The heat produced by the power dissipation in the transistor must be transferred to a heat sink and water cooling to control the temperature of the amplifier. The transistor package is clamped to the cold copper plate and aluminum heat sink by fasteners and thermal grease. Thermal loading of these components can be simulated by the ANSYS software. For impedance matching, a coaxial balun transformer is connected in parallel to the input and also the output of the module. Impedance matching sections can be designed with 50 Ω feed ports. A circulator with a 50 Ω rf termination is integrated in each

module to protect the transistors from reflected power. Each module shielding aluminum housing. Every module is fed by a separate switching power supply delivering about 2000 W at voltage adjustable from 50 up 55 v dc with low ripple. The schematic drawing of 1 KW amplifier module design can be seen in figure 3 part (a) in 107.5 MHz frequency. The power combination scheme for 10KW amplifier is described in part (b) of figure 3. The basic structure consists of 12 modules each one of 1 KW connected by a 12-way power splitter at input and a 12-way power combiner at the output considering the lost of combiner. The required input power to reach an output of 10 KW is 50 W. Complete block diagram of 200 KW amplifier assembly is shown in part (c) of figure 3. The complete plan include twenty of 10KW amplifier

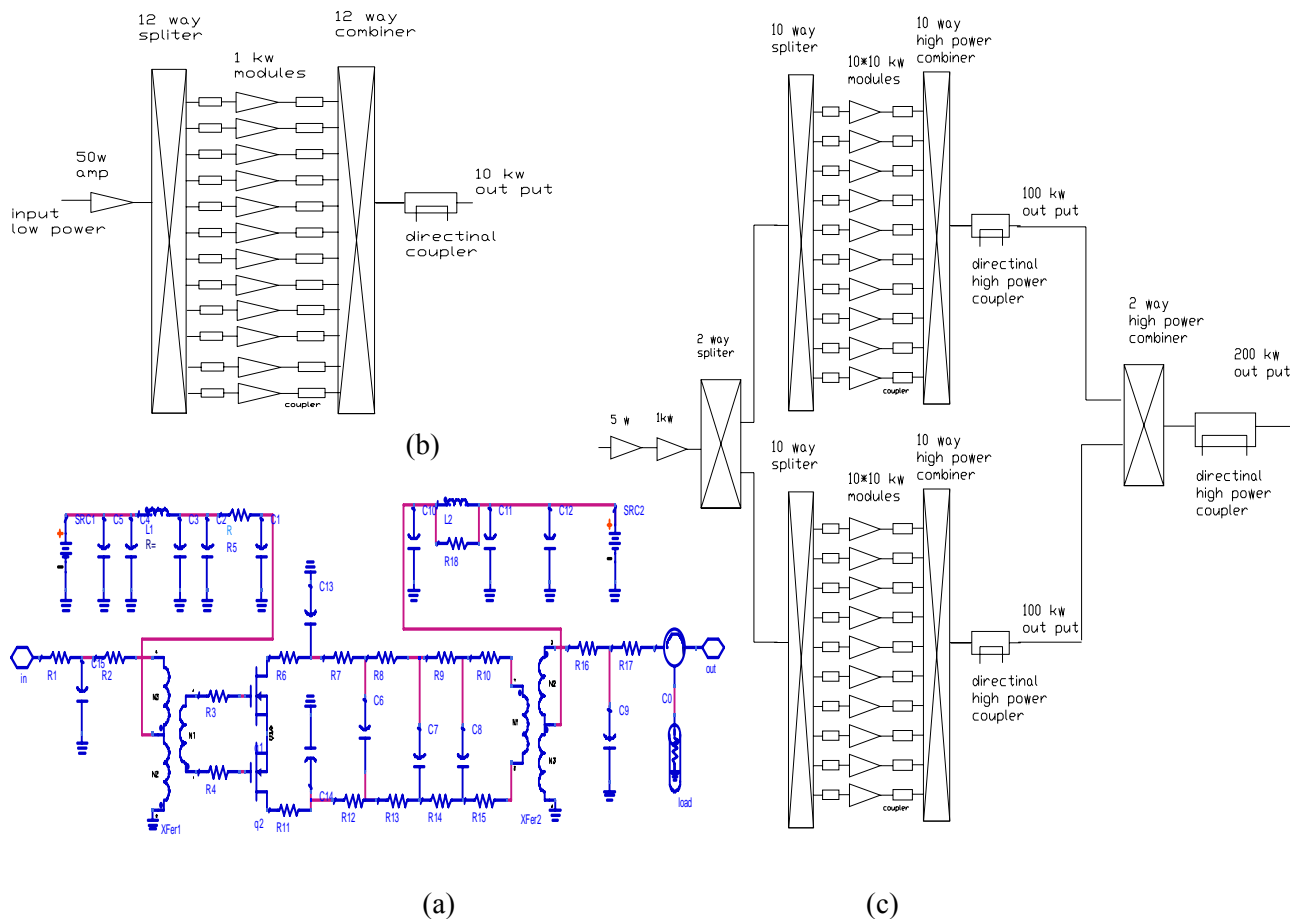


Figure3:the 200KW solid state amplifier for industrial electron accelerators

The required components are 2-way and 10-way power splitter at input and a 10-way and 2-way high power combiner at output. Radial power combiner offers low loss excellent amplitude and phase balance with high power handling capability. Design of combining path and peripheral ports was carried out by circular geometry as uniformly spaced circular array of coupled to transmission line. For 10-way and 2-way high power combiner must be carefully design to obtain good matching and high coupling efficiency. In splitter the power coming from one module can be divided in many equal parts to be sent to the other modules. Each module monitoring by couplers and control by PLC. The 240 module current are permanently monitored by PLC through a multiplexing system as other part of rf system so The control system allows checking the system continuously. The block diagram of new design of 200 KW cw rf system for high power electron accelerator is shown in figure 4.

The rf system includes the feedbacks for amplitude and phase controls. The rf control system as a comprises that are responsible for the control of the amplifier. two cavity pickup feedback taken in the midline of cavity control the phase and power of rf in cavity. Voltage regulation and phase discriminator circuits by feedbacks control the voltage and phase and resonating frequency. The modulator control

amplitude of accelerating voltage in the cavity by changing the input power of amplifier and VCO control the frequency of rf system.

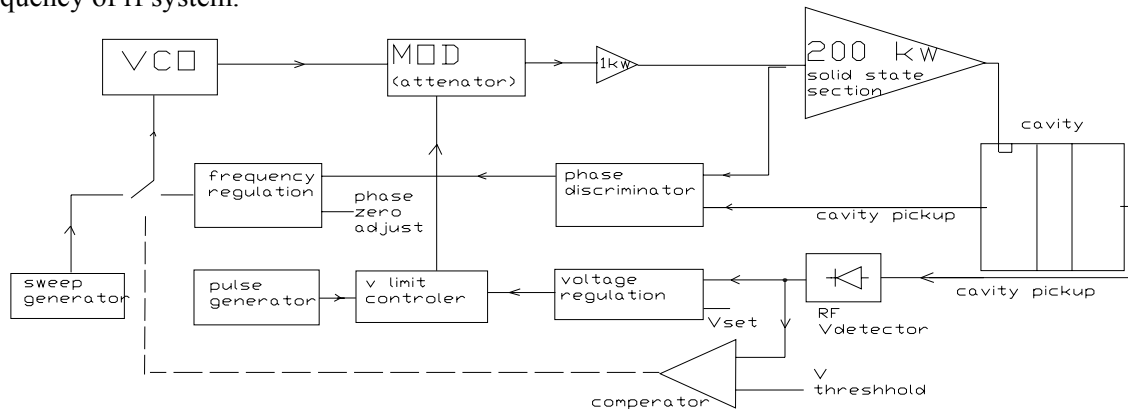


Figure4: New rf system for high power industrial electron accelerator

4. Conclusions:

The new design of rf system by solid state high power amplifier produced cw output power 200 KW that can be use this method for mostly of RF industrial electron accelerators. Some advantage of new rf system for industrial electron accelerator by solid state are such as: Solid state amplifiers are free from thermal running time so they do not require periodical replacement like vacuum tubes. It is low operational costs in running and maintenance. Solid state have a Modularity structure and is redundancy, no need the HV and is In house expertise so the solid state high power amplifier is a suitable for industrial electron accelerators.

References

- [1]-F.Scarpa,A.Facco,V.Zviagintesev,Z.lipeneng"A 2.5KW,low cost 352 MHz solid state amplifier for cw and pulsed operation"synchrotron soleil,proceedings of EPAC 2002,france.
- [2]P.marchand,r.lopes,j.polian,f.ribeiro,t.ruan"high power 352 mhz solid state amplifier for synchrotron soleil"synchrotron soleil,EPAC2004,Lucerne,switzerland
- [3]a. nguyen, k.. uhiastovski, j. pottier, j.h. capdevila, f. uine, j.p. nicolai" rhodotron first operations " cea dein cen saclay 91191 gif/yvette france.
- [4] pottier "a new type of rf electron accelerator:the:rhodotron"physics research b40/41/943-945-1989
- [5] Y. JongenM. Abs, T. Delvigne Arnold Herer, J.M. Capdevila, F. Genin, A. Nguyen"rhodotron accelerators for industrial electron-beam processing : a progress report" 1991,france
- [6]ion meam application (iba co publications)'tt200 rhodotron maintenance guide,belguim,1998
- [7]freescale semiconductor technical data (www.freescale.com/rf)
- [8] D. Horan, B. Brajuskovic, Jeff T. Collins, L. Morrison, G. Waldschmidt"352-mhz solid-state rf power system development at the advanced photon source" PAC09, Vancouver, BC, Canada
- [9]freescale semiconductor rf division "LDMOS FETS with 1KWpeak power to 150MHz"microwave journal ,2007

New Holographic Methods for Creation of 2D and 3D Micro- and Submicro-Scale Gratings in Photorefractive Materials

Anahit Badalyan, Ruben Hovsepyan, Vahram Mekhitarian,
Paytsar Mantashyan and Rafael Drampyan

*Institute for Physical Research, National Academy of Sciences of Armenia, 0203
Ashtarak-2, Republic of Armenia*

The Bessel standing wave and combined interferometric-mask techniques are suggested and realized for formation of 2-dimensional and 3-dimensional micro- and nano-metric scale holographic gratings in photorefractive materials. The experiments are realized by 532 nm and 633 nm laser beams in Fe-doped, as well as Fe-Mn and Fe-Cu doubly doped lithium niobate (LN) crystals taking into account their high photorefractive properties and possibility of creating the persistent gratings. The gratings formed have ~ 10 μm period in radial and azimuthal directions and ~300 nm in axial direction, and up to 10% diffraction efficiency.

1. Introduction

Materials with spatial periodic structure such as the photonic crystals [1-4] currently find applications in many fields of physics and optical device engineering. There are different methods for the fabrication of artificial periodic structures, including etching processes, electronic beam and deep UV lithography [2-4] and holographic technique [5].

Photonic crystals have a great potential for numerous applications in advanced photonics and nonlinear optics. Photonic crystals are promising materials for conversion of laser radiation frequency, for controlling and manipulating the flow of light, they serve as fibers, microcavities, bandgaps etc. Periodically poled crystals are widely used for generation of new frequencies of laser radiation: second harmonic generation [6], difference frequency generation and optical parametric oscillators [7,8]. The second [9,10] and third [11] harmonic generation and nonlinear diffraction effect [12] have been studied in annular periodically poled crystals.

For many applications, including guiding and trapping systems, optical devices, telecommunications, information storage, optical computers etc, 2-dimensional (2D) 3-dimensional (3D) periodic structures are more promising. In spite of many successes in this field, further development of the techniques for fabrication of various photonic nano- and micro-structures is an actual problem.

Holographic technique [5] is one of simple and promising methods for fabrication of spatially periodic structures in photorefractive materials. The mask [13] and recently suggested Bessel beam methods [14] are very promising for creation of 2- dimensional spatial periodic structures in photorefractive materials by holographic technique.

In this report we present the results of investigations for creation of 2D and 3D gratings by Bessel standing wave and combined interferometric-mask technique.

2. Formation of 2D gratings by counter-propagating Bessel beam technique

A counter-propagating non-diffracting Bessel beam technique is suggested for creation of 2D gratings. The Bessel beam [15] has no intensity gradient along the propagation axis and can be represented as a set of co-axial hollow light cylinders surrounding the central light rod (Fig.1a). The profile of Bessel beam is a set of concentric rings (Fig.1b). The counter-propagating beam geometry builds up the Bessel standing wave with periodic annular structure in each anti-node (Fig.1c).

The Bessel standing wave technique allows the creation of 2D holographic periodic structures in photorefractive materials. 2D periodical structure formed by the suggested method is a combination of annular and planar gratings. The non-diffracting Bessel beam is formed by optical element – axicon [16]. Fig.1b shows the fragment of radial intensity distribution of Bessel beam formed by an axicon.

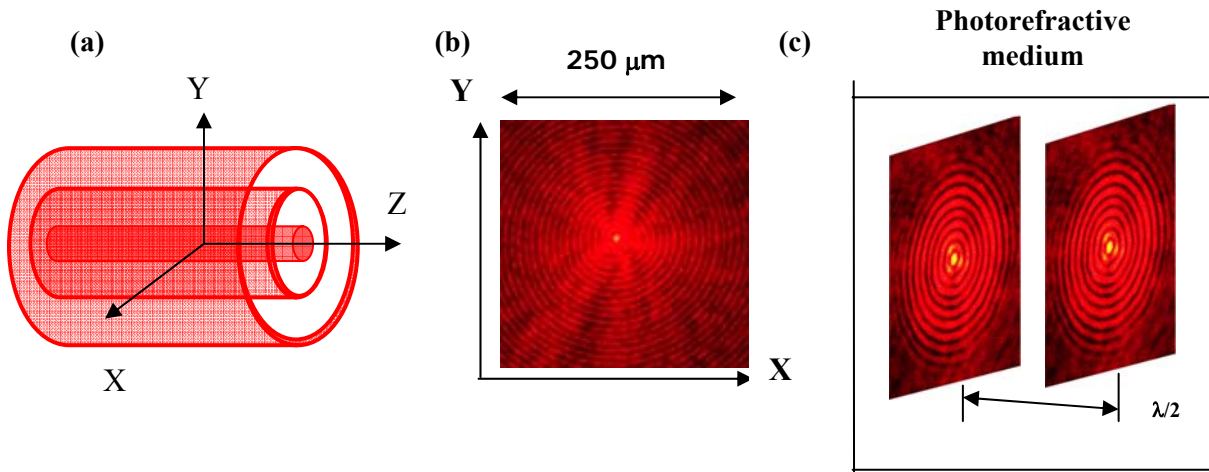


Fig.1.(color online). a) Schematic of ideal Bessel beam which has no intensity gradient along the propagation axis. (b) Fragment of radial intensity distribution of Bessel beam formed by an axicon using 633 nm laser beams. Number of rings reaches up to 1000. (c) Schematic of two neighboring planes of standing wave with maxima of light intensities, separated by half wavelength $\lambda/2$, where the concentric rings are located. In (c) the scale along the direction of standing wave (Z-axis) is enlarged relative to X and Y axes.

The recording of the gratings is performed by both single mode He-Ne laser beam at 633 nm with power 17 mW and cw second harmonic of YAG: Nd laser at 532 nm with beam power 100 mW (Fig.2). The refractive gratings are recorded in both Z and Y-cut 2 mm thick LN: Fe, as well as Y-cut LN: Fe:Cu and LN:Fe:Mn crystals during 60 min illumination.

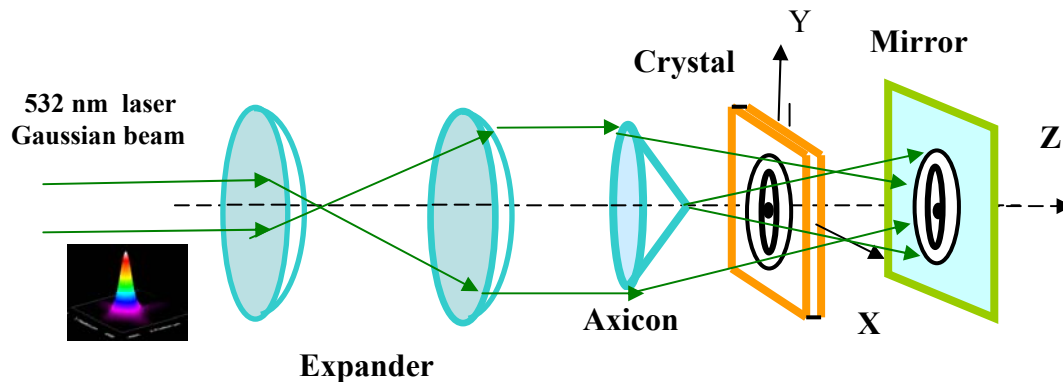


Fig.2. (color online). Schematic for creation of 2D grating by single axicon and back-reflecting mirror. The set of concentric rings on the surfaces of crystal and mirror show the Bessel beam profile.

The electro-optic effect is responsible for formation of gratings inside the photorefractive crystal illuminated by non-uniform light beam. The non-diffracting character of the Bessel beams allows the creation of high contrast gratings. The phase microscope image of the grating recorded by 532 nm, 17 mW beam inside the LN:Fe:Cu is obtained (Fig.3a), allowing the exact measurements of radial period of the grating. The measurements gave a value of $9.0 \mu\text{m}$ for grating radial period. Fig.3a shows that the grating formed in the medium has pronounced azimuthal dependence.

The read-out of 2D grating is performed by Gaussian and Bessel beams at 633 nm and 532 nm. Diffraction pattern from the grating recorded in Y-cut LN:Fe by 532 nm beam during 60 min, for nearly orthogonal incidence of the probe Gaussian beam at 633 nm to the crystal surface is shown in Fig.3b. The appearance of the ring structure itself is the result of diffraction of the reading beam on the refractive index circular structure inside the crystal. Such diffraction leads to the restoration of the set of rays lying on the cone (light cone), which form a ring in the far field.

The azimuthal dependence of ring intensity with higher diffracted intensity in the direction of C-axis of the crystal (Fig.3b) is a result of pronounced azimuthal dependence of recorded grating (Fig.3a). Diffraction patterns, observed both in transmission and reflection, allowed the measuring of the diffraction efficiency of the gratings. The formed 2D gratings have the half-wavelength standing wave period of $\sim 300 \text{ nm}$ in

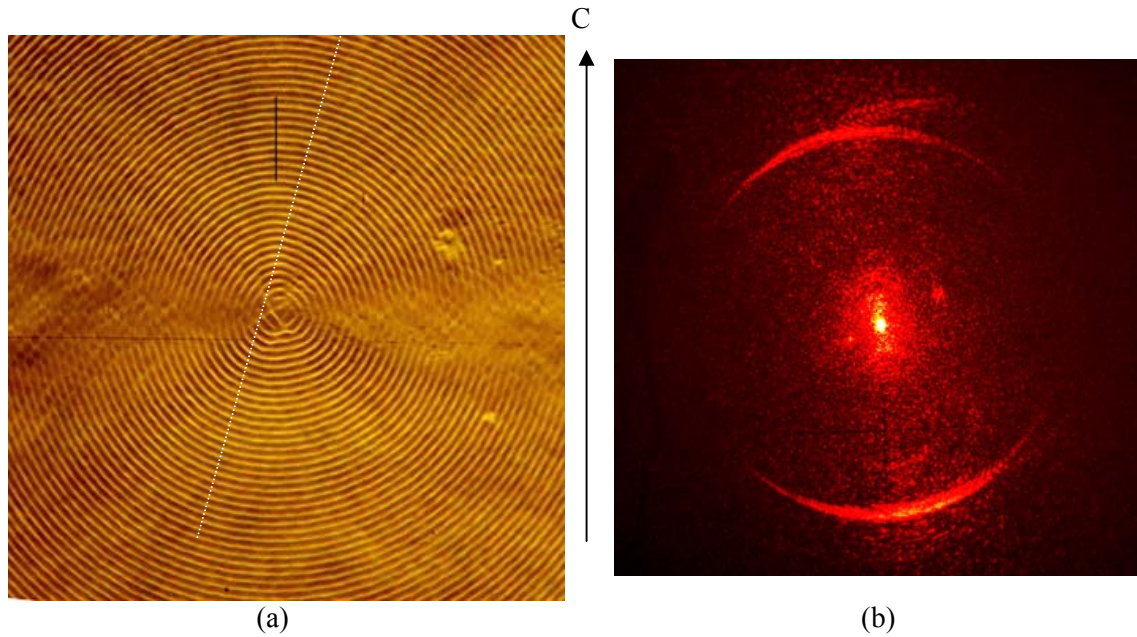


Fig.3. (color online). (a) Phase microscope image of the grating inside the LN:Fe:Cu crystal. The arrow shows the direction of optical C-axis of the crystal. The distance between the rings is measured $9.0 \mu\text{m}$. The dashed lines mark the areas where the grating is recorded with high contrast (upper and lower sectors) and does not recorded at all (left and right sectors). (b) Far field transmitted diffraction pattern from 2D grating, recorded in Y-cut LN:Fe by 532 nm beam during 60 min, for nearly orthogonal incidence of the probe Gaussian beam at 633 nm to the crystal surface.

longitudinal direction, the period of $\sim 10 \mu\text{m}$ in radial direction, and up to 10 % diffraction efficiency.

3. Combined interferometric-mask method for creation of 3D periodic and quasi-periodic structures

A new combined interferometric-mask method is suggested and realized for creation of 3D periodic and quasi-periodic structures in photorefractive materials. The method is based on the preparation of 2D masks having micrometric scale speckles disposition with different symmetries and illumination of the crystal through the mask by Gaussian beam in combination with back reflecting mirror.

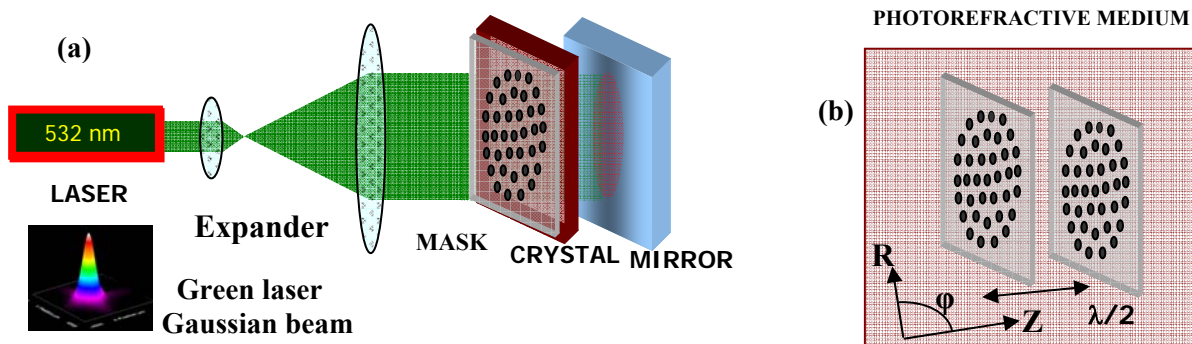


Fig.4. (color online). a) Experimental setup for recording of 3D gratings by combined interferometric –mask method. b) Schematic of two neighboring anti-nodes of standing wave, where the mask created quasi-periodic structures are located. The grating is modulated in radial R , azimuthal φ and axial Z directions. The scale along the direction of standing wave (Z -axis) is enlarged relative to R and φ directions.

The counter-propagating beam geometry builds up Gaussian standing wave, which determines the third half-wave period of the grating in the axial direction. The experimental scheme is given in Fig.4a. Thus, the created 3D intensity pattern is a set of numerous mask-generated 2D quasi-periodic structures located in each anti-node of standing wave (Fig.4b). The created intensity pattern was imparted into the photorefractive

medium via electro-optic effect, thus creating micro- and sub-micro scale 3D refractive index volume grating.

From 1 to 8 fold axial symmetry masks were generated by computer graphic technique. The masks consist from black spots periodically disposed along the equidistantly positioned concentric circles, surrounding the central spot. The number of spots on the i -th circle was equaled $M_i = ji$, where $i = 1, 2, 3, \dots$ is integer and j is the symmetry order of the mask. The masks of reduced size (0.8 cm) with $i = 100$ were printed by high resolution printer (3300 dpi) on the transparent film. Fig.5a-b shows the examples of the fragments of 2 and 7-fold symmetry negative masks. The whole mask consisted from 100 circles had ~ 35000 holes.

The interference patterns from prepared masks were studied by cw red (633 nm) and green (532 nm) Gaussian and Bessel beams. When the masks were illuminated by Gaussian beam the observations showed that for even symmetry masks the symmetry of mask and diffraction pattern from the mask were same. However, for odd symmetry masks the symmetry of diffraction pattern is twice as high compared to the symmetry of the mask. Diffraction patterns from 2-fold and 7-fold symmetry masks obtained by green cw Gaussian laser beam are shown in Fig.5c and 5d, respectively.

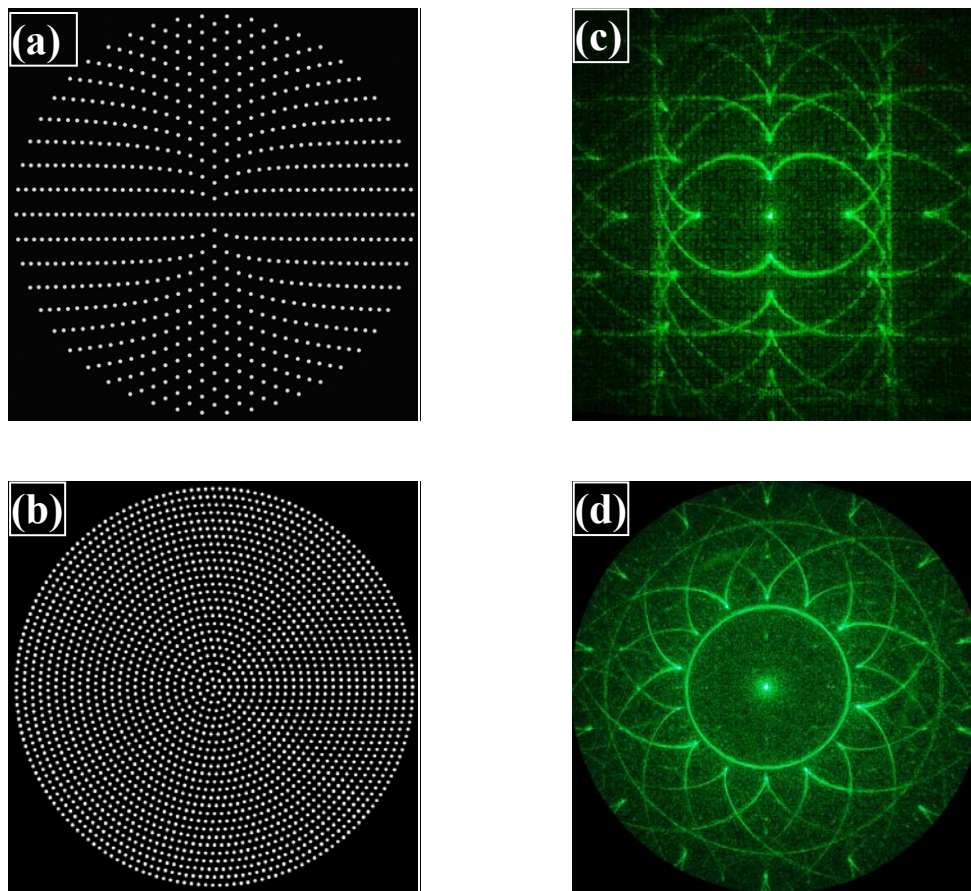


Fig.5. (color online). (a-b) Examples of fragment of enlarged pattern of negative masks with 2 and 7-fold symmetries. The masks had a diameter of 0.8 cm and a distance around $30 \mu\text{m}$ between $\sim 10 \mu\text{m}$ transparent holes. (c-d) Corresponding interference patterns from the masks obtained by green laser beam.

7-fold symmetry mask was used for creation of 3D gratings in Y-cut LN:Fe crystals by combined interferometric-mask technique. For comparison the recording of 2D grating using only mask technique, without standing wave, was also performed. The gratings were recorded by cw single mode 100 mW green 532 nm laser beam during 60 min illumination of LN:Fe crystal. The recorded gratings were tested using both red (633 nm) and green (532nm) laser beams by observing the diffraction patterns from the 2D and 3D gratings in the far field.

Fig.6 shows the obtained diffraction patterns from 2D grating recorded by mask technique (a) and from 3D grating recorded by interferometric-mask technique (b) using 7-fold symmetry mask. For comparison the

diffraction pattern from original mask is also shown in Fig.6c. The diffraction pattern from 2D grating has pronounced azimuthal dependence of intensity distribution with higher diffracted intensity along the C- axis of the crystal. The diffraction from 3D gratings shows more isotropic intensity distribution in diffraction patterns.

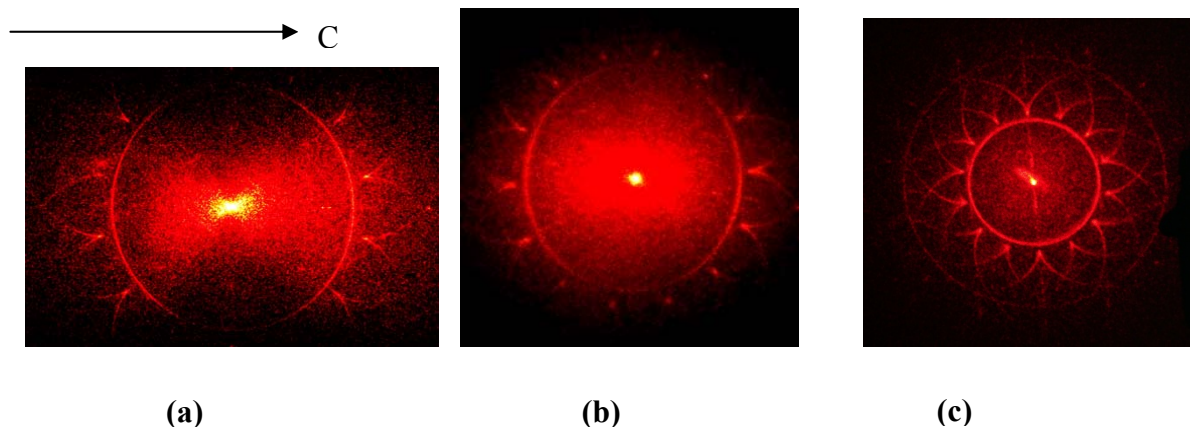


Fig.6. (color online). Diffraction patterns from 2D grating recorded by mask technique (a), from 3D grating recorded by interferometric-mask technique (b) in LN:Fe crystal and from 7-fold symmetry original mask (c). The arrow shows the direction of optical C-axis of the crystal relative to the diffraction pattern. The scales in the figures are different.

The physical mechanism of formation of the holographic gratings in photorefractive materials is based on the electro-optic effect. The redistribution of charges inside the crystal by non-uniform light beam builds up the internal electric fields, which, in turn, lead to the change of refractive index. The charge transport in doped LN crystal is due to the photovoltaic effect and diffusion of the charge carriers [17].

For 2D gratings recorded by mask technique with the periods in radial and azimuthal directions around $30\ \mu\text{m}$, corresponding to the spatial frequency $K \sim 3 \times 10^2$ lines/cm, the photovoltaic effect is the main process for charge transport along the C-axis of the crystal and predominant modulation of refractive index along C-axis. This leads, in turn, to the pronounced azimuthal dependence of intensity distribution in diffraction pattern with higher diffracted intensity in the direction of C-axis of the crystal. For the recorded 3D gratings the half-wave period in the axial direction provides enough high spatial frequency of $\sim 4 \times 10^4$ lines/cm and except photovoltaic effect along the crystalline C-direction, the diffusion effect also gives contribution to the grating formation in the axial direction. Thus the created gratings are more uniform and diffraction from 3D gratings shows more isotropic intensity distribution in diffraction patterns.

4. Conclusions

The Bessel standing wave and combined interferometric–mask techniques are suggested and realized for formation of 2D and 3D holographic gratings in photorefractive materials. 2D and 3D periodic and quasi-periodic artificial structures in photorefractive materials are promising for many applications including band gap materials, guiding and trapping systems, high capacity information storage etc.

References

- [1] E.Yablonovitch, “Inhibited spontaneous emission in solid-state physics and electronics”, *Phys. Rev. Lett.* **58**, 2059 (1987).
- [2] J. Joannopoulos, S.Johnson, R.Meade, J. Winn, *Photonic crystals*, Princeton Univ. Press. 2008.
- [3] Arishmar Cerqueira S Jr, “Recent progress and novel applications of photonic crystal fibers”, *Rep. Prog. Phys.* **73**, 024401 (1-21) (2010).
- [4] T.F.Krauss, R.M.De La Rue, “Photonic crystals in the optical regime – past, present and future”, *Progress in Quantum Electronics*, **23**, 51-96 (1999)
- [5] R.J.Collier, Ch.B.Buckhard, L.H.Lin, *Optical holography*, Academic press, New York, 1971.
- [6] A.Arie, G.Rosenman, A.Korenfield A.Skiliar, M.Oron, D.Eger, “Efficient resonant frequency doubling of a cw Nd:YAG laser in bulk periodically poled KTiOPO_4 ”, *Opt. Lett.* **23**, 28 (1998).

- [7] T.Kartalolu, K.G.Korpulu, O.Aytur, M.Suidheimer, W.R.Risk, “Femtosecond optical parametric oscillator based on periodically poled KTiOPO₄”, *Opt. Lett.* **23**, 61 (1998).
- [8] M.Ebrahimzadeh, G.A.Turnball, T.J.Edwards, D.J.M.Stothard, I.D.Lindsay, M.H.Dunn, “Intracavity continuous-wave singly resonant optical parametric oscillators”, *JOSA B*, **16**, 1499-1511 (1999).
- [9] D.Kasimov, A. Arie, E. Winwbrand, G.Rosenman, A.Bruner, P. Shaier, D.Eger, “Annular symmetry nonlinear frequency converters”, *Optics Express*, **20**, 9371-9376 (2006).
- [10] S.M.Saltiel, D.N.Neshev, R.Fischer W.Krolikowski, A.Arie, Yu.S.Kivshar, “Generation of second harmonic Bessel beams by transverse phase matching in annular periodically poled structures”, *Japanese J. Appl.Phys.* **47**, 6777-6783 (2008).
- [11] N.Voloch, T.Ellenbogen, A.Arie, “Radially symmetric nonlinear photonic crystals”, *JOSA B*, **26**, 42-49 (2009).
- [12] S.M.Saltiel, D.N.Neshev, W.Krolikowski, N.Voloch-Bloch, A.Arie, O.Bang, Yu.S.Kivshar, “Nonlinear diffraction from a virtual beam”, *Phys. Rev. Lett.* **104**, 083902 (2010).
- [13] Wai-Hon Lee, “Computer generated holograms: Techniques and applications”, in *Progress in Optics*, Editor Emil Wolf, Vol. XVI, North-Holland, 1978, , Chapter 3, pp. 121-232.
- [14] A.Badalyan, R.Hovsepyan, V.Mkhitaryan, P.Mantashyan, R. Drampyan, “New holographic method for formation of 2D gratings in photorefractive materials by Bessel standing wave”, in “Fundamentals of Laser Assisted Micro- and Nanotechnologies 2010”, Edited by V.P.Veiko, T.A Vartanyan, *Proceedings of SPIE*, Vol. 7996, (SPIE, Bellingham, 2011) 7996 11-1-9 .
- [15] J.Durnin, J.J. Mikely, Jr, J.H.Eberly, “Diffraction-free beams”, *Phys. Rev. Lett.* **58**, 1499-1501 (1987).
- [16] F.P. Shafer, “On some properties of axicons” *Appl. Phys. B*, **39**, 1-8 (1986).
- [17] A.M.Glass, D.von der Linde, T.J.Negran, “High-voltage bulk photovoltaic effect and the photorefractive process in LiNbO₃”, *Appl. Phys. Lett.* **25**, 233-235 (1974).

C and Ku-Band, Two-Frequency, Polarimetric, Combined Doppler Scatterometer-Radiometer System for Land and Sea Surface Microwave Remote Sensing

A.K. Arakelyan¹, A.K. Hambaryan¹, V.V. Karyan¹, G.G. Hovhannisyan¹, A.A. Arakelyan¹, M.G. Simonyan¹, M.L. Grigoryan¹, T.N. Poghosyan², N.G. Poghosyan²

¹ *ECOSERV Remote Observation Centre Co. Ltd., 2 G. Njdeh Str., #24, Yerevan, 0006, Armenia
E-mails: arakelyanak@yahoo.com, ecoservroc@yahoo.com*

² *Institute of Radiophysics & Electronics of ANAS, 1 Alikhanyan Br. str., Ashtarak, 0410, Armenia*

In this paper a developed C-, and Ku-band, two-frequency, multi-polarization, combined, short-pulse Doppler scatterometer-radiometer system is described, for short (from low altitude platform), middle (from vessel) and long (from aircraft) distance remote sensing applications, suitable for water surface, soil, vegetation, sea ice and land snow cover's microwave reflective and emissive characteristics simultaneous and spatially coincident, multi-frequency and polarimetric microwave measurements.

1. Introduction

The retrieval of surface parameters from microwave remote-sensing data requires accurate models for the relationship between the desired geophysical parameters of a target and the observed quantities. As natural surfaces generally are described as random functions, the modeling should involve both electromagnetic and stochastic aspects. Therefore, for an unambiguous and accurate retrieval of land snow cover and soil moistures and classification of soil vegetation a wider set of independent measurements and a synergy of various sensors are welcomed. Since, microwave signals backscattered from and emitted by the soil surface are partially uncorrelated from each other and in practice may be considered as independent variables, the synergetic application of microwave radar and radiometer observations represents special interests. For its successful implementation it is important and suitable to develop multi-band complex of polarimetric, combined radar-radiometer systems and to perform multi-frequency, polarimetric, microwave, active-passive combined measurements of snow, bare and vegetated soils under well controlled conditions. On the basis of the acquired data, it will be possible to validate and to improve reflective (scattering) and radiative transfer models, and to develop new methods and algorithms providing the possibility to reach high precision in snow and soil moistures retrieval. At present time, only single frequency (S, C, Ku, K and Ka-band), polarimetric, combined radar-radiometer systems for various platform applications are developed and are used for soil, snow, vegetation and water surface microwave active passive characteristics preliminary measurements [1-7].

In this paper C-, and Ku-band, dual frequency, multi-polarization, combined, short-pulse scatterometer-radiometer system (ArtAr-C&Ku) is described, for short (from low altitude platform), middle (from vessel) and long (from aircraft) distance remote sensing applications, for water surface, soil and land snow cover's microwave reflective and emissive characteristics simultaneous and spatially coincident, multi-frequency and multi-polarization measurements [8-10]. The system ArtAr-C&Ku is developed in Armenia, in the framework of the International Science and Technology Center (ISTC) Project #A-1524, by ECOSERV Remote Observation Centre Co.Ltd. (ECOSERV ROC), in co-operation with the Institute of Radiophysics & Electronics of Armenian National Academy of Sciences.

2. C-, and Ku-Band, Combined Scatterometer-Radiometer System

The principal requirements for a development of the system were:

- Functional and constructive combining both C-, and Ku-band, microwave, combined active and passive means of sensing as a single microwave device, providing simultaneous operational peculiarities.
- Coherent-pulse construction of system's scatterometers functional schemes, provided high level of decoupling between transmitting and receiving sections, allowed realize short range operational potential for both scatterometers beginning from 4m.

- Series (periodical) transmissions of the signals at two different frequencies at specified (vertical or horizontal) polarizations and simultaneous receiving of both co- and cross-polarized components of backscattered radar signals at two different frequencies.
- Possibility for application of developed principles and methods for signals forming and processing for space-aerial based prototype of the system.

In comparison with earlier developed single-frequency, combined scatterometer-radiometer systems of S (~3GHz), C (~5.6GHz), Ku (~15GHz), K (~20GHz) and Ka (~37GHz) band of frequencies [1-8], the described system has two transmitting and four receiving channels, which allow simultaneously receipt co- and cross polarized components of the backscattered signals at 5.6GHz and 13.6GHz and the signals of the observed surface proper radiothermal emissions at 5.6GHz and 13.6GHz, at vertical and horizontal polarizations.

In Fig.1 a simplified block diagram of ArtAr-C&Ku, dual-frequency, multi polarization, combined scatterometer-radiometer system is presented. Detailed block diagrams of C-, and Ku-band modules of ArtAr-C&Ku system are fully described in [3-6].

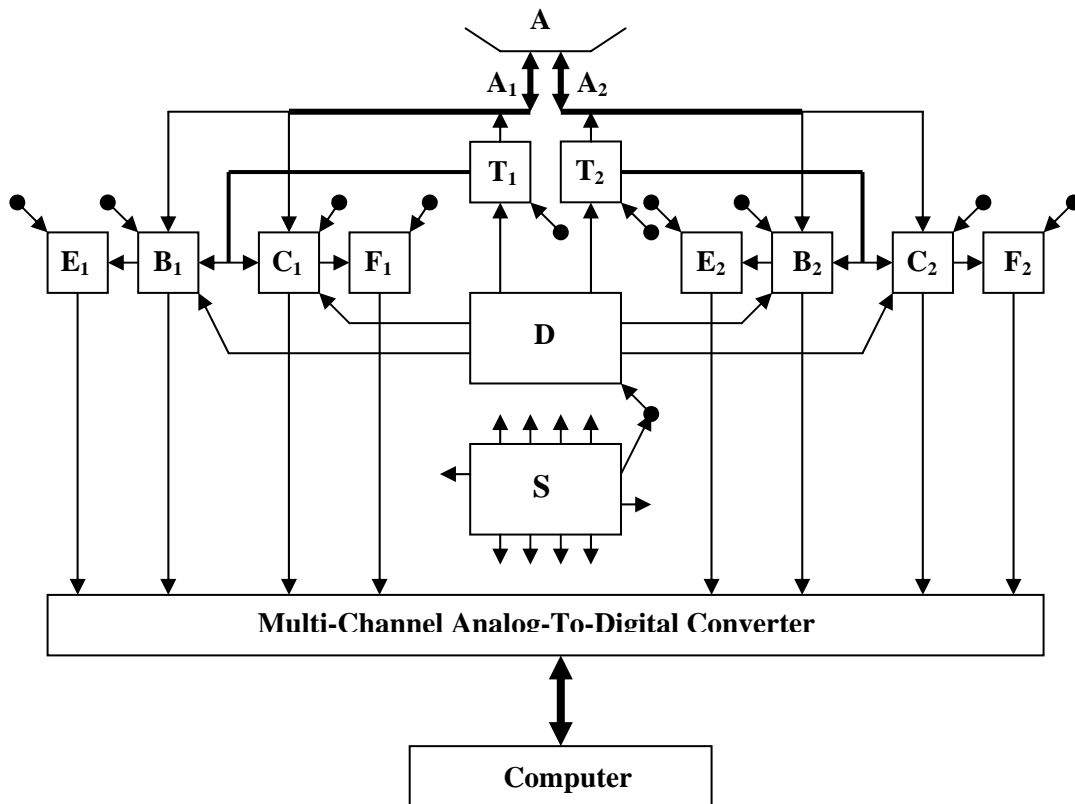


Fig. 1 A simplified block diagram of ArtAr-C&Ku, dual-frequency, combined scatterometer-radiometer system

A – Parabolic antenna (dish and subdish), **A₁ and A₂** – C-, and Ku-band antenna feeds, **T₁ and T₂** – C-, and Ku-band transmitter modules, **B₁ and B₂** – C-, and Ku-band radar receivers for backscattered signals co-polarized components, **C₁ and C₂** – C-, and Ku-band radar receivers for backscattered signals cross-polarized components, **E₁ and E₂** – C-, and Ku-band radiometric receivers for radiothermal signals' vertical polarized components, **F₁ and F₂** – C-, and Ku-band radiometric receivers for radiothermal signals' horizontal polarized components, **D** – Reference signal module, **S** – Synchronizer

The system has three operational modes for the transmitter, suitable to short (5m-50m), middle (30m-250m) and long distance (150m-2500m and more) applications from flying, moving or stationary fixed measuring platforms. Time-division channeling of scatterometers and radiometers functioning was used for the system functional scheme development. In Fig.2a and Fig2b time diagrams of the system's operation are presented for a short range operational mode (Fig.2a) and for a middle and a long distance operation modes (Fig.2b).

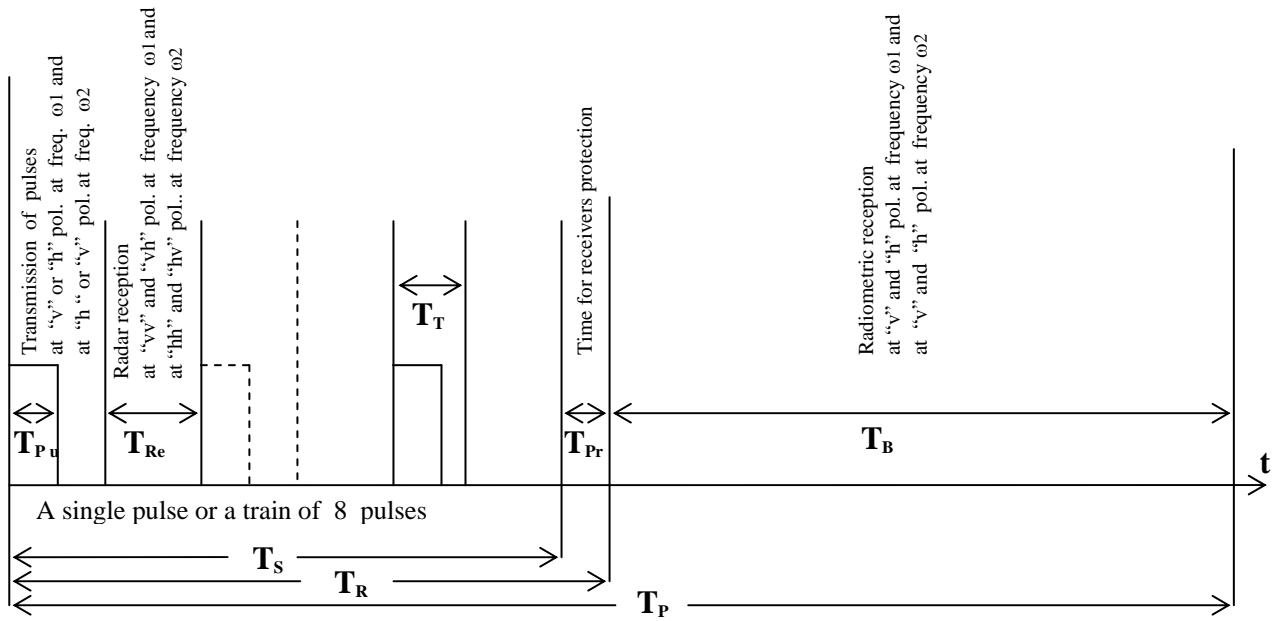


Fig.2a A time diagram of the system's operation, for a short range application case

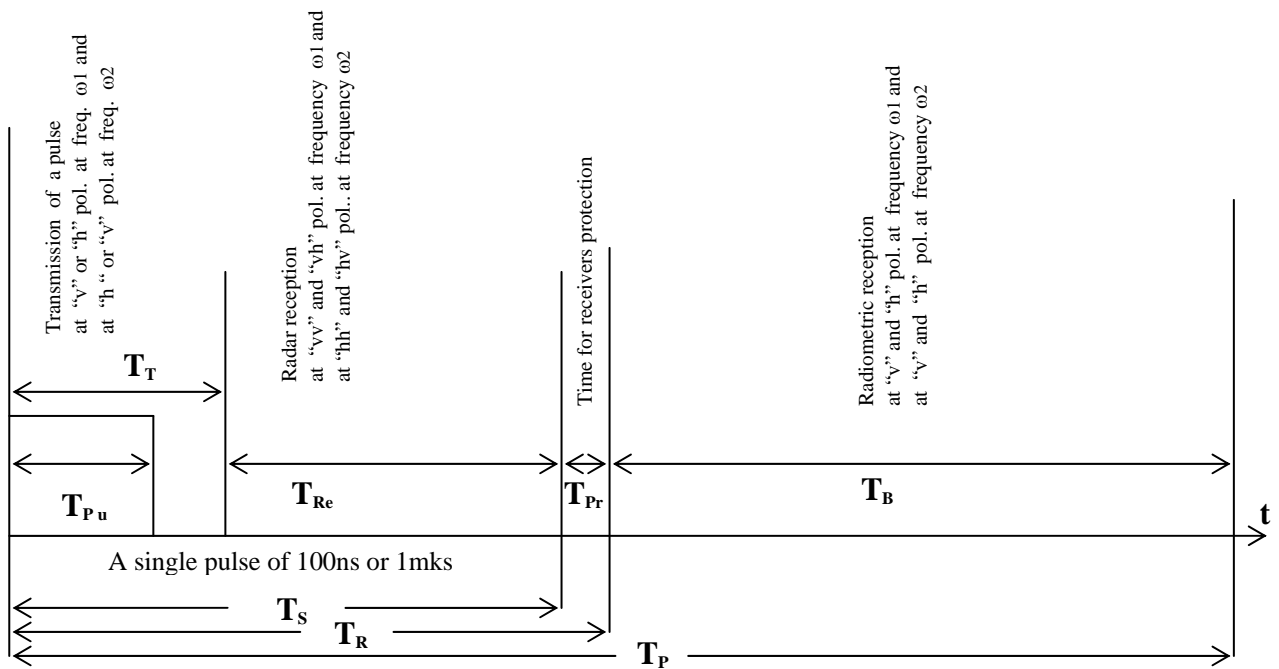


Fig.2a A time diagram of the system's operation, for a middle and for a long distance application cases

The work while of the system is divided by T_P time periods, in which the while T_R is equal to $\sim 10\%$ of the period $T_R = 0.1T_P$ is used for radar channel operation and the rest of the period $T_B = T_P - T_R$ is used for radiometric channels operation. The while T_S is used for transmission of a single probing pulse or of a train of **8** probing pulses at both frequencies and for reception of corresponding (vv or hh) and cross (vh or hv) polarized components of the backscattered pulse signals at both frequencies. The reception of the backscattered pulse signals is implemented during the while T_{Re} . The transmission is implemented during the while T_T , where T_{Pu} is the pulse duration. The while T_{Pr} of the period is used for protection of the radiometer receivers inputs from the residual influence of both transmitters. The while T_B is used for

reception of proper radio thermal signals of the observed surface at both frequencies, at vertical and horizontal polarizations.

The transmitted signals' polarizations may be changed periodically (periodically changing operating mode) or may be changed stepwise by issuing the outside command (polarization stability operating mode). Such a construction allows improve relative accuracy of measurements by cross polarized signals, simplify calibration procedures and reduce complicity and value of the system by using microwave and intermediate frequency modules of the system as a common modules for both scatterometric and radiometric channels. Of cause, time-division channeling of scatterometers and radiometers functioning has its shortage connected with a reduction of backscattered signals accumulation efficiency. However, for stationary and low speed platform applications this fact is not sufficient, if the main requirement for the system's operation its work stability and accuracy of measured data. A detail description of the system's operation features is presented in [7-9].

3. Realized Parameters

In Fig.3 and Fig.4 realized work prototype of ArtAr-C&Ku, dual frequency, multi-polarization, combined scatterometer-radiometer system is presented. The system was built on the basis of in-house design modules. In Fig.3 a C-band part (module) of the system is presented. In Fig.4 a Ku-band part of the system is presented. In Figs.3 and Fig.4 the system's antenna and dual-frequency antenna feed are presented too.

Due to some construction peculiarities of the microwave inputs of both C-, and Ku-band modules of the system, the developed system allows carry out absolute measurements of the observed surface brightness temperatures (antenna temperatures) at both frequencies, with an accuracy better than 10K for both bands.

The main technical characteristics of the realized prototype are presented in the Table 1.

Table 1

ArtAr-C&Ku	C - Band		Ku - Band	
	Radar Channel	Radiometric Channel	Radar Channel	Radiometric Channel
Central frequency	5.6GHz	5.6GHz	13.6GHz	13.6GHz
Dual Frequency Parabolic Antenna Gain / Beamwidth / Sidelobes	~ 22dB / 8° / -18dB		~ 28dB / 3° / -20dB	
Radar pulses, type and duration for a short range application for a vessel and aircraft application	a train of 8 or a single pulse	pulses, 25ns each of 100ns or 1mks	a train of 8 or a single pulse	pulses, 25ns each of 100ns or 1mks
Pulse repetition frequency within the train	1.6MHz		1.6MHz	
Repetition frequency of the train or of the single pulse	1KHz		1KHz	
Pulse power	50mW - 1W		75mW - 2W	
Polarization: Transmission Reception	"v" or "h" "vv, "vh" or "hv, "hh"	"v" and "h"	"v" or "h" "vv, "vh" or "hv, "hh"	"v" and "h"
Pre-detection bandwidth	~100MHz	~500MHz	~100MHz	~500MHz
Receiver's sensitivity (at 1s)	-130dB/W	~0.1K	-130dB/W	~0.15K
Absolute measurements accuracy	better than 10K		better than 10K	
Operational range	4 - 2500m			
Dimensions / weight	240 x 440 x 600mm ³ / 25kg			

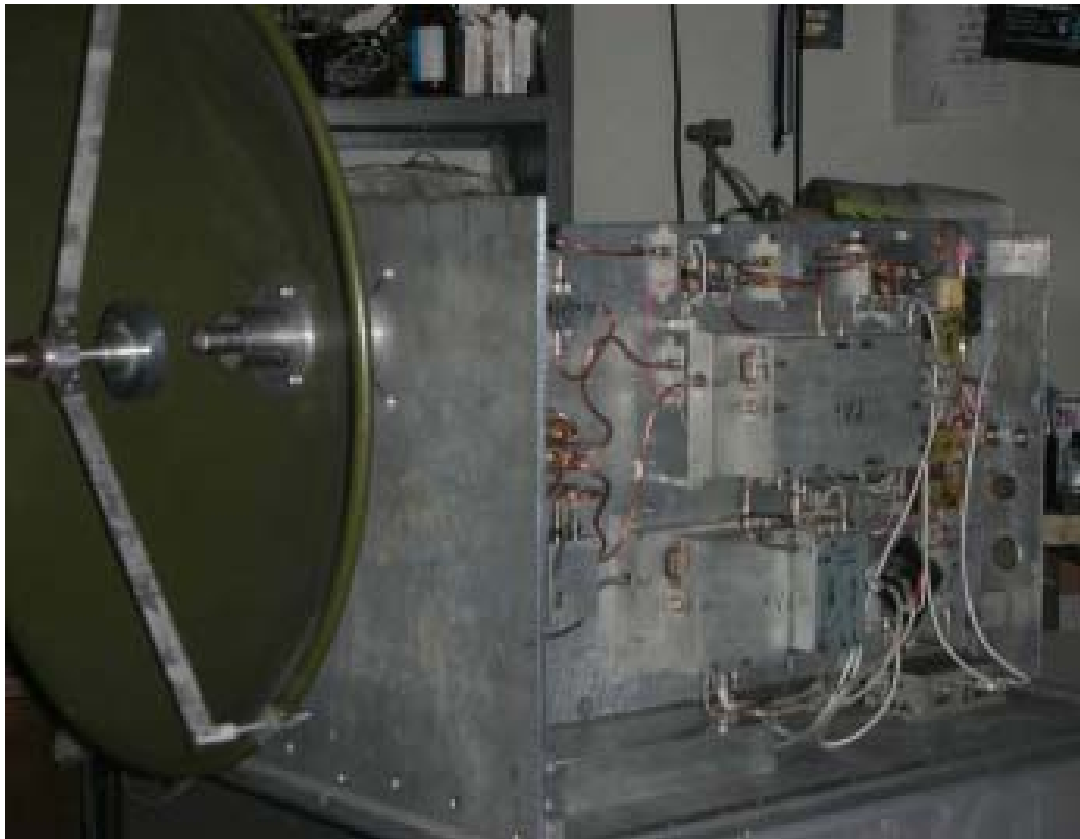


Fig.3 A C-band module of ArtAr-C&Ku system

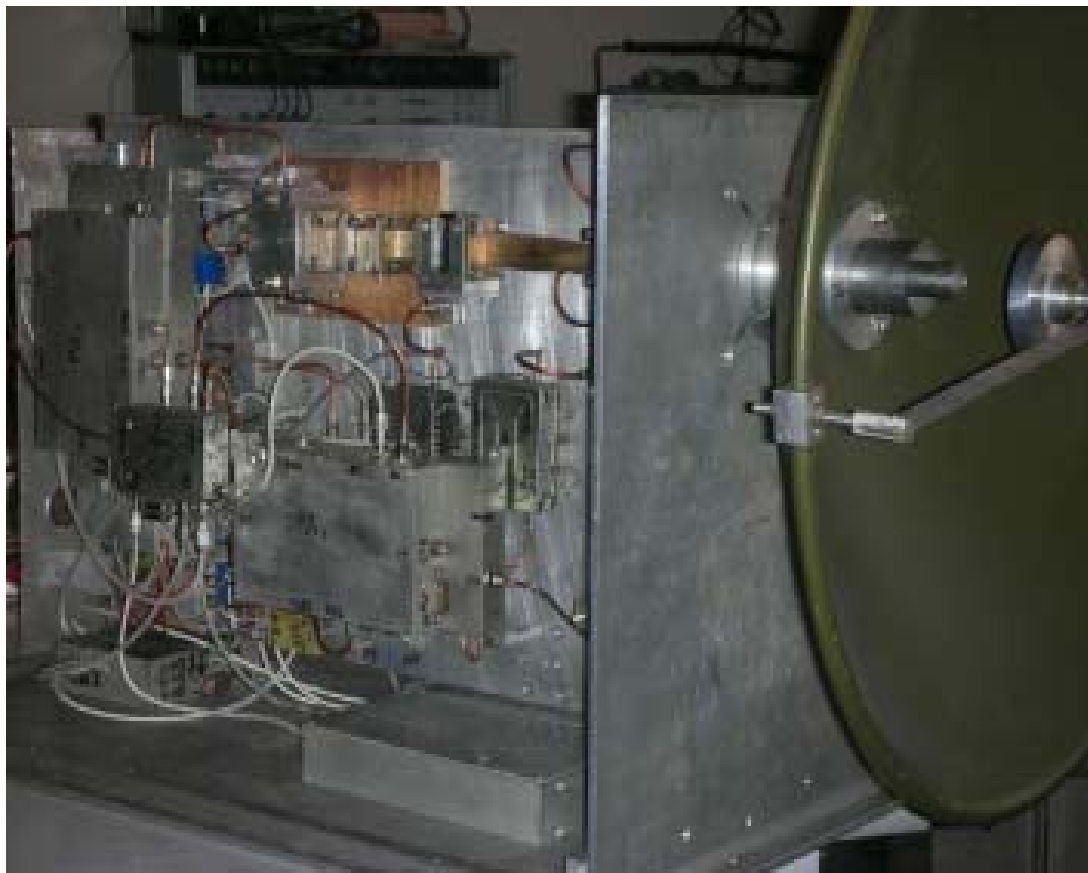


Fig.4 A Ku-band module of ArtAr-C&Ku system

4. Conclusion

Thus, C-, and K_u-band, dual frequency, multi-polarization, combined scatterometer-radiometer system is developed. The developed system allows investigate peculiarities of relationships between power (amplitude) and phase characteristics of the backscattered radar signal and between power characteristics of backscattered radar and emitted proper radio thermal signals of the observed surface or object, under test-control laboratory conditions at two different frequencies from two different frequency bands. The system may be used as a detector and identifier and will allow to detect and to classify at least 256 types of anomalies, originating on the background due to the changes of the observed surface geo-physical and biochemical parameters. The developed device is the first from the series of dual frequency, multi-polarization, combined radar-radiometers, which are planned for development and manufacturing in the framework of the ISTC (International Science and Technology Center) Project A-1524 applied to multi-frequency, multi-polarization measurements of snow, bare and vegetated soil, perturbed water surface microwave reflective and emissive characteristics angular dependences, under test-control, quasi-field conditions, by spatio-temporally combined active-passive systems.

5. Acknowledgement

Authors express their gratitude to the International Science and Technology Center of Moscow for its financial support and maintenance provided through the ISTC Project A-1524 allowed to patent the idea, to develop, to built, to realize and to test in quasi field conditions dual-frequency, multi-polarization, combined scatterometer-radiometer system.

6. References

- [1] A.K. Arakelyan, A.K. Hambaryan, A.I. Smolin, V.V. Karyan, N.G. Poghosyan, M.A. Sirunyan, M.R. Manukyan, A.A. Arakelyan, "Polarimetric, Ka-Band, Combined, Short Pulse Scatterometer and Radiometer System", Progress in Contemporary (Present-Day) Radio Electronics, No.7, 2005, pp. 73-77. (In Russian).
- [2] A.K. Arakelyan, I.K. Hakobyan, A.A. Arakelyan, A.K. Hambaryan, M.L. Grigoryan, E.A. Vardanyan, V.V. Karyan, M.R. Manukyan, G.G. Hovhannisyanyan, N.G. Poghosyan, "Short Pulse, Polarimetric, Combined Scatterometer-Radiometer at 20GHz", Progress in Contemporary (Present-Day) Radio Electronics, No.9, 2007, pp.56-63. (In Russian).
- [3] A.K. Arakelyan, I.K. Hakobyan., A.A. Arakelyan, A.K. Hambaryan, M.L. Grigoryan, V.V. Karyan, M.R. Manukyan, G.G. Hovhannisyanyan, N.G. Poghosyan and T.N. Poghosyan, "Dual - Channel, Polarimetric, Combined Scatterometer - Radiometer at 5.6GHz", Electromagnetic Waves and Electronic Systems, Vol.11, No.2, 2007, pp.41-47. (In Russian).
- [4] A.K. Arakelyan, A.A. Arakelyan, S.A. Darbinyan, M.L. Grigoryan, I.K. Hakobyan, A.K. Hambaryan, V.V. Karyan, M.R. Manukyan, G.G. Hovhannisyanyan, T.N. Poghosyan, N.G. Poghosyan and S.F. Clifford, "Polarimetric, combined, short pulse scatterometer-radiometer system at 15GHz for platform and vessel application", Proceedings of SPIE edited by Robert N. Trebits, James L. Kurtz., Radar Sensor Technology XI, Vol. 6547, 2007, pp 6547OH-1 - 6547OH-10.
- [5] A.K. Arakelyan, I.K. Hakobyan., A.A. Arakelyan, A.K. Hambaryan, M.L. Grigoryan, V.V. Karyan, M.R. Manukyan, G.G. Hovhannisyanyan, N.G. Poghosyan and S.F. Clifford, "Ku-Band, Short Pulse, Dual-Polarization, Combined Scatterometer-Radiometer", Progress in Contemporary (Present-Day) Radio Electronics, No.12, 2007, pp. 41-50. (In Russian).
- [6] A.K. Arakelyan, I.K. Hakobyan, A.A. Arakelyan, A.K. Hambaryan, M.L. Grigoryan, V.V. Karyan, M.R. Manukyan, G.G. Hovhannisyanyan and N.G. Poghosyan, "S-Band, Polarimetric, Short Pulse, Short Distance application, Combined Scatterometer - Radiometer", Electromagnetic Waves and Electronic Systems, Vol.12, No. 3, 2007, pp. 52-60. (In Russian).
- [7] A. Arakelyan, "Dual-frequency, multi-polarization, combined radar-radiometer system by Artashes Arakelyan", Armenian National Patent, # 2257A, 2009. (in Armenian).
- [8] A. Arakelyan, "Dual-frequency, multi-polarization, combined scatterometer-radiometer system", Armenian National Patent, # 2313A, 2009. (in Armenian).
- [9] A. Arakelyan, "Multi-polarization, combined radar-radiometer system", International Patent Application (PCT Patent), PCT/IB2009/000165, 02.02.09.

Multi-Frequency (at 5.6GHz, 15GHz and 37GHz) and Polarization Measurements of Clouds and Rain Effects on Perturbed Water Surface Microwave Reflection and Emission

Melanya L. Grigoryan, Artashes K. Arakelyan, Astghik K. Hambaryan., Vardan K. Hambaryan, Vanik V. Karyan, Mushegh R. Manukyan, Gagik G. Hovhannisyan and Arsen A. Arakelyan

*ECOSERV Remote Observation Centre Co. Ltd., 2 G. Njdeh Str., #24, Yerevan, 0006, Armenia
E-mails: arakelyanak@yahoo.com, ecoservroc@yahoo.com*

In this paper the results of simultaneous and spatially coincident, multi-frequency (three-frequency), multi-polarization, spatio-temporally collocated measurements of wavy pool water surface microwave reflective and emissive characteristics angular dependences at 5.6GHz, 15GHz and 37GHz are presented. The measurements were carried out under clear air, cloudy and have rain-hail conditions by C, Ku and Ka-band, polarimetric, combined scatterometric-radiometric systems.

1. Introduction

Since, the sea surface microwave reflective and emissive characteristics (radar backscattering coefficients and brightness temperatures) are complex functions of various principal parameters, such as: a current wind speed and a wind direction, a sea wave condition (a swell condition), near sea surface air and sea water temperatures, water salinity and surface pollution, meteorological conditions, etc., for unambiguous and precise retrieval of a specified parameter, such as current wind speed or direction, a sea wave force and swell's direction, water salinity or temperature, near sea surface air temperature, type and thickness of surface pollution, it is necessary to have a priori information about other influenced parameters or to synergy various independent and differing techniques and measurements. Spatio-temporally combined, multi-frequency, polarimetric, active-passive measurements is a sample of such synergy [1,2]. At present, there are several combined scatterometer-radiometer systems operating in various frequency bands [1-8]. Some of them are acceptable for very short distance remote sensing application [3-8], and allow carry out measurements under test-control, quasi-field conditions. Therefore, a reason for a performance of spatio-temporally collocated, multi-frequency and multi-polarization, microwave active-passive measurements under test-control, quasi field conditions is appeared. Such experimental researches are very important for a validation and for an improvement of existed theoretical models describing sea surface, for a development new methods for sea surface mapping, for detection and classification surface signatures and subsurface targets, as well as for entire solution of the sea surface remote sensing inverse problem.

In this paper the results of spatio-temporally collocated, multi-polarization, combined scatterometric-radiometric measurements of perturbed, rippled and smoothed pool water surface microwave reflective (a radar backscattering coefficient) and emissive (a brightness temperature) characteristics angular dependences at three frequencies, at ~5,6GHz, ~15GHz and ~37GHz are presented. The measurements were carried out under clear air, heavy clouds and rain conditions by C-, and Ku-band, single frequency, multi-polarization, combined scatterometric-radiometric systems. The measurements were carried out in the experimental site of ECOSERV Remote Observation Centre Co. Ltd. (ECOSERV ROC), from a quarter circle shaped measuring platform of 7m of radius. All three scatterometric-radiometric systems and the measuring platform were developed and built in Armenia by ECOSERV ROC, under the framework of ISTC (International Science and Technology Center) Projects A-872 and A-1524, in co-operation with the Institute of Radiophysics and Electronics of Armenian National Academy of Sciences.

2. Measuring Facilities and Used Microwave Devices

The measurements were carried out in Armenia, in ECOSERV ROC's experimental site, equipped by two quarter circle shaped stationary measuring platforms of 7m of radius R , one built over the experimental pool of 10m x 3m x 1.5m of sizes and another built over a soil test area of 10m x 3m of sizes. For these measurements C-, Ku-, and Ka-band, ArtAr-5.6, ArtAr-15 and ArtAr-37, combined scatterometric-radiometric systems (CSRS) were used, worked under short range application modes (Fig.1). The CSRS set

on the mobile buggy smoothly moved along a quarter circle shaped path of the measuring platform, from the base (Fig.2) to the top (Fig.3). A drive mechanism of the buggy allows stop it at any point of the path along the platform and perform measurements under any angle of incidence from the interval $0-80^{\circ}$. Detail descriptions of used CSRS are presented in [3-6]. The principal advantages of these unique devices and the whole measuring complex are the capability to perform, multi-frequency, spatio-temporally combined angular and polarization measurements of water surface microwave, active-passive characteristics from the distance $\sim 6m$, under the far field condition of sensing.

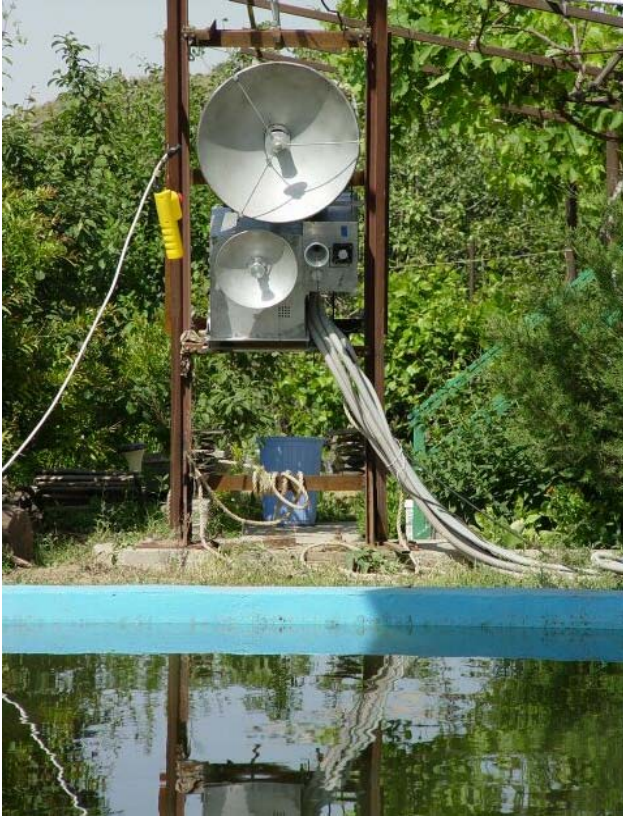


Fig.1 ArtAr-5.6, ArtAr-15 and ArtAr-37 CSRS set on the mobile buggy at the base of the measuring platform



Fig.2 ArtAr-5.6, ArtAr-15 and ArtAr-37 CSRS set on the mobile buggy at the top of the measuring platform



Fig. 3 An indoor calibration and measuring complex of sky, precipitation and ABB layer's brightness temperatures

The experimental site equipped as well by external calibration facilities, built just near the measuring platforms, including two moving test benches (layers): one of the Absolute Black Body (ABB) and another of a metallic sheet (Fig.3). In the experimental site, an indoor calibration facility is available as well, for the

systems external calibration purposes, by sky (Fig.4) and indoor ABB layer (Fig.5). Besides of calibration needs this indoor measuring complex is acceptable for researches of clouds and precipitations microwave features.

Except of the above mentioned external calibration facilities both systems have internal calibration input modules, including two thermo stabilized, controlled microwave keys for each radiometric channel of any of the system. In their switched off operational mode these keys are used as well as an internal calibration levels for calibration of all measured data, including water surface, external calibration ABB layers, sky and precipitation brightness temperatures.

3. The Results of Measurements

Before all series of measurements of pool water surface microwave reflective and emissive characteristics, preliminary measurements of indoor ABB layer's (Fig.3) and sky brightness temperatures (antenna temperatures) were performed, under observation angles 10^0 and 30^0 from a nadir. After that, the CSRS was set on the mobile buggy and measurements of smoothed (SWP), hand perturbed (HPWS) and rippled (RWS) water surfaces were carried out at each angle of incidence from 80^0 to 0^0 . In Figs.1,2,4,5 the samples of such surfaces are presented. The measurements were carried out at "v" and "h" polarizations for radiometric observations and at "vv" and "vh" or "hh" and "hv" polarizations for scatterometric observations, under various conditions of water t_w and air t_a temperatures. During each series of measurement, at the beginning and at the end of the series, an internal calibration noise signals of 18K (for both polarizations of Ku-, and Ka-band systems) and 7.7K and 12K (for "h" and "v" polarization of C-band system, respectively) of level were used for calibration of data obtained by radiometric channels of observation. For scatterometric channels calibration, internal calibration signals of a level of $\sim 10^{-11}W$ were used, estimated to the radar receivers inputs. These calibration signals allow approximately estimate absolute values of water surface radar backscattering coefficients and its brightness temperatures.

Multi-frequency and multi-polarization measurements of water surface microwave active and passive characteristics were carried out by two ways. The first has included measurements at 9 fixed position of the buggy, corresponding to the angle of incidence from 80^0 to 0^0 , by a step of 10^0 . The second way has included uninterrupted measurements during a smooth movement of the buggy from the position corresponding to 80^0 or 0^0 to the position corresponding to 0^0 or 80^0 .

During each series of measurements a calibration of radiometric data was performed by measurements of horizontally positioned ABB test bench's and metallic sheet's reflective and emissive characteristics, at the angle of incidence $\vartheta \sim 0^0$, to provide full coverage of the observed surfaces (ABB and metallic sheet) by antenna footprint. The absolute values of water surface brightness temperature were estimated from internal and external ABB layers' brightness temperatures, defined as $T_B = (273 + t_a) \cdot \chi$, where the ABB layers' coefficient of emission χ was taken equal to 0.97. The absolute values of water surface radar backscattering coefficients were estimated as $\sigma_{ij}[dB] = C + 10 \cdot \log_{10}(U_w \cdot \cos \vartheta / U_c)$, where indices $i = "v" \text{ or } "h"$ and $j = "v" \text{ or } "h"$ show transmitted and received radar signals polarizations, U_w and U_c are increments of radar outputs of the system, corresponding to water surface and radar channel calibration signals, relatively to the radar receiver's noise ("0") level, and C is a constant value, defined from antenna gain, beamwidths in both planes, transmitter and calibration signals powers, and of the radius $R \sim 7m$ of the circle of the measuring platform, through which the systems have moved.



Fig. 7 Hand Perturbed Water Surface

Fig. 8 Rippled Water Surface

Fig. 9 Rain Perturbed Water Surface

Measured data of the absolute values of perturbed and smoothed pool water surfaces radar backscattering coefficients at vv and hh polarizations and brightness temperatures at v and h polarizations allowed estimate and research angular and polarization features of radar and radiothermal contrasts originated on the water surface due to the changes of surface roughness parameters. Radar and radiothermal contrasts between perturbed and smoothed water surfaces were defined as: $\Delta\sigma_{vv, hh} [dB] = \sigma_{vv, hh} (HPWS) [dB] - \sigma_{vv, hh} (SWS) [dB]$ and $\Delta T_{Bv, h} [K] = T_{Bv, h} (HPWS) [K] - T_{Bv, h} (SWS) [K]$, respectively.

Since, the perturbations of pool water surface were made by hand (See Fig.3), due to the absence of powerful fans for wind waves generation, the results of performed unique measurements have only qualitative sense. Therefore, only, radar and radiothermal contrasts angular and polarization peculiarities will be considered further.

In Fig.10-Fig.12 the curves of angular dependences of pool water surface radar and radiothermal contrasts at 5.6GHz, 15GHz and 37GHz are presented, respectively. The curves of Fig.10 and Fig.11 correspond to radar signals “vv” and “vh” and radiometric signals “v” and “h” polarizations. The curves of Fig.12 correspond to radar signals “vv” and radiometric signals “v” polarizations, only. Since, it was impossible to change and to control surface perturbations, the radar contrasts’ angular dependences were built for angles of incidence 0-32°, only. However, obtained angular dependences represented in Fig.10 - Fig.12 are in good agreement with the theoretical results of [9,10].

An interesting situation has happened during one series of measurements. A very fast change in atmospheric condition took place during that experiment. At the beginning of the experiment the sky was clear. During several minutes, when the buggy has stopped at a position corresponding to the angle of incidence 30°, a huge rain-cloud (cumulo-nimbus) has appeared on the scene, from a mountain, and very fast passed the experimental site. Therefore, the cloud’s effect was recorded at the angles of incidence 30° and 20°, only. The measurements were not interrupted, and when the buggy stopped at a position corresponding to the angle of incidence 20°, a cloudburst with hail has begun and continued about 10minutes. Rain-hail drops have perturbed the pool water surface as shown in Fig.6. When the rain stopped and the water surface has been smoothed, the measurements of hand perturbed water surface reflective and emissive characteristics were continued for angles of incidence 20°, 10° and 0°. A light rain effect was recorded as well at the angle of incidence 10°.

For a comparison, in Fig.10-Fig.12 rain and clouds influences on water surface microwave reflective and emissive characteristics in a form of corresponding radar and radiothermal contrasts are presented. In accordance with the measured data, radar backscattering coefficients of RPWS and HPWS or corresponding radar contrasts are practically equal. The radiothermal contrast due to the rain perturbation of a water surface (that is the difference between brightness temperatures of RPWS and SWS) is smaller, than a radiothermal

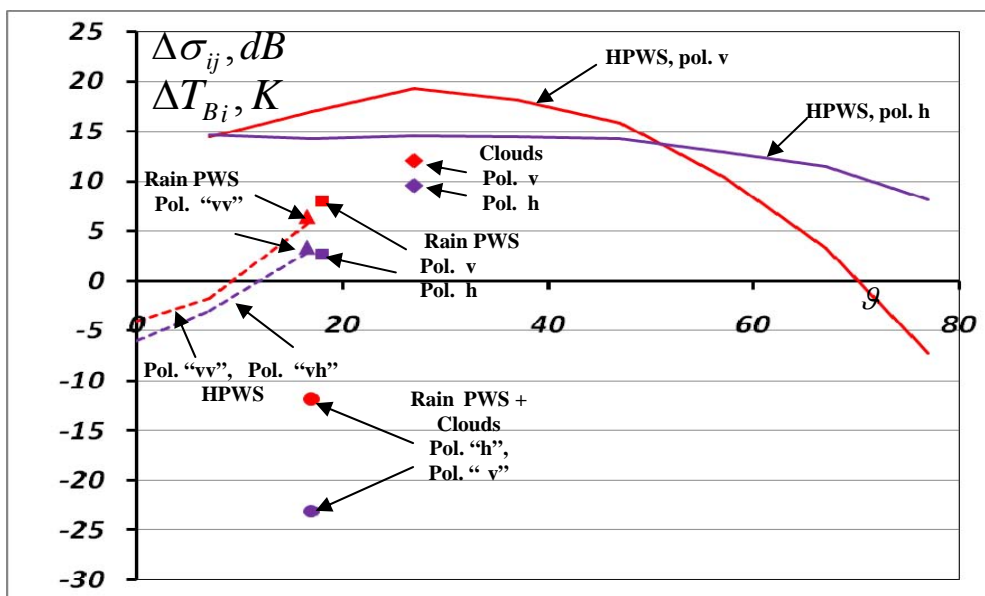


Fig.10 Angular dependences of pool water surface radar and radiothermal contrasts at 5.6GHz

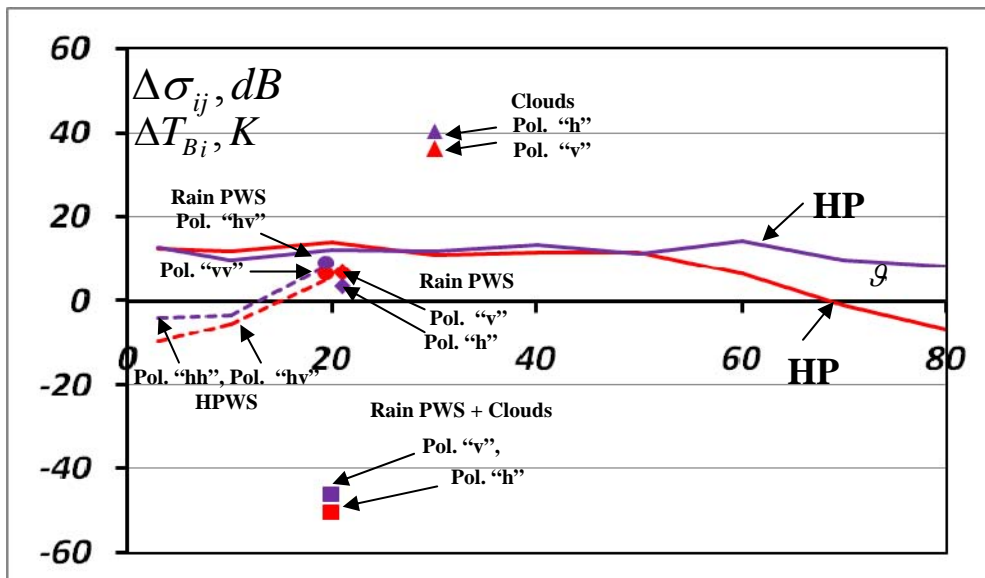


Fig.11 Angular dependences of pool water surface radar and radiothermal contrasts at 15GHz

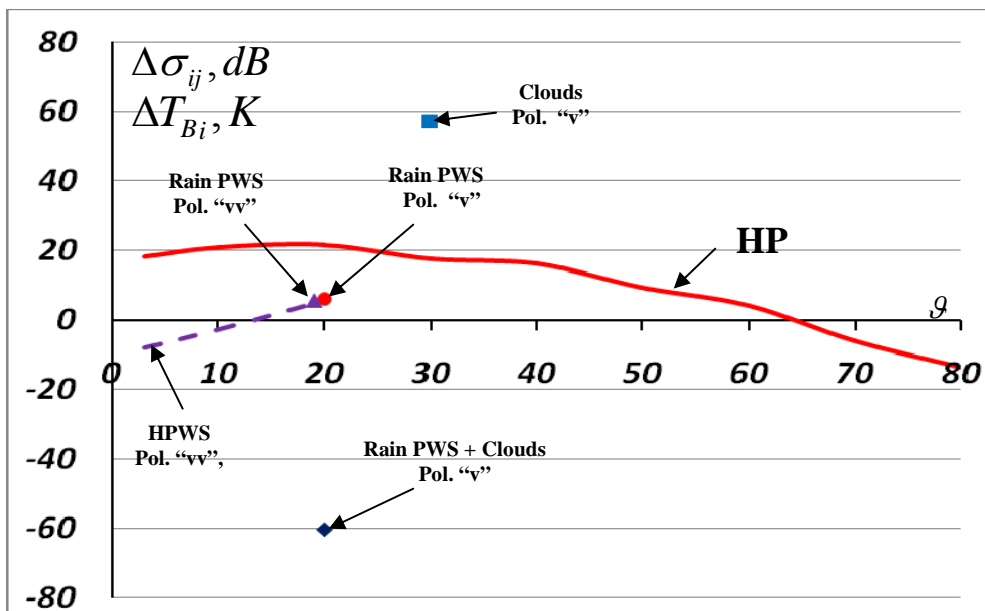


Fig.12 Angular dependences of pool water surface radar and radiothermal contrasts at 37GHz

contrast defined as a difference between brightness temperatures of HPWS and SWS. It may be due to a change of a specular component of reflection of cloud's emission, only.

The results of Fig.10 - Fig.12 show, that the absolute values of radiothermal contrasts due to nimbuses at frequencies 5.6GHz, 15GHz and 37GHz may reach the values 25K, 40K and 60K, respectively. Such contributions in water surface brightness temperatures may be explained by specular reflections of a cloud's emission through water.

4. Conclusion

Thus, preliminary results of simultaneous and spatially coincident measurements of water surface microwave reflective and emission characteristics at 5.6GHz, 15GHz and 37GHz under clear air, cloudy and rain conditions have shown that combined radar-radiometer sensing is an actual and significant tool for improvement existed reflective and radiative transfer models for the sea surface. As well as it is an effective way for solution of problems applied to near sea surface wind and sea surface wave fields parameters precise and unambiguous retrievals, for sea surface mapping, for detection and classification of sea surface and sub-

surface signatures and targets. The paper shows as well the existed experimental site built for water surface, snow, bare and vegetated soils microwave reflective and emissive characteristics simultaneous and spatially coincident multi-frequency and multi-polarization measurements, under test-control, quasi-field conditions and equipped by combined, short pulse, short range application combined scatterometric-radiometric systems of S, C, Ku, K and Ka-band of frequencies. As well as by facilities for microwave devices absolute calibration, by a set of stations (spatially distributed) for in-situ control measurements of soil moisture and temperature, as well as for precipitations (rain, snow), wind (speed and direction) and air (temperature) characteristics sustainable monitoring and recording. The paper has an aim as well to attract attention of interested researchers and to invite them to perform their own or joint researches using available devices and facilities.

5. Acknowledgement

Authors express their gratitude to the International Science and Technology Center of Moscow (ISTC), since the experimental site and combined scatterometric-radiometric systems ArtAr-5.6. ArtAr-12 and ArtAr-37 were developed and built due to the financial maintenance provided by ISTC through the Projects A-872 and A-1524.

6. References

- [1] E.Njoku, W.Wilson, S.Yueh, T.Jackson, V.Lakshmi, "Soil Moisture and Vegetation Observations During SGP99 using the PALS Airborne Microwave Radiometer-Radar System", Proceedings of IGARSS'2000, 24-28 July, Hawaii, USA, 2000, TU06 AM, CD-ROM.
- [2] E.G.Njoku, W.J.Wilson, S.H.Yueh and Y.Rahmat-Samii, "A Large-Antenna Microwave Radiometer-Scatterometer Concept for Ocean Salinity and Soil Moisture Sensing", IEEE Transactions on Geoscience and Remote Sensing, Vol. 38, No. 6, November 2000, pp. 2645-2655.
- [3] A.K.Arakelyan, E.R.Alaverdyan, A.A.Arakelyan, S.A.Darbinyan, A.K.Hambaryan, V.K.Hambaryan, V.V.Karyan, G.G.Ogannisyan, N.G.Poghosyan, A.I.Smolin, "Polarimetric, Ka-Band, Combined, Short Pulse Scatterometer and Radiometer System for Platform Application", Radar Sensor Technology IX, edited by Robert N.Trebits, James L.Kurtz, Proceedings of SPIE, Vol. 5788 (SPIE, Bellingham, WA, 2005), pp.172-177.
- [4] A.K.Arakelyan, A.K.Hambaryan, A.I.Smolin, V.V.Karyan, N.G.Poghosyan, M.A.Sirunyan, M.R.Manukyan, A.A.Arakelyan, "Polarimetric, Ka-Band, Combined, Short Pulse Scatterometer and Radiometer System", Progress in Contemporary Radio Electronics, No.7, 2005, pp.73-77. (In Russian).
- [5] A.K.Arakelyan, I.K.Hakobyan, A.A.Arakelyan, A.K.Hambaryan, M.L.Grigoryan, E.A.Vardanyan, V.V.Karyan, M.R.Manukyan, and G.G.Hovhannisyan, "Short Pulse, Polarimetric Scatterometer at 5.6GHz", Progress in Contemporary Radio Electronics, No.6, 2006, pp.44-49. (In Russian).
- [6] A.K.Arakelyan, I.K.Hakobyan, A.A.Arakelyan, A.K.Hambaryan, M.L.Grigoryan, V.V.Karyan, M.R.Manukyan, G.G.Hovhannisyan, N.G.Poghosyan and S.F.Clifford, "Ku-Band, Short Pulse, Dual-Polarization, Combined Scatterometer-Radiometer", Progress in Contemporary (Present-Day) Radio Electronics, No. 12, 2007, pp. 41-50. (In Russian).
- [7] A.K.Arakelyan, I.K.Hakobyan, A.A.Arakelyan, A.K.Hambaryan, M.L.Grigoryan, E.A.Vardanyan, V.V.Karyan, M.R.Manukyan, G.G.Hovhannisyan and N.G.Poghosyan, "Short Pulse, Polarimetric, Combined Scatterometer-Radiometer at 20GHz", Progress in Contemporary (Present-Day) Radio Electronics, No. 9, 2007, pp. 56-63. (In Russian).
- [8] A.K.Arakelyan, I.K.Hakobyan, A.A.Arakelyan, A.K.Hambaryan, M.L.Grigoryan, V.V.Karyan, M.R.Manukyan, G.G.hovhannisyan and N.G.Poghosyan, "S-Band, Polarimetric, Short Pulse, Short Distance application, Combined Scatterometer-Radiometer", Electromagnetic Waves and Electronic Systems, No. 3, 2007, pp. 52-60. (In Russian).
- [9] A.K.Arakelian, "An Analysis of Characteristics of Temperature-Wind Variations of Sea Surface Brightness Temperature", Izvestia RAN, Series of Fizika Atmosferi i Okeana, 1992, vol.28. no.2, pp.196-205, (in Russian).
- [10] A.K.Arakelyan and A.A.Arakelyan, "Possibility for Atmospheric Stratification Condition Unambiguous Determination by Synergy Data of Sea Surface Altimetric and Scatterometric Observations", Russian Journal on Electromagnetic Waves and Electronic Systems, vol.9, no.9-10, 2004, pp.16-21. (In Russian).

Three-Frequency and Multi-Polarization Measurements of Bare and Vegetated Soils Microwave Reflective and Emissive Characteristics Angular Dependences by C, Ku and Ka-Band Combined Scatterometric-Radiometric Systems

Artashes K. Arakelyan, Astghik K. Hambaryan,, Vardan K. Hambaryan, Vanik V. Karyan,
Mushegh R. Manukyan, Melanya L. Grigoryan, Gagik G. Hovhannisyan
and Arsen A. Arakelyan

*ECOSERV Remote Observation Centre Co. Ltd., 2 G. Njdeh Str., #24, Yerevan, 0006, Armenia
E-mails: arakelyanak@yahoo.com, ecoservroc@yahoo.com*

In this paper the results of simultaneous and spatially coincident, multi-frequency (three-frequency), multi-polarization measurements of bare and vegetated soils microwave reflective and emissive characteristics angular dependences at 5.6GHz, 15GHz and 37GHz are presented. The measurements were carried out under various conditions of observation, soil moistures, fire, smock and ash conditions, by C, Ku and Ka-band, polarimetric, combined scatterometric-radiometric systems.

1. Introduction

The main obstacle to achieve unambiguous and precise solution for inverse problems of the Earth (sea, land) remote sensing is multi-parametric dependences of the observed surfaces radar backscattering coefficients and brightness temperatures. To overcome these obstacles it is necessary to synergy data of multi-frequency and multi-polarization measurements obtained by various means of sensing. In particular, spatio-temporally combined, multi-polarization, multi-frequency active-passive measurements of observed surfaces reflective and emissive characteristics are a sample of such a synergy. For precise and unambiguous solution of bare and vegetated soils microwave remote sensing inverse problems it is necessary as well to improve reflective and radiative transfer models for soil and vegetation. For this purpose it is necessary and very significant to develop and to manufacture multi-frequency and multi-polarization complex of combined radar-radiometers, suitable for short range remote sensing application and to perform field or quasi-field measurements under controlled conditions. Such a task was solved in Armenia by ECOSERV Remote Observation Centre Co. Ltd. (ECOSERV ROC) in co-operation with the Institute of Radiophysics and Electronics of Armenian national Academy of sciences in the framework of the ISTC (International Science and Technology Center) Projects A-872 and A-1524. As a result, C (~5.6GHz), Ku (~15GHz) and Ka (~37GHz) band multi-polarization, combined, short pulse scatterometer-radiometer systems for short range remote sensing application (the minimum operational range of the systems' scatterometers is 4m) were developed and tested in field conditions. To perform angular measurements the ECOSERV ROC built in its experimental site corresponding measuring platforms and calibration facilities.

In this paper the results of simultaneous and spatially coincident, multi-frequency (three frequency), polarimetric, spatio-temporally collocated measurements of bare, dry vegetated and ash covered soils microwave reflective (radar backscattering coefficient) and emissive (brightness temperature) characteristics angular dependences at ~5.6GHz, ~15GHz and ~37GHz are presented. During these experiments the observed area was set ablaze and multi-frequency, multi-polarization, microwave active and passive measurements at 30⁰ incidence angle were continued for smock, fire and ash situations.

2. Measuring Facilities and Used Microwave Devices

The measurements were carried out in Armenia, in ECOSERV ROC company's experimental site, equipped by two quarter circle shaped stationary measuring platforms of 7m of radius R , one built over the experimental pool of sizes of 10m x 3m x 1.5m and another built over soil test area of sizes of 10m x 3m (Fig.1). The experimental site is equipped as well by external calibration facilities, built just near the measuring platforms, including two moving test benches (layers): one of the Absolute Black Body (ABB) and another of a metallic sheet (Fig.1). In the experimental site, an indoor calibration facility is available as well, for the systems external calibration purposes, by sky and indoor ABB layer (Fig.2). Besides of calibration needs this indoor measuring complex is acceptable for researches of clouds and precipitations microwave features.



Fig. 1 The Experimental Site of the ECOSERV ROC Company



Fig. 2 An Indoor Calibration and Measuring Complex

For these measurements C-, Ku-, and Ka-band, ArtAr-5.6, ArtAr-15 and ArtAr-37, combined scatterometric-radiometric systems (CSRS) were used, all worked under short range application modes. All CSRS set on the mobile buggy silki moved along a quarter circle shaped path of the measuring platform, from the base (Fig.3) to the top (Fig.1). A drive mechanism of the buggy allows stop it at any point of the path along the platform and perform measurements under any angle of incidence from the interval $0-80^{\circ}$. The principal advantages of these unique devices and the whole measuring complex are the capability to perform multi-

frequency, spatio-temporally combined, angular and polarization measurements of soil, snow, water ice and water surface microwave, active-passive characteristics, under far field conditions of sensing. The main technical characteristics of these systems are presented below, in the Table 1.

Table 1.

	C -	Band	Ku -	Band	Ka -	Band
	Radar Channel	Radiometric Channel	Radar Channel	Radiometric Channel	Radar Channel	Radiometric Channel
Central frequency	5.6GHz	5.6GHz	13.6GHz	13.6GHz	37GHz	37GHz
Antenna: Gain / Beamwidth / Sidelobes	Parabolic ~ 22dB /	Antenna 8 ⁰ / -18dB	Parabolic ~ 25dB /	Antenna 6.5 ⁰ / -20dB	Horn ~ 23dB /	Antenna 9 ⁰ / -18dB
A train of radar pulses, duration of each pulse	8 pulses, 25ns each		8 pulses, 25ns each		8 pulses, 25ns each	
Pulse repetition frequency within the train	1.6MHz		1.6MHz		1.6MHz	
Repetition frequency of the train	1KHz		1KHz		1KHz	
Pulse power	50-50mW		75-00mW		30mW	
Polarization: Transmission Reception:	“v” or “h” “vv”, “vh” or “hv”, “hh”	“v” and “h”	“v” or “h” “vv”, “vh” or “hv”, “hh”	“v” and “h”	“v” or “h” “vv” or “hh”, or “vh” or “hv”	“v” or “h”
Pre-detection bandwidth	~100MHz	~500MHz	~100MHz	~500MHz	~100MHz	~800MHz
Receiver’s sensitivity	-30dB/W	~0.1K	-30dB/W	~0.15K	-126dB/W	~0.3K
Operational range	4 - 250m		4 - 250m		4 - 50m	
Dimensions / weight	24 x 26 x	50cm ³ /12kg	38 x 34 x	54cm ³ /25kg	18 x 22x	50cm ³ / 7kg

3. The Results of Measurements

Before all series of measurements of soil and vegetation microwave reflective and emissive characteristics a calibration of the measured data were performed by measuring of indoor and outdoor ABB layer’s and sky brightness temperatures. Simultaneously with scatterometric and radiometric measurements, a complete set of ground truth data, including soil moisture, air, soil and water temperatures were also collocated and recorded. Remote control of the CSRS, measured data recording and processing were performed by personal computers set in the work laboratory built just near the platforms. The measurements of soil surface microwave characteristics were carried out from 9 fixed positions of the buggy, corresponding to the angles of incidence from 80⁰ to 0⁰, by a step of 10⁰. During all series of measurements internal calibration noise signals were used for radiometric channels calibration. For scatterometric channels calibration, internal calibration signals of a level of ~10⁻¹¹W were used, estimated to the receivers inputs. These calibration signals allow approximately estimate absolute values and changes of the observed surface radar backscattering coefficients and brightness temperatures. At the inputs of all three devices there are thermo stabilized microwave keys, which may switch off receivers’ inputs from antennas and work as input matched loads for receivers. Since, the outputs of these matched loads might be used as starting points for estimation of absolute values of brightness temperatures (antenna temperatures) of the observed surface, during all series of measurements these keys switched off antennas for a few times for 15-20 seconds.

The absolute values of observed surface brightness (antenna) temperatures were estimated from the following equation: $T_{Bi} = T_i^K - (U_i^K - U_i^S) / \Delta U_i^{cal}$, where, $T_{Bi} = \chi \cdot (273 + t_K)$ is a brightness temperature of matched load, t_K is a temperature of the matched load in centigrade, the coefficient of emission the matched load χ was taken equal to 0.99. U_i^K , U_i^S and ΔU_i^{cal} are outputs of radiometers, corresponding to the matched load, observed surface and the increment of the radiometric output’s due to internal calibration noise signal switching, respectively.

The absolute values of observed surface radar backscattering coefficients were estimated from the following equation: $\sigma_{ij}[dB] = C + 10 \cdot \log_{10} \left(\frac{U_{ij}^S \cdot \cos \theta}{U_{ij}^{cal}} \right)$, where indices $i = "v" \text{ or } "h"$ and $j = "v" \text{ or } "h"$ show transmitted and received radar signals polarizations, U_{ij}^S and U_{ij}^{cal} are increments of the system scatterometric outputs estimated from scatterometric receiver's noise ("zero") level, corresponding to soil surface and switched on radar channel calibration signal. C is a constant value, defined from antenna gain, beamwidths in both planes, transmitter and calibration signals powers, and of the radius $R \sim 7m$ of the circle of the measuring platform, through which the systems have moved. For ArtAr-5.6 and ArtAr-15 systems the constant C is about 2dB and 5dB, respectively.

Angular measurements were carried out for wet and dry soils covered by mature grass (Fig.3), dry soil covered with dry, cut grass, and ash covered soil after extinguished fire. In Figs.4 – 6 pictures of measured soil samples are presented.



Fig. 3 The CSRS at 5.6GHz, 15GHz and 37 GHz set on the mobile buggy at the bottom of the platform



Fig.4 A set ablaze of dry, cut grass covered dry soil



Fig.5 Smock and fire covered soil



Fig.6 The soil covered by chilled (extinct) ash

In Figs. 7 and 8 simultaneously measured at 5.6GHz and 15GHz data of soil surfaces (Figs. 4–6) radar cross sections angular dependences are presented. In Figs. 9 and 10 simultaneously measured at 5.6 GHz and 15 GHz data of soil surfaces (Figs. 4–6) brightness temperatures angular dependences are presented.

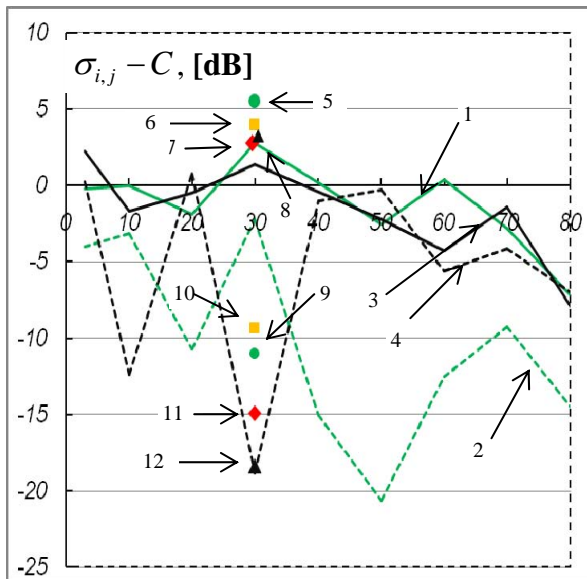


Fig.7 Radar cross section angular dependence at 15GHz
 1 - Cut grass at "vv", 2 - Cut grass at "vh", 3 - Chilled ash at "vv", 4 - Chilled ash at "vh", **Markers:** 5 - Cut grass at "vv" (Green), 6 - Smock at "vv" (Yellow), 7 - Fire at "vv" (Red), 8 - Hot ash at "vv" (Black), 9 - Cut grass at "vh" (Green), 10 - Smock at "vh" (Yellow), 11 - Fire at "vh" (Red), 12 - Hot ash at "vh" (Black)

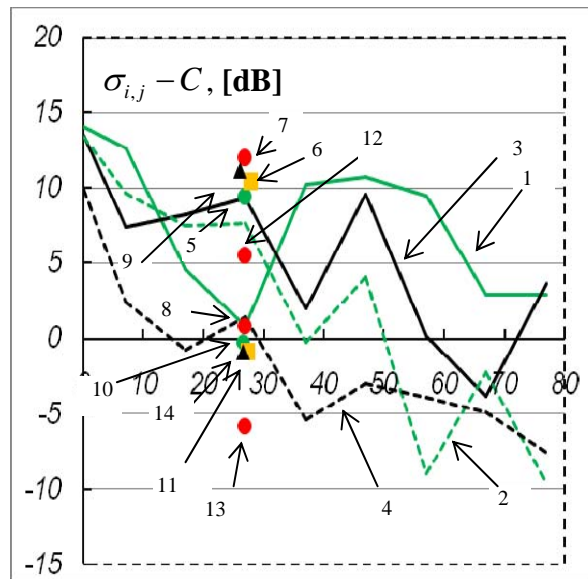


Fig.8 Radar cross section angular dependence at 5.6GHz
 1 - Cut grass at "vv", 2 - Cut grass at "vh", 3 - Chilled ash at "vv", 4 - Chilled ash at "vh", **Markers:** 5 - Cut grass at "vv" (Green), 6 - Smock at "vv" (Yellow), 7 - Fire max. at "vv" (Red), 8 - Fire min. at "vv" (Red), 9 - Hot ash at "vv" (Black), 10 - Cut grass at "vh" (Green), 11 - Smock at "vh" (Yellow), 12 - Fire max. at "vh" (Red), 13 - Fire min. at "vh" (Red), 14 - Hot ash at "vh" (Black)

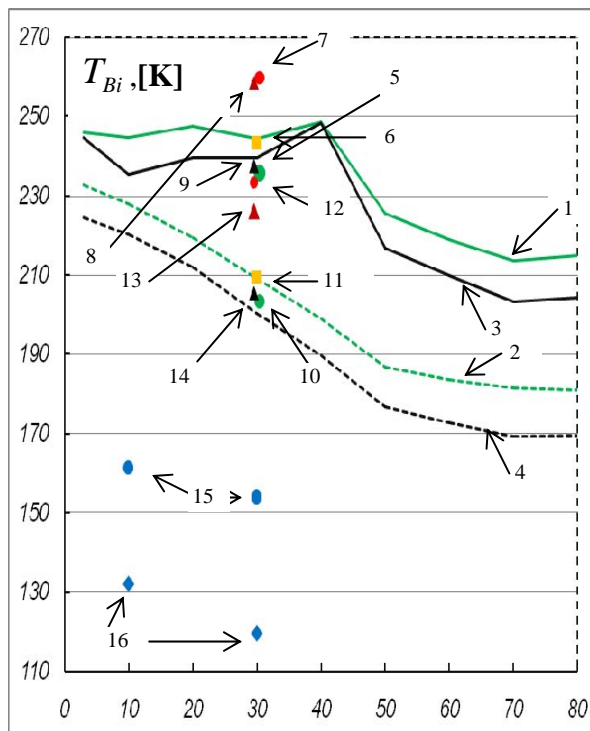


Fig.9 Brightness temperature angular dependence at 15GHz
 1 - Cut grass at "v", 2 - Cut grass at "h", 3 - Chilled ash at "v", 4 - Chilled ash at "h", **Markers:** 5 - Cut grass at "v" (Green), 6 - Smock at "v" (Yellow), 7 - Fire at "vv" (Red), 8 - Smolder at "v" (Purple), 9 - Hot ash at "v" (Black), 10 - Cut grass at "h" (Green), 11 - Smock at "h" (Yellow), 12 - Fire at "h" (Red), 13 - Smolder at "h" (Purple), 14 - Hot ash at "h" (Black), 15 - Clear sky at "v", 16 - Clear sky at "h"

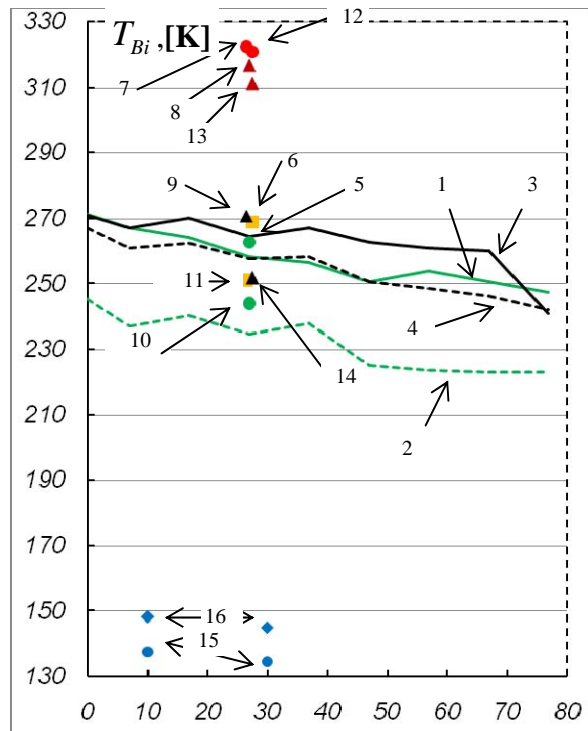


Fig.10 Brightness temperature angular dependence at 5.6GHz
 1 - Cut grass at "v", 2 - Cut grass at "h", 3 - Chilled ash at "v", 4 - Chilled ash at "h", **Markers:** 5 - Cut grass at "v" (Green), 6 - Smock at "v" (Yellow), 7 - Fire at "vv" (Red), 8 - Smolder at "v" (Purple), 9 - Hot ash at "v" (Black), 10 - Cut grass at "h" (Green), 11 - Smock at "h" (Yellow), 12 - Fire at "h" (Red), 13 - Smolder at "h" (Purple), 14 - Hot ash at "h" (Black), 15 - Clear sky at "v", 16 - Clear sky at "h"

4. Conclusion

Thus, preliminary results of simultaneous and spatially coincident measurements of soil and vegetation microwave reflective and emission characteristics at 5.6GHz, 15GHz and 37GHz under various conditions of observation, soil moistures, fire, smock and ash conditions have shown that combined radar-radiometer sensing is an actual and significant tool for improvement existed reflective and radiative transfer models for bare and vegetated soils. As well as it is an effective way for solution of problems applied to soil moisture precise and unambiguous retrievals. The paper shows as well the existed experimental site built for water surface, snow, bare and vegetated soils microwave reflective and emissive characteristics simultaneous and spatially coincident multi-frequency and multi-polarization measurements, under test-control, quasi-field conditions and equipped by combined, short pulse, short range application combined scatterometric-radiometric systems of S, C, Ku, K and Ka-band of frequencies. As well as by facilities for microwave devices absolute calibration, by a set of stations (spatially distributed) for in-situ control measurements of soil moisture and temperature, as well as for precipitations (rain, snow), wind (speed and direction) and air (temperature) characteristics sustainable monitoring and recording. The paper has an aim as well to attract attention of interested researchers and to invite them to perform their own or joint researches using available devices and facilities.

Acknowledgement

Authors express their gratitude to the International Science and Technology Center of Moscow (ISTC), since the experimental site and combined scatterometric-radiometric systems ArtAr-5.6, ArtAr-12 and ArtAr-37 were developed and built due to the financial maintenance provided by ISTC through the Projects A-872 and A-1524.

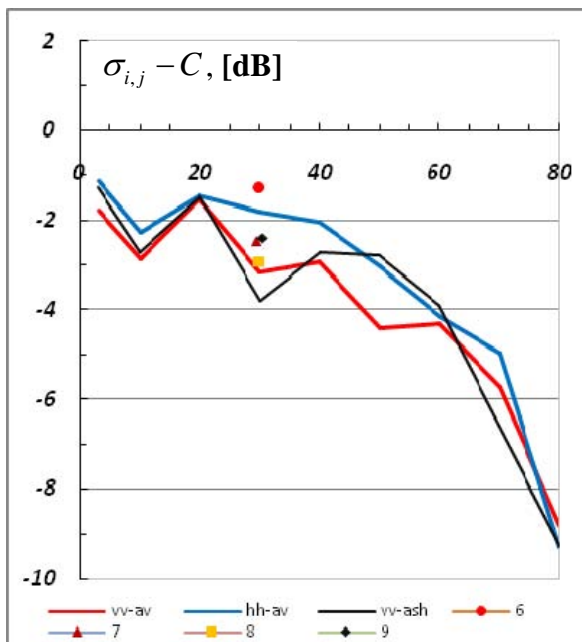


Fig.9 Covered by dry, cut grass dry soil radar cross sections angular dependences at 37GHz
 Red – soil moisture 8-9%, $t_a \sim 23^{\circ}\text{C}$, $t_s \sim 23^{\circ}\text{C}$, at vv-pol.;
 Blue solid – soil moisture 8-9%, $t_a \sim 23^{\circ}\text{C}$, $t_s \sim 23^{\circ}\text{C}$, at hh-pol.;
 Black solid – the soil covered by ash at vv-pol.;
Markers: Yellow Square –smock coverage at vv-pol.;
 Red Circle –fire at vv-pol.; Purple Triangle – smolder at vv-pol.; Black Rhomb – ash at vv-pol.

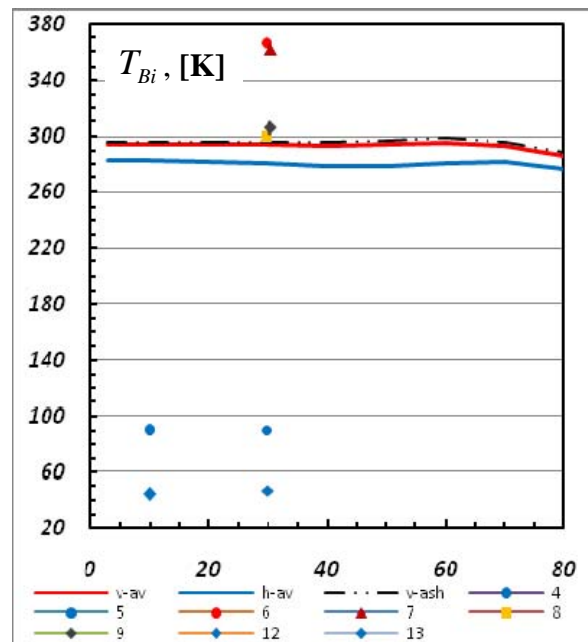


Fig.10 Covered by dry, cut grass dry soil brightness (antenna) temperatures angular dependences at 37GHz
 Red – soil moisture 8-9%, $t_a \sim 23^{\circ}\text{C}$, $t_s \sim 23^{\circ}\text{C}$, at v-pol.;
 Blue solid – soil moisture 8-9%, $t_a \sim 23^{\circ}\text{C}$, $t_s \sim 23^{\circ}\text{C}$, at h-pol.;
 Black solid – the soil covered by ash at vv-pol.;
Markers: Yellow Square –smock coverage at v-pol.;
 Red Circle –fire at v-pol.; Purple Triangle – smolder at v-pol.; Black Rhomb – ash at v-pol.; Blue Circle – clear sky at v-pol.; Blue Rhomb – clear sky at h-pol.

Section 3:
Microwave Antennas and Devices

Автоматический комплекс для определения параметров антенн диапазона КММВ методом планарного сканирования в их ближнем поле

В.Г. Аветисян

*Ереванский НИИ Средств Связи, Армения, Ереван 0015, ул. Дзорани 26
Российско-Армянский (Славянский) Университет, физико-технический
факультет, Ереван 0051, ул. Овсепя Эмина 123*

Предлагается построение автоматического измерительного комплекса для определения параметров антенн диапазона коротких миллиметровых волн (КММВ, $f = 60...300 \text{ ГГц}$) по методу планарных измерений ближнего комплексного поля испытываемых антенн. Приводятся решения для построения составных систем комплекса – радиоизмерительной, механического сканирования и системы автоматического управления. Требования к основным узлам систем соответствуют уровню современной технологии. В результате возможно достижение точностей измерения амплитуды и фазы ближнего поля испытываемых антенн диапазона КММВ, сравнимых с точностями при подобных измерениях антенн диапазона сантиметровых волн. Комплекс универсален для применения в различных спектральных участках диапазона КММВ, что существенно снизит затраты на тестирование антенн.

1. Введение

Потребность в увеличении информационной емкости разного рода радиотехнических систем, в увеличении разрешения и уменьшении габаритов их антенных устройств диктует построение аналогов таких систем в диапазоне КММВ. Следствием этого является перенос техники измерений и, в частности, антенных измерений в этот диапазон. Из существующих методов антенных измерений выделяется прогрессирующий метод измерений по ближнему полю испытываемой антенны (ИА), обладающий потенциально более высокой точностью определения характеристик ИА по сравнению с методами по дальнему полю. Разработанные модификации метода по ближнему полю ИА представлены в [1-8]. Они основаны на сканировании зонда по определенной поверхности (плоскость, сфера, цилиндр и т.д.) в ближнем поле ИА и измерении либо амплитуды и фазы этого поля, либо только амплитуды. При только-амплитудных измерениях возрастает либо время измерений ([5, 6]), либо имеем сложный алгоритм математической обработки для получения конечных результатов о восстановленном дальнем поле ([5-7]) или имеем ограниченный диапазон измерений (до 20 дБ [8]). Из всех модификаций скоротечностью процесса обработки результатов измерений выделяется, так называемый сейчас, обычный метод планарных измерений. Он отличается большой надежностью конечных результатов и апробирован в течение более чем трех десятилетий. Метод использует сканируемый по траектории “растр” единственный пробный зонд, а в узлах прямоугольной сетки координат плоскости сканирования измеряются как амплитуда, так и фаза ближнего поля ИА, измерение которой резко усложняется с повышением рабочей частоты.

В работе [9] представлена реализация такого метода автоматизированным измерительным комплексом для ИА диапазона длин волн 0.5...0.61 мм ($\sim 550 \text{ ГГц}$). В нем исходным сигналом является СВЧ сигнал на частоте 5 ГГц. Он передается от стационарной аппаратуры к несущей непосредственно зонд каретке посредством подвижной линии передачи (ПЛП). Она построена на вращающихся сочленениях отрезков коаксиальной линии. Специально разработанная конструкция такой ПЛП обеспечивает великолепную стабильность передачи исходного полезного сигнала (фазовая нестабильность 0.07°). Сигнал же рабочей частоты ИА получается частотным умножением исходного сигнала в 100 раз с помощью установленного на этой каретке умножителя частоты. Затем этот сигнал излучается пробным зондом на приемную ИА.

Однако, такая реализация метода приводит к неизбежному 100-кратному умножению фазовых уходов, возникающих при передаче исходного сигнала, а вынужденная установка умножителя частоты на движущейся каретке не способствует обеспечению надежной и стабильной работы умножителя. Отметим, что при измерениях таким комплексом, ИА должна работать только в режиме приема, что неприемлемо при определении характеристик передающих антенных систем с невзаимными элементами.

В данной работе предлагается построение высокоточного автоматического измерительного комплекса для антенн диапазона КММВ, также реализующего обычный метод планарных измерений. Комплекс обеспечивает измерения как передающих, так и приемных ИА. Исходным полезным сигналом в комплексе, в отличие от [9], является сигнал уже рабочей частоты ИА диапазона КММВ. С точки зрения работы комплекса в различных спектральных участках диапазона КММВ он универсален. Блок-схема комплекса (при работе ИА в режиме передачи) и блок-схема формирования опорного и полезного сигналов приведены ниже.

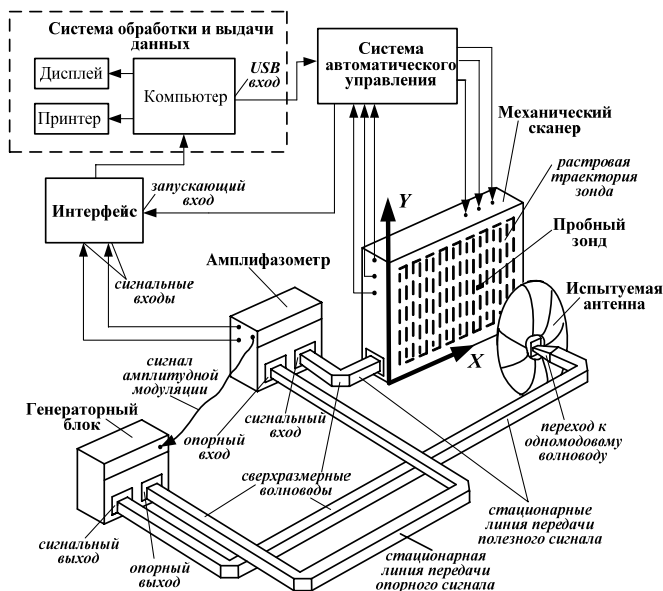


Рис.1. Блок-схема автоматического комплекса

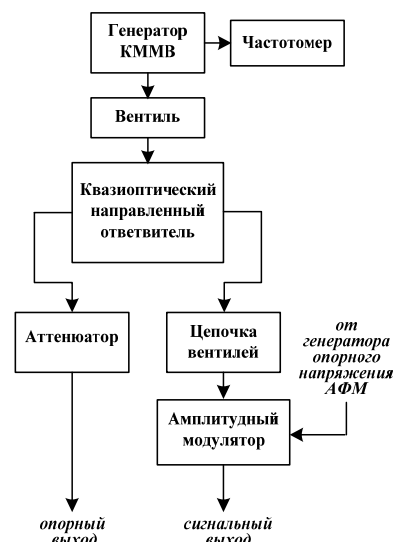


Рис.2. Блок-схема формирования опорного и полезного сигналов

Радиоизмерительная система (см. рис. 1) содержит генераторный блок, ИА, пробный зонд, амплифазометр, интерфейс, стационарные линии для передачи опорного и полезного сигналов и смонтированную на сканере ПЛП полезного сигнала. ПЛП осуществляет его передачу на отрезке «сканируемый зонд - стационарная аппаратура». Система механического сканирования состоит из механического сканера с приводом движения массивной X -каретки, на которой смонтирован привод движения легкой Y -каретки, несущей непосредственно сканируемый зонд. В систему сканирования входят также смонтированные на сканере два механизма компенсации изменения длины ПЛП. Система автоматического управления обеспечивает управление процессом измерений и их автоматизацию. Система обработки и выдачи данных по измеренным данным о ближнем поле, поступающих с выхода интерфейса, восстанавливает дальнее поле и определяет рабочие характеристики ИА.

2. Радиоизмерительная система

2.1. Радиоаппаратурная часть

Сигнал рабочей частоты ИА (см. рис. 2), генерируемый генератором КММВ, проходит через вентиль и в квазиоптическом направленном ответвителе делится на две части. Одна часть с опорного выхода генераторного блока направляется через стационарную линию передачи опорного сигнала к опорному входу амплифазометра (АФМ) радиоаппаратурной части системы. Другая же часть проходит через цепочку вентиля и затем модулируется по амплитуде, преобразуясь в полезный сигнал. В режиме приема ИА, он с сигнального выхода генераторного блока передается через ПЛП к излучающему на ИА зонду и с выхода ИА поступает на другой сигнальный вход АФМ. В режиме передачи ИА, полезный сигнал с сигнального выхода генераторного блока передается на вход излучающей ИА и с выхода приемного зонда через ПЛП далее направляется на сигнальный вход АФМ. Управляющий сигнал амплитудного модулятора подается от НЧ или СВЧ генератора опорного напряжения АФМ. Радиоизмерительные системы для случаев НЧ и СВЧ амплитудных модуляций

приведены в [10], где проведен анализ работы этих систем. Выходными сигналами АФМ являются квадратурные I, Q компоненты полезного сигнала, поступающие на сигнальные входы интерфейса.

Поясним наиболее существенные моменты при построении предложенных радиоизмерительных систем. Для корректного проектирования таких систем необходимы оценки основных исходных параметров [11]. Первый параметр - максимальная полоса частот $\Delta F_{S_{max}}$ полезного сигнала, определяющая наименьшую возможную шумовую частотную полосу ΔF_N системы по условию $\Delta F_{S_{max}} \leq \Delta F_N$. Относительно второго параметра отметим следующее. Значения коэффициента передачи K_{AP} участка “ИА – пробный зонд” при различных точках нахождения зонда на краях зоны сканирования вообще-то являются разными. Наибольшая величина K_{AP}^{max} из этих значений и принимается за второй параметр. Он зависит от размеров и типа ИА, от размеров и типа зонда и от наперед заданного динамического диапазона измерений по мощности K_d , обуславливающего протяженность зоны сканирования. С другой стороны, параметр K_{AP}^{max} в основном обуславливает минимальный полезный сигнал $P_{S_{min}}$ на входе АФМ, поскольку ослабление сигнала на участке “ИА – пробный зонд” намного превосходит ослабления на других участках тракта его передачи. В свою очередь, величины $P_{S_{min}}$ и ΔF_N являются определяющими в отношении сигнал/шум радиоизмерительной системы, от величины которого зависят точности измерения по амплитуде и фазе. Исходные параметры оцениваются следующими выражениями [11]

$$K_P^{max} \approx \frac{S_P}{S_A K_d} v^A v^P \quad (1)$$

$$\Delta F_{S_{max}} \approx \frac{V_{max}}{\delta} \quad (2)$$

где: S_A -площадь апертуры антенны; $S_P = ab \approx 0,8\lambda \times 0,4\lambda = 0,32\lambda^2$ -площадь апертуры зонда (предполагается зонд в виде открытого конца прямоугольного одномодового волновода, применение которого наиболее целесообразно в диапазоне миллиметровых волн и в примыкающей к нему области частот сантиметрового диапазона); $v^A = v_1^A v_2^A v_3^A v_4^A$; v_1^A -коэффициент согласования антенны по поляризации; v_2^A -коэффициент согласования антенны по мощности; v_3^A -коэффициент полезного действия антенны; v_4^A -коэффициент использования площади антенны; $v^P = v_1^P v_2^P v_3^P v_4^P$; v_i^P ($i = 1,2,3,4$) -те же коэффициенты, но для зонда; V_{max} -максимальная скорость сканирования зонда, δ -ошибка позиционирования зонда по осям X, Y . При измерениях ИА с диаметрами $D_A \leq 1000\lambda$, $V_{max} \leq 100$ мм/сек, $v_1^A \approx v_2^A \approx v_3^A \geq 0,9$, $v_4^A \geq 0,5$, $K_d = 30\text{дБ}$, $v_1^P \approx v_2^P \approx v_3^P \geq 0,9$, $v_4^P \approx 0,8$ [12] и $\delta \approx \lambda/100$ имеем $K_{AP}^{e_{max}} \geq -100$ дБ, $\Delta F_{S_{max}} \leq 10$ кГц.

В случае НЧ модуляции производится двойное преобразование частоты полезного сигнала. Вторая промежуточная частота (ПЧ) равна частоте НЧ модуляции и минимальная шумовая полоса $\Delta F_{N_{min}}$ АФМ равна полосе ΔF_{SA} селективных усилителей на второй НЧ ПЧ, поэтому имеем $\Delta F_{N_{min}} \approx \Delta F_{SA} \approx \Delta F_{S_{max}} \approx 10$ кГц, а частота НЧ модуляции составляет 100...200 кГц. Выбор первой СВЧ ПЧ обусловлен степенью вклада шумовых компонент гетеродина КММВ в полосу полезного сигнала и совокупностью требований на СВЧ малощумящие усилители (МШУ) по простоте в эксплуатации, по шумовым параметрам (эквивалентная шумовая температура менее 50°K) и по обеспечению необходимых передаточных характеристик (нестабильность коэффициента передачи по амплитуде менее $0,1$ дБ) а по фазе- 1°). Узкополосные (относительная полоса частот менее 5 %) транзисторные МШУ дециметрового (ДМ) диапазона наилучшим образом обеспечивают эти требования. При вышеприведенных величинах СВЧ ПЧ может быть $F_{IF}^{mic} \geq 2$ ГГц [13]. С учетом показателей современных смесителей диапазона КММВ с СВЧ ПЧ (эквивалентная шумовая температура около 1000°K , потери преобразования около 10 дБ), выполненные по изложенной в [14] методике расчеты показывают, что радиоаппаратурная часть системы может обеспечить погрешности измерения по амплитуде $\Delta A_{max} \leq 1$ дБ и по фазе $\Delta \varphi_{max} \leq 6^{\circ}$. При этом потери в тракте передачи полезного сигнала составляют 10 дБ; потери в линии передачи опорного сигнала – 3 дБ; коэффициент усиления МШУ полезного сигнала – 30 дБ; коэффициент усиления МШУ опорного сигнала – 20 дБ;

при нахождении зонда на краях зоны сканирования минимальное отношение сигнал/шум на выходах узкополосных балансных смесителей ДМ диапазона – 20 дБ; подавление помех гетеродинных входов балансных смесителей диапазонов КММВ и ДМ – 20 дБ, а на их выходах уровень этих помех на 10 дБ меньше уровня шума, поступающего с сигнального входа смесителей; достаточная мощность на сигнальном выходе квазиоптического направленного ответвителя генераторного блока около 3 мВт; достаточная мощность генератора КММВ около 5 мВт; спектральная плотность АМ шумов генератора КММВ на частотах отстроек более 200 кГц – менее (–145 дБ/Гц); обратные потери вентиляционной цепочки для обеспечения необходимого подавления паразитного сигнала, отраженного от модулятора и проникающего в опорный тракт, – 60 дБ; спектральная плотность АМ шумов гетеродина КММВ на частотах отстроек более 2 ГГц – менее (–165 дБ/Гц).

Радиоаппаратурная часть с СВЧ модуляцией по структуре значительно проще варианта с НЧ модуляцией. Выбор СВЧ ПЧ F_{IF}^{mic} , которая в данном случае равна частоте СВЧ модуляции F_M^{mic} , обусловлен наличием соответствующего амплитудного модулятора диапазона КММВ. Развитие технологии полупроводниковых приборов позволяет надеяться на наличие в ближайшем будущем амплитудных модуляторов для всего диапазона КММВ с СВЧ модуляцией $F_M^{mic} \geq 1$ ГГц. Большей F_M^{mic} , а значит и F_{IF}^{mic} , соответствует меньший вклад шумовых компонент генератора КММВ в полосу полезного сигнала. Однако, при неизменной относительной полосе МШУ с увеличением F_{IF}^{mic} увеличивается абсолютное значение шумовой полосы ΔF_N АФМ, а значит, и мощности шумового сигнала. Выбирая $F_{IF}^{mic} = 1...2$ ГГц можно обеспечить $\Delta F_N \leq 10$ МГц [10]. При тех же величинах $D_A \leq 1000\lambda$, $K_d = 30$ дБ и потерь в передающих линиях, расчет дает следующее: спектральная плотность АМ шумов генератора КММВ менее (–166 дБ/Гц) при частотах отстроек более 1...2 МГц; обратные потери цепочки вентиля более 68 дБ. При упомянутых выше погрешностях измерения $\Delta A_{max} \leq 1$ дБ, $\Delta \varphi_{max} \leq 6^\circ$ достаточная сигнальная мощность генератора КММВ такой системы возрастает и равна $3Bm$ из-за увеличения ΔF_N на три порядка.

Заметим, что в радиоаппаратурных частях обоих случаев модуляции при переходе работы в другой спектральный участок диапазона КММВ потребуются замена узлов спектрального участка этого диапазона соответствующими узлами другого участка. При этом СВЧ и последующие блоки остаются неизменными. Частотная нестабильность генераторов КММВ в обоих случаях радиоаппаратурных частей должна быть порядка $\Delta f/f \approx 5 \times 10^{-6}$, что для $D_A \leq 1000\lambda$ обеспечивает вносимую фазовую погрешность $|\Delta \varphi| \leq 1^\circ$, обусловленную минимальной нескомпенсированной разностью $\Delta l \approx D_A/2$ длин l опорного и сигнального трактов при условии $l/\Delta l \approx 10...15$ [10].

2.2. Линии передачи опорного и полезного сигналов

Особенность линий передачи опорного сигнала и ПЛП полезного сигнала состоит в том, что они имеют квазиоптический характер и построены на отрезках сверхразмерных полых волноводов [15].

Другая особенность - ПЛП смонтирована на сканере и содержит два волноводных трембона с подвижными сочленениями таких волноводных отрезков. Колена трембонов перемещаются поочередно и синхронно (посредством специальных механизмов компенсации системы механического сканирования) с перемещениями зонда вдоль осей X и Y . При этом перемещения колен таковы, что геометрическая длина ПЛП остается неизменной. В волноводах обеих линий передач размещены фильтры для подавления паразитных мод. Выбор конструкции фильтров зависит от типа сверхразмерного полого волновода (металлический или металло-диэлектрический полые волноводы [16] - [18]) и от типа основной рабочей моды в нем [15]. В подвижных сочленениях волноводов установлены поглотители электромагнитной энергии. Они обеспечивают экранировку ПЛП, соответствующую вносимой возможной фазовой нестабильности полезного сигнала менее 1° .

При размерах $25\text{мм} \times 25\text{мм}$ квадратного волновода ПЛП и работе в частотной области всего диапазона КММВ ожидаемые в ПЛП нестабильности передачи по амплитуде и по фазе составляют соответственно менее $|0,5\text{дБ}|$ и $|7^\circ|$, а потери – менее 3дБ [19].

3. Система механического сканирования

Современные технологии изготовления узлов точной механики позволяют обеспечить плоскостность Δz перемещений и отклонения $\Delta x, \Delta y$ от прямолинейности перемещения вдоль осей X и Y с точностью менее $10 \mu\text{м}$ на расстояниях до 2м [20]. Таким образом, при точностях сканирования $\Delta z \approx \Delta x \approx \Delta y \leq \lambda/100$ и $f = 300 \text{ ГГц}$ протяженности зоны сканирования могут достигать значения 2000λ , а размеры ИА – значения 1350λ . При $f = 60 \text{ ГГц}$ будем иметь соответственно – 400λ и 270λ .

Особенности построения системы сканирования таковы. Первое – массивная X -каретка, несущая на себе Y -каретку и механизм ее привода, имеет следящий гидропривод [19]. Его применение обусловлено рядом преимуществ [21]. Это надежность и долговечность в работе современных гидроприводов, способных обеспечить линейные перемещения около 2м ; малая инерционность подвижных узлов и малая зависимость скорости выходного звена от нагрузки на нем; возможность плавного управления параметрами движения выходного звена следящего гидропривода. Последнее позволяет реализовать на начальном отрезке шагового перемещения X -каретки постепенное нарастание ее скорости движения с нулевого значения до некоторого максимального, а на конечном отрезке – постепенное гашение скорости до нулевого значения. Такой привод способен обеспечить точность шаговых повторяющихся перемещений X -каретки порядка $0,01 \text{ мм}$.

Второе – два упомянутых механизма компенсации, осуществляющие неизменность геометрической длины ППП, смонтированы на сканере и построены на пантографах [15]. Ожидаемая точность компенсации изменения длины ППП при протяженностях зон сканирования около 2м по осям X и Y составляет около $10 \mu\text{м}$.

4. Система автоматического управления

Основные узлы и работа системы автоматического управления описаны в [19], [22]. Особенностью построения этой системы является использование компактного фотодатчика нового типа для точного Y -позиционирования зонда. Фотодатчик имеет диск с щелевой периодической структурой и шток, который осуществляет поступательное перемещение вдоль радиуса диска при его вращении. В фотодатчике исходные импульсы вырабатываются с помощью двух светодиодов, неподвижного и подвижного. Поступательное Y -перемещение сканируемого зонда, вращение диска и перемещение штока синхронизированы простым механизмом с двумя звеньями. В первом звене механизма синхронизации предусмотрены учет его люфта и конечности ширины щелей периодической структуры путем регулировки начальной задержки вращения диска относительно начала перемещения зонда при реверсе направления Y -движения зонда. Путем же замены шкивов в этом звене обеспечивается широкий диапазон выбора значений минимального шага дискретизации измерений (от долей мм до нескольких мм), что способствует универсальности устройства для работы в различных участках диапазона КММВ. Фотодатчик и механизм синхронизации смонтированы на X -каретке и размещены вне зоны измерений. Для X -позиционирования зонда служит лазерный интерферометрический датчик.

В электрической схеме системы, построенной с применением логических элементов, на основе исходных импульсов фотодатчика и лазерного датчика, формируются импульсы управления. Ими управляется работа сканера и автоматизация дискретных отсчетов измеряемого ближнего поля ИА. В схеме предусмотрена электронная установка положения и протяженности достаточной зоны сканирования по оси Y , которые определяются для каждой конкретной ИА до ее тестирования, что экономит время измерений. Электронная установка реализуется заданием программно-управляемых опорных напряжений компараторов в каналах электрической схемы для прямого и обратного движений Y -каретки. При этом задание опорных напряжений производится с учетом люфта второго звена механизма синхронизации.

В результате упомянутых решений исключается зависимость Y -позиционирования зонда от скорости его движения вдоль оси Y , что приводит к ненужности управления скоростью Y -перемещения зонда и к упрощению системы автоматического управления по сравнению с подобными системами в комплексах-роботах для тестирования ИА по ближнему полю [4]. При этом реализуются допустимые ошибки позиционирования зонда $\delta_x \approx \delta_y \leq \lambda/100$ для всех частот диапазона КММВ.

5. Выводы

Предлагаемое построение автоматического измерительного комплекса и приведенные технические решения для реализации его составных систем позволят производить высокоточное, сравнительно краткое по времени и надежное тестирование ИА диапазона КММВ при любом режиме работы ИА, а при соответствующих ограниченных заменах некоторых узлов систем обеспечивается возможность измерений в любом спектральном участке отмеченного диапазона. В результате появляется возможность существенного снижения затрат на тестирование антенн диапазона КММВ.

6. Литература

- [1] П.М. Геруни. Труды ВНИИРИ (ВНИИРИ, Ереван, 1983).
- [2] E.B. Joy. *Microwave J.*, 119 (January 1990).
- [3] A.D. Yaghjian. *IEEE Trans. on Antennas and Propagation* **34**, 30 (1986).
- [4] D. Slater. *Near-Field Antenna Measurements* (Artech House, Boston – London, 1991).
- [5] R. G. Yaccarino and Y. Rahmat-Samii. *IEEE Trans. on Antennas and Propagation* **47**, 574 (1999).
- [6] O.M. Bucci, G. D'Elia, and M.D. Migliore. *IEEE Trans. on Antennas and Propagation* **47**, 1377 (1999).
- [7] R. Pierri, G. D'Elia, and F. Soldovieri. *IEEE Trans. on Antennas and Propagation* **47**, 792 (1999).
- [8] J.E. Will, J.D. Norgard, R.M. Sega, M. Seifert, A. Pesta, J. Clearly, C. Stubenrauch, K. MacReynolds. *Proc. 18th Antenna Meas. Tech. Assoc. Meet. Symp.*, Seattle, WA. (October 1996) 198.
- [9] D. Slater. *Proc. Antenna Measurement Techniques Association Conf.* (1994) 267.
- [10] М.В. Маркосян, В.Г. Аветисян. *Радиотехника*, 59 (Декабрь 2006).
- [11] В.Г. Аветисян. *Радиотехника*, 27 (Сентябрь 2006).
- [12] А.Л. Драбкин, В.Л. Зузенко, А.Г. Кислов. *Антенно-фидерные устройства* (Сов. радио, Москва, 1974).
- [13] Edited by T. Koryu Ishii, *Handbook of Microwave Technology. Vol. 1 - Component and Devices* (Academic Press Inc.: San-Diego, New-York, Boston, London, Sidney, Tokyo, Toronto, 1995).
- [14] М.В. Маркосян, В.Г. Аветисян. *Радиотехника*, 9 (Май 2007).
- [15] V.H. Avetisyan. *IEEE Trans. on Antennas and Propagation* **52**, 2500 (2004).
- [16] Б.З. Каценеленбаум. *УФН*, **LXXXIII**, 81 (1964).
- [17] Ю.Н. Казанцев, О.А. Харлашкин. *Радиотехника и электроника*, 2060 (Октябрь 1978).
- [18] Ю.Н. Казанцев, О.А. Харлашкин. *Радиотехника и электроника*, 1441 (Август 1984).
- [19] V.H. Avetisyan. *IEEE Trans. on Antennas and Propagation* **58**, 2149 (2010).
- [20] В.К. Свешников, А.А. Усов. *Станочные гидроприводы* (Машиностроение, Москва, 1988).
- [21] Т.М. Башта, С.С. Руднев, Б.Б. Некрасов, О.В. Байбаков, Ю.Л. Кириловский. *Гидравлика, гидромашин и гидроприводы* (Машиностроение, Москва, 1982).
- [22] В.Г. Аветисян. *Радиотехника*, 20 (Февраль 2007).

Coaxial Microwave Radial Power Combiner/Divider

A. Hakhoumian, N. Poghosyan, T. Poghosyan, A. Gasparyan

Institute of Radiophysics and Electronics, Alikhanian Brothers str. 1, 0203 Ashtarak, Armenia

An X-Band radial power combiner/divider and non-conventional coaxial line matching system has been proposed and realized. The full design steps and methods of this matching system were developed. The length of the designed matching section is three times smaller than those of conventional quarter wave coaxial lines transformers and transformers of continuously changing inner and outer diameters of coaxial lines which provide impractical lengths of matching section.

1. Introduction

With growing interest in high power solid-state sources for several applications such as radar transmitter, particle accelerator, UWB system [1] design of high power amplifier (HPA) has received enormous attention. The most promising method to design HPA is combining output powers from a sufficient number of comparable low power solid-state amplifiers. As a result the HPA characteristics are dependent on that power combiner/divider. That's why development of high efficient combiners to sum output significant number of amplifiers is in focus. The commonly used the tree type structures based on quadrature hybrids or Wilkinson dividers have simpler design, but they have disadvantage of using multitude of transmission line segments, which provide add losses increasing with increase of number of summing amplifiers (N). The radial structures of the power combiner/divider due to symmetry of the circuit provide good port-to-port isolations, low losses and structural redundancy [2, 3]. Unlike corporate combining structures, radial structure permits placement of a large number of ports very close to central feed port, thus minimizing combining path and losses. A careful optimization of physical structure is essential over desired bandwidth. In this paper the result of X-band HPA design based on coaxial radial type combiner are presented.

2. Combiner structure

The designed HPA consist from 16 identical micro-strip PA which via micro-strip-to-coax 50Ω adapter are directly connected to receiving coaxial line main port as a load Fig.1.

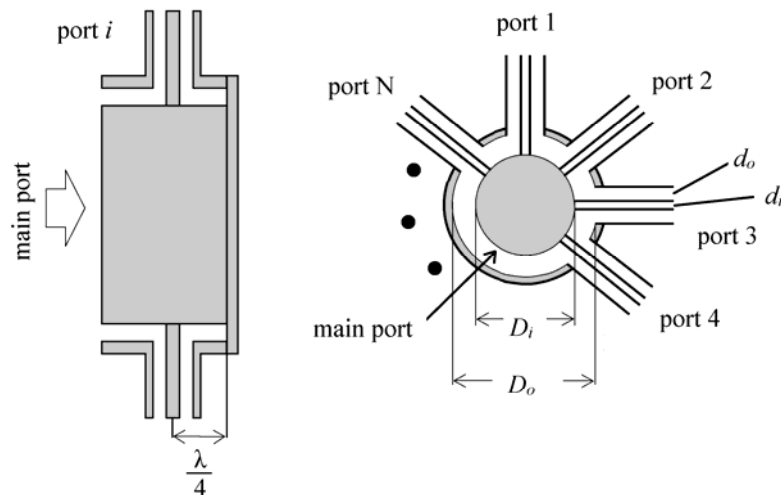


Fig. 1 structure of divider

The corresponding impedances and dimensions of coaxial lines can be determined from [4]

$$Z_N = 60 \frac{1}{\sqrt{\epsilon}} \ln \frac{d_o}{d_i}, \quad Z_M = 60 \frac{1}{\sqrt{\epsilon}} \ln \frac{D_o}{D_i}, \quad Z_M = \frac{Z_N}{N} \quad (1)$$

$$D_o > \frac{1}{\pi} N d_o, \quad D_i > \frac{1}{\pi} N d_i \quad (2)$$

As it follow from (1) and (2) $Z_M = 3.1\Omega$ and ($Z_N = 50\Omega$, $N = 16$) $D_i, D_o \approx N d_o$ therefore combiner design meet the serious problem to match receiving coaxial line, having extra low impedance and big inner and outer diameters, with the standard 50Ω output coaxial line Fig.2.

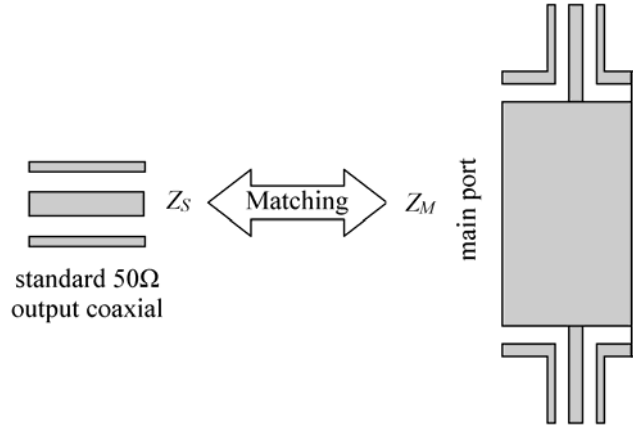


Fig. 2

In order to match circuits with high ratio of own impedances both conventional methods using $\lambda/4$ coaxial lines transformers and continuously changing inner and outer diameters of coaxial lines provide to unavailable lengths of matching section. Alternative promising method allow significantly reduce the length of matching transformer was purposed by Bramham and Regier [5, 6] presented that matching can be done by connecting lines with appropriate impedances ($Z_1, Z_2, Z_3, Z_4, \dots, Z_n$) and lengths ($L_1, L_2, L_3, L_4, \dots, L_n$). Lengths of matching lines are about $\lambda/12$ (Fig.3).

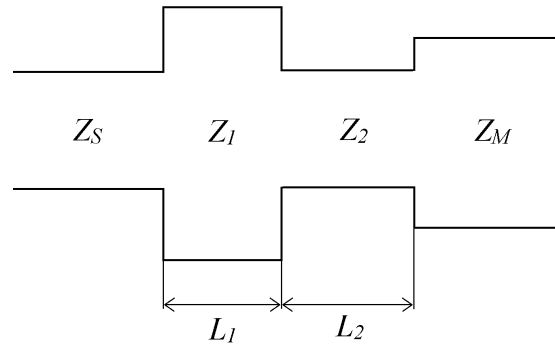


Fig. 3

For two - section matching system Z_1, Z_2 are

$$Z_S, Z_2 < Z_1 \text{ and } Z_S, Z_2 > Z_M \quad (3)$$

In differ from conventional transformers in this type of matching system impedance changing have alternated behavior. Take in account high ratio of Z_S to Z_M and big difference between input and output coaxial lines diameters the 12-sectional series matching system to minimize $|S_{11}|$ was choused and corresponding impedance distribution was found. Because impedance of coaxial line depends on ratio of outer and inner diameters but not from their absolute values there are infinity set of coaxial matching sections. To solve this problem we have placed boundary condition that inner and outer diameters of matching system sections step by step changes from those for input and output coaxial lines. But change of diameters in coaxial lines brings another problems caused by coaxial lines discontinuities.

It was shown [7] that effects from such discontinuities may be calculated from an equivalent circuit in which the local waves excited at the change in section are accounted for by a lumped discontinuity admittance shunted between lines at the junction Fig.4.

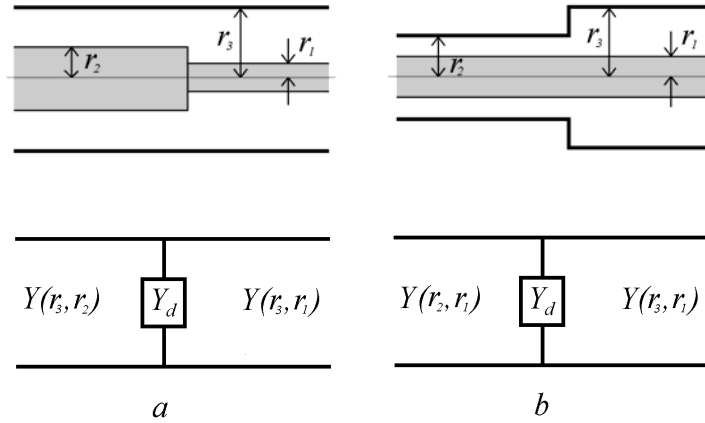


Fig. 4 Equivalent circuits of coaxial line discontinuity

Discontinuity admittance Y_d can be calculated for a (Sudden Change in Diameter of Inner Cylinder) and b (Sudden Change in Diameter of Outer Cylinder) as follow:

$$Y_d = \frac{j2\pi\omega\epsilon}{\left(\ln \frac{r_3}{r_2}\right)^2} \sum_n \frac{2A_0^2(k_n r_2)}{K_n k_n \{ [k_n r_3 A_1(k_n r_3)]^2 - [k_n r_1 A_1(k_n r_1)]^2 \}} \quad (4)$$

$$Y_d = \frac{j2\pi\omega\epsilon}{\left(\ln \frac{r_2}{r_1}\right)^2} \sum_n \frac{2A_0^2(k_n r_2)}{K_n k_n \{ [k_n r_3 A_1(k_n r_3)]^2 - [k_n r_1 A_1(k_n r_1)]^2 \}} \quad (5)$$

The $A_0(k_n r)$ and $A_1(k_n r)$ ($r = r_1, r_2, r_3$) can be calculated from

$$A_0(k_n r) = J_0(k_n r) + G_n N_0(k_n r), \quad A_1(k_n r) = J_1(k_n r) + G_n N_1(k_n r) \quad (6)$$

Where J_p and N_p are p -th order Bessel functions of the first and second kinds accordingly and

$$G_n = -\frac{J_0(k_n r_1)}{N_0(k_n r_1)} = -\frac{J_0(k_n r_3)}{N_0(k_n r_3)} \quad (7)$$

Wave number k_n calculated from transcendental equations

$$J_0(k_n r_1)N_0(k_n r_3) - J_0(k_n r_3)N_0(k_n r_1) = 0 \quad (8)$$

and K_n from

$$K_n = \sqrt{1 - \left(\frac{2\pi}{\lambda k_n}\right)^2} \quad (9)$$

Using discontinuity admittance Y_d and impedance distribution defined above the series matching system can be designed completely. Design process consist in estimation of overall ABCD matrix (10) by multiplication of accordance $ABCD_{L^i}$ matrix for regular parts of transformer (11) and coaxial line discontinuity $ABCD_{Y_d^i}$ (12).

$$ABCD = \begin{bmatrix} A & B \\ C & D \end{bmatrix} = \prod_{i=1}^M ABCD^i \quad (10)$$

$$ABCD_{L^i} = \begin{bmatrix} \cosh \gamma L^i & jZ^i \sinh \gamma L^i \\ \frac{j \sinh \gamma L^i}{Z^i} & \cosh \gamma L^i \end{bmatrix} \quad i = 2, 4, 6 \dots N \quad (11)$$

$$\gamma = \frac{2\pi}{\lambda} \quad (10)$$

$$ABCD_{Y_d^i} = \begin{bmatrix} 1 & 0 \\ Y_d^i & 1 \end{bmatrix} \quad i = 1, 3, 5 \dots N+1 \quad (12)$$

Resulted ABCD matrix is a function from inner and outer radii and steps lengths

$$ABCD = f(r_{in}^i, r_{out}^i, L^i) \quad (13)$$

Passing on to S matrix [4] and assign S_{11} minimum at central frequency, the overall length, steps number and operating bandwidth desired transformer can be found using computational method Matlab and optimization procedure [8]. Cross section of 12 step matching transformer is presented on Fig.5.

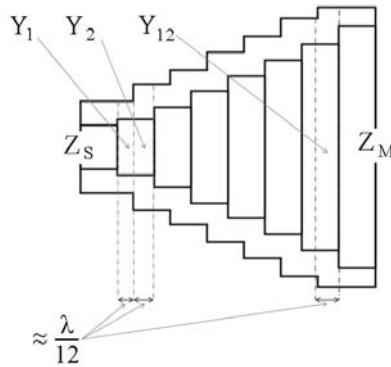


Fig. 5 Cross section of 12 step matching transformer

3. Design of X-band HPA

On base of coaxial combiner described above the HPA with output power 140W operating in frequency 8.5-9.5 GHz was designed. The designed transformer was tested using Ansoft HFSS. Each input port amplifier using (FLM 1596) FET transistor provides 10 W output power therefore $N = 16$ input ports was needed. The designed combiner and measured $|S_{11}|$ of output port are presented in Fig.6 and Fig.7 accordingly. The length of designed matching section is $L=3\text{cm}$ or $L=\lambda$ which three times smaller compared same condition conventional quarter waves transformer. Insertion loss of combiner is less than 0.5dB.

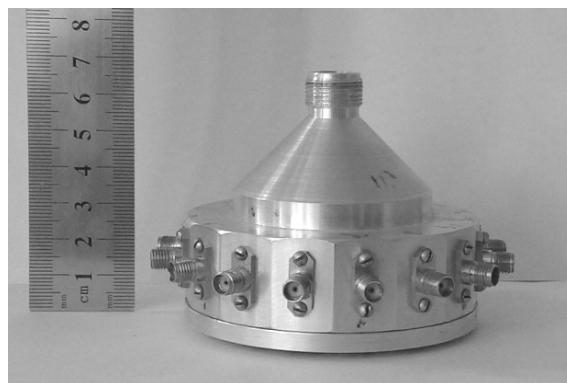


Fig. 6 X-Band 16 port combiner

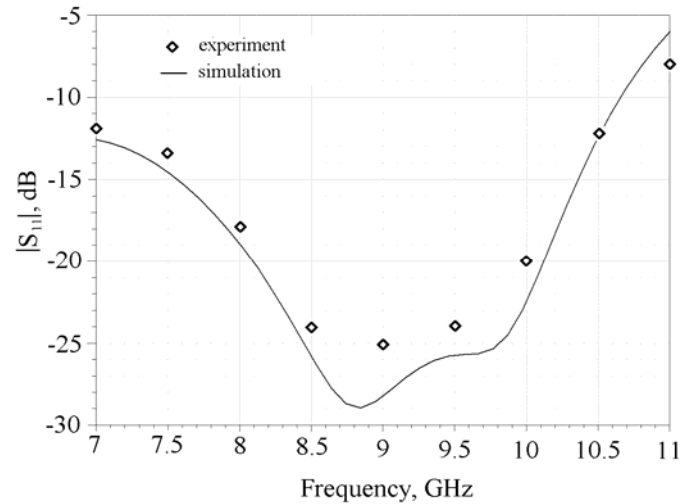


Fig. 7 $|S_{11}|$ of divider

4. Conclusion

An X-Band radial type 16-way coaxial power combiner / divider has been proposed and realized. The design method of non-conventional coaxial matching circuits was developed. The length of the designed matching section is three times smaller than those of conventional quarter wave transformer. On base of proposed combiner X-Band HPA with output power 140W in CW mode was assembled.

References

- [1] P. Marchand, et al. Proceedings of EPAC 2004.
- [2] P.C. Jia, L. -Y. Chen , and A. Alexanian, IEEE Trans Microwave Theory Tech, 51, 2469 (2003).
- [3] Rheem, Jae-Wook, Kang, Won-Tae, Lee, Sang-Ho, Kim, Duk-Yong, Chang, Ik-Soo, Microwave Journal, 40, 22-34 (1997).
- [4] D.M. Pozar. Microwave Engineering, New York, Wiley; 2 edition (1997).
- [5] B. Bramham, Electron. Eng, 33, 42 (1961).
- [6] F. A. Regier, Proc IEEE, 159 1133, (1971).
- [7] Whinnery, J.R. Jamieson, H.W. Robbins, Proc. IRE, 32, 695 (1944).
- [8] J. Kiusalaas, Cambridge University press, (2005).

Modeling of Double Reflector Spherical Antennas

A. Sargsyan¹, H. Abrahamyan², V. Minasyan³

¹ Radiophysics Research Institute, Komitas Ave., 49/4, State Engineering University of Armenia, Teryan Str., 105, 562336, Yerevan, Armenia

² Radiophysics Research Institute, Komitas Ave., 49/4, 234990, Yerevan, Armenia

³ American University of Armenia, 40 Baghramyan Ave., 512791 Yerevan, Armenia

Article is devoted to modelling of optical scheme of Antenna and to make a modern software package for calculation of its electrical parameters. Implemented software creates profiles of primary mirror and subreflector. It also visualizes geometroptical model of electromagnetic processes in the aperture of Antenna. Software package provides an opportunity to make analyses and realize variations on different schemes of Spherical Double Reflector Antennas. Based on these results we are able to estimate, analyze and select the optimal scheme for Antenna. Software allows both estimation of efficiency of existing system and realizing calculation of electrical parameters of antenna. Using the results of software we have derived several dependencies between various parameters of antenna which allow us to evaluate the efficiency of antenna's different optical schemes.

1. Introduction

1.1 Goals of Software Package

The general requirements for implemented software package were that it should provide possibility to estimate and calculate dependencies between parameters of antenna and its scheme. The idea was to consider different cases for different schemes of antenna and at the end derive corresponding dependencies which will allow to define an optimal scheme for double reflector spherical antenna.

In contrast from other mirrors like parabolic or cylindrical mirrors, spherical mirrors gather reflected field not in point or line, but in focal region. The detection of coordinates of focal region is one of the goals of prepared software package. It is important to place the secondary mirror in a way in which it would not intersect the caustic curve. In the case when profile of mirror is intersecting the focal region, valuable part of radiation is reflected by backside of secondary mirror, which is meaningless loss of power of the field.

Another goal of software package is to provide a possibility to dynamically change the coordinates of secondary mirror. Based on the results of experiments like that, it will be possible to figure out dependences between focus of secondary mirror and its coordinates. Also program should have feature to change dynamically shape of secondary mirror. This feature will provide possibility to create dependency between shape of mirror and effective surface, also between shape of mirror and coordinates of focus point.

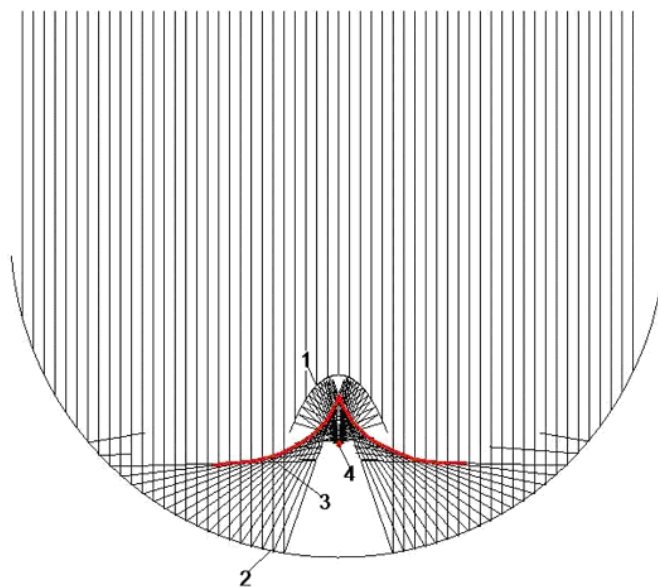


Figure 1. Geometroptical scheme

1. Subreflector, 2. Primary Mirror,
3. Caustic's curve, 4. Focus Point (feed should be placed as close to it as it is possible)

1.2 Software Structure

The software package is composed from two parts. First part is implemented in Java programming language. The second is created using MatLab. First part of program composed from following sections:

1. Calculation of profiles of mirrors
2. Visualization of electromagnetic field in aperture of antenna

3. Calculation of Sizes of focal region
4. Analyses and creation of dependences

The last part, is somehow finalizing the purpose of thesis. That section shows how parameters of antenna behave in different positions and shapes of secondary part. Especially are considered cases where top coordinates, aperture and focus point of secondary mirror are different.

Second part of package is implemented in MatLab and has following functionality:

1. Calculation of Pattern of feed in E and H surfaces
2. Calculation of amplitude distribution in aperture of antenna
3. Calculation of Pattern of whole antenna

This part also has user interface so calculation may be done using different input parameters like working frequency of antenna or length of receiving or radiating wave.

2. Dependencies

2.1 Derived Dependencies

The result of our research shows that there are some dependence between shape and place of secondary mirror and between other parameters of antennas. Table 1 shows exactly which dependences are considered in thesis work.

Table 1. Dependences considered

N	Reflector's parameters	Antenna parameters
1	Subreflector shape (Aperture an Height)	Focus (x,y coordinates)
2	Top coordinate of reflector	Percentage of efficiency of usage of caustic curve.
3	Focus Position	Surface Efficiency
4	Aperture \leftrightarrow Height	Height \leftrightarrow Aperture

Let's clarify why these dependences exist and why they are important for parameters of antenna.

1. The spherical front of wave will gather in different positions in dependence from shape of subreflector. So changing the position of primary mirror is resulted into change of position of focus. From Fig. 2 we can conclude the following tendency. By enlarging the height of mirror we making focus position closer to the reflector. We have the opposite tendency when we are enlarging the width of mirror. In that case focus point is moving away from reflector. Using Fig. 2 we can select an optimal place of feed, because knowing the height and width of mirror we are able to define the focus.
2. Another important issue is that if we will place the reflector very closely to the primary mirror, it may intersect with curve of caustic. During this kind of intersections the valuable radiation may be reflected from back side of secondary mirror and lost. So another issue is to figure out this dependency. The results of experiments are provided in Fig. 3. Having this dependency in our arsenal we can define the best position for reflector. By saying the best we mean the location of reflector, in which it can gather the highest percentage of radiation. So in focus point, the power of signal should be the highest. The optimal distance between primary mirror and subreflector could be defined from Fig.3.
3. We also consider another combination of dependencies which can provide possibility to make reverse engineering. These dependencies are between, width and height of reflector, and between focus and Surface Efficiency .One of these functional dependencies is shown in Figure 4.

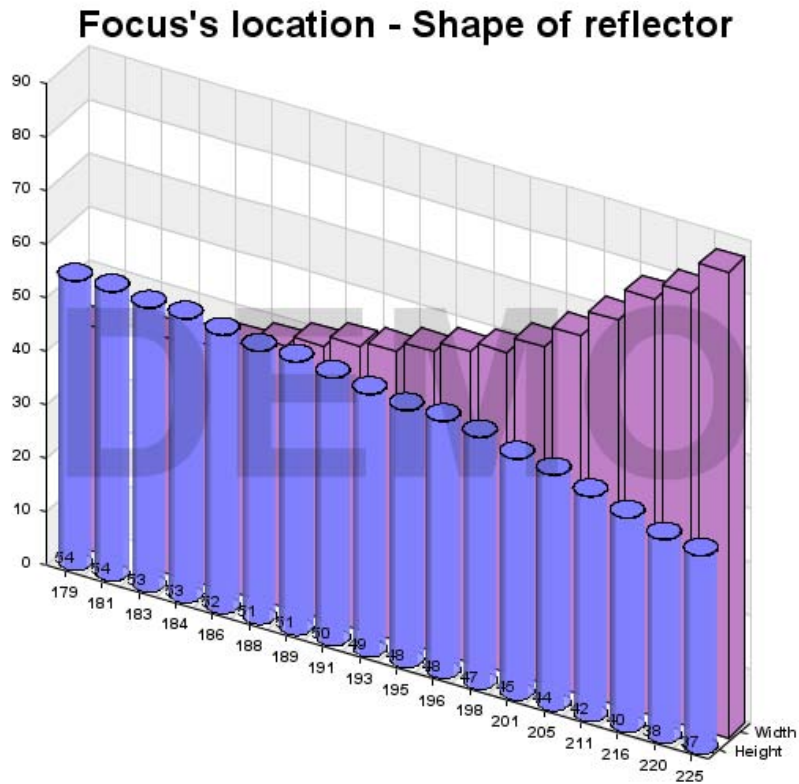


Figure 2. Optimal place of feed

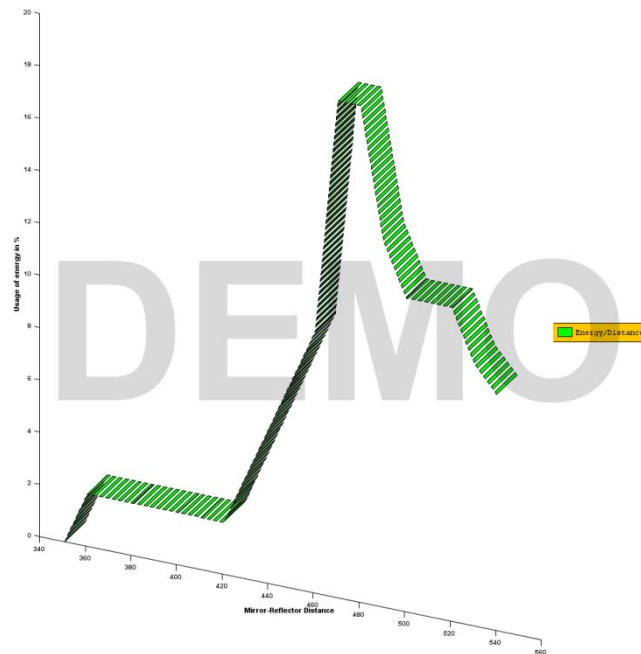


Figure 3. The optimal distance between primary mirror and subreflector

All Graphs and charts that are presented are composed by combining different replications of different experiments. Beside these kinds of graphs we also have possibility to consider results of each experiment separately. In the Fig. 5 it is presented the surface efficiency after different experiments.

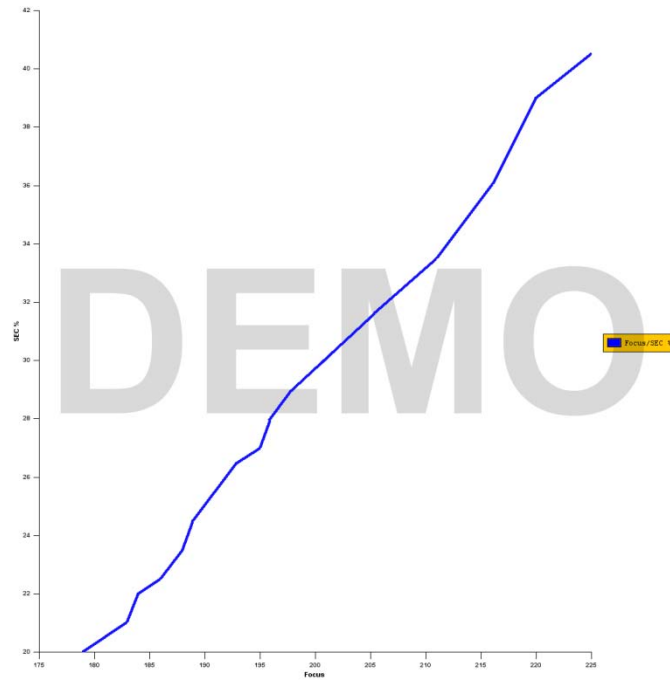


Figure 4. Combination of dependencies

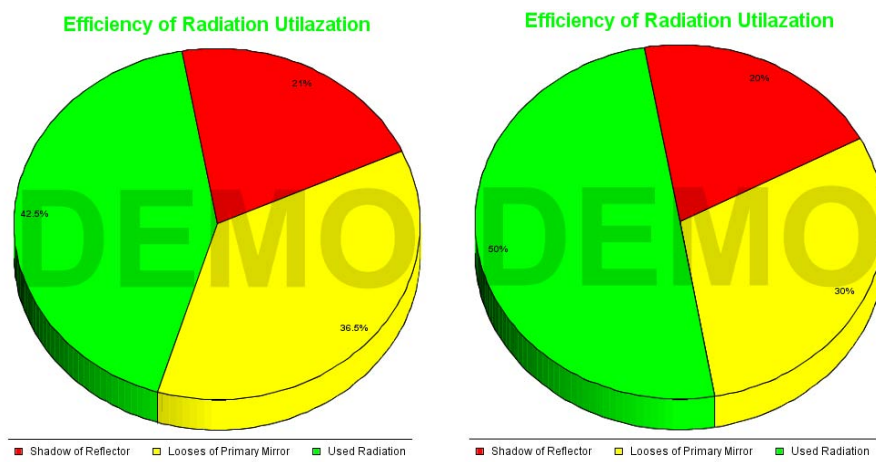


Figure 5. Surface efficiency

3. Conclusion

Derived dependencies between various parameters of antenna allow us to evaluate the efficiency of antenna's scheme. According to the data that we have figured out we can define an optimal place and shape for reflector. It will also be possible to realize a reverse engineering: for example having one of the parameters of reflector like its height we can define its width. So let's consider more explicitly what results do we have.

1. Using the dependencies that we have derived, we can select an optimal place of radiator, because knowing the height and width of mirror we are able to define the focus.
2. The optimal distance between primary mirror and reflector could be defined from results of software.
3. An optimal location for reflector could be found.
4. Software package allows realizing reverse engineering. Having one of above mentioned parameters others can be calculated.

So in conclusion we can say that a tool has been created for searching and finding optimal parameters for creation of double reflector spherical antennas.

References

- [1] Herouni P.M. "Issues on Double Reflector Antenna's Calculation", "Radiotechnica i Electronica", N1, 1964, pp. 3-12.
- [2] A. Sargsyan "Calculation of Double Reflector Antennas" Software package, MAU, Moscow, 1989
- [3] L.D. Bahrah, G.K. Galimov "Scanning Mirrored Antennas", "Nauka", 1981, pp.144-160
- [4] P. Herouni, Karapetyan K. E., Axinyan P.A. "Research of Electromagnetic Field In Caustic Area Near Reflector", VNIIRI Report 12.01.09.09, 52 p.
- [5] Stephen J. Chapman "Essentials of MATLAB Programming" CL-Engineering Dec. 2008.
- [6] Timothy Budd "Introduction to Object Oriented Programming" Pearson Education (Singapore) Pte. Ltd., 2008.
- [7] Altschuller D.R. 'The National Astronomy and Ionosphere Center (NAIC) Arecibo Observatory in Puerto Rico', Single-Dish Astronomy. Astronomy Society of Pacific, San Francisco, 2002, Vol. 278, pp. 1-24.

Mutual Coupling Reduction in Fractal Patch Antenna Based Phase Array

A. Hakhoumian, N. Pogosyan, A. Gasparyan, A. Kuzanyan
Institute of Radiophysics and Electronics NAS RA, Ashtarak, Armenia

In this paper microstrip patches with fractal geometry are proposed to use in array antennas instead of rectangular ones to reduce mutual coupling between elements of array. The use of fractal geometries has significantly impacted many areas of science and engineering; one of which is antenna design. Parameters for different polarization and the effect of fraction on mutual coupling of fractal patches are studied. Simulations and experimental results show that the resulting array antenna has reduced mutual coupling effect compared to patch array.

Introduction

Advance antenna attributes for both military and commercial sectors are

1. Compact size
2. Low profile
3. Scanning beam
4. Low cost

Antennas that satisfy these objectives are microstrip (especially microstrip patch) arrays. Microstrip array antennas [1-5] are widely used in phased array antenna applications such as pattern beam forming, and electronic scanning radars because of their simple manufacturing, small size, light weight and low cost. The design of array antenna with scanning beam starts with designing a single antenna element and then the whole array. But the mutual coupling effect between array elements (Fig.1) is significant and can't be avoided because large errors in beam forming and null string will appear [6, 7]. In [8-10] several methods have been reported such as change of feeding point position, structure and patch geometry. For example, concave rectangular patches are proposed to decrease mutual coupling effect.

In this paper we propose use of microstrip patches with fractal geometry to reduce mutual coupling. Furthermore, patch parameters and the

effect of fraction on mutual coupling for different polarization of fractal patches have been studied and compared to results of mutual coupling for microstrip patch antenna arrays. Fractal and patch antenna arrays have been simulated by FEM modeling for various distances between antenna elements. Simulation and experimental results show that mutual coupling for the resulting array antenna is weaker.

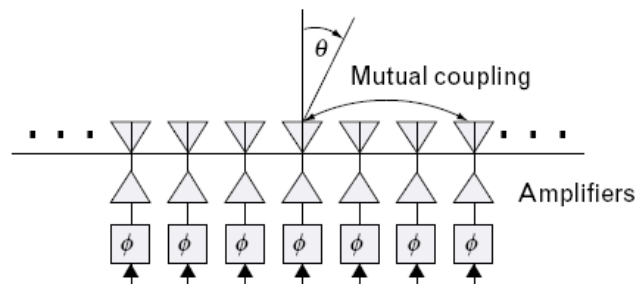


Fig.1 Mutual coupling between the elements of array

Effect of mutual coupling in microstrip phased array antenna

When two antennas (or array elements) are widely separated, the energy coupled between them can be neglected. The influence of one element on the pattern and current excitation of other one is very small. When antennas are brought closer the coupling effect increases. The magnitude of coupling depends on the distance between array elements, their patterns, and the vicinity structure of the elements [11]. When many elements are placed together in one array, the effect of coupling is significant and the pattern and impedance of array elements are drastically changed. Large arrays with wide beam can exhibit scanning blindness. When a phased array scans, the input reflection coefficient of every element at certain angles rapidly increases to 1. The array fails radiation and forms a pattern null.

Mutual coupling causes change of the scanning impedance, which leads to scanning blindness, which is hard to predict accurately except where array structure supports a surface wave. The most natural method to decrease mutual coupling effect is to increase the distance between elements, which will also increase the gain of the system. But this method will increase the whole system size making it impractical and also, when the distance become larger than the wavelength, it leads to grating lobes in the pattern. The farther we move

elements from each other, the closer become grating lobes, and after each wavelength of distance one more lobe occurs in each side of pattern.

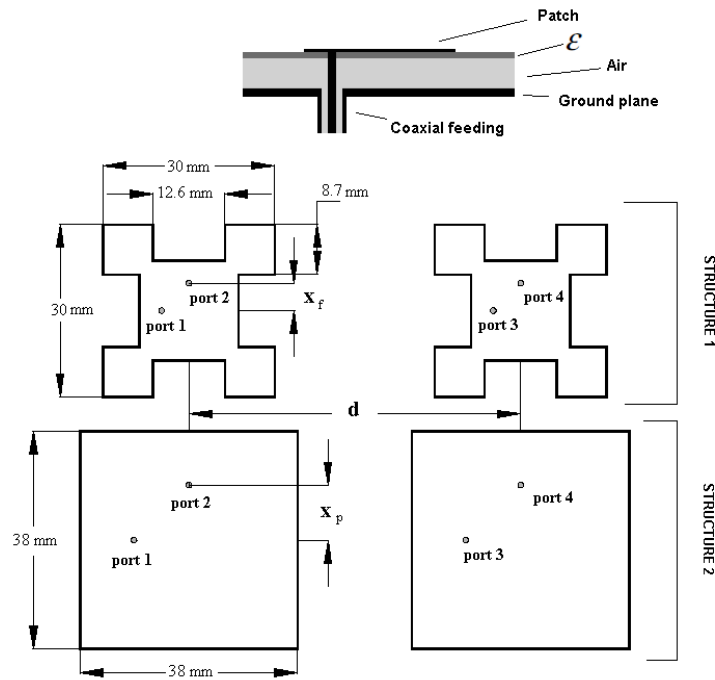


Fig.2 Demonstrate of Fractal and Patch Structure Size

Proposed method, fractal geometry

We propose to use fractal (1st iteration of Minkowski pattern) antennas instead of rectangular patches (0th iteration of Minkowski pattern). Fractals are complex geometric designs that repeat themselves, or their statistical properties on different scales (are self-similar). Fractals, because of their self-similar property, are natural systems where this complexity provides the desired antenna properties. Fractal structures have been applied to various fields, such as antenna and electromagnetic bandgap structure design.

Structures of the array antennas

In our research each antenna array structure consists of two elements (Fig.2). Each element is made of two conductive and one dielectric layers. The lower conductive layer is aluminum ground plane. Cooper patch (or fractal) patterns are placed on the top. The dielectric relative permittivity ϵ is equal to 2.2.

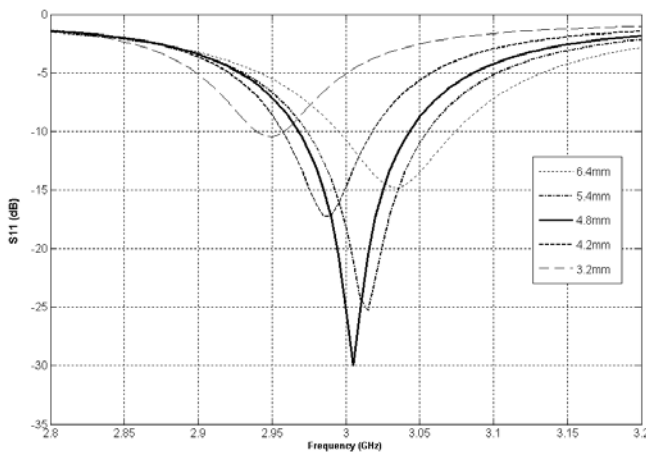


Fig.3 Reflection coefficient (S_{11}) dependence on coaxial feeding point position (x_f).

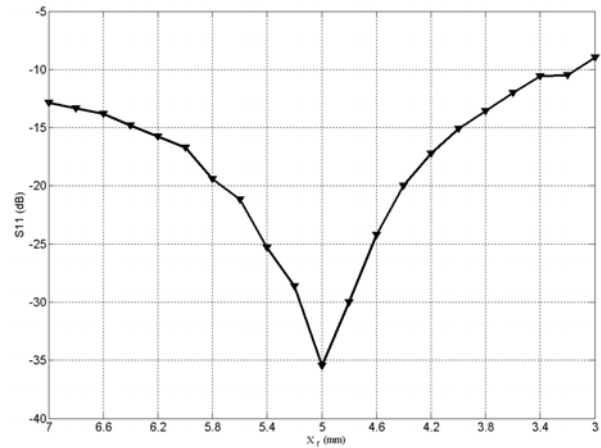


Fig.4 Reflection coefficient minimum ($\min(S_{11})$) dependence on coaxial feeding point position (x_f).

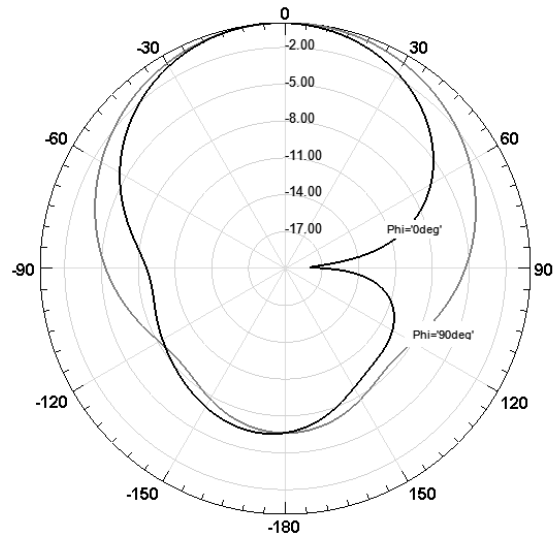
Reflection coefficient and radiation pattern of single fractal antenna

It is observed that fractal antenna parameters depend on feeding point position. All this experiments and simulations have been done on 3GHz. Here the dependence of reflection coefficient on feeding point (x_f) vertical move is presented (Fig.3 and Fig.4).

It can be seen that the operating frequency varies depending on feeding point location. The reflection coefficient varies as well. The dependence curve is presented. The effect of patch geometry fraction on reflection coefficients dependence on x_f (feeding point distance from center of fractal) and radiation pattern are studied (Fig.5). For the optimal feeding point location the gain in two planes is presented. Comparing to patch antenna (on the same frequency) the gain is decreased by 2 dB.

Mutual coupling comparison for patch and fractal results

We have studied mutual coupling effect for fractal and patch array antennas structures (Fig.2) for two types of feeding techniques – horizontal (ports 1 and 3) and vertical (ports 2 and 4). It is known that mutual coupling effect is stronger for parallel feeding type. Corresponding curves for reflection coefficients are presented (Fig.6-Fig.9). It can be seen that for fractal pair we get the reflection coefficient 2-5dB less than for rectangular patches.



E-plane amplitude patterns (dB)

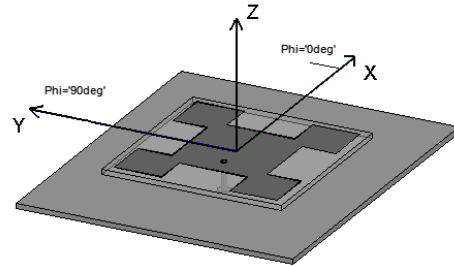


Fig.5. Radiation pattern for $X_f = 4.8$ mm

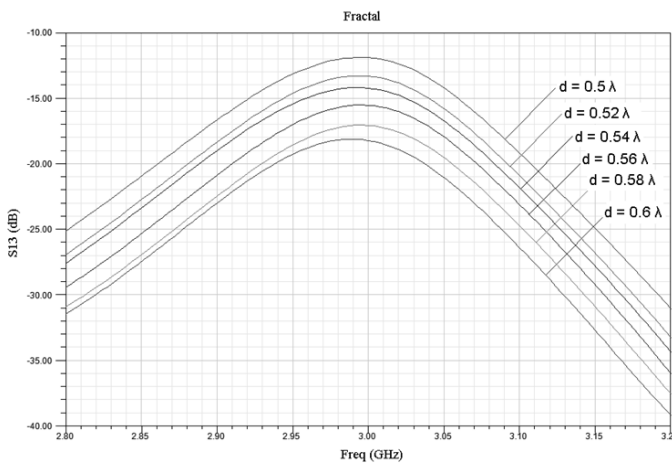


Fig.6 Reflection coefficient (S_{13}) of fractal depending on distance d

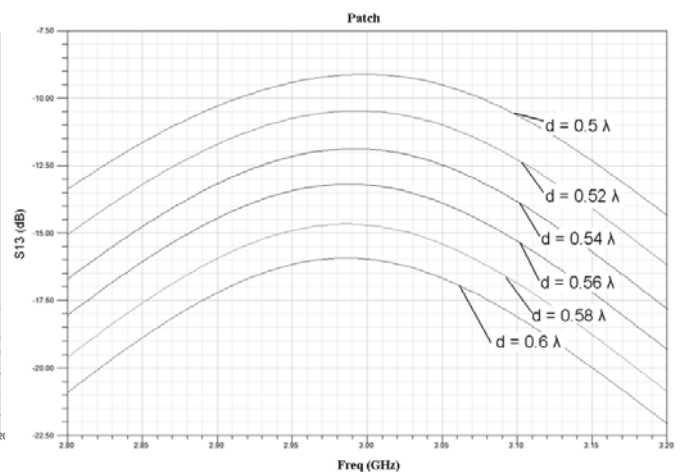


Fig.7 Reflection coefficient (S_{13}) of patch depending on distance d

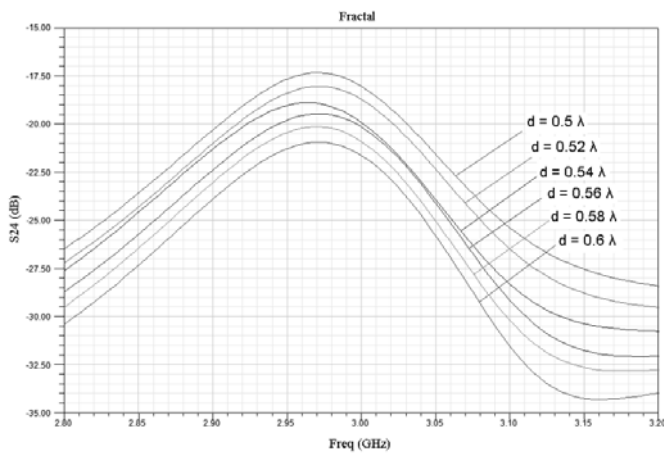


Fig.8 Reflection coefficient (S24) of fractal depending on distance d

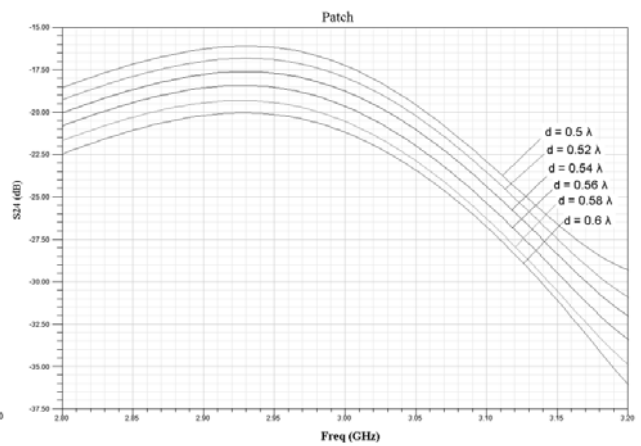


Fig.9 Reflection coefficient (S24) of patch depending on distance d

Conclusion

This paper proposes a new method for mutual coupling reduction in array of microstrip antennas by using fractal structures instead of ordinary rectangular patches. Also, an optimal feeding point position has been found by employing simulation techniques. The main advantage of proposed method is that it not only reduces mutual coupling but also decreases linear sizes of patch antennas.

References

1. David M. Pozar, "Microstrip antenna", Proceeding of the IEEE, Vol. 80, 1992.
2. K. R. CARVER AND J. W. MINK, "Microstrip Antenna Technology", IEEE Transactions on Antennas and Propagation, Vol. 29, NO. 1, 1981.
3. M. I. Skolnik, ed., *Radar Handbook*, McGraw-Hill, New York, 2008
4. R. Osman, "Microstrip array antenna for automobile radar system", MSc thesis, University Technology Malaysia, 2006.
5. Robert J. Mailloux, "Phased Array Antenna Handbook", ARTECH HOUSE, 2005
6. K.R. Dandekar, H. Ling and G. Xu, "Effect of mutual coupling on direction finding in smart antenna applications", Electronics Letters, Vol. 36, 2000.
7. R. Bhagavatula, R. W. Heath Jr., A. Forenza, N. J. Kirsch and K. R. Dandekar, "Impact of mutual coupling on adaptive switching between MIMO transmission strategies and antenna configurations", Springer Science and Business Media, 2008.
8. A. Farahbakhsh, S. Mohanna and S. Tavakoli, "Reduction of mutual coupling in microstrip array antennas using concave rectangular patches", 2009 international symposium on Antennas and propagation, Bangkok, Thailand, October 2009
9. A. Farahbakhsh, S. Mohanna, S. Tavakoli and M. Oukati Sadegh, "New Patch Configurations to Reduce the Mutual Coupling in Microstrip Array Antennas", Antennas and Propagation Conference, Loughborough, England, November 2009.
10. Shahram Mohanna, Ali Farahbakhsh, and Saeed Tavakoli, "Mutual Coupling Reduction in Two-Dimensional Array of Microstrip Antennas Using Concave Rectangular Patches", JOURNAL OF TELECOMMUNICATIONS, VOLUME 2, ISSUE 2, MAY 2010
11. T. Milligan, "Modern Antenna Design", 2-nd ed., WILEY Interscience

Radar Cross-Section Near-Field Measurements

M. Ivanyan¹, N. Khachatryan¹, E. Tagvoryan¹

¹Radiophysics Research Institute, Komitas av. 49/4, 0051, Yerevan, Armenia

The paper describes the scattering properties determination of the radar objects using near-field measurements. Measurements performed by the help of the scanning measurement probes using spherical scanning surfaces. The method allows obtaining the full information about scattered far field of the object. The basic algorithm is supplemented with the proposed method of exclusion of the real probe diagram influence. The inclusion is based on the probe diagram representation by the vector spherical harmonics series expansion and doesn't require the additional measurements: only the mathematical treatment is changed. The variations of the method, allowing avoiding the external background noise and direct inclusion of the radiating probe radiation influence, are presented as well.

1. Introduction

As it was shown earlier [1,2] there is the possibility to obtain the Radar Cross-Section Area (RCSA) patterns of different objects, making field measurements in its near region (Near Field, NF). It was worked out the methods and algorithms of NF to far field (FF) transformation. In said methods the illumination of the object and measurements of the scattered field components are executed with help of two point electrical dipoles (probes), displaced on the given scanning surfaces which are fully or partially embracing the object [2].

This paper presents the modified algorithms, giving the possibility to except any disturbing external influence, received by the measuring probe. The algorithm is generalized for cases of radiating and measuring probes with the arbitrary forms of radiation pattern and for excluding external parasitic radiation or external noises as well.

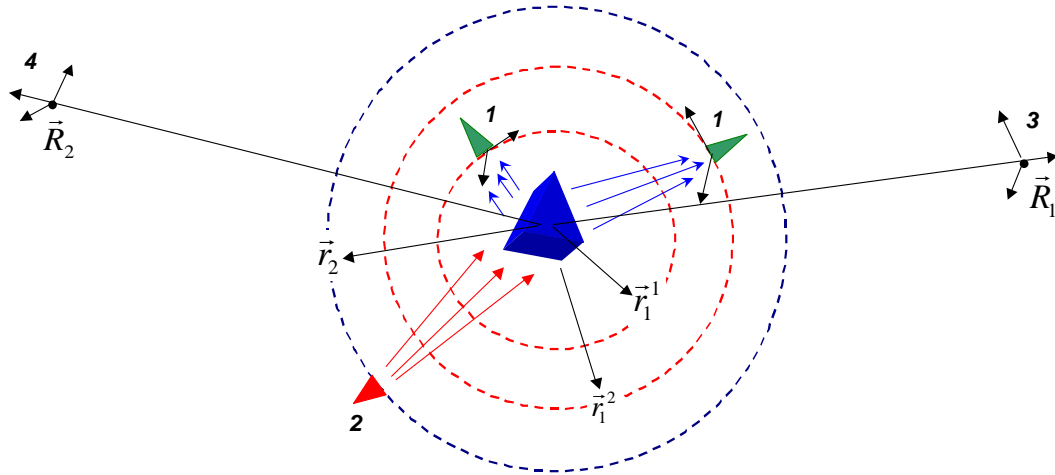


Fig. 1. The geometry of the problem: 1 measuring probes, 2 radiator, 3 far-field imaginary measuring probe, 4 far-field imaginary radiator.

The results of investigations, presented below (Sections 3-6), are obtained for the case of the concentric spherical scanning surfaces of the probes, which are embracing the object in its near space. The case of ideal dipole probes is describing in Section 2.

2. Objects scattered field reconstruction by using of dipole probes

The main version of the measuring system (Fig. 1) includes three concentric spherical surfaces (with radii $r_1^1 < r_1^2 < r_2$). The first two of them are scanning surfaces for measuring probe (probes), and third one is for radiating probe. Both measuring and radiating probes are point electrical dipoles: their moments are tangent to the corresponding surfaces and can have orientation along the angular ors $\vec{e}_\theta, \vec{e}_\varphi$ of the spherical

coordinate system connecting with the common center of spheres. The results of measurements can be presented as a matrix:

$$E_p^q(\vec{r}_2, \vec{r}_1^{1,2}), \quad p, q \rightarrow \theta, \varphi. \quad (1)$$

Here and further: the first argument indicates the point of radiating probe displacement, second one the observation (measurement) point; the higher index indicates the radiation probe moment orientation direction, lower one shows the measuring probe moment orientation direction. Under results of measurements (1) we understand the registered measuring probe full field real components of the “radiating probe - object” system.

The data of measurement results (1) permit ones to reconstruct the object scattered field in arbitrary point of space \vec{R}_1 ($R_1 \geq r_1^2$) induced by radiating dipole, placed in arbitrary point of space \vec{R}_2 ($R_2 \geq r_1^2$) as well, i.e. to obtain the RCSA pattern of the object. The electrical components of scattered field are presented by series of complex electrical vectorial spherical harmonics $\vec{E}_N(\vec{R})$ [3]:

$$E_p^q(\vec{R}_2, \vec{R}_1) = \sum_{N,M} \alpha_{NM} E_{N,q}(\vec{R}_2) E_{M,p}(\vec{R}_1) \quad (2)$$

Generalized indexes of summation N, M includes the parameters which describes the whole set of the orthogonal vectorial spherical harmonics. The expansion coefficients α_{NM} are defined in two stages:

1) For the each position of radiation probe the expansion coefficients of the measured field are determined for the each of two scanning surfaces of measuring probe:

$$\alpha_{N_{1,2}}(\vec{r}_2) = \hat{F} \{ E_\theta^q(\vec{r}_2, \vec{r}_1^{1,2}), E_\varphi^q(\vec{r}_2, \vec{r}_1^{1,2}), N, r_1^{1,2} \} \quad (3)$$

The operator \hat{F} is represented as integral on measuring surface:

$$\hat{F}(E_\theta, E_\varphi, N, r) = \int_S [\vec{E} \times \vec{H}_N(\vec{r})] d\vec{S} / \int_S [\vec{E}_N \times \vec{H}_N(\vec{r})] d\vec{S} \quad (4)$$

The first two arguments in LHS of (4) are the angular components of measured field; the third argument indicates the index of the determining coefficient (according with the index of magnetic spherical harmonic $\vec{H}_N(\vec{r})$) and fourth one determinates the radius of integration spherical surface.

The dependence of decomposition coefficients from the radius of measuring sphere caused of external (regarding to measuring sphere) source of radiation. It is possible to distinguish the objects scattered field coefficients of decomposition with help of (3) by formula

$$\alpha_N^q(\vec{r}_2) = \{ \alpha_N^q(\vec{r}_2) \chi_N(r_1^1) - \alpha_N^q(\vec{r}_2) \chi_N(r_1^2) \} / (\chi_N(r_1^2) - \chi_N(r_1^1))$$

$$\chi_N(r) = \hat{F} \{ E_{N\theta}, E_{N\varphi}, N, r \}, \quad \vec{E}_N(\vec{r}) = \text{Re} \{ \vec{E}_N(\vec{r}) \} \quad (5)$$

The external radiation, which caused of the possible disturbing fields, in region into sphere can be represented in series of real vectorial spherical harmonics $\vec{E}_N(\vec{r})$:

$$E_p^q(\vec{r}_2, \vec{R}) = \sum_N \beta^q(\vec{r}_2) E_{N,p}(\vec{R}), \quad R \leq r_2$$

$$\beta_N^q(\vec{r}_2) = \{ \alpha_{N_2}^q(\vec{r}_2) - \alpha_{N_1}^q(\vec{r}_2) \} / (\chi_N(r_1^2) - \chi_N(r_1^1)) \quad (6)$$

2) Repeating application of operator \hat{F} (4):

$$\alpha_{NM} = \hat{F}(\alpha_N^\theta(\vec{r}_2), \alpha_N^\varphi(\vec{r}_2), M, r_2) \quad (7)$$

This operation is used on base of the principle of reciprocity for the two point electrical dipoles [4]. For the real radiating and measuring probes the additional mathematical treatment is necessary. The measuring probe compensation methods are presented in series of works (see, for example [5] and papers, cited there). The method, presented below, uses the peculiarities of the far field reconstruction method (Section 2) and the measurement data set (1). Method includes both the measuring and radiating probes pattern influence improvements. The preliminary studies in this direction were performed in work [6].

3. Measuring probe pattern compensation

The relationship between results of measurements and fields expansion coefficients (fixing by point electrical dipole) can be obtained by using only single measuring sphere (with radius $r_1 = r_1^1$ or $r_1 = r_1^2$) and is realized with help of expansion coefficients $C_N^{q,m}(\vec{r}_1)$, $C_N^{q,d}(\vec{r}_1)$, $\Psi_N^q(\vec{r}_2)$ and $D_N^{q,M}(\vec{r}_2)$ of the patterns (without tested object) of measuring real probe $E_p^{q,m}(\vec{r}_1, \vec{r})$, ideal electrical dipole $E_p^{q,d}(\vec{r}_1, \vec{r})$, of undisturbed (measured with the help of ideal electrical dipole) field $E_p^{q,l}(\vec{r}_2, \vec{r}_1)$, exited from the object and of the same field, measured by the real probe $E_p^{q,M}(\vec{r}_2, \vec{r}_1)$:

$$\begin{aligned} E_p^{q,m}(\vec{r}_1, \vec{r}) &= \sum_N C_N^{q,m}(\vec{r}_1) E_{Np}(\vec{r}), \quad E_p^{q,d}(\vec{r}_1, \vec{r}) = \sum_N C_N^{q,d}(\vec{r}_1) E_{Np}(\vec{r}), \\ E_p^{q,l}(\vec{r}_2, \vec{r}_1) &= \sum_N \Psi_N^q(\vec{r}_2) E_{Np}(\vec{r}_1), \quad E_p^{q,M}(\vec{r}_2, \vec{r}_1) = \sum_N D_N^{q,M}(\vec{r}_2) E_{Np}(\vec{r}_1) \end{aligned} \quad (8)$$

The measured by real probe field components may be presented by two different ways:

$$E_p^{q,M}(\vec{r}_2, \vec{r}_1) = \sum_N D_N^{q,M}(\vec{r}_2) E_{Np}(\vec{r}_1) = \sum_N \frac{C_N^{q,m}(\vec{r}_1)}{C_N^{q,d}(\vec{r}_1)} \Psi_N^q(\vec{r}_2) E_{Np}(\vec{r}_1) \quad (9)$$

Finally from equation (9) one obtain the linear system of equations for expansion coefficients $\Psi_N^q(\vec{r}_2)$:

$$D_L^{q,M}(\vec{r}_2) = \sum_N \eta_{NL}^q \Psi_N^q(\vec{r}_2), \quad \eta_{NL}^q(\vec{r}_2) = \hat{F} \left(\frac{C_N^{q,m}(\vec{r}_1)}{C_N^{q,d}(\vec{r}_1)} E_{N\theta}(\vec{r}_1), \frac{C_N^{q,m}(\vec{r}_1)}{C_N^{q,d}(\vec{r}_1)} E_{N\phi}(\vec{r}_1), L, r_1 \right) \quad (10)$$

The equation (10) can be solved by taking limited numbers of L in (10) and equal to it numbers of summation terms by N. The system of equations should be solved for the each fixed position of radiating probe. In the general case the method of the system (10) evaluation and solution is not need any limitations for probe pattern form and doesn't require any additional measurements. The method can be used both for the radar cross-section area determination of passive objects, and for active antenna testing as well. The method can be generalized for the case of external radiation presence.

4. Objects illumination by arbitrary probe pattern

In analogy with previous results it can be reconstructed the testing object's scattered field components $E_p^{q,i}(\vec{r}_2, \vec{r}_1)$, initialized by the ideal electrical dipole on the measuring surface r_1 by help of expansion coefficients $G_N^{q,R}(\vec{r}_2)$, $C_N^{q,d}(\vec{r}_2)$, $\Phi_N^q(\vec{r}_1)$ and $P_N^{q,r}(\vec{r}_1)$ of the patterns (without tested object) of radiating real probe $E_p^{q,R}(\vec{r}_1, \vec{r})$, ideal electrical dipole $E_p^{q,d}(\vec{r}_1, \vec{r})$, and with the help of scattered from the object field distribution in the cases of ideal $E_p^{q,i}(\vec{r}_1, \vec{r}_2)$ and real $E_p^{q,r}(\vec{r}_1, \vec{r}_2)$ radiator.

$$\begin{aligned} E_p^{q,R}(\vec{r}_2, \vec{r}) &= \sum_N G_N^{q,R}(\vec{r}_2) E_{Np}(\vec{r}), \quad E_p^{q,d}(\vec{r}_2, \vec{r}) = \sum_N C_N^{q,d}(\vec{r}_2) E_{Np}(\vec{r}), \\ E_p^{q,i}(\vec{r}_2, \vec{r}_1) &= \sum_N \Phi_N^p(\vec{r}_1) E_{Nq}(\vec{r}_2), \quad E_p^{q,r}(\vec{r}_2, \vec{r}_1) = \sum_N P_N^{p,r}(\vec{r}_1) E_{Nq}(\vec{r}_2). \end{aligned} \quad (11)$$

Here the field, exciting from the object and initialized by real radiator and electrical dipole as well are presented by these formal expansions on the radiator scanning sphere versus radiator's displacement point:

$$\begin{aligned} \Phi_N^p(\vec{r}_1) &= \hat{F} \left(E_p^{\theta,i}(\vec{r}_2, \vec{r}_1), E_p^{\phi,i}(\vec{r}_2, \vec{r}_1), N, r_2 \right) \\ P_N^{p,r}(\vec{r}_1) &= \hat{F} \left(E_p^{\theta,r}(\vec{r}_2, \vec{r}_1), E_p^{\phi,r}(\vec{r}_2, \vec{r}_1), N, r_2 \right) \end{aligned} \quad (12)$$

Similarly to (9) one can write:

$$E_p^{q,r}(\vec{r}_2, \vec{r}_1) = \sum_N P_N^{p,r}(\vec{r}_1) E_{Nq}(\vec{r}_2) = \sum_N \frac{G_N^{p,R}(\vec{r}_2)}{C_N^{p,d}(\vec{r}_2)} \Phi_N^p(\vec{r}_1) E_{Nq}(\vec{r}_2) \quad (13)$$

Finally from equation (13) one obtains the linear system of equations for expansion coefficients $\Phi_N^p(\vec{r}_2)$ similarly to (10):

$$P_L^{p,r}(\vec{r}_1) = \sum_N \tilde{\eta}_{NL}^p \Phi_N^p(\vec{r}_1), \quad \tilde{\eta}_{NL}^p = \hat{F} \left(\frac{G_N^{p,R}(\vec{r}_2)}{C_N^{p,d}(\vec{r}_2)} E_{N\theta}(\vec{r}_2), \frac{G_N^{p,R}(\vec{r}_2)}{C_N^{p,d}(\vec{r}_2)} E_{N\phi}(\vec{r}_2), L, r_2 \right) \quad (14)$$

5. Determination of the scattering properties of the object

In the common case of the arbitrary patterns of both of probes, the field, initiating by radiating dipole probe and measured by the same kind of ideal dipole probe may be reconstructed with the help of the sequentially application of algorithms, developed in sections 3 and 4 by using the initial results of measurements

$$E_p^q(\vec{r}_2, \vec{r}_1), \quad p, q \rightarrow \theta, \varphi \quad (15)$$

Both the radiator and measurer are real with the corresponding decomposition coefficients $G_N^{q,R}(\vec{r}_2)$ and $G_N^{q,m}(\vec{r}_1)$ of these radiating patterns.

At the first step the reconstruction of the field distribution, measured by the ideal dipole probe should be done with the help of determination $\Psi_L^q(\vec{r}_2)$:

$$\Psi_L^q(\vec{r}_2) = \hat{T} \{ \eta_{NL}^q(\vec{r}_2), D_L^q(\vec{r}_2) \} \quad (16)$$

where \hat{T} is the linear operator, gives solution of linear system of equations and $D_L^q(\vec{r}_2)$ is a corresponding expansion coefficients of initial measured data (15)

$$E_p^q(\vec{r}_2, \vec{r}_1) = \sum_N D_L^q(\vec{r}_2) E_{Np}(\vec{r}_1) \quad (17)$$

The undisturbed field, measured by the ideal dipole probe, when can be presented as follows:

$$E_p^{q,i}(\vec{r}_2, \vec{r}_1) = \sum_N \Psi_L^q(\vec{r}_2) E_{Np}(\vec{r}_1) \quad (18)$$

which should be presented as an expansion on the sphere r_2 versus radiator displacement point:

$$E_p^{q,i}(\vec{r}_2, \vec{r}_1) = \sum_N P_N^{p,r}(\vec{r}_1) E_{Nq}(\vec{r}_2) \quad (19)$$

Finally, after determination of the function $\Phi_N^p(\vec{r}_1)$:

$$\Phi_L^p(\vec{r}_2) = \hat{T} \{ \tilde{\eta}_{NL}^p(\vec{r}_2), P_L^p(\vec{r}_2) \} \quad (20)$$

the field, distribution, initialized by the ideal dipole radiator and measured by the help of ideal dipole probe as well, may be reconstructed:

$$E_p^{q,i}(\vec{r}_2, \vec{r}_1) = \sum_N \Phi_N^p(\vec{r}_1) E_{Nq}(\vec{r}_2) \quad (21)$$

6, Determination of the cross-section area pattern

To obtain the radar cross-section area of the tested object without using the etalon object, the additional measurements of the fixed radiator radiation on the sphere r_1 should performed. Measurements must perform by the measuring probe, used during of the testing process and the far field of the radiator should be reconstructed.

The object scattered field in case of using the radiating and measuring probes having arbitrary patterns, can be presented, similar to (2), as a series of vectoral spherical harmonics The expansions are related to the spherical frame of reference, associated with the common center of the concentric spherical scanning surfaces {Fig. 1).

In this case of determination the coefficients α_{NM} , the measured data, before using far field reconstruction algorithm (Section 2), should be treated by algorithm, presented in Section 5. In the case of external radiation presence the algorithm of exclusion of this disturbing effect should be applied in addition. In this case two measuring spherical surfaces should be used (Section 2). Then the RCSA of tested object pattern may be presented as follows:

$$\sigma_p^q(\vec{R}_2, \vec{R}_1) = 4\pi R^2 \frac{|E_p^q(\vec{R}_2, \vec{R}_1)|^2}{|E_0^q|^2} \quad (22)$$

where $R_1 = R_2 = R \gg r_2$ and E_0^q is a reconstructed far field value of the radiator in the principal direction.

Thus, it's possible to perform the relative measurements of the one- or multidirectional (multipositional) RCSA and RCSA directional patterns of different object in its close (near) space instead of using the etalon object.

7. Conclusion

The methods and algorithms to obtain the scattering properties of the objects by near field measurements are presented. The possibility of correction the influence coming from the external radiation and probes patterns influence improvements are shown.

References

- [1] P.M. Herouni, III Conf. of Antenna Measurements, RMI, Yerevan, **III** (1984) 28.
- [2] P.M. Herouni, M.I. Ivanian. DAN SSSR, **292** (1987) 849.
- [3] J.A. Stratton, Electromagnetic Theory, New York, McGraw - Hill, (1941).
- [4] L.D. Landau, E.M. Lifshitz, Electrodynamics of Continuous Media, Course of Theoretical Physics, Moscow, Fizmatlit, 4-th Edition, **8** (2005) 656 (in Russian).
- [5] A.D. Yaghjian A.D. IEEE Trans. AP-**34** (1986) 30.
- [6] P.M. Herouni, M.I. Ivanian, III Intern. Conf. ICARSM-97, Voronezh, **3** (1997), 50.

Temperature Performance of a Two-Stage S-Band 40 Watt LDMOS Power Amplifier

Apet Barsegyan , Vinodh Kumar Thangam, John Titizian
Integra Technologies Inc., 321 Coral Circle, El Segundo, CA 90245, USA
apetb@integratech.com

This article presents the thermal characterization of a two-stage LDMOS power amplifier operating from 3.1-3.5GHz. The RF performance of the amplifier under pulse conditions with 1ms pulse width and 10% duty cycle is characterized versus temperature. The amplifier is designed for S-band pulsed radar applications and can operate both under short pulse/low duty cycle and long pulse/high duty cycle conditions. The temperature was varied from -45 to +85°C and the RF performance characterized. The RF test results show a decrease in the power output and power gain of the amplifier as the case temperature increases.

1. Introduction

In this paper the temperature performance of a LDMOS based RF power amplifier designed for the upper S-band frequency range optimized for radar applications was characterized. The power amplifier operates over the instantaneous bandwidth of 3.10-3.50GHz and produces a minimum of 40 Watts of output power operating under pulsed signal conditions with a 1ms pulse width and 10% duty cycle. The power amplifier is operated in class-B mode with input drive level of 0.3Watt.

The first stage (driver stage) of the power amplifier is a 10 Watt LDMOS transistor internally matched to 50-ohm [1] optimized for operating over the instantaneous bandwidth of 3.10-3.50GHz. The transistor supplies a minimum of 10 Watts operating peak power under the conditions of 1ms pulse width and 10% duty cycle. It has a typical gain of 11dB across the operational bandwidth. The transistor is biased into Class B mode of operation with drain voltage $V_{ds}=28V$ and a gate voltage $V_{gs}=2.2V$. The trimmer potentiometer resistor in the gate bias circuitry can be used to vary the quiescent current and thereby adjust the gain of the transistor.

The second stage (final stage) consists of two LDMOS transistors combined in parallel via Wilkinson power combiner [4]. Each transistor supplies a minimum of 22 Watts of peak output power and is optimized to operate over the bandwidth of 3.10-3.50 GHz under the conditions of 1ms pulse width and 10% duty cycle. Each transistor has a typical gain of 10 dB across the band. The transistor is biased in Class B mode of operation with drain voltage $V_{ds}=28V$ and a gate voltage $V_{gs}=2.2V$.

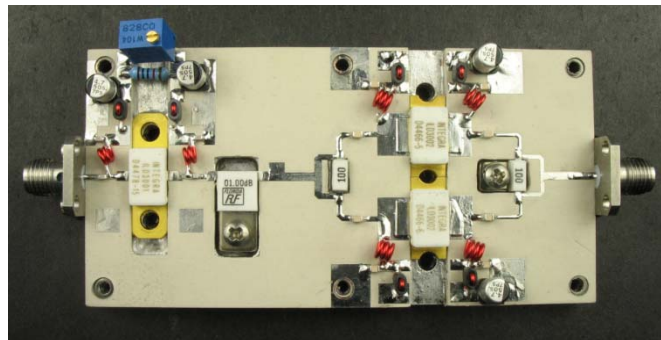


Fig.1: Two Stage LDMOS Power Amplifier optimized for 3.1-3.5GHz operation for pulsed radar applications. The PCB size measures 3.30" x 1.65" x 0.212" using 25 mil thick RO6010.

The output power from the driver stage is divided using a 2-way equally split Wilkinson power divider and provided as input for both of the final stage amplifiers. An attenuator is used between the driver stage and the Wilkinson divider for controlling the RF drive level of the final stages. The output power from the final stage transistors are combined using a 2-way Wilkinson power combiner. The transistors are matched to 50 ohms using traditional micro-strip transmission line methods.

Fig.1 shows a picture of a two stage power amplifier optimized for pulsed radar applications in the upper S-band from 3.1-3.5GHz. Rogers RO6010 circuit board material with a high dielectric constant of 10.2 is utilized in order to minimize the size and loss from the transmission line matching networks which is critical at these frequencies.

2. Results and Discussion

A 40 Watt, two stage RF power amplifier designed and optimized for pulse signal operation has been used to study the variation in the RF electrical characteristics to variation in temperature. The pallet amplifier has a typical gain of 21dB at room temperature across the band of operation. All performance characteristics are measured with input drive level of $P_{in}=0.3W$. The output power and gain performance at room temperature under 1ms pulse width and 10% duty cycle pulse versus the frequency is shown in Figure 2 below.

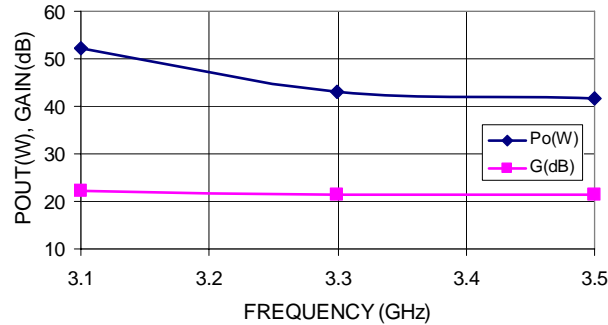


Fig.2: Power Output P_o (W) and Power Gain G (dB) versus frequency under 1ms/10% pulse at $T_{case}=25C$. Amplifier demonstrates typical gain flatness of 1dB across the operating 400MHz bandwidth.

The measured power output is 52.3, 43.1 and 41.6W at 3.1, 3.3 and 3.5GHz frequencies with corresponding power gain of 22.35, 21.52 and 21.35dB. Amplifier has power gain flatness of 1dB across the operating frequency band.

Figure 3 below shows power output performance vs. case temperature across the operating 3.1, 3.3 and 3.5GHz frequencies. As it was expected, power output/gain of the amplifier increased with lowering the case temperature and decreased with increased case temperature. Here also all measurements have been taken with fixed input drive level of 0.3 Watt. At 3.5GHz, power output/gain increase at $-40^{\circ}C$ was 2.03dB compared to $+25^{\circ}C$, whereas at 3.1 and 3.3GHz frequencies the change was 0.92 and 0.81dB, respectively.

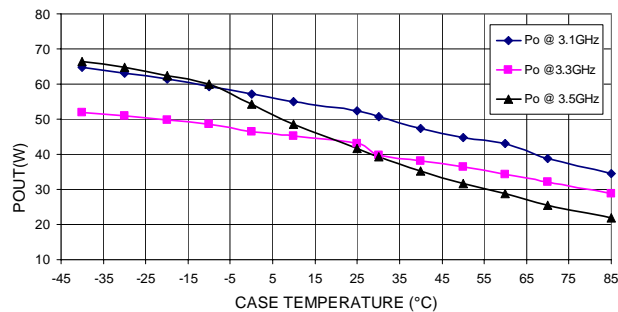


Fig.3: Power Output vs. Case Temperature measured at 3.1, 3.3 & 3.5GHz frequencies. Recorded variation in Pout was 2.73dB across $-40^{\circ}C$ to $+85^{\circ}C$ temperature range at 3.1GHz frequency.

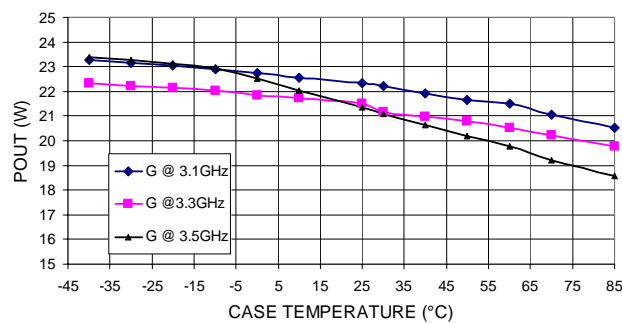


Fig.4: Power Gain versus Case Temperature.

For Si based transistors theoretical gain variation versus temperature is $-0.1dB$ per $+10^{\circ}C$. Since we have

a two stage amplification here and both stages are Si based transistors, expected gain variation from +25°C to -40°C was +1.3dB. At 3.1 and 3.3GHz frequencies power gain increase was below that number whereas at 3.5GHz it is exceeded by about 0.7dB. This may be contributed by the mismatch on the output of each transistor and inter-stage matching.

It must be mentioned also that amplifier had stable performance across the operating temperature and frequency range. The stability was verified against up to 2:1VSWR mismatch on the output and no pulse break-up has been detected across the entire temperature range of -40°C to +85°C.

Figure 4 shows power gain performance versus case temperature under 1ms/10% pulse.

The recorded variation in power gain across the entire -40°C to +85°C temperature range was 2.73, 2.57 and 4.81dB at 3.1, 3.3 and 3.5GHz frequencies. Again, power gain variation is much larger at 3.5GHz than at the other two frequencies and further investigation is necessary to determine the root cause of the variation.

Table 1 below summarizes the data taken at 3.1GHz. It is worth mentioning that power gain variation in $T_c=25^\circ\text{C}\pm 25^\circ\text{C}$ range (from 0°C to +50°C) is only 1.06dB. Gain variation from 25°C to 0°C is +0.38dB and from 25°C to 50C is -0.68dB.

F (GHz)	P _o (W)	P _{in} (W)	G	T _c (°C)
3.10	34.5	0.30	20.54	85
3.10	38.8	0.30	21.05	70
3.10	43.2	0.30	21.51	60
3.10	44.8	0.30	21.67	50
3.10	47.5	0.30	21.92	40
3.10	50.7	0.30	22.21	30
3.10	52.3	0.30	22.35	25
3.10	55.0	0.30	22.56	10
3.10	57.2	0.30	22.73	0
3.10	59.3	0.30	22.89	-10
3.10	61.5	0.30	23.05	-20
3.10	63.1	0.30	23.16	-30
3.10	64.7	0.30	23.27	-40

Table 1. Power output/gain versus case temperature at 3.1GHz. Gain variation is higher at elevated than at lower temperatures. For example, from 30°C to 70°C delta gain is -1.16dB whereas it is only +0.68dB from 30°C to -10°C.

Table 2 shows the data (power and gain versus temperature) at 3.3GHz and Table 3 at 3.5 GHz frequencies, respectively.

F (GHz)	P _o (W)	P _{in} (W)	G	T _c (°C)
3.30	28.7	0.30	19.76	85
3.30	32.0	0.30	20.23	70
3.30	34.3	0.30	20.52	60
3.30	36.5	0.30	20.79	50
3.30	38.1	0.30	20.99	40
3.30	39.8	0.30	21.17	30
3.30	43.1	0.30	21.52	25
3.30	45.3	0.30	21.74	10
3.30	46.4	0.30	21.84	0
3.30	48.6	0.30	22.04	-10
3.30	49.7	0.30	22.14	-20
3.30	50.8	0.30	22.24	-30
3.30	51.9	0.30	22.33	-40

Table 2. Power output/gain versus case temperature at 3.3GHz. Gain variation is more linear here compared to 3.1GHz. For example, from 30°C to 70°C delta gain is -0.94dB whereas it is only +0.87dB from 30°C to -10°C.

At 3.3GHz power gain variation in $T_c=25^\circ\text{C}\pm 25^\circ\text{C}$ range (from 0°C to $+50^\circ\text{C}$) is 1.05dB, similar to 3.1GHz operation. Variation from 25°C to 0°C is $+0.32\text{dB}$ and from 25°C to 50°C is -0.73dB .

F (GHz)	P _o (W)	P _{in} (W)	G	T _c (°C)
3.50	21.9	0.30	18.57	85
3.50	25.4	0.30	19.21	70
3.50	28.9	0.30	19.76	60
3.50	31.8	0.30	20.18	50
3.50	35.2	0.30	20.63	40
3.50	39.3	0.30	21.10	30
3.50	41.6	0.30	21.35	25
3.50	48.5	0.30	22.02	10
3.50	54.3	0.30	22.50	0
3.50	60.0	0.30	22.94	-10
3.50	62.4	0.30	23.11	-20
3.50	64.7	0.30	23.27	-30
3.50	66.4	0.30	23.38	-40

Table 3. Power output/gain versus case temperature at 3.5GHz. Although gain variation linear here compared to 3.1GHz operation, but the absolute number is much higher compared to both 3.1GHz and 3.3GHz operation. For example, from 30°C to 70°C delta gain is -1.89dB and it is $+1.84\text{dB}$ from 30°C to -10°C .

At 3.5GHz power gain variation in $T_c=25^\circ\text{C}\pm 25^\circ\text{C}$ range (from 0°C to $+50^\circ\text{C}$) is 2.32dB. Variation from 25°C to 0°C is $+1.15\text{dB}$ and from 25°C to 50°C is -1.17dB .

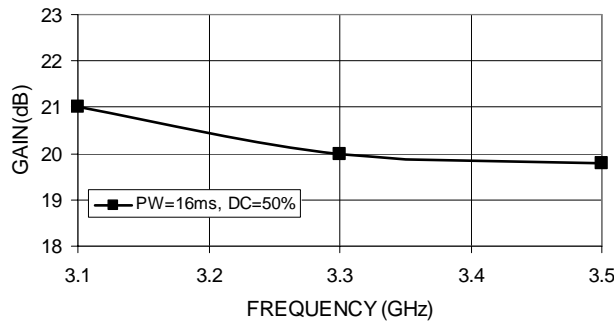


Fig.5: Power gain versus frequency at constant output power of 40W with a 16ms pulse width and 50% duty cycle and $T_{\text{case}}=25^\circ\text{C}$.

The RF power amplifier was also tested under extremely long pulse conditions with a 16ms pulse width and a heavy duty cycle of 50%. Under both of these conditions there are minimal cooling effects of the pulse signal and the temperature rise inside the device results in gain flatness of 1.2 dB across the frequency band of operation. Even under these harsh conditions, however, the power gain has been maintained at approximately 20dB while biased in Class B mode of operation.

3. Summary

One observation from the tables 1, 2 and 3 is that the power gain variation across the -40°C to $+85^\circ\text{C}$ temperature range is much higher at 3.5GHz compared to 3.1 and 3.3GHz frequencies. For example, gain variation from $+25^\circ\text{C}$ to $+85^\circ\text{C}$ is -1.81dB , -1.76dB at 3.1, 3.3GHz frequencies and -2.78dB at 3.5GHz. This results in $-0.302\text{dB}/10^\circ\text{C}$, $-0.293\text{dB}/10^\circ\text{C}$ and $-0.463\text{dB}/10^\circ\text{C}$ at 3.1, 3.3 and 3.5GHz, respectively. In $+25^\circ\text{C}$ to -40°C temperature range, gain variation is 0.92dB , 0.81dB and 2.03dB at 3.1, 3.3 and 3.5GHz, respectively, which results in $0.142\text{dB}/10^\circ\text{C}$, $0.125\text{dB}/10^\circ\text{C}$ and $0.312\text{dB}/10^\circ\text{C}$ at 3.1, 3.3 and 3.5GHz. There is good correlation in performance at 3.1 and 3.3GHz frequencies, but at the high end of the band variation is as high as 60% more compared to mid-band and lower frequencies.

4. Conclusions

RF performance of a two-stage, 40 Watt, S-band LDMOS power amplifier has been characterized over -40 to +85C temperature range. . The test results show that the power amplifier has a higher gain at lower operating temperatures and lower gain at higher operating temperatures. The recorded gain variation at 3.5GHz is much larger than at 3.1 and 3.5GHz frequencies. Further investigation is needed to determine the root cause of the variation.

Table 4 below summarizes power gain variations versus case temperature at temperature extremes and versus room temperature measurements (25C). It also includes the gain variation versus frequency and temperature (ΔG_3).

F (GHz)	3.10	3.30	3.50
$\Delta G_1(\text{dB})=G(85^\circ\text{C})-G(-40^\circ\text{C})$	-2.73	-2.57	-4.81
$\Delta G_2(\text{dB})=G(25^\circ\text{C})-G(-40^\circ\text{C})$	-0.92	-0.81	-2.03
$\Delta G_3(\text{dB})=G(85^\circ\text{C})-G(25^\circ\text{C})$	-1.81	-1.76	-2.78
$\Delta G_3(\text{dB})=G(\text{MAX})-G(\text{MIN})$	4.81		

Table 4. Power gain variation versus case temperature at temperature extremes across the operating 3.1 to 3.5GHz band. Recorded worst case variation is -1.81dB, -1.76dB and -2.76dB at 3.1, 3.3 and 3.5GHz frequencies, respectively.

It has been demonstrated that a two-stage silicon RF LDMOS amplifier performs well under extreme temperature ranges from -40 to +85C. The RF performance under long pulse conditions (pulse widths exceeding 1ms and duty cycles at or above 10%) produce more power on target, a key parameter in radar systems. The LDMOS design provides more than 20dB of gain across the frequency band of operation. The power amplifier demonstrates the utilization of a 50 ohm matched device in the first stage which allows the PCB size to remain small and reduces the passive component count both of which reduce the overall cost of the system.

Acknowledgement

The authors would like to thank Brian Battaglia for his support and helpful discussions during this work and Fernando Malit for his support in amplifier assembly.

References

- [1] Datasheet MPAL3135M15 www.integratech.com
- [2] V. Kumar, D. H. Kim, A. Basu and I. Adesida, "0.25 μm Self-Aligned AlGaIn/GaN High Electron Mobility Transistors," *2008 IEEE EDL.*, Vol. 29, No. 1, pp. 19-20.
- [3] G. Formicone, F. Boueri, J. Burger, W. Cheng, Y. Kim, and J. Titizian, "Analysis of Bias Effects on VSWR Ruggedness in RF-LDMOS for Avionics Applications," *2008 EuMW-2008*.
- [4] Robert E. Collin, *Foundations for Microwave Engineering*, 2nd Edition, John Wiley & Sons.

High Power RF/Microwave Transistors, Pallets and Amplifiers from Integra Technologies, Inc.

A. Barsegyan

Integra Technologies Inc., 321 Coral Circle, El Segundo, CA 90245, USA
apetb@integratech.com

Integra Technologies, Inc. is engaged in design and manufacturing of High Power RF/Microwave transistors, 50-ohm matched pallet amplifiers, miniaturized power amplifiers (MPA) and High Power Amplifiers (HPA) based on silicon Bipolar and FET technologies, including LDMOS, operating from VHF to S-band frequencies. Currently, extensive development work is being done on Gallium Nitride technology, which will enable operations for X-band and higher frequencies.

Incorporated in the state of California in 1997, Integra has become a leading supplier of RF transmitter modules for Radar and Avionics equipment and system manufacturers. Today Integra is a multi-million dollar, ISO9001 certified company with a broad customer base spanning the globe including Armenia.

The purpose of this paper is to familiarize the audience with the company and how its products can be used in Armenia.

The 50 Ohm pallets are essentially building blocks combined in parallel to achieve any required system level power for a conventional high power transmitter or can be used individually as radiating elements for a Phased Array Radar (PAR) system.

Institutions in Armenia have been utilizing such products to build RF transmitters. This knowledge base which appears to be growing over the years can be extended to cover other types of RF transmitters used in Avionics, Broadcast, Cell phone infrastructure, SATCOM and miscellaneous wireless communication systems.

The photo below illustrates an S-band 3.1-3.5GHz, 2-stage, 650 Watt HPA, where Integra transistors and pallets are employed on both stages of amplification. The unit also includes digital circuitry to monitor output Voltage Standing Wave Ratio (VSWR) and flange temperature of transistors. Systems designers use several such HPA's combined in parallel to achieve desired system level power.

1. IBA3135M650 Amplifier

The IBA3135M650 is a solid state, base plate cooled, pulsed RF amplifier operating in the 3.1-3.5GHz frequency range. Its operating voltage is 36.0 ± 0.2 VDC and operating temperature is -25 to +65°C. The amplifier has an optional internal circuitry to monitor temperature and operating power levels (input, output, and reflected). RF input to the amplifier is through a female SMA connector and output is via a female N connector.

This amplifier is intended for use in military radar systems and is capable of a wide variety of pulse formats and duty cycles. Its output is protected against high VSWR by an internal circulator. The nominal output power at 25°C is 650W with 25W input power.

Specifications @ 25 degree Celsius

- Operating frequency range – 3.1 to 3.5GHz
- Instantaneous Bandwidth – 400MHz
- Output Power - > 650W peak
- Input Power – 25W peak
- Input Return Loss - > 10dB
- Pulse Width – up to 150us
- Duty Cycle – 10% max
- Pulse Amplitude Droop – 1dB max
- Insertion Phase – $0 \pm 20^\circ$
- Peak DC Current – 80A max
- RF Envelope Rise time – 130ns max
- RF Envelope Fall time – 110ns max
- Spurious Outputs – 50dBc min

- Harmonics (2nd through 4th) – 30dBc
- Note: Amplifier can operate at higher duty cycles with reduced power output

2. Amplifier Architecture

The IBA3135M650 is a solid state two-stage pulsed power amplifier. The RF amplifier assembly consists of a hybrid coupled first stage driver module followed by a 4-way hybrid power splitter. The four outputs from the power splitter are fed to 4 identical hybrid coupled power modules whose outputs are combined and routed to the internal output circulator, protecting the module from high VSWR load conditions.

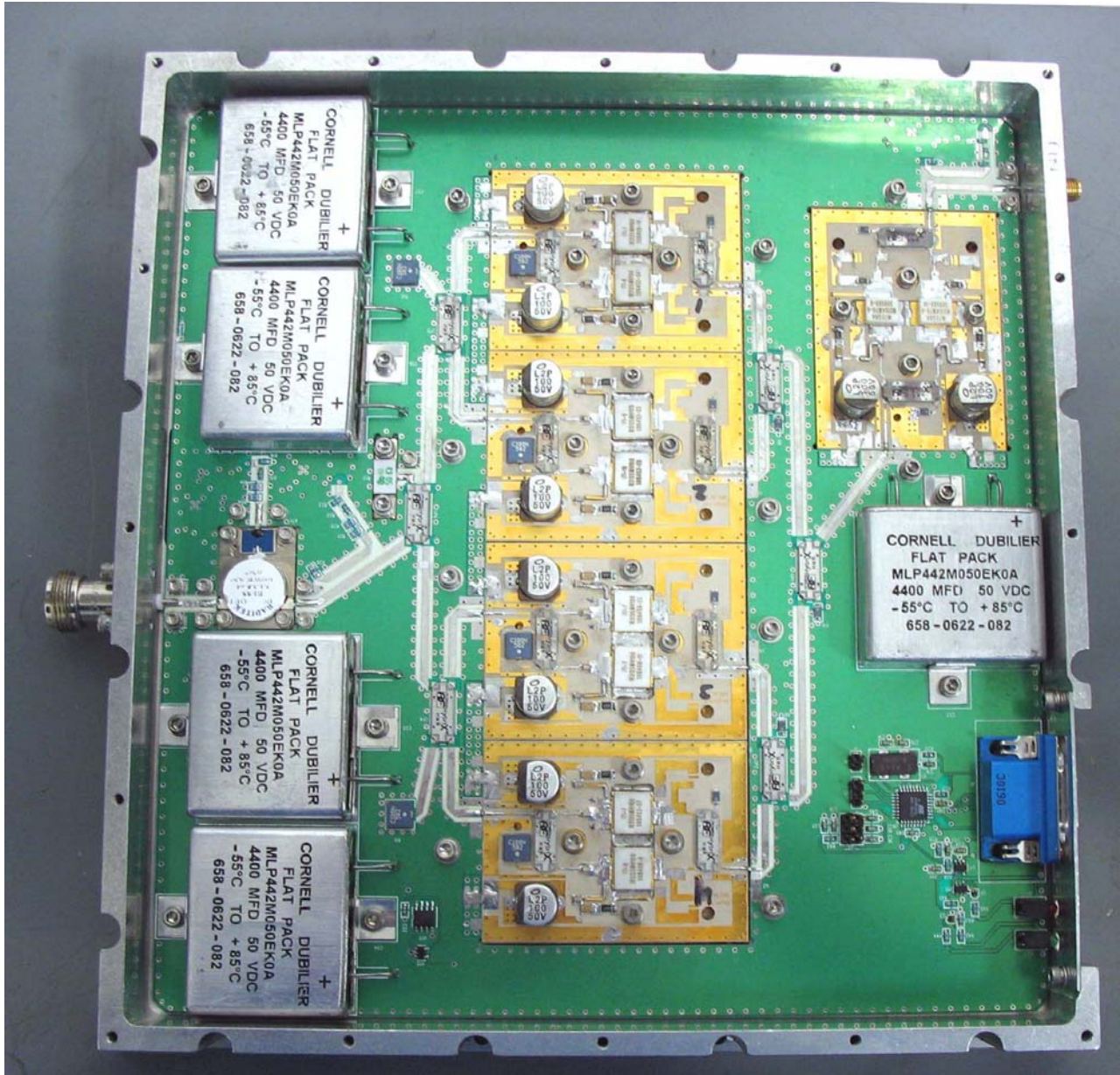


Fig. 1. 3.1-3.5GHz, 2-stage, 650 Watt Pulsed Power Amplifier

The first stage of amplification is realized via Integra IBP3255 pallet. This driver module consists of two IB3135M70 transistors combined in parallel and amplifies the 25W input signal to minimum of 130 Watt level.

The output of IBP3255 pallet is then split via a 2 stage, 4-way hybrid splitter into four equal signals used to drive the second stage power module IBP3249.

IBP3249 pallet is based on the Integra IB3135MH100 power transistor – 2 combined in parallel and has typical Power Output of 200 Watts and Power Gain of 8dB . It operates under 36Volt collector bias. The outputs from the 4 power modules are combined via a 2- stage, 4-way hybrid combiner and routed to the output power coupler and circulator.

The output of the amplifier is protected against high VSWR conditions by a Raditek RI-SS-3.1-3.5-CD-100WR-A30 circulator.

The amplifier has a built in RF power detectors and a microprocessor which monitors a sample of the input, output and reflected output power in addition to the amplifier temperature. There is a green and a red LED near the D-subminiature power connector that provide indication of DC power and over-temperature respectively. BIT features to include:

- Input power fault – over range
- Output VSWR fault – over range
- Over temperature fault – over range

Typical RF performance data is given in the table below:

Part No.	Freq(GHz)	P _o (W)	RL(dB)	Gain (dB)	Nc (%)	Droop
	3.10	779	18.0	14.93	25.24	-0.38
IBA3135M650	3.30	709	24.0	14.53	27.77	-0.44
	3.50	670	21.0	14.28	28.32	-0.31

The rated 650 Watt minimum power is achieved by combining four IBP3249 pallets in parallel. The insertion losses associated with power combining and output isolator are about 0.8dB at the high end of the band.

Output Power/Gain Flatness of the amplifier is less than 1dB maximum and typical number is about 0.7dB. This is achieved by implementation of Gain Equalizing Networks employed on both stages of amplification. Both IBP3255 and IBP3249 pallets include the Gain Equalizing Networks on the input of the matching networks.

3. IBP3249 and IBP3255 pallet amplifiers

As we mentioned above, IBP3255 pallet consists of two IB3135M70 transistors combined in parallel. It operates under 36Volt collector bias and has typical Power Gain of 7.5dB. Typical RF data is given in the table below:

Part No.	Freq(GHz)	P _o (W)	RL (dB)	Gain (dB)	Nc (%)	Pulse Droop (dB)
	3.10	157	17.8	7.98	41.34	-0.25
IBP3255	3.30	175	17.4	8.46	43.29	-0.20
	3.50	143	14.0	7.57	40.35	-0.19

IBP3249 pallet is based on the Integra IB3135MH100 power transistor, operates under 36Volt collector bias and has typical Power Output of 200 Watts and Power Gain of 8dB. Typical RF data is given in the table below:

Part No.	Freq (GHz)	P _o (W)	RL (dB)	Gain (dB)	Nc (%)	Pulse Droop (dB)
	3.10	225	13.2	8.34	44.46	-0.18
IBP3249	3.30	221	14.4	8.25	41.48	-0.20
	3.50	197	18.4	7.75	40.88	-0.22

4. IB3135M70 and IB3135MH100 transistors

The primary building block of a reliable High Power RF amplifier is the RF circuit and the High Power RF transistor itself. It is in the design of this transistor that reliability related factors, such as metallization and ballasting, must be taken into account. Integra's transistors utilize high f_t process, interdigitated geometry and gold metallization for the highest possible functional performance and reliability. Emitter ballast resistors assure devices are less susceptible to thermal runaway and prevent hot spotting across the transistor chip.

Integra's IB3135M70 transistor is used for the 1st stage of the amplifier. The second stage of amplification is realized via IB3135MH100 transistor. Both transistors are Common Base, Class C, hybrid bipolar junction transistors, are gold metallized and use gold bonding wires for electrical connections to enhance device reliability.

IB3135MH100 device is specified at 100 Watt minimum output power over the given frequency with 7.90 dB minimal gain. The device has internal input and output matching networks and operates from a single 36V power supply. It is rated at 2:1 VSWR for survivability. IB3135M70 device is specified at 70 Watt minimum output power over the given frequency with 7.65 dB minimal gain. The device has internally matched input and output networks and operates from a single 36V power supply. The device is also rated at 2:1 VSWR for survivability.

5. Conclusion

Integra Technologies, Inc is a vertically integrated company with unique ability to provide high power RF solutions from basic transistors to pallet and amplifier levels, covering operations from VHF to S-band frequencies. Over the past several years Integra has proven many times its ability to design and mass produce state of the art transistors, pallets and amplifiers in very short time intervals. Integra products are used in critical systems such as Air traffic Control, Phased Array, Shipboard and other military and civilian use radars. Therefore, regardless of your needs in RF High Power industry – transistors, pallets or amplifiers, Integra Technologies, Inc is able and willing to help you to find and produce solutions. If you have a system level requirement, for example, transmitter box or complete radar system, Integra team can help you to select right component from the existing reach portfolio or if necessary, will develop one that will work for you. We will work with you to create component specifications based on the given system level requirement and support your needs through production cycle.

Development of the Software Architecture for Control and Diagnosis of Devices in Heterogeneous Systems

M. V. Markosyan¹, A. L. Grigoryan^{1,2}, T. A. Papoyan¹

¹ Yerevan Telecommunication Research Institute (YeTRI), Dzorap str. 26, (37410) 56 60 61 Yerevan, Armenia

² State Engineering University of Armenia, Teryan str. 105, Yerevan, Armenia

We consider the software architecture for automated diagnosis and management of devices across heterogeneous systems. The proposed architecture is modular, which provides simplicity and flexibility. We consider in detail the structure and function of all modules. Management and diagnosis is based on the expert data, which are defined in the scripting language JavaScript.

1. Preface

With the development of programme-device compound systems in the sphere of information technologies the demand for automatized systems increases from year to year. The architecture of program providing for automatic diagnostics and the management of devices in heterogeneous systems is being observed. The system is characterised by the presence of two interacting independent moduls – the client and the server which commonly can be realised on different computers, exchanging data through the net.

2. The architecture of the system

The program must carry out the following tasks:

1. Ask data from devices periodically
2. Work out the received data
3. Realize scripts of diagnostics and management defined by the expert
4. Write down the information about the events in database

The following architecture is suggested (Fig. 1):

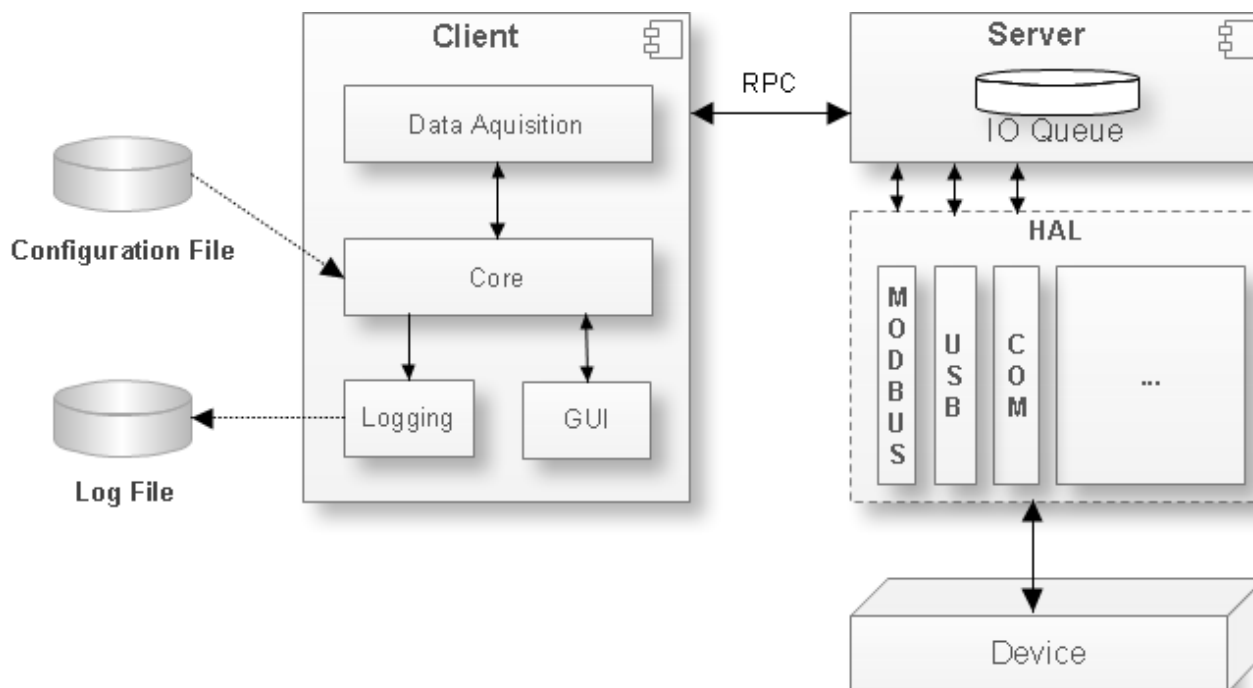


Fig. 1 The architecture of the system

The program providing consists of 2 basic moduls and an additional layer: client module, server module and Hardware Abstraction Layer.

Commonly, the computer to which the devices are connected, may differ from the operator's computer that is why the system is divided into client and server parts. The client module sends requests to be written down or read from the device to the server module which realises them and returns the result. The client module receiving the data from devices works them out according to certain scripts, as well as gives graphical interface for the operator. Both modules interact with the help of RPC protocol. For the abstraction from definite protocols of interaction with devices, an additional layer HAL (Hardware Abstraction Layer) is imported between the server and the devices. Let us observe the parts of the system in detail.

2.1. Hardware Abstraction Layer

There is a great number of protocols of interaction with the devices. It would not be appropriate to realize such a great number of protocols in the server module as for the given system only a few or one protocol may be necessary. To solve the problem of the dead code and to make the structure of the server easier, the realization of certain protocols was exported to a separate layer called Hardware Abstraction Layer (HAL). HAL is a great member of program modules, let us call them drivers, each of which realizes a certain protocol of working the device and gives a program interface of input/output for the server module.

Firstly, HAL increases the flexibility of the program as drivers can be added and removed at your discretion not touching its remaining parts. Secondly it hides the whole difficulty of interaction with the devices from the server module. From server's point of view now our heterogeneous system is simple uniform structure which can be presented as a table (Table 1):

Protocol ID	Device ID	Address			
0	0	0x0000	0x0001	...	0xFFFF
	1	0x0000	0x0001	...	0xFFFF

1	0	0x0000	0x0001	...	0xFFFF
	1	0x0000	0x0001	...	0xFFFF

...					

Table 1

For the request to any device the server needs to know the following data:

1. the number of the protocol
2. the number of the device
3. the access mode
4. the linear address
5. the number of data units

Each device in the system is unequivocally defined by the number of protocol and the number of the device. The number of the protocol defines which definite driver server the given device. In addition, each device has its identifier – the number of the device as one driver can serve several devices at a time. The mode of access may have the following meanings (Table 2):

	1 bit	8 bit	16 bit	32 bit
Read-Only	0	2	4	6
Read-Write	1	3	5	7

Table 2

Depending on the concrete driver realisation and on the device type address distance for different modes may and may not coincide. As both cases are possible, this detail must be specified in the driver documentation.

2.2. Server

Server module introduces program interface to the client module for the device interaction. This interface represents the functions of reading and writing which are brought forth distantly by the client module with the help of RFC protocol. In case of receiving inquiry the server redirects it to the corresponding HAL driver and returns the result or error message. Both consequent and parallel operations of input and output are supported. If the device is occupied the inquiry is queued.

2.3. Client

Client module carries out the main part of the task – periodically inquires the demanded data from the server, carries out the working out script, saves the diagnostic information in the database and reflects graphically the system condition. Given module consists of 4 main sub-systems: the core, the sub-system of data collection, the sub-system of logging and the sub-system of graphic interface for interaction with the operator. When starting the client module the object of core is the first to be created which downloads the file of configuration. In fact that file is the description of the whole system and contains all the necessary data for the operation of the program such as: server IP address, the number of used protocols, the hierarchy of devices, the names of devices and variables, the addresses used by each device, the scripts of working out etc. The configuration file has XML format.

All the logic of diagnostics and management is realised in the form of scripts written in JavaScript language, which are carried out on the interpretator embedded in core. Using files from the configuration database, the core creates and initializes the other sub-system, after which creates a working out flow and the carrying out of the main task is started. The core periodically counts the data in the sub-system database and saves in the named variables that are available in the JavaScript area. In this way the data from devices can also be dealt with the same way as common variables with the difference that the first are read-only. Having received the data the scripts are carried out which realise the operations specified by the expert.

The sub-system of data collection provides the delivery of the data necessary for the core as well as for the feedback connection, provides recording function in the device. When starting working out process the given sub-system creates separate flow for each protocol, connects to the server and starts counting data from the address configuration file with given frequency. Received data are saved in the dynamic memory and are available for reading from the core. In the process realisation it should be taken into consideration that the data are changed in one flow and read in another, consequently access synchronization should be taken care of.

The sub-system of logging is meant for saving all the necessary diagnostic information in the database. It is necessary for restoring the pace of actions and finding out the cause in case of errors. Each record should contain minimum 4 fields: the exact time, the level (debug, dangerous, critical), the source and the message. The quantity of the fields can be enlarged if necessary. Given sub-system is realised as singleton class, i.e. it's only sample is created that is available both for the other sub-systems and the JavaScript area.

The sub-system of graphic interface is meant for the visualisation of the system state. It also gives a convenient mechanism for the operator. The given sub-system is maximally autonomic from the other sub-system and interacts with them only in the area of JavaScript. Such independence gives an opportunity to change or fully redo the graphic interface, not touching upon the code of the other parts.

3. Conclusion

As the process of diagnosis of systems is a problem of paramount importance from the point of ensuring normal working functionality, so expert systems of diagnosis are intensively expanding and developing. The proposed architecture is modular, which provides simplicity and flexibility.

References

- [1] J.C. Giarratano, G.D. Riley, Expert Systems: Principles and Programming (Williams Publishing Corporation, Moscow. St. Petersburg. Kiev, 1152pp., 2007)
- [2] A. Birger, Technical Diagnostics(Mechanical engineering Corporation, Moscow,241pp., 1978)

Измеритель мощности миллиметрового и ИК диапазона

Р.А. Симонян¹, А.Г. Гулян¹, А.А. Саноян¹, Р.М. Киракосян²

¹ Institute of Radiophysics and Electronics, Alikhanian Brothers str. 1, 378410 Ashtarak, Armenia

² Université de Toulouse, Laplace UMR CNRS 5213, UPS, 118 Route de Narbonne, 31062 Toulouse FR

Описан измеритель поглощаемой мощности падающего излучения ММ и ИК диапазона длин волн, который обеспечивает измерение поголощаемой мощности излучения начиная от $0,1 \times 10^{-3}$ Вт с точностью порядка 1%. Прибор отличается от известных тем, что нагрев нагрузки сравнения осуществляется при помощи совмещенного в одном транзисторе функции датчика температуры и нагревателя. Этим обеспечивается полная идентичность по теплофизическим параметрам обеих нагрузок. Разность температур между нагрузками $\leq 0,01^\circ\text{C}$, при этом измерительная нагрузка нагревается поглощенным в нагрузке СВЧ излучением, а нагрузка сравнения нагревается низкочастотными импульсами. Описанный измеритель может найти применение при разработке высокоточных чувствительных ваттметров как в области ММ волн, так и в области ИК диапазона длин волн.

Широкое применение калориметрических методов измерения мощности СВЧ излучения оправдано простотой превращения энергии электрического тока в тепловую и удобствам измерения теплоты. Среди колориметрических измерителей мощности временные и точностные характеристики существенно улучшаются при введении в их состав нагрузок сравнения. В основу работы таких колориметров заложен принцип сравнения теплового воздействия измеряемой мощности подаваемого на измерительную нагрузку первичного измерительного преобразователя с тепловым воздействием известной мощности постоянного или переменного тока низкой частоты подаваемого на нагрузку сравнения и фактически процесс измерения СВЧ мощности сводится к измерению мощности подаваемой на нагрузку сравнения. На таблице 1 приведены основные параметры ваттметров поглощаемой мощности имеющие измерительные камеры и камеры сравнения.

Таблица 1

	Тип колориметра	Мощность измерения	Диапазон измерения	Погрешность измерения	примечание
1	МЗ-11А	$(10 \times 10^{-3} \dots 10)$ Вт	(1МГц...11,5) ГГц	$\leq 5,8 \%$	Жидкостный теплообменник, замена на МЗ-56, МЗ-95
2	МЗ-13	$(2 \dots 2 \times 10^3)$ Вт	(30МГц...1,6) ГГц	4-8 %	Жидкостный теплообменник, замена на МЗ-48, МКЗ-68
3	МЗ-13/1	$(6 \dots 2 \times 10^3)$ Вт	(2,59ГГц...37,5) ГГц	4-8 %	Жидкостный теплообменник, замена на МЗ-45, МЗ-46, МЗ-47, МКЗ-70, МКЗ-71
4	МКЗ-18А	(0,1...10) мВт	(0,4...3,5) мкМ	$\pm 10 \%$	Сухой калориметр
5	МЗ-24	(10...1000) мВт	(0,22...7,5) мкМ	$\pm 12,5 \%$	Сухой калориметр

Как следует из таблицы, ваттметры сравнения отличаются широкополосностью, большим динамическим диапазоном и с погрешностью измерения 4-8%, а для ваттметра оптического диапазона до 12,5%. Это объясняется тем что в калориметрах с жидким теплоносителем, источником погрешности могут служить недостаточная интенсивность перемешивания жидкости, образования пузырьков в трубопроводе, флуктуация температуры потока жидкости и т.д.. В сухих калориметров основным источником погрешности служат различные температурные поля для измерительной нагрузки и нагрузки сравнения. Наличие нагревателя для нагрузки сравнения уже создает различие теплофизических параметров между нагрузками, что и является источником погрешности.

Для существенного улучшения параметров сухих (статических) измерителей мощности целесообразно применить решения принятое [4], где благодаря временному разделению функции измерения и регулированию температуры стало возможным изготовление нагрузки с полностью одинаковыми теплофизическими параметрами.

Упрощенная функциональная схема разработанного измерителя мощности (ИМ) показан на рис.1. На рисунке показаны цифрами: 1 термодатчик (р-п переход биполярного транзистора), нагрузки измерения, 2-термодатчик-нагреватель (транзистор) нагрузки сравнения, 3,4,5-ограничивающие или развязывающие резисторы, 6-резистор для измерения тока коллектора транзистора 2, 7,8,9,10-электронные ключи, при этом, ключи 9,10 работают в противофазных режимах относительно ключей 7,8, 11-генератор меандра с противофазными выходами, 12-блок управления нагревом нагрузки сравнения, 13,14-блоки измерения температуры, 15-дифференциальный усилитель, 16-блок измерения мощности, 17-нагрузка измерения, 18-нагрузка сравнения, 19-тепловой экран, 20-теплоизолятор (пенопласт). Схема питается от двух стабилизированных источников $\pm 15\text{В}$ и источника 20В для нагрева нагрузки сравнения.

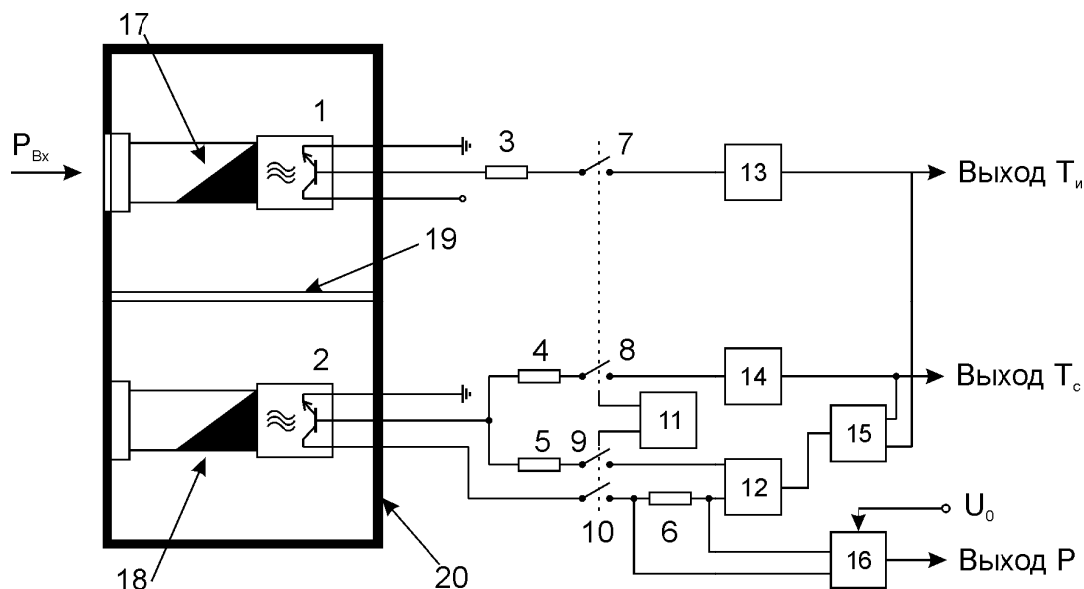


Рис.1 Функциональная схема измерителя мощности. 1-термодатчик камеры измерения, 2-термодатчик камеры сравнения, работающего также в режиме нагревателя, 3,4,5,6-резисторы, 7,8,9,10-электронные ключи, 11-генератор меандра с противофазными выходами, 12-блок управления нагревом камеры сравнения, 13,14-блоки измерения температуры, 15-дифференциальный усилитель, 16-блок измерения мощности, 17-измерительная нагрузка, 18-нагрузка сравнения, 19-тепловой экран, 20-теплоизолятор.

Отметим, что 1 и 2 элементы выполнены на одностипных транзисторах, при этом коллектор транзистора 1 не используется. Нагрузки 17 и 18 совершенно однотипные и для создания хорошего теплового контакта с корпусами транзисторов 1 и 2 использована теплопроводящая паста. Нагрузки изолированы от окружающей среды пенопластом ПХВ-1 и имеют общий медный тепловой экран 19. При этом вход нагрузки 17 открыт для падающего излучения, а вход нагрузки 18 закрыт.

Измеритель мощности работает следующим образом. После включения сетевого напряжения включается источник СВЧ излучения, подключенный к входу нагрузки измерения. Нагрузка 17, согласованная с волноводным СВЧ трактом ($K_{СВН} < 1,2$) начинает нагреваться, что приводит к тому, что на выходе электронного термометра 13 образуется напряжение, пропорциональное температуре нагрузки 17. При этом, процесс нагрева будет продолжаться до тех пор, пока приращения температуры измерительной нагрузки $\Delta T_{и}$ будут удовлетворять условию

$$\Delta T_{и} = P_{СВЧ} \cdot R_{Ти}, \quad (1)$$

где $P_{СВЧ}$ -мощность поглощаемой нагрузки, $R_{Ти}$ -коэффициент, определяющий количество тепла, переданное измерительной нагрузкой окружающей среде (тепловому экрану), $R_{Ти}$ -фактически, это величина теплового сопротивления, нагрузка-окружающая среда (тепловой экран).

Почти одновременно с нагревом измерительной нагрузки 17 нагревается также нагрузка сравнения 18, т.к. нагрузка сравнения представляет из себя следящий термостат с датчиком,

которым является термометр 13, выходное напряжение которого служит как задающее напряжение термостата на основе транзистора 2.

Так как тепловая постоянная времени установления температуры нагрузки измерения почти на порядок больше, чем время установления температуры нагрузки сравнения, то после установления температуры нагрузки измерения 17 также устанавливается температура нагрузки сравнения 18. Для измерения мощности необходимо для нагрева нагрузки сравнения на температуру $\Delta T_{нс}$ измеряться ток коллектора транзистора 2 с последующим умножением на напряжения на коллекторе U_k , что реализуется в блоке 16. Для этого импульсное напряжение с обоих концов резистора 6, включенное последовательно с коллектором транзистора 2, усиливается, преобразуется в напряжение постоянного тока при помощи синхронного детектора-фильтра (для обеспечения высокой помехоустойчивости), для которого в качестве опорной фазы используется напряжение с выхода меандра 11 (в схеме 1 не показан). Умножение тока на напряжение на коллекторе производится прецизионным аналоговым умножителем AD534L, с допустимой ошибкой умножения не более $\pm 0,25\%$. Выходное напряжение постоянного тока блока 16 с высокой точностью пропорционально мощности нагрева нагрузки сравнения.

Таким образом, поглощаемая в нагрузке измерения 17 мощность привела к нагреву нагрузки на $\Delta T_{и}$, что привело к росту напряжения на выходе термометра 13 на $\Delta U_{и}$. Такой рост напряжения датчика термостата (фактически нагрузки сравнения) привел к росту температуры на $\Delta T_{ср}$. Настолько температуры $\Delta T_{и}$ и $\Delta T_{ср}$ равны, фактически зависит и основная погрешность измерения. Отметим, что стабильность установленного значения температуры нагрузки 18 и ее дрейф зависят от стабильности и дрейфа дифференциального усилителя 15. При исполнении дифференциального усилителя на прецизионном операционном усилителе ОР-07, временной дрейф температуры нагрузки будет иметь порядка $0,2 \times 10^{-3} \text{ }^\circ\text{C}/\text{месяц}$, а температурный дрейф не более $0,3 \times 10^{-3} \text{ }^\circ\text{C}$, при изменении температуры окружающей среды на 1°C .

Так как нагрузка сравнения и нагрузка измерения по своим теплофизическим параметрам абсолютно не отличаются друг от друга, то можно утверждать, что при применении большого усиления и прецизионной микросхемы $\Delta T_{и} = \Delta T_{ср}$, или же $P_{свч} = P_{имп}$, где $P_{свч}$ часть падающей мощности поглощенная в измерительной нагрузке, $P_{имп}$ мощность для нагрева нагрузки сравнения, измеренное блоком 16. Обычно измерительные нагрузки имеют КСВН от 1,15 до 1,6. Величина падающей мощности определяется по формуле

$$P_{свч} = \frac{P_{иц}}{K_3(1-|\Gamma_{нр}|^2)} \quad (2),$$

где $K_3 \approx 1$ (при полном равенстве $T_{из} = T_{ср}$), а модуль коэффициента отражения

$$|\Gamma_{нр}| = \frac{E_{отр}}{E_{под}} \quad (3),$$

$E_{отр}$ -напряженность поля отраженной волны, $E_{под}$ -напряженность поля подающей волны или же

$$|\Gamma_{нр}| = \frac{КСВН-1}{КСВН+1} \quad (4).$$

При изготовлении макета измерителя мощности была проверена долговременная стабильность разницы $T_{из} - T_{ср} \leq 0,01^\circ\text{C}$.

Основные технические параметры разработанного измерителя мощности следующие:

- Диапазон частот измерителя от ММ волн до ИК диапазона,
- Диапазон измеряемых мощностей $0,1 \times 10^{-3} \dots 200 \times 10^{-3} \text{ Вт}$,
- Точность измерения поглощаемой мощности $\pm 1\%$,
- Габариты $250 \times 200 \times 80 \text{ мм}$
- Вес $\leq 6,5 \text{ кг}$

Разработанный измеритель мощности может найти применение благодаря высокой точности, простоте изготовления и широкому диапазону измеряемых частот, начиная от субмиллиметровых и миллиметровых волн и кончая инфракрасным диапазоном. Очевидно, что в каждом поддиапазоне

следует применять согласование с волновым сопротивлением нагрузки. Для высокой стабильности показания целесообразно термостатировать тепловой экран (с точностью $\pm 0,1^{\circ}\text{C}$).

Литература

1. Справочник по радиоизмерительным приборам, Под. Ред. В.С. Насопова, том 2, М. 1977, 212 ст.
2. Измеритель мощности на СВЧ, М.И. Билько, А.К. Томащевский, Радио и связь, М. 1986, 168 ст.
3. Симонян Р. А., Везирян Э. Г., АС 1557458, Устройства для измерения температуры, Бюл. 14, 15.04.1990
4. Симонян Р. А., Торилян Д. Э, АС 1501006, Устройство для регулирования и измерения температуры, Бюл. 30, 15.08.1989

The Application of the Developed Methods of Materials Joining in Electronic Engineering

V. Avagyan, T. Mkrtchyan, R. Mikaelyan

Center for the Advancement of Natural Discoveries using Light Emission, Acharian 31, 375040 Yerevan, Armenia

The presented is the technology of diffusion joining of dissimilar metals: copper+ stainless steel, copper+ steel 3, stainless steel+ titanium. New method of diffusion joining of the copper and stainless steel excluding the chrome oxidization from vacuum chamber residual gases in stainless steel is experimentally developed. Diffusion joining of stainless steel and steel-3 used in accelerator technology for electromagnets development is studied. It is proposed to make diffusion joining of stainless steel and steel-3 by a thin shell preventing carbon to be reconstructed. Technological processes of diffusion joining of stainless steel and titanium are studied using intermediate metallic shells in joining zones. As a result, successive layers of stainless steel, copper, vanadium and titanium are chosen, during which diffusion welding the intermetallic brittle alloys are absent in their joining zones. Micro-hardness values are measured in the joining zones.

When you create a product of accelerator technology, is a very topical problem of obtaining bimetallic elements, reliable connections designs of machines and devices of dissimilar materials [1, 2].

Modern accelerator technology consists mainly of welded structures - vacuum chamber, a device for transportation of elementary particles, vacuum system, pipes and fittings, working in a wide temperature range (from 673 to 4.2 K) and under different load conditions (static and cyclic for level of stress and temperature). They are characterized by a variety of forms, the degree of complexity of design solutions, a broad enough range of materials and weld methods.

Complex variables influence in the operation temperature and force factors, while ensuring a vacuum leak [2], or increased sensitivity of materials at low temperatures to stress concentration and their tendency in some cases, to structural changes (formation intermetallics or solid solutions) cause increased special requirements for the design and fabrication of welded structures in accelerator technology [3,4].

Reliability and durability of the units of accelerator technology largely depends on the properties and qualities of materials used to manufacture them.

By the nature of the materials in accelerator technology can be divided into three groups: employed in the manufacture of parts for the inner cavity of products; protecting the inner cavity of products from the atmosphere; for external components.

The materials for each of the groups subject to various requirements, so the content of the first group should be limited to the contents evaporated in vacuum impurities (Zn, Bi, Sb, Sn, Mn, I, S, etc.).

The presence of these impurities in metals leads to technological heating (for example, the evacuation of electronic systems) to their evaporation and deposition on the elements of the vacuum system. In these same materials should be limited to the content of gases. Increased gas separation materials for the parts of the inner cavity complicates the process of pumping equipment and storage products, particularly when they use gas emission leads to burn them.

The materials enclosing a vacuum chamber from the atmosphere than previously presented above is still very important requirement - they must be vacuum-tight ie, they should not have microscopic cracks, pores and cavities. Thus, when building products are used in accelerator technology welding clean impurities from the materials.

In the manufacture of products in accelerator technology uses a variety of materials to be welded, is traditional austenitic steel 12X18H10T. In recent years significantly increased the use of welded structures accelerator chamber aluminum alloys [5], we note that a further increase in the volume of aluminum alloys limited by their lack of strength, is currently underway to implement and improve processes welded dissimilar alloys: copper + stainless steel, copper + aluminum, copper + steel, stainless steel + titanium.

Currently, the vast majority of designs of vacuum chambers are made of welded, so the main requirement for materials is their good weldability. This term refers not only an opportunity to get out of this material permanent connection of all existing methods of welding, but also, more importantly, the preservation of strength, ductility, resistance to brittle fracture in heat affected zone.

For most combinations of dissimilar metals and alloys that have welding, there are substantial differences in melting temperature, density, coefficient of thermal properties, especially the linear expansion. However, difficulties arise because in most cases with limited mutual solubility for the main combinations of weld metal is extremely difficult to avoid the formation of stable intermetallic phases with high hardness and brittleness.

Among the new methods of welding metals in accelerator technology occupies a special place in a vacuum diffusion bonding, which allows to solve many problems of dissimilar metals, brazing and fusion welding, which are difficult or impossible. Feature of this process is a compound of metals without melting in a vacuum, under conditions excluding contamination of abutting surfaces of harmful impurities, the gases in the development of appropriate technology to obtain a connection to the minimum allowed by plastic deformation.

It is known that during welding of dissimilar materials containing chromium, oxidized, even in high vacuum, but a minimum of isothermal holding is not enough for the formation of chromium oxides [6].

To obtain the vacuum-tight connection bimetallic blanks from copper and steel 12X18H10T developed a method of joining dissimilar materials, whose principle is as follows [7]. On the vacuum chamber of the diffusion welding plant MDV -301 on the lower rod bearings installed flange of copper on the upper rod is fixed flange, stainless steel, which is located at some distance from the copper flange. RF inductor heats the copper flange to a temperature of 1123 K, after unheated stainless steel with the top rod is squeezed onto a copper flange and a pressure up to 20 MPa for 30 seconds .. RF inductor heats team bimetallic billet to a temperature diffusion bonding and welding is obtained by optimally good connection, because the soft copper is heated microplastic deformation creates maximum contact between the surfaces of contact, which is required for the formation of physical contact and developed after interdiffusion at this through close contact prevents the oxidation of stainless steel vacuum chamber residual gases.

Experimental data showed that the temperature welding $T = 1173$ K, pressure $P = 1$ MPa and welding time $t = 20$ min, achieved equally strong, tight and vacuum-tight connection, Fig. 1 shows the microstructure of a bond.

Strength of welded joints of copper to stainless steel obtained under these conditions, when tested in tension was 220-240 MPa, which is close to the ultimate strength of copper. Fig. 1 shows the microstructure of the copper - steel 12H18H10T. As can be seen from the figure, the interface of dissimilar metals are clear and thin, the pores and non-metallic inclusions are absent. This indicates the high quality weld components bimetal obtained by diffusion welding in vacuum, the microhardness of these sites did not significantly change, indicating the absence of intense diffusion interaction in the areas of their contacts, resulting in their solid-solution strengthening. This can be attributed to the fact that the solubility of carbon in copper is very small, but this does not preclude obtaining a lasting and vacuum-tight connection.

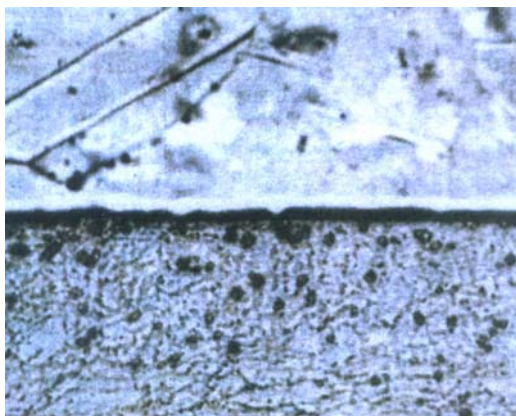


Fig. 1. Microstructure of a bond copper - steel 12X18H10T (x 500)

Some welding of dissimilar materials in terms of scientific research does not cause much difficulty, and their use are the most rational construction sites and products meet the needs of modern science and practice. For example, the welding of dissimilar materials with stainless steel St.3 12X18H10T made fundamental changes in the design and manufacture of the magnet (Fig. 2), where the fixation and orientation of the poles of the unit are provided with guiding elements in the form of pins welded diffusion bonding of steel 3 and 12X18H10T. Pins arranged in a horizontal plane in mutually perpendicular faces of the main pole nakanechnika so that their axes lie in the median plane leveled the gap, and their diameter exceeds the value

of this gap. In addition, in order to eliminate the influence of pins on a uniform field, she made three layers, with upper and lower segment of the pin, located in the corresponding slots of the main magnetic pole piece and made of ferromagnetic material, and the middle part of a nonmagnetic material. Such kind of fixing unit pole at the same time and it is fitting, since the mutually perpendicular arrangement to exclude any bias block relative to the yoke. In addition, the pins in this case, the work of compression, in contrast to the well-known option, which allows the same diameter screw carry heavier loads. Thus, we have a strict system of the yoke-pole block, which is capable of withstanding the stresses produced in the electromagnet, we note that to ensure the homogeneity of the magnetic field lag screw pole unit is also made of magnetic and nonmagnetic steel. Fig. 3 shows the results of the study metallographic interface bimetal. To relieve tension before the final machining performed vacuum annealing, it turned out that after heat treatment, is developing a transition zone between layers of dissimilar steels, mainly carbon from steel 3 in the direction of steel 12X18H10T (Fig. 3., right). Education and development of transition zones between dissimilar steels eliminated by blocking the diffusion redistribution of carbon between them by introducing an intermediate layer of copper.

For the connection the titanium to steel 12H18H10T used a double lining of the steel copper, titanium from vanadium.

The analysis testifies that there is currently no data on the regularities of formation and growth of intermetallic compounds between titanium alloys and steel, no data of microhardness in the joint zone, which is necessary for the evaluation of the weldability of dissimilar metals. To assess the weldability according to the recommendations of the International Institute of Welding (IIW) toughness of heat affected zone should not exceed $HV = 350$ [8].

The results of studies of the microhardness in the joint zone of transition elements titanium-steel joined by various methods into a vacuum of $1,3 \times 10^{-3}$ Pa. In the study used the following methods:

1. diffusion welding in vacuum with a layer of vanadium-copper;
2. Vacuum brazing Ti / L-CuSn12 / 316 L, $T = 1040^\circ \text{C}$;
3. Vacuum brazing, Ti / L-Ni-2 / 316 L, $T = 1080^\circ \text{C}$

Fig. 4 shows graphs of microhardness in the joint zone, the results of studies that the greatest plasticity in the bond titanium to steel is achieved through the use of vanadium-copper strip. Tensile fracture occurs on copper. Mechanical tests on the stretching shows that failure occurs on copper and is 200-220 MPa, carried out research and industrial performance testing of compounds at a temperature of 4.2 K.

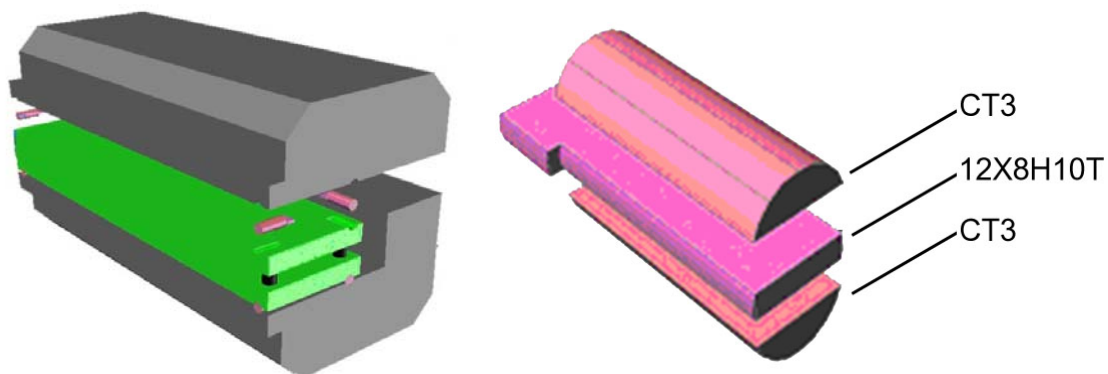


Fig. 2. Left – schematic model of the magnet; right – a schematic model of the pin design of heterogeneous materials.

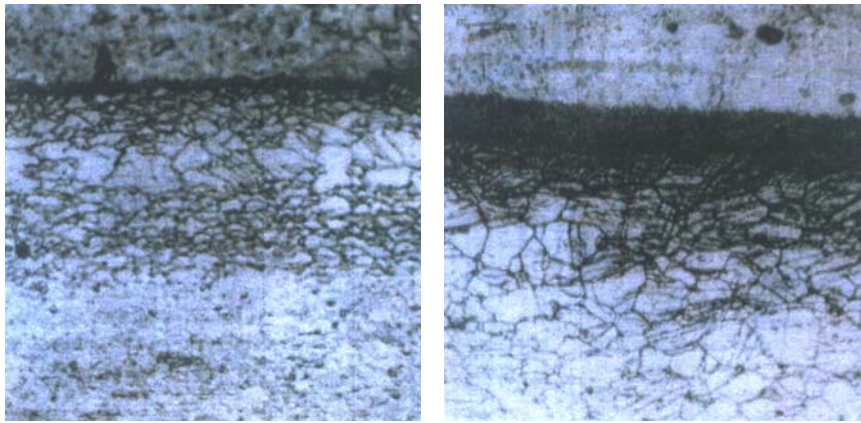


Fig. 3. Left - the microstructure of the interfaces St.3-12X18H10T; right - microstructure of interfaces St.3-12X18H10T, after heat treatment.

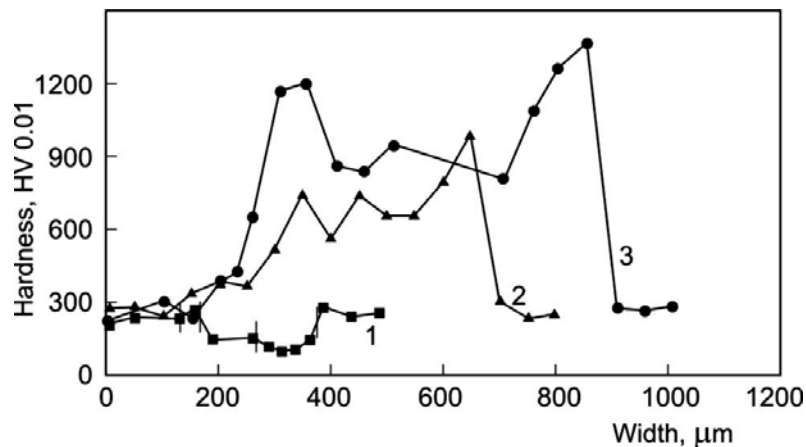


Fig. 4. Distribution of the microhardness in the joint zone: 1 – Diffusion welding of Ti / V / Cu / 12H18H10T (T = 1000 °C, R = 5 MPa, t = 15min); 2 – Vacuum brazing Ti / L-CuSn12 / 316 L, T = 1040 °C; 3 – Vacuum brazing, Ti / L-Ni-2 / 316 L, T = 1080 °C.

References

- [1] Abashian A., Aghasyan M., Amatuni G., Arakelyan V., Avagyan V. et al. ASLS-CANDLE R-001-02, July (2002) 117-125.
- [2] Tunyan S., Avagyan V., Aghasyan M., Ivanyan M. in Advanced Radiation and Applications. (ed. H. Wiedemann), Spinger, (2006) Printed in the Netherlands, 431-436.
- [3] Brinkmann R., Materlik G., Rossbach J., Wagner A., DESY 1998-048 and ECFA (1997), 182.
- [4] Aghasyan M., Avagyan V., Tunyan S. 3 rd International Workshop on Mechanical Engineering Design of Synchrotron Radiation Equipment and Instrumentation, Grenoble, France, MEDSI . (2004).
- [5] Hsiung G.Y., Chan C.K. et al. NSRRC conf., Taiwan.
- [6] Sysoev, AP, Sergeev AV, Kazakov, in Diffusion welding mednromovogo pseudoalloy with copper, "Poroshk", (1984), 45-47.
- [7] Avagyan V.S. Patent N 1533 A2, 24.03.2004, "Inventions and Discoveries" Official Bulletin, N 5 (46), Yerevan, (2004), 4.
- [8] Yu. Ruge Technique Welding Handbook. Trans. with him., Moskow, Metallurgy, (1984) 552.

УНИВЕРСАЛЬНОЕ УСТРОЙСТВО ДЛЯ ОПРЕДЕЛЕНИЯ ЗАРЯДА ХИМИЧЕСКИХ ИСТОЧНИКОВ ТОКА

А. Р. Симонян¹, А. А. Саноян¹, А. Г. Гулян¹, Р. А. Симонян¹

¹ Institute of Radiophysics and Electronics, Alikhanian Brothers str. 1, 378410 Ashtarak, Armenia

Описан точный измеритель количества заряда полученного химическим источником тока (ХИТ) во время заряда и отдавшего нагрузке во время разряда.

Устройство работает как зарядник ХИТ, как разрядник ХИТ, как зарядник ХИТ с асимметричным режимом заряда и как измеритель количества заряда при заряде и при разряде.

Благодаря высокой точности измерения, универсальности и простоте обслуживания прибор может найти применение и для разработчиков ХИТ и для эксплуатационщиков и специалистов по ремонту ХИТ.

Ключевые слова: заряд, разряд, асимметричный режим, напряжение, ток.

В [1] описано устройство для измерения емкости ХИТ, измеряющего как полученного от источника питания, так и отданного нагрузке количество зарядов. Однако, описанное устройство требует обслуживающий персонал высокого класса и кроме того, из-за наличия внутреннего сопротивления система измерения напряжения на зажимах ХИТ приводит к дополнительной погрешности при срабатывании системы отключения (или включения) режимов заряда (разряда).

В данной статье описано устройство для точного измерения емкости как при получении, так и при отдаче зарядов во время разряда на резистивной нагрузке, при этом ток стабилизируется как при зарядке так и при разрядке ХИТ.

В прибор введен дополнительный режим- режим асимметричного заряда, когда в одном полупериоде ХИТ заряжается, а во время второго полупериода разряжается. Этим режимом согласно литературе [2,3] ХИТ (серебряно-цинковые, свинцовые и т.д.) частично восстанавливается. Полученное значение ампер-часов сохраняется для регистрации.

Отметим, что известный прибор “Кулон-12ns”, фирмы “А и Т ситемы”, хотя и индицирует емкость свинцовых аккумуляторов, но не измеряет. Упрощенная функциональная схема блока управления разработанного измерителя имеет следующий вид (рис. 1).

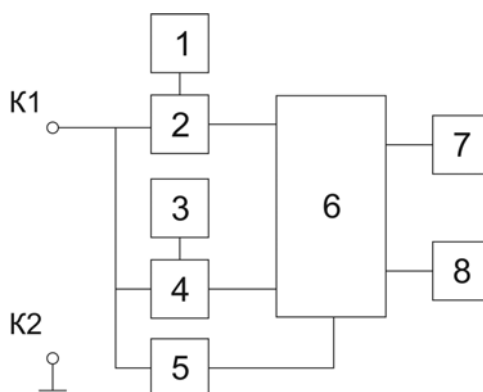


Рис. 1 . Упрощенная функциональная схема блока управления. K1, K2 клеммы ХИТ, 1,3,7,8 источники напряжения, 2 источник стабилизированного тока заряда, 4 нагрузка тока разряда, 5 блок измерения напряжения, 6 блок управления

Блок управления процесса заряда и разряда ХИТ состоит из следующих узлов и элементов: K1 и K2 клеммы для подключения аккумуляторов, при этом к клемме K1 подключается положительный вывод, а на K2 подключается отрицательный вывод и одновременно K2 соединяется с общим проподом устройства. 2 и 4 блоки заряда и разряда соответственно. Для установления величины тока во время заряда к блоку 2 подключен управляемый источник стабилизированного напряжения (УИСН) 1, а для установления величины тока разряда к блоку 4 подключен УИСН 3. 5- блок измерения напряжения заряжаемого (разряжаемого) аккумулятора. Для снятия влияния внутреннего сопротивления ХИТ, измерение напряжения производится во время отсутствия тока заряда (разряда).

Выходной сигнал блока 5 поступает на вход блока управления 6, который в зависимости от уровня напряжения на клеммах ХИТ и от полученной команды включает или блок 2 (заряд) или блок 4 (разряд).

Уровень напряжения при котором отключается блок 2 определяет блок УИСН 7, а уровень напряжения для отключения процесса разряда определяет УИСН 8. Блок управления работает следующим образом. После подключения клеммы устройства к зажимам ХИТ и включения питания устанавливается при помощи блоков УИСН 1,3,7,8 величина токов заряда и разряда напряжения при которых отключаются процессы заряда и разряда, после чего с помощью кнопок команд включается один из следующих режимов:

1. Режим заряда аккумулятора
2. Режим разряда аккумулятора
3. Режим заряда аккумулятора в асинхронном режиме
4. Режим измерения емкости аккумулятора

Измерения количества заряда полученного или отданного аккумулятором производится по функциональной схеме согласно рис. 2.

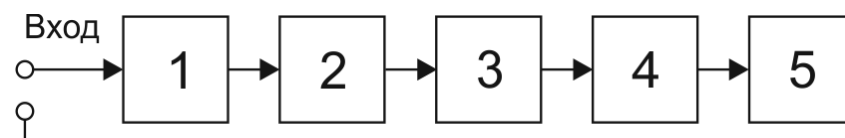


Рис. 2. Функциональная схема измерения количества заряда. 1 усилитель напряжения, 2 преобразователь напряжения-частота, 3 счетчик импульсов, 4 цифро-аналоговый преобразователь, 5 вольтметр.

Схема измерения заряда работает следующим образом. Напряжение образованное на токоизмерительном резисторе подается на вход усилителя 1 и после усиления поступает на вход линейного преобразователя напряжения-частота 2. Полученная на выходе преобразователя 2 последовательность импульсов в течении заряда (или разряда) накапливается в счетчике импульсов 3. Количество импульсов счетчика 3 преобразуется в напряжения постоянного тока цифро-аналоговым преобразователем 4, выходное напряжение которого измеряется вольтметром постоянного тока 5.

Система измерения количества зарядов отданных аккумулятором нагрузке во время разряда, не отличается вышеописанного. Отметим, что перед началом любой команды счетчики обнуляются.

При режимах заряда, разряда и в режиме асимметричного заряда вольтметр 6 подключен к выходу измерителя напряжения 5 (рис. 1), а при режиме измерения заряда вольтметр показывает количество ампер-часов в режиме разряда. Измерения ампер-часов производится следующим образом. После подключения ХИТ к клеммам К1 и К2 по команде измерение ампер-час происходит полный заряд. После отключения режима зарядки когда напряжение на аккумуляторе превышает установленный уровень происходит автоматический переход из режима заряда в режим разряда. Как только напряжение уменьшается на клеммах ниже установленного блоком 8 (рис. 1) уровня процесс разряда останавливается и вольтметр показывает количество ампер-часов отданное нагрузке. Для устранения влияния внутреннего сопротивления на точность показания измерителя напряжения 5 (рис. 1) измерения производится во время специально созданной паузы, когда система управления останавливает процесс заряда или разряда. После каждой выполненной операции устройство переходит в дежурный режим с малым (менее 0,5 Вт) потреблением мощности. В этом режиме устройство может находиться неограниченно долгое время.

Разработанный измеритель имеет следующие основные параметры:

- 1) Режим заряда ХИТ
 - a) Диапазон величины тока заряда 0,1...10 А
 - b) Дискретность установки тока заряда 0,1 А
 - c) Диапазон установки напряжения отключающего процесс заряда 11...15 В
- 2) Режим разряда ХИТ
 - a) Диапазон величины тока разряда 0,1...10 А
 - b) Дискретность установки тока разряда 0,1 А
 - c) Диапазон установки напряжения отключающего процесс разряда 9,5...12 В
- 3) Режим асимметричного заряда ХИТ
 - a) Диапазон установки величины тока в полупериоде заряда 0,1...10 А
 - b) Диапазон установки тока в полупериоде разряда 0,1...10 А
 - c) Дискретность установки тока 0,1 А
 - d) Диапазон установки напряжения отключающего процесс заряда асимметричным током 11...15 В
- 4) Режим измерения ампер-часов ХИТ
 - a) Диапазон измерения емкости во время разряда 0,1...200 Ач
 - b) Допустимая погрешность $\leq 1,5\%$

Разработанный прибор может найти применение как среди разработчиков, так и среди пользователей ХИТ так как обеспечивает

- a) Точное измерения емкости ХИТ,
- b) Позволяет исследовать влияние заряда при асимметричном токе на параметры аккумулятора
- c) Позволяет контролировать ток и напряжение как во время заряда так и во время разряда ХИТ.

ЛИТЕРАТУРА

1. Симонян Р.А., Мартиросян О.А., Устройство для измерения емкости в ампер-часах аккумуляторных батареек, изв. НАН РА и ГИУА, ТН. 2004, TLVII, N3, ст. 334
2. Тимофеев Ю.П., Ильин Н.М., Электрооборудование автомобиля, неисправности и техническое обслуживание, М., Транспорт, 1981, 140с.
3. Романов В.В., Хасиев Ю.М., Химические источники тока, М., Сов. Радио, 1968, 378с.

Универсальный термостатный модуль

Р. А. Симонян¹, А. А. Саноян¹, А. Г. Гулян¹

¹ *Institute of Radiophysics and Electronics, Alikhanian Brothers str. 1, 378410 Ashtarak, Armenia*

Дается описание модуля для построения термостатов, имеющих простую конструкцию, высокую точность поддержания температуры, малую инерционность, прямой выход для измерения температуры внешним прибором. Эти качества получены благодаря применению биполярного транзистора как в качестве термодатчика, так и в качестве нагревателя, а также временному разделению процесса измерения и регулирования температуры. Описанный модуль может найти применение при разработке термостатов, измерителей мощности СВЧ диапазона, термоанемометров, эталонных источников радиотеплового излучения (горячих нагрузок).

Известны термостаты, в которых биполярный транзистор используется в качестве нагревателя и одновременно является датчиком температуры [1,2]. Такое включение позволяет значительно снизить тепловое сопротивление между нагревателем и датчиком температуры, что приводит к повышению точности, ускорению процесса установления температуры в камере и упрощению конструкции термостата.

Однако в указанных решениях отсутствует возможность измерения температуры в камере без дополнительного внешнего термометра, что существенно ограничивает возможности указанных термостатов. Кроме этого, в этих термостатах напряжение на датчике температуры (переход база-эмиттер) зависит не только от температуры, но и от приложенного к коллектору напряжения, что требует дополнительной стабилизации коллекторного напряжения. В [3] описан термостат в котором введен ключевой элемент, благодаря чему уменьшается разница между температурой отключения и включения транзисторного нагревателя. Несмотря на это, сложность регулирования режимов измерения температуры и калибровки термостата является основным недостатком указанного термостата, к тому же не имеющего выхода для непосредственного измерения температуры в камере.

В настоящей работе описан термостатный модуль, собранный согласно [4,5], при этом в [5] описано устройство для измерения температуры, датчик которого работает в импульсном режиме на прямосмещенном р-п переходе (ток стабилизирован, скважность импульса 2), выходное напряжение пропорционально температуре перехода. В [4] описано устройство для регулирования температуры, (термостат) в котором в качестве измерителя температуры использован термометр согласно [5], а регулирование температуры осуществляется переключением транзистора из режима измерения прямосмещенным р-п переходом в режим регулирования температуры транзистора (коллекторного перехода) который может быть приклеен к камере с любой конфигурацией.

Таким образом, в этом устройстве произведено временное разделение процесса измерения температуры и ее регулирования.

Упрощенная функциональная схема разработанного термостатного модуля показана на рис. 1.

На рисунке показаны цифрами 1-транзистор, работающий как термодатчик, так и в качестве нагревателя. К транзистору прикрепляется камера термостата. 2,3,4- ограничивающие и развязывающие резисторы. 5,6,7-электронные ключи, при этом ключ 5 и ключи 6,7 работают в противофазных режимах. 8-генератор меандра с противофазными выходами, 9-блок управления нагревом, 10-блок термометра, 11-дифференциальный усилитель, 12- источник регулируемого стабильного напряжения постоянного тока (задатчик), Схема термостата питается от двухполярного стабилизированного источника напряжения постоянного тока не показанного на рисунке.

Схема работает следующим образом. После включения питания на выходе генератора 8 получается два противофазных напряжения с частотой примерно 40-80Гц. В одном полупериоде включается ключ 5 и отключаются ключи 6 и 7. В течение этого полупериода происходит измерение температуры блоком 10, на выходе которого имеем напряжение пропорциональное температуре. В другом полупериоде работы генератора 8 ключи 6 и 7 включаются, а ключ 5 отключается. В этом полупериоде происходит нагрев транзистора 1, пропорционально уровню сигнала на входе блока управления нагревом 9. Входной сигнал блока 9 получается с выхода дифференциального усилителя 11. На одном входе усилителя 11 имеем выходной сигнал термометрического блока 10, на другом входе выходное напряжение задатчика 12 (регулируемого источника напряжения постоянного тока).

Если выходное напряжение датчика 12 больше, чем напряжение термометра 10, то на выходе блока 11 имеем положительное напряжение, пропорциональное разности входных напряжений блока 11. Этим напряжением и управляется нагрев транзистора 1 блоком 9.

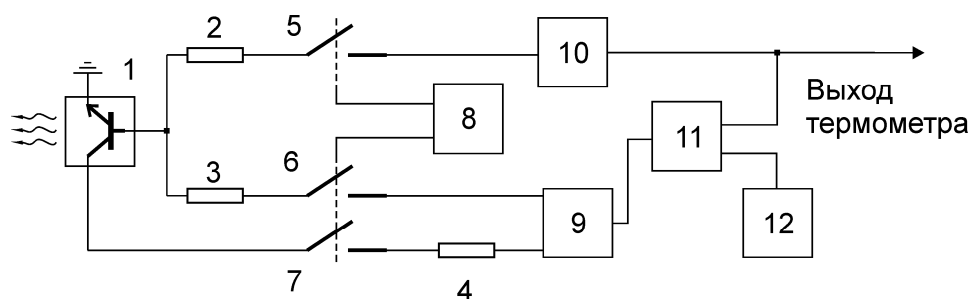


Рис.1 Функциональная схема термостата. 1-термодатчик-нагреватель на транзисторе (КТ961), 2,3,4-резисторы, 5,6,7-электронные ключи, 8-генератор меандра с противофазными выходами, 9-блок управления нагревом транзистора, 10-блок измерения температуры, 11-дифференциальный усилитель, 12-источник регулируемого стабильного напряжения постоянного тока.

Очевидно что быстродействие термостатного модуля будет в основном определяться быстродействием термометра 10 и быстротой (мощностью) нагрева транзистора 1, питающего блоком 9. В данном устройстве время передачи температуры от термодатчика (переход база-эмиттер) к системе терморегулирования определяется частотой генератора 8 (находится в пределах $12 \div 25 \times 10^{-3}$ сек.). Стабильность установленного значения температуры модуля т.е. транзистора 1 и ее дрейф будет определяться кроме параметров датчика, также временем и температурным дрейфом дифференциального усилителя 11. При исполнении блока 11 на прецизионном операционном усилителе ОР-07, временной дрейф температуры модуля будет иметь величину порядка $0,2 \times 10^{-3}$ °С /месяц, а температурный дрейф - $0,3 \times 10^{-3}$ °С при изменении температуры окружающей среды на 1 °С.

Для определения связи между дрейфом датчика 12 и временным и температурным дрейфом температуры модуля приведена эквивалентная схема исходя из того, что в термостатном модуле происходит временное разделение процесса измерения и регулирования температуры, при этом в одном полупериоде работают только переход база-эмиттер транзистора 1 и термометрический блок 10 (остальные узлы блока не действуют). В полупериоде управления работают все блоки, кроме блока измерения, хотя на выходе блока 10 имеется постоянное напряжение, величина которого пропорциональна температуре р-п перехода транзистора 1. В полупериоде измерения происходит тепловыделение в переходе база-эмиттер измерительным током блока 10 (до 10×10^{-6} Вт), а во время регулирования в переходе база-коллектор мощность нагрева может достиг до единиц и десятки ватт. Учитывая вышенаписанное упрощенная функциональная схема будет иметь следующий вид (рис. 2).

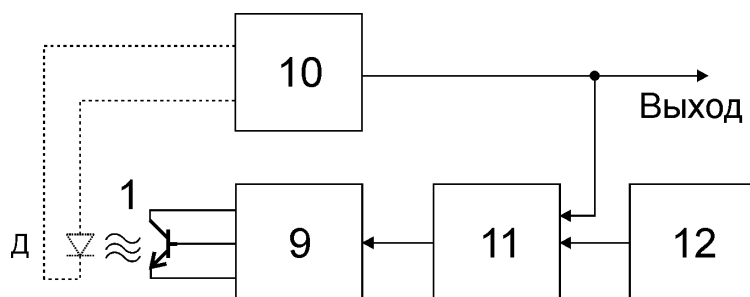


Рис.2 Упрощенная функциональная схема термостата. 10-блок измерения температуры, 11-дифференциальный усилитель, 12-источник регулируемого стабильного напряжения постоянного тока.

В упрощенной схеме термостатный модуль показан в полупериоде регулирования температуры, а пунктиром нарисован датчик температуры Д (переход база-эмиттер транзистора 1) лишь подчеркивает независимость полупериода измерения датчиком Д. Учитывая реальные теплотехнические параметры ВЧ и СВЧ мощных транзисторов, на которых целесообразнее всего построить выше описанный модуль, построим теплотехническая эквивалентная схема модуля (рис.3).

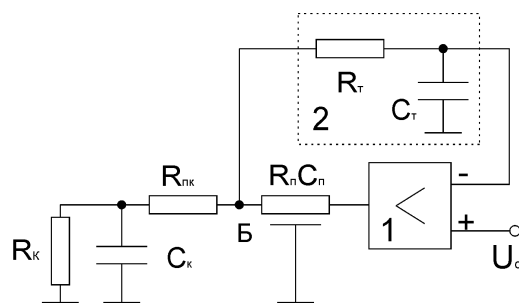


Рис.3 Теплотехническая эквивалентная схема термостатного модуля

В упрощенной схеме все практически безинерционные элементы объединены в блоке усилителя 1, оставляя только $R_T C_T$ интегрирующее звено (эквивалент синхронного фильтра и детектора блока измерения [5]) в блоке термометра 2. Транзистор показан с теплотехническим эквивалентом распределенной емкости и теплового сопротивления коллекторного перехода, тепловых сопротивлений $R_{пк}$ переход-корпус, тепловая емкость корпус-окружающая среда $C_к$, сопротивлением корпус-окружающая среда $R_к$. Подключения входа термометрического блока (блок 2 рис.3) после распределенной цепи $R_п C_п$ наиболее соответствует физической картине измерения температуры, так как элементы $R_{пк}$, $C_к$ и $R_к$ косвенно входят в цепь обратной связи, практически не влияя на процесс регулирования температуры коллекторного перехода.

Для предотвращения самовозбуждения и повышения помехоустойчивости системы, постоянная времени синхронного фильтра термометра [5] $\tau = R_T C_T$ выбиралась порядка 0,5 секунд, при этом суммарная зарядка по цепи $R_п C_п$ для указанных транзисторов на 1-2 порядка меньше. Следовательно, особых мер для предотвращения самовозбуждения в замкнутом контуре терморегулирования не требуется. В данной системе были изменены коэффициенты усиления блока 1 (рис. 3) начиная от 10^4 до 10^4 , в результате чего величина напряжения задатчика U_0 практически стала равной напряжению термометра. Это значит, что для получения высокой точности термостатирования следует применить высокостабильный источник. Для этого найдено целесообразным применение нормального элемента второго класса (X480) с соответствующей согласующей схемой.

Измеренное значение изменения температуры в камере термостатирования менее чем $0,01^\circ\text{C}$, при теплоизоляции камеры пенопластом ПХВ-1 толщиной 10мм и при изменении температуры окружающей среды $\pm 10^\circ\text{C}$ а дрейф связанный с дрейфом задатчика температуры составляет порядка $0,001^\circ\text{C}$.

Для измерения быстродействия термостата на выходе задатчика температуры была сформирована ступень напряжения на величину нагрева 10°C , и фронтом менее 10^{-4} секунд. В результате измеренное значение постоянной времени термометра и термостата составили порядка $< 0,3$ с, при средней мощности нагрева 2,4 Вт.

Благодаря высокой точности, малоинерционности и малым габаритам, данный термостатный модуль может найти широкое применение в радиотехнике (стабилизация тепловых режимов схемных элементов и блоков), в измерительной технике для эталонирования термометров, для построения малогабаритных регулируемых источников радиотеплового излучения миллиметрового, субмиллиметрового и ИК диапазона. Кроме этого, термостатический модуль может найти применение при разработке термоанемометров.

ЛИТЕРАТУРА

1. Борисов Л. Г., АС 622066, Устройство для регулирования температуры, Бюл. 32, 30.08.1978
2. Долотов П. Н., Преображенский В. П., АС 997004, Устройство для регулирования температуры, Бюл. 6, 15.02.1983
3. Аржанникова Т. В., Сосин Ю. В., АС 862124, Регулятор температуры микросхем, Бюл. 33, 07.09.1981
4. Симонян Р. А., Торикян Д. Э, АС 1501006, Устройство для регулирования и измерения температуры, Бюл. 30, 15.08.1989
5. Симонян Р. А., Везирян Э. Г., АС 1557458, Устройства для измерения температуры, Бюл. 14, 15.04.1990
6. Давидов П. Д., Анализ и расчет тепловых режимов полупроводниковых приборов, М. 1967

Sponsored by:



State Committee of Science of Armenia



National Academy of Sciences of Armenia



Erebuni Biosecurity LLC



International Science and Technology Center (ISTC)



The National Foundation of Science and Advanced Technologies

